

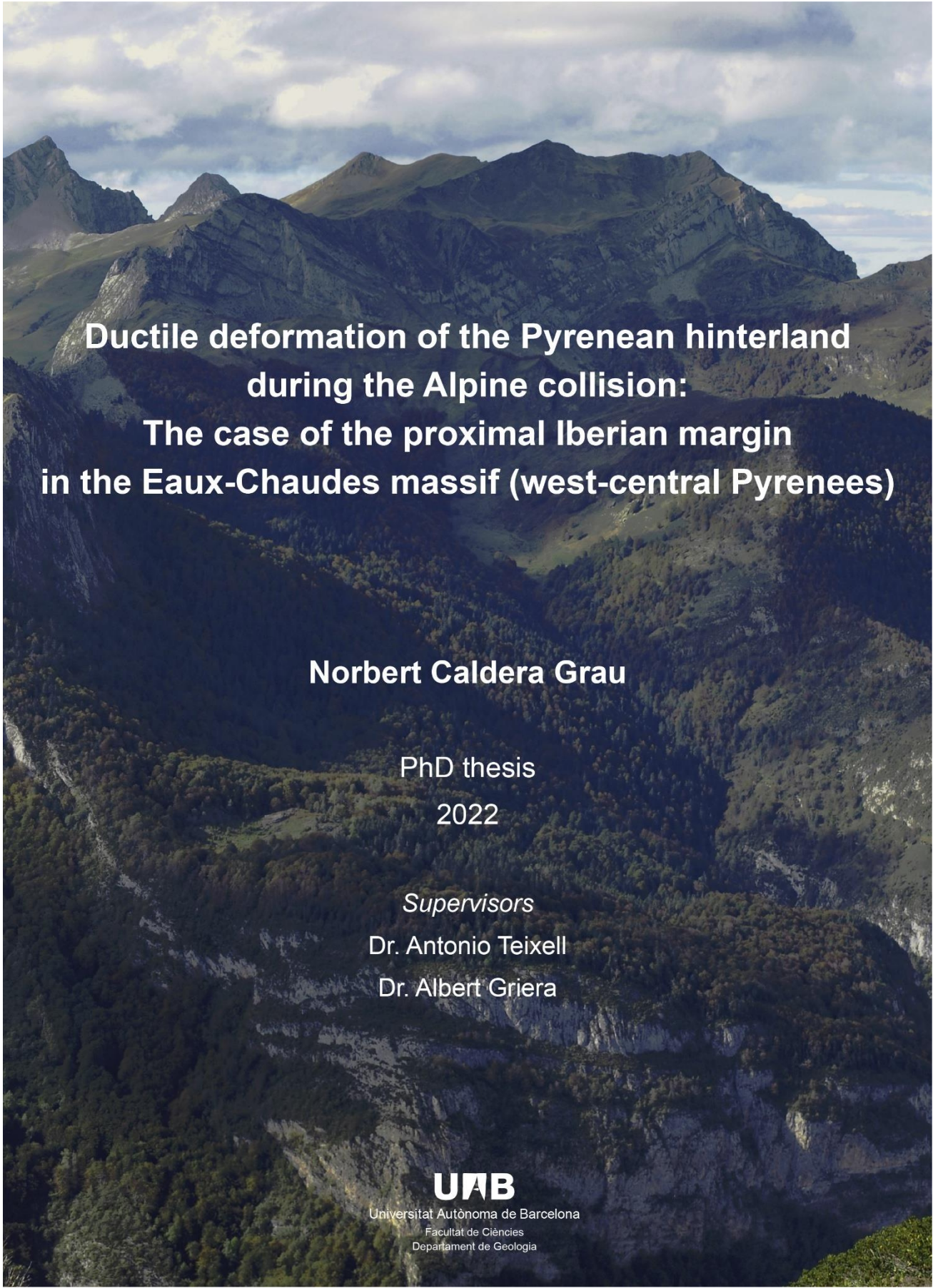


Universitat Autònoma de Barcelona

**ADVERTIMENT.** L'accés als continguts d'aquesta tesi queda condicionat a l'acceptació de les condicions d'ús establertes per la següent llicència Creative Commons:  [http://cat.creativecommons.org/?page\\_id=184](http://cat.creativecommons.org/?page_id=184)

**ADVERTENCIA.** El acceso a los contenidos de esta tesis queda condicionado a la aceptación de las condiciones de uso establecidas por la siguiente licencia Creative Commons:  <http://es.creativecommons.org/blog/licencias/>

**WARNING.** The access to the contents of this doctoral thesis it is limited to the acceptance of the use conditions set by the following Creative Commons license:  <https://creativecommons.org/licenses/?lang=en>



**Ductile deformation of the Pyrenean hinterland  
during the Alpine collision:  
The case of the proximal Iberian margin  
in the Eaux-Chaudes massif (west-central Pyrenees)**

**Norbert Caldera Grau**

PhD thesis

2022

*Supervisors*

Dr. Antonio Teixell

Dr. Albert Griera

**UAB**

Universitat Autònoma de Barcelona

Facultat de Ciències  
Departament de Geologia

**Ductile deformation of the Pyrenean hinterland  
during the Alpine collision:  
The case of the proximal Iberian margin  
in the Eaux-Chaudes massif (west-central Pyrenees)**

Memòria presentada per Norbert Caldera Grau per optar al títol de Doctor en Geologia

Setembre, 2022

*Tesi doctoral dirigida per*

Dr. Antoni Teixell Cácharo, Departament de Geologia de la Universitat Autònoma de Barcelona

Dr. Albert Griera Artigas, Departament de Geologia de la Universitat Autònoma de Barcelona

Dr. Antonio Teixell Cácharo

Dr. Albert Griera Artigas

Norbert Caldera Grau

**Cover image:** *The Eaux-Chaudes Fold Nappe from an eastern viewpoint in the fold core next to the Cézy Pic.*

This research was supported by a predoctoral PIF grant from the Universitat Autònoma de Barcelona and projects CGL2014-54180-P and PGC2018-093903-B-C21 of MINECO and MICIU. This PhD project was part of the Orogen project community (CNRS-BRGM-TOTAL).



*A la meva família*

*Com una pedra. Una pedra sempre té raó. Com un núvol*

Josep Lluís Badal, "Les coses que realment han vist aquests ulls inexistentés"

*Comme tout y est pur,*

*dans nos montagnes.*

*Ces montagnes qui sont si hautes  
et que l'on chantera longtemps encore...*

*Tant qu'il y aura des Pyrénées*

*Et tant qu'il y aura des Pyrénées,*

*Poètes et conteurs chanteront*

*Aqueres mountannes que tan haute son...*

Maguelonne Toussaint Samat, «Contes et légendes des Pyrénées»

*Il est encore dans ces montagnes des crêtes escarpées;*

*il est encore de fines arêtes et des ravins profonds,*

*qui ont échappé aux investigations*

Yves Ternet «Étude du synclinal complexe des Eaux-Chaudes (Basses-Pyrénées)»

# Index

<b>Abstract</b> .....	<b>11</b>
<b>Resum</b> .....	<b>12</b>
<b>Chapter 1: Introduction</b> .....	<b>13</b>
1.1. The Mesozoic rift and the Pyrenean orogeny .....	14
1.2. Geological setting .....	19
1.3. Classical structural interpretation of the Eaux-Chaudes massif .....	20
1.4. Motivation of the study .....	25
1.5. Thesis structure .....	26
<b>Chapter 2: Stratigraphy of the Eaux-Chaudes massif and surroundings</b> .....	<b>28</b>
2.1. Paleozoic basement and lower Triassic .....	28
2.2. Allochthonous Keuper sheet .....	30
2.3. Upper Cretaceous .....	30
<b>Chapter 3: Methodology</b> .....	<b>33</b>
3.1. Field work .....	33
3.2. Petrography and microstructure from thin sections .....	35
3.3. Geological mapping and cross-section construction .....	36
3.4. Paleothermometry .....	37
3.4.1. Raman Spectroscopy of Carbonaceous Material (RSCM) .....	37
3.4.2. Electron Microprobe analysis (EMPA) .....	38
3.5. Micro-scale fabric: SEM-Electron Backscattered Diffraction (EBSD) .....	40
3.6. Sample preparation for EBSD and SEM analyses .....	42
3.7. Cathodoluminescence analysis .....	43

<b>Chapter 4: Macroscale structure of the Eaux-Chaudes massif (ECM)</b>	
<b>and implications for the deformation of the Pyrenean hinterland .....</b>	<b>44</b>
4.1. Structural units in the study area .....	47
4.1.1. The Eaux-Chaudes Nappe (ECN) .....	48
4.1.2. The Paleozoic nappes over the ECN .....	51
4.1.3. The Lakora thrust system and the Chaînons Béarnais Belt .....	51
4.2. Structural cross-sections of the Eaux-Chaudes massif .....	52
4.2.1. Western sector (Ossau Valley): The Eaux-Chaudes Fold Nappe (ECFN) .....	54
4.2.2. Eastern sector (Pic de Ger massif): The ductile fold-thrust system .....	58
4.3. Discussion .....	64
4.3.1. On the variation of the tectonic style .....	64
4.3.2. What caused the structural contrast between the fold nappe and the fold-thrust domain?	
Constraints from the recumbent fold .....	64
Granitic vs non-granitic basement .....	66
The mechanical role of weak units:	
the underlying Silurian and overlying Keuper .....	68
4.3.3. Weld structures within the upper Cretaceous .....	70
4.4. Sequential evolution of the upper Iberian margin: the Eaux-Chaudes fold nappe and the eastern Eaux-Chaudes fold-thrust system .....	73
4.4.1. Sequential evolution of the Eaux-Chaudes fold nappe (Fig. 4.16) .....	73
4.4.2. Sequential evolution of the eastern Eaux-Chaudes fold-thrust imbricate fan (Fig. 17) .....	77
4.5. Implications on the collision of the Iberian margin during the Pyrenean orogeny .....	79
4.6. Conclusions from the macroscale structural study .....	80
<b>Chapter 5: Paleotemperature of the Eaux-Chaudes massif .....</b>	<b>82</b>
5.1. Raman Spectroscopy results .....	83

5.1.1. Paleothermometry of the Mesozoic of the Eaux-Chaudes massif .....	88
5.1.2. Paleothermometry of Paleozoic rocks and the allochthonous Keuper sheet .....	90
5.1.3. Paleothermometry around the western termination of the Axial Zone .....	91
5.2. Electron Microprobe results .....	92
5.3. Paleothermal implications .....	99
5.3.1. Thermal record in the Eaux-Chaudes massif .....	99
Thermal history of the North Pyrenean Zone: the rift axis .....	106
Thermal history of the northern Iberian margin during the Pyrenean collision .....	107
5.4. Conclusions of the paleothermal work .....	109
 <b>Chapter 6: Microstructure and fabric</b> .....	<b>111</b>
6.1. Deformation of the Cretaceous carbonates .....	112
6.1.1. Domains of strain in the Eaux-Chaudes massif .....	114
6.1.2. Field structural data in relation to the strain domains .....	115
6.2. Microstructures from petrographic microscopy .....	117
6.3. EBSD analysis .....	119
6.3.1. Textural analysis of the upper Cretaceous carbonates .....	122
Phase content .....	122
Grain size .....	124
Fabric strength .....	125
6.3.2. Paleopiezometry and mechanisms of calcite deformation .....	135
6.4. Deformation of quartz in the Eaux-Chaudes massif .....	138
6.5. Results for deformation domains from the EBSD analysis .....	139
6.5.1. Undeformed Eaux-Chaudes Fold Nappe domain (normal limb) .....	139
6.5.2. Deformed Eaux-Chaudes Fold Nappe domain (overturned limb and hinge area).	140
6.5.3. Weakly deformed autochthon domain .....	141
6.5.4. Deformed eastern autochthon domain .....	141



6.6.	Discussion .....	142
6.6.1.	Fabric strength from Crystallographic-Preferred Orientations .....	142
	Monomineralic mylonites .....	142
	Polymineralic mylonites .....	144
6.6.2.	Calcite grain size distribution .....	146
6.6.3.	Spatial distribution of the deformation .....	148
6.7.	Implications and conclusions .....	150
 <b>Chapter 7: Cathodoluminescence of upper Cretaceous carbonates .....</b>		<b>152</b>
7.1.	Calcite .....	154
7.1.1.	Calcite 1 (yellow CL) .....	156
7.1.2.	Calcite 2 (blue CL) .....	156
7.1.3.	Calcite 3 (red-brownish CL) .....	157
7.1.4.	Calcite 4 (non-luminescent) .....	157
7.2.	Dolomite .....	160
7.2.1.	Dolomite dull-violet CL .....	164
7.2.2.	Dolomite dull to bright magenta CL .....	164
7.2.3.	Dolomite dull to bright red CL .....	164
7.2.4.	Complex dolomitization processes .....	165
7.3.	Implications and conclusions .....	166
 <b>Chapter 8: General discussion .....</b>		<b>169</b>
8.1.	Alpine deformation of the west-central Pyrenean hinterland .....	169
8.1.1.	The upper Cretaceous carbonates of the Eaux-Chaudes massif .....	169
8.1.2.	The upper Triassic of the Eaux-Chaudes massif .....	171
8.1.3.	The Paleozoic rocks of the Eaux-Chaudes massif .....	171
8.1.4.	The fate of the upper Iberian margin .....	172
8.2.	Paleotemperature of Iberian plate .....	174

8.3.	Microfabrics .....	175
8.4.	Diagenetic evolution .....	177
8.5.	Orogen-scale implications .....	179
<b>Chapter 9: Conclusions .....</b>		<b>181</b>
9.1.	Reinterpretation of the large-scale structure .....	181
9.2.	Paleothermal record of the Alpine orogeny .....	182
9.3.	Micro-scale structure .....	183
9.4.	Diagenetic evolution .....	184
9.5.	Orogen-scale conclusions .....	184
<b>Chapter 10: References .....</b>		<b>185</b>
<b>Agraïments / Acknowledgments .....</b>		<b>199</b>
<b>Appendix I .....</b>		<b>202</b>
<b>Appendix II .....</b>		<b>214</b>

## Abstract

Alpine deformation in the hinterland of the Pyrenean belt is poorly constrained due to the strong erosion of the post-Paleozoic rocks in the topographic axis of the Pyrenees. The upper Cretaceous limestones of the Eaux-Chaudes massif, enclosed by Paleozoic rocks in the interior of the west-central Pyrenees, show evidence of complex ductile deformation and a large-scale structural style not reported hitherto for the Alpine collisional stage.

This thesis proposes an innovative reinterpretation of the structure and evolution for the Eaux-Chaudes massif, addressing the collisional deformation of the upper Iberian margin previously developed during the Mesozoic rifting. Paleothermal and microstructural inspection of the upper Cretaceous limestones emphasize the ductility occurred in the main deformation event.

The Pyrenean orogeny started by the flexure of the Iberian margin deepening to the north, evidenced by the sedimentation of a Campanian-Maastrichtian flysch. As the collision of the Iberian and European margins progressed, the flexure of the Iberian plate resulted in the deep burial of the future Eaux-Chaudes massif. The climax of the main deformation event occurred under moderately high temperatures accounting for ductile structures and penetrative foliation and lineation. The strong Eaux-Chaudes granite in the Paleozoic basement near the Ossau valley favoured the development of a large-scale recumbent fold nappe in conjunction with two effective detachment levels, one in the upper part of the Paleozoic basement (in the Silurian), and the other in an allochthonous Keuper salt sheet emplaced by the major structure inverting the margin (the Lakora thrust system). Structural inheritance and rheological heterogeneity of the basement induced strong changes in the lateral evolution of this fold, turning eastward into a simpler, ductile thrust imbricate fan.

The novel scheme proposed in this work warns about the difficulties of unravelling this type of deformation in the interior of the Pyrenees and other orogens due to the strong erosion and the structural superposition in the ancient rocks which dominate in outcrop.

## Resum

La deformació Alpina al cor de la serralada dels Pirineus és poc coneguda degut a la forta erosió de les roques post Paleozoiques resultant de l'extensa exhumació. Les calcàries del Cretaci superior del massís d'Eaux-Chaudes, envoltades de roques Paleozoiques a la part més interna del Pirineu centre-occidental, presenten evidències de deformació dúctil complexa i estructures a diverses escales, amb un estil estructural que no havia estat descrit abans per a la col·lisió Alpina en aquesta serralada. Aquesta tesi proposa una nova interpretació de l'estructura i evolució per al massís d'Eaux-Chaudes, situat originalment en el marge Ibèric del rift Mesozoic. L'estudi paleotermal i microestructural de les calcàries del Cretaci superior emfasitzen la ductilitat ocorreguda durant el principal estadi de deformació col·lisional.

L'orogènia Pirinenca va iniciar-se amb la flexió del marge Ibèric profunditzant cap al nord, evidenciada per la sedimentació del flysch Campanià-Maastrichtià. Amb la progressió de la col·lisió dels marges Ibèric i Europeu l'efecte de la flexió va induir l'enterrament profund del futur massís d'Eaux-Chaudes. El clímax dels principals processos de deformació es va desenvolupar en un marc de temperatures moderadament elevades, així com ho indiquen les estructures dúctils, la foliació i la lineació penetrativa. El granit d'Eaux-Chaudes afavoreix el desenvolupament del plec ajagut de gran escala (*fold nappe*) en consonància amb dos nivells efectius de desenganxament, un a la part més alta del basament (al Silurià), i l'altre en una làmina al·lòctona d'evaporites del Keuper emplaçada per la principal estructura que controla la inversió del marge (el sistema d'encavalcaments de Lakora). L'herència estructural i l'heterogeneïtat reològica del basament indueixen forts canvis en l'evolució lateral d'aquest plec ajagut cap a l'est a un ventall imbricat d'encavalcaments dúctil.

El nou esquema que es presenta en aquesta tesi alerta de les dificultats d'identificar aquest tipus de deformació en la zona axial d'orògens com els Pirineus i d'altres similars, donada la forta erosió i superposició estructural en les roques més antigues.

## Chapter 1: Introduction

Inversion tectonics processes along collided continental margins are strongly dependent on the specific geodynamic history within the Wilson Cycle (e.g. Manatschal et al., 2021). Inherited factors such as the mechanical stratigraphy of the sedimentary cover and the nature of basement structures formed during previous tectonic events, control the initial steps of the orogenic process (e. g. Butler et al., 2006). At upper crust levels, contractional deformation typically occurs by the reactivation of extensional faults and by the development of detachment levels following weak mechanical horizons as evaporitic and shale units. In foreland fold-and-thrust belts, synorogenic sediments give key information to decipher this early history, but in the interiors of the orogens to constrain the early structural evolution becomes challenging given the absence of reliable markers in the cropping geology dominated by polydeformed basement rocks. This study focuses on the structure of the Paleozoic, Triassic and upper Cretaceous rocks of the Eaux-Chaudes Massif (ECM) and surroundings, which bring important insights on the nature of the Iberian rifted margin precursor to the Pyrenean collision, and on the complex evolution of the early stages of the Pyrenean orogeny.

The Pyrenean orogen has been scientifically investigated for decades resulting in a well-documented tectonic evolution. Two main rift episodes (Permo-Triassic and late Jurassic-early Cretaceous) and two orogenic cycles (Variscan and Alpine-Pyrenean) have configured the structural architecture of this belt. The Variscan orogeny developed in between ca. 380Ma – 280Ma, configured the Paleozoic basement structure (Cochelin et al., 2017, and references therein), with a late episode of granitic plutons intrusion. The subsequent extension in the Permo-Triassic is characterized by the sedimentation of terrestrial red beds, siliciclastic sandstones, and conglomerates of the low to mid Triassic Buntsandstein facies. In the Pyrenean domain. Buntsandstein facies are generally overlain by the Keuper facies (Stevaux & Winnock, 1974), mainly consisting of claystone and evaporites with abundant dolerites (ophites) and alternations of fine-grained Muschelkalk limestones.



## 1.1. The Mesozoic rift and the Pyrenean orogeny

The Wilson cycle of the Alpine orogeny in the Pyrenees is well-constrained by two main stages. The first begins with the most important rifting episode occurred during the early to the mid-Cretaceous times imparting a strong crustal stretching, with maximum basin subsidence during the Albian-early Cenomanian times (Lagabrielle & Bodinier, 2008; Jammes et al., 2009; Lagabrielle et al., 2010; Masini et al., 2014; Mouthereau et al., 2014; Tugend et al., 2014; Teixell et al., 2016; Grool et al., 2018; Espurt et al., 2019; Labaume & Teixell, 2020). Today, the rift axis is mainly represented by the Mesozoic sediments in the North Pyrenean Zone (NPZ), tectonically inverted as a large pop-up structure (Fig. 1.1). The resultant hyper-extension of the rifted margins from Iberia and Eurasia, lead to the exhumation of the upper mantle (e.g. Jammes et al., 2009; Lagabrielle et al., 2010) (Fig. 1.1c) in the central part of the basin, between two continental margins defined as the Eurasian and Iberian, along great extension coinciding with the nowadays extension of the cropping Pyrenees (~400 km).

Complex damage zones were developed at the edge of both margins by the occurrence of extensional detachment levels and boudinaged zones, resulting in the reworking of the upper mantle and crustal domains. Melanges and tectonic lenses of mixed rocks from both, S-type lherzolites and lower crust rocks, were occasionally arranged and included in the overlying upper Triassic facies (e.g. Lagabrielle & Bodinier, 2008; Jammes et al., 2009; Lagabrielle et al., 2010, 2019a, 2019b; Corre et al., 2016), nowadays outcropping in the core of weld structures, such as Tres Crouts or Urdach. Mantle exposure propitiated HT-LP metamorphism (e.g. Clerc & Lagabrielle, 2014; Clerc et al., 2015, and references therein) which mainly affected the pre and synrift sediments with high thermicity recorded by carbonaceous material of the Mesozoic rocks (Clerc et al., 2015; Menant et al., 2016; Villard, 2016; Corre, 2017; Ducoux, 2017; Saspiturry et al., 2020; Ducoux et al., 2021b) (Fig. 1.2).

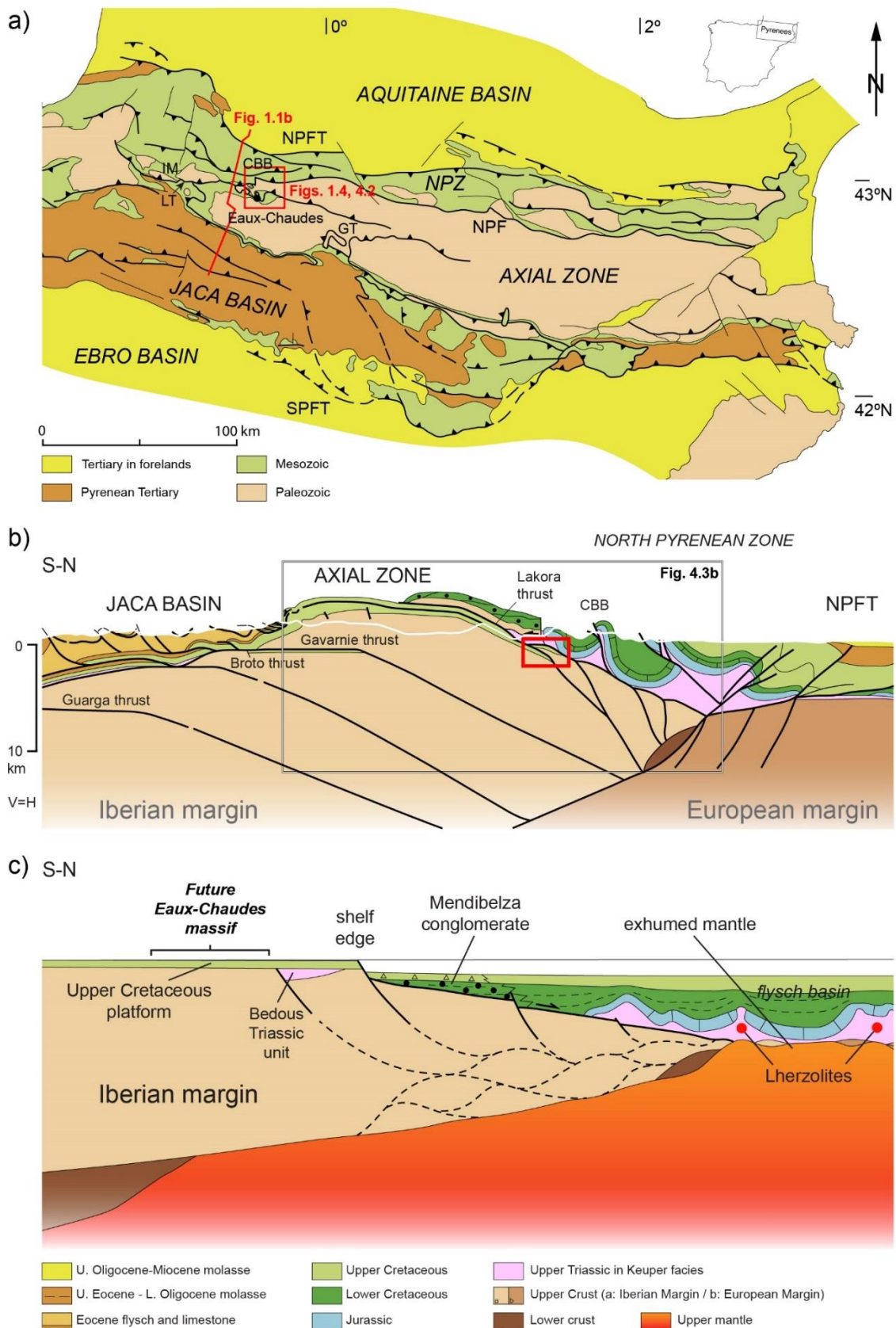


**Fig. 1.1.** (a) Geologic sketch map of the Pyrenees showing the location of the Eaux-Chaudes massif. The red frame indicates the mapped area (Figs. 1.4, 4.2) and the red line indicates the cross-section in Fig. 1.1b. (b) Crustal cross-section of the Pyrenees west of the study area (simplified from Teixell et al., 2016) showing the

tectonic setting of the Eaux-Chaudes structures (red frame). The black frame indicates the part of the section used to show the Lakora thrust system trace in Fig. 4.3b. (c) Restored crustal cross-section of the Iberian margin and rift axis to the Late Cretaceous (Santonian) from Fig. 1.1b (modified from Teixell et al., 2016). CBB: Chaînons Béarnais Belt; IM: Igountze and Mendibelza massifs; GT: Gavarnie thrust; LT: Lakora thrust; NPZ: North Pyrenean Zone; NPF: North Pyrenean Fault; NPFT: North Pyrenean Frontal thrust; SPFT: South Pyrenean Frontal thrust.

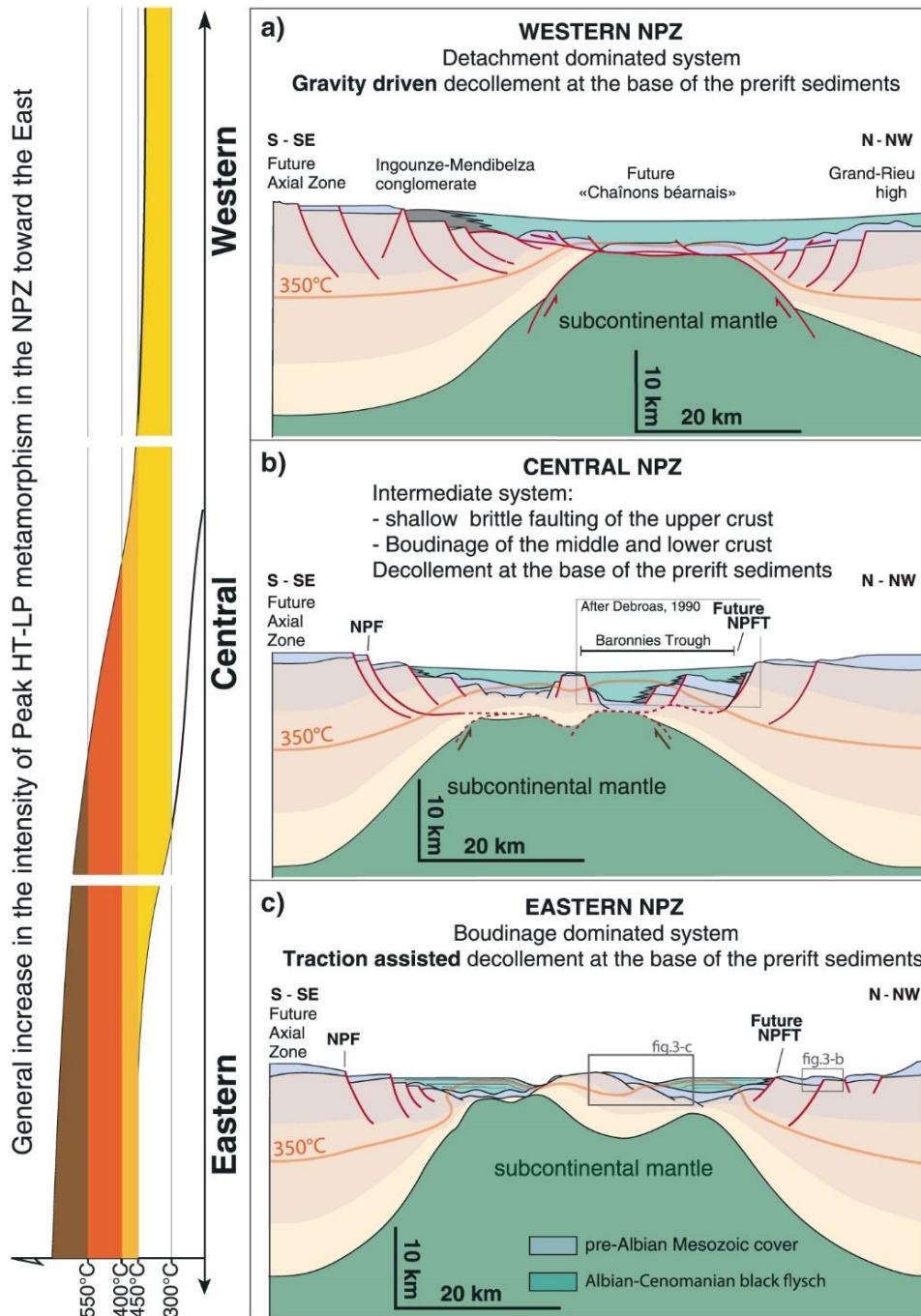


**Fig. 1.2.** West (a) to east (c) paleomargins architecture of the Pyrenean late to post-rift stage in the Cenomanian from Clerc & Lagabrielle (2014). Hyperextended domains favour the mantle exhumation and gravity-driven detachments. HT-LP metamorphism enhances high thermicity in the Cretaceous rocks by elevated geothermal gradients expressed by the 350°C isotherm (orange curve).

The Pyrenean orogeny, which occurred from late Cretaceous (ca. 84Ma) to mid Cenozoic (ca. 20Ma), conforms the second stage of the Wilson cycle of this belt, dominated by collision that may be subdivided into: (1) the initiation of the convergence by subducting the exhumed mantle tract and provoking the overlying rift-axis inversion, compressing the previous extensional salt diapiric structures, along with drowning of the post-rift platforms and flysch deposition, and (2) the main collision and deformation of the continental margins (Mouthereau et al., 2014; Teixell et al., 2016) by a south-verging thick-skinned thrust stack in the Iberian plate, which now represents the Axial Zone (Teixell et al., 2016, 2018) (Fig. 1.3) in brittle deformation conditions. The transition from syn- to post-rift is attributed to the mid Cenomanian, recorded by an important unconformity (e.g. Debroas, 1987, 1990; Berastegui et al., 1990) by which expansive late Cenomanian deposits overlap the basement or the Triassic of the rift shoulders. Late Cretaceous is dominated by shallow platform carbonates (“Calcaires des Cañons” in the study area and vicinities) well-developed in the upper margins of both Iberia and Europe. Meanwhile, deep-seated sediments, such as turbidite deposits, were still accumulated in the former rift axis (e.g. Cuvillier et al., 1964; Puigdefàbregas & Souquet, 1986; Floquet et al., 1988; Razin, 1989). The Paleocene quiescence (e.g. Ford et al., 2016; Rougier et al., 2016; Ternois et al., 2019) conforms the transition between the rift to the collision stage.

The Pyrenees are characterized by a non-cylindrical shape, attributed to the extensional inheritance (e.g. Chevrot et al., 2018), and due to the mechanical weakening of the basement. Crustal-scale transfer zones recently proposed by Saspiturry et al. (2022), of ensembled narrow segments, partition the western Pyrenees favouring the rapid lateral structural variation.

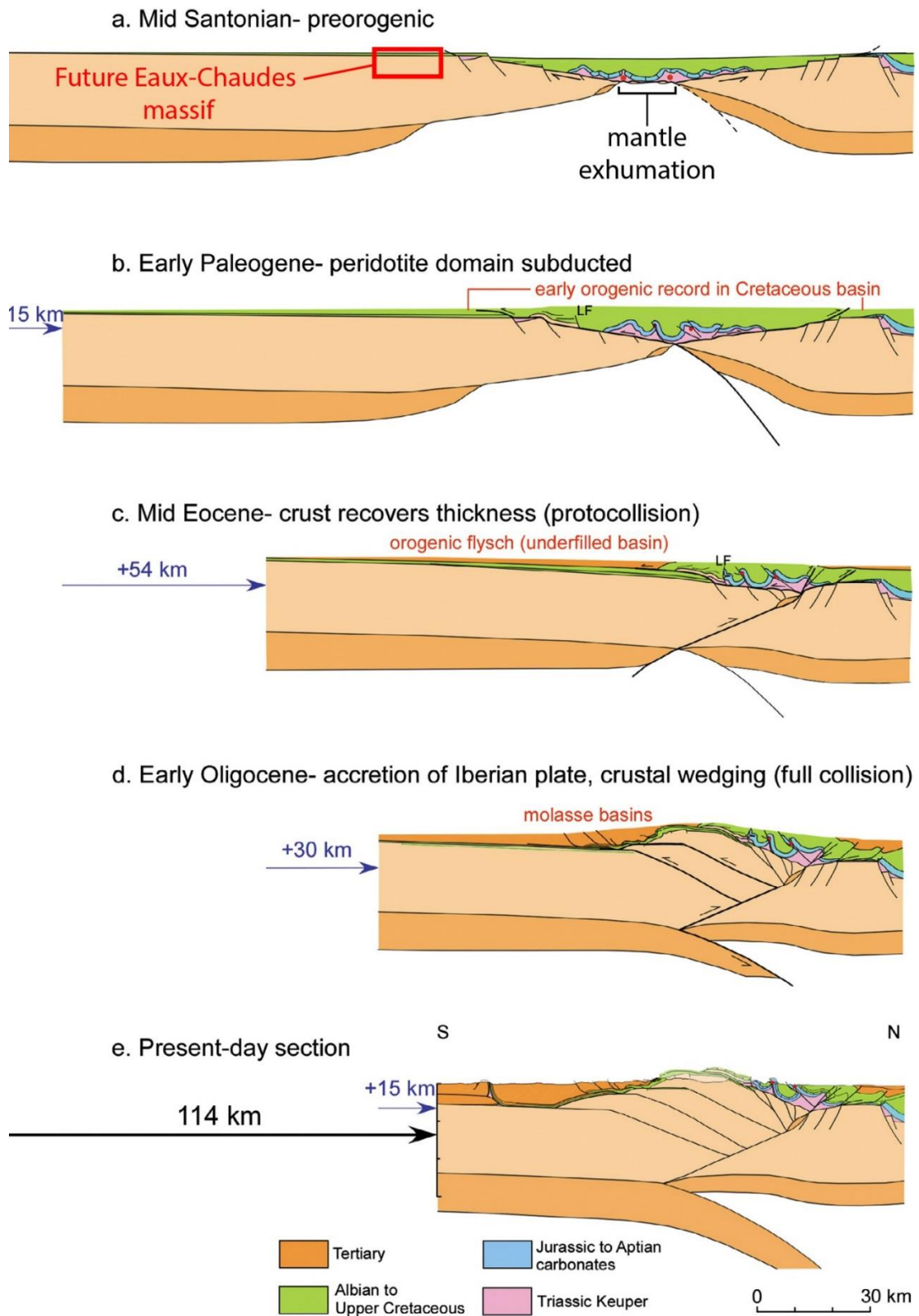


**Fig. 1.3.** Sequential evolution of the crustal-scale to the preorogenic stage (mid Santonian), from the west-central Pyrenees from Teixell et al. (2016). a) Corresponds to the pre-orogenic stage with still mantle exhumed. The red frame indicates the location of the future Eaux-Chaudes massif. e) Shows the south-verging thick-skinned thrust stack in the Iberian plate, the current Pyrenean Axial Zone. Note the thin-skinned tectonics developed within the detached Mesozoic sediments from the former rift.



## 1.2. Geological setting

The Eaux-Chaudes massif (ECM) preserves a large upper Cretaceous carbonates inlier between Paleozoic metasedimentary and igneous rocks in the hinterland of the Pyrenean orogenic belt, in the north-western closure of the Pyrenean Axial Zone (Fig. 1.1a). Paleotectonic reconstructions place those platform carbonates of the ECM in the uppermost part of the Iberian margin (Fig. 1.1c), later affected by the Alpine compression witnessing the Pyrenean hinterland deformation (Fig. 1.1b) and maximum paleotemperature conditions. The ECM is tectonically overlain by Paleozoic-bearing, south-directed thrust units and by the Lakora thrust system, carrying upper Triassic rocks (mostly Keuper and ophites) and the detached Jurassic-Lower Cretaceous rocks that conform the southern Chaînons Béarnais Belt (Ternet et al., 2004; Labaume & Teixell, 2020). The whole tectonic system (ECM and units above) was uplifted in the hanging-wall of the Gavarnie thrust that raised the Axial Zone. The emplacement of the Lakora-Eaux-Chaudes units is considered to be developed from the latest Cretaceous to mid-Eocene, while subsequent Gavarnie thrusting in the western Axial Zone is attributed to the late Eocene-early Oligocene (Teixell, 1996; Labaume et al., 2016).

Unexpectedly, ductile deformation is identified within the Cretaceous carbonates from the ECM. Strongly strained limestones, related to south-verging fold-and-thrust processes, suggest moderately deep deformation conditions, supported by ductile fabrics. Slices of Paleozoic rocks conform apparent klippe structures as proposed by Ternet (1965) and Ternet et al. (2004) (Fig. 1.4). Enigmatic remnants of Keuper facies rocks (Stevaux & Winnock, 1974) enclosed in or overlying the upper Cretaceous limestones of the ECM (Fig. 1.4) suggest a sort of salt tectonics processes with an unusual track record. Those rocks correspond to the upper Triassic and enclose claystones, marine limestones, and thick evaporite layers (Biteau et al., 2006; Ortí et al., 2017; Soto et al., 2017), with abundant embedded bodies of dolerites, known regionally as ophites. The source of the upper Triassic is enigmatic because of the lack of Keuper in between the Paleozoic-Mesozoic unconformity of the Eaux-Chaudes massif.

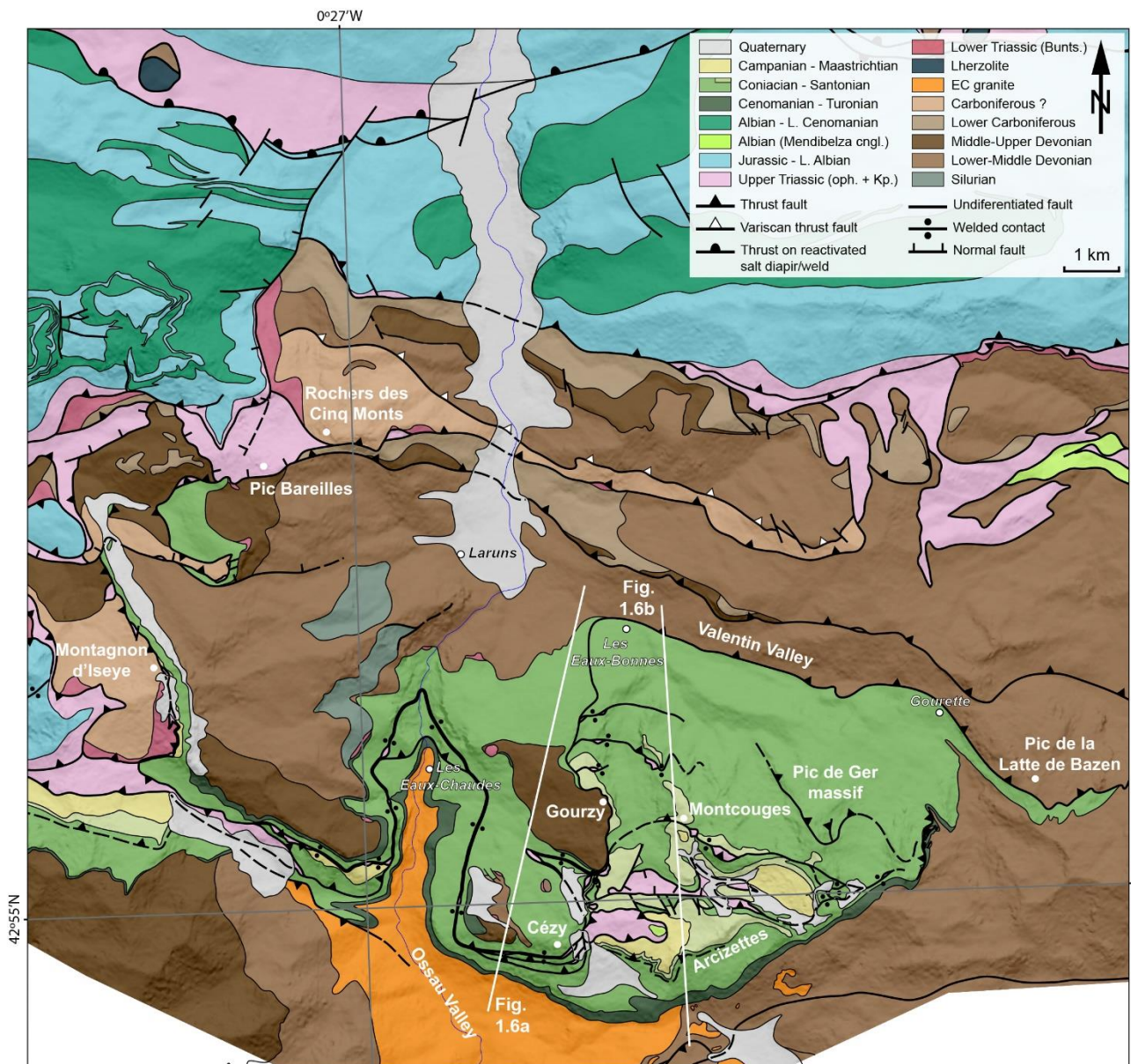


**Fig. 1.4.** Geological map of the Eaux-Chaudes massif and surrounding areas (location in Fig. 1.1a). Data compiled from published maps (Ternet, 1965; Ternet et al., 2004; Labaume & Teixell, 2020; Caldera et al., 2021), and own field observations.

### 1.3. Classical structural interpretation of the Eaux-Chaudes massif

The Eaux-Chaudes massif has been investigated by several authors in a varied range of geological disciplines (e.g. structural geology and sedimentology), as e.g. Ternet (1965), Déramond et al. (1985), Alhamawi (1992), Izquierdo-Llavall et al. (2012, 2020), Dumont et al. (2015), Cochelin (2016). The first meticulous structural study performed in was the thesis of Yves Ternet (1965). He described the

stratigraphy, elaborated a geological and a structural map and constructed 21 structural cross-sections along the massif in a N-S trend showing the lateral evolution of what he named as “du synclinal complexe des Eaux-Chaudes”. The excellent work by Ternet highlighted the structural complexity of the massif establishing fairly innovative hypothesis at that time. It is important to emphasize the identification of a small recumbent fold in the restricted frontal edge of this complex structure, specifically in Cézy Peak (Fig. 1.5a), which abruptly terminates few hundred meters to the north. It is tentatively shown in his structural map and also in the manuscript. His main hypothesis of the complex duplex has been adopted for more than fifty years by the scientific community (e.g. Déramond et al., 1985; Dumont et al., 2015; Cochelin, 2017 and Corre, 2017; Fig. 1.5). Dumont proposed a structural cross-section showing a real Cretaceous duplexing with all the stratigraphy in a right way-up position, a bit to the east where the recumbent fold is not preserved. On top of the upper Cretaceous there is a succession of thrusts carrying Paleozoic and Triassic rocks interpreted as klippe, also replicated by Cochelin (2017) and Corre (2017). Ternet’s interpretation has been perpetuated for decades with some circumstantial modifications.

Ternet also proposed a schematic structural reconstruction for the two main areas according to rheological differences on its basement: a) the granite basement, corresponding to the western sector, and b) the Paleozoic basement in the eastern sector. For the granite case (a) he suggested a schematic structural evolution in five steps, resembling a large-scale recumbent fold at step 4 (Fig. 1.6). Such large-scale recumbent fold is not represented nor defined in any of the 21 sections and manuscript from his thesis, and neither in the more recent or actual cross-sections of the massif (e.g. Fig. 1.5a and also see Ternet et al., 2004), although a strongly overturned fold limb of Paleozoic and upper Cretaceous rocks is represented in the southern slopes of the Cézy peak (Fig. 1.4 for location). As a result, he defined a complex duplex structure of the upper Cretaceous limestones with a roof-thrust carrying the Paleozoic rocks southwards, resembling klippe structures (e.g. Fig. 1.6, step 5). In the manuscript of his thesis, he refers to this structure as a small recumbent fold restricted in the southernmost edge of the massif, abruptly finishing to the north in detailed cross-sections.



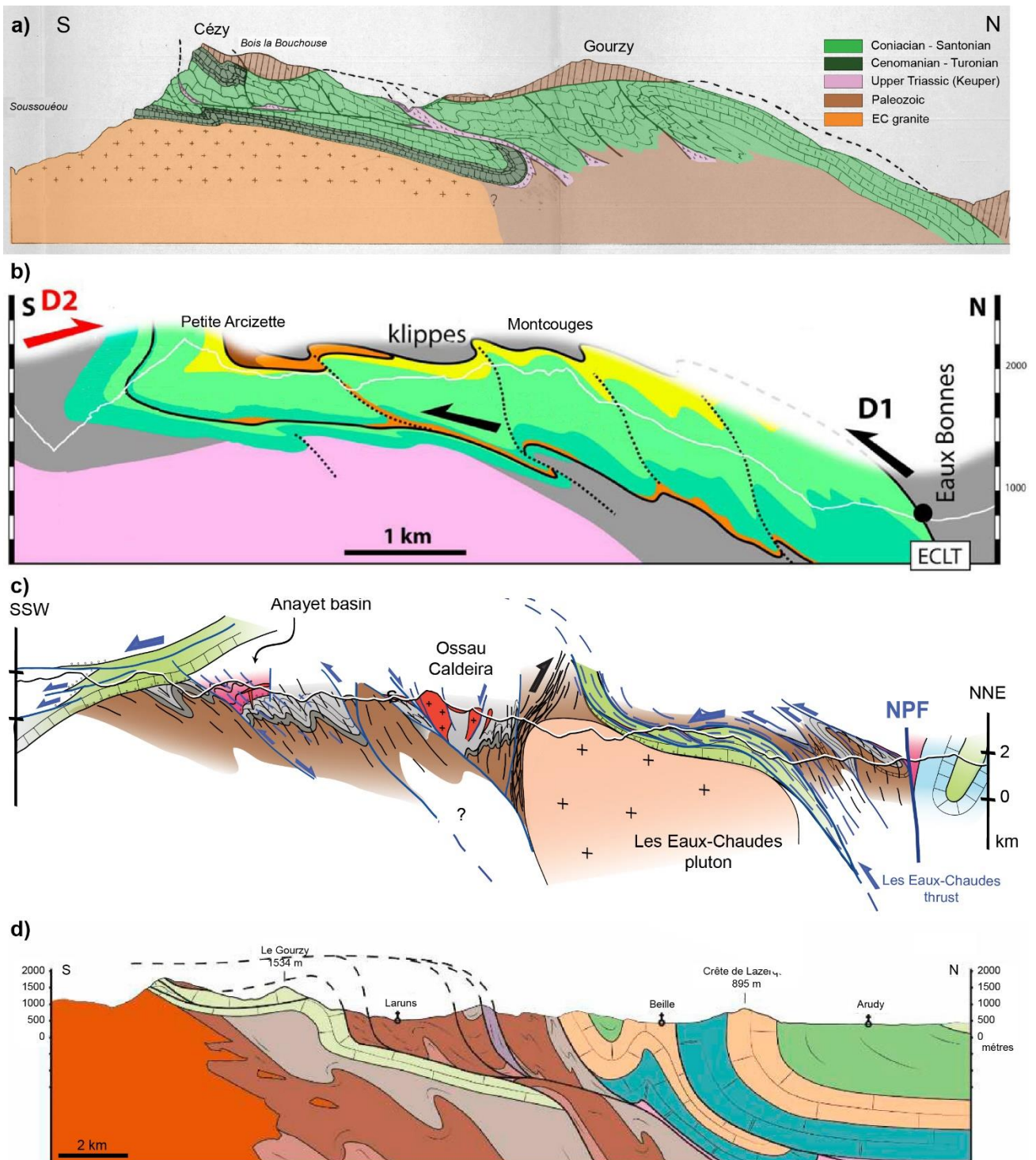


**Fig. 1.5.** a) Cross-section from the granite basement sector passing through Cézy and Gourzy peaks from Ternet (1965). Ternet shows a small recumbent fold in Cretaceous rocks at southern edge of the section (Cézy peak) with the overturned polarity of the whole stratigraphy and a roof thrust carrying Paleozoic metasediments to the north. b) Cross-section from the metasediments basement sector, passing through the Petite Arcizette and Montcougues peaks, from Dumont et al. (2015). Dumont proposes a true duplex for the upper Cretaceous rocks in a right way-up polarity with a roof thrust carrying Triassic and Paleozoic rocks on top. Note the interpretation of the upper Triassic (Keuper) to be autochthon in both sections and the preservation of the Cretaceous sediments to the Campanian flysch. c) Synthetic cross-section from the Eaux-Chaudes massif on

the granite basement sector, showing complex stratigraphic and tectonic relationships within the upper Cretaceous from Cochelin (2017). Again, a roof thrust of Paleozoic metasediments over the Mesozoic stratigraphy is proposed, as well as Alpine foliation affecting the Paleozoic basement. d) Synthetic cross-section on the metasediments basement sector, showing complex tectonism in the Paleozoic which is emplaced by a roof thrust over the upper Cretaceous duplex, from Corre (2017). See cross-section lines in Fig. 1.4. Section line of c) is equivalent to a), and d) to b).

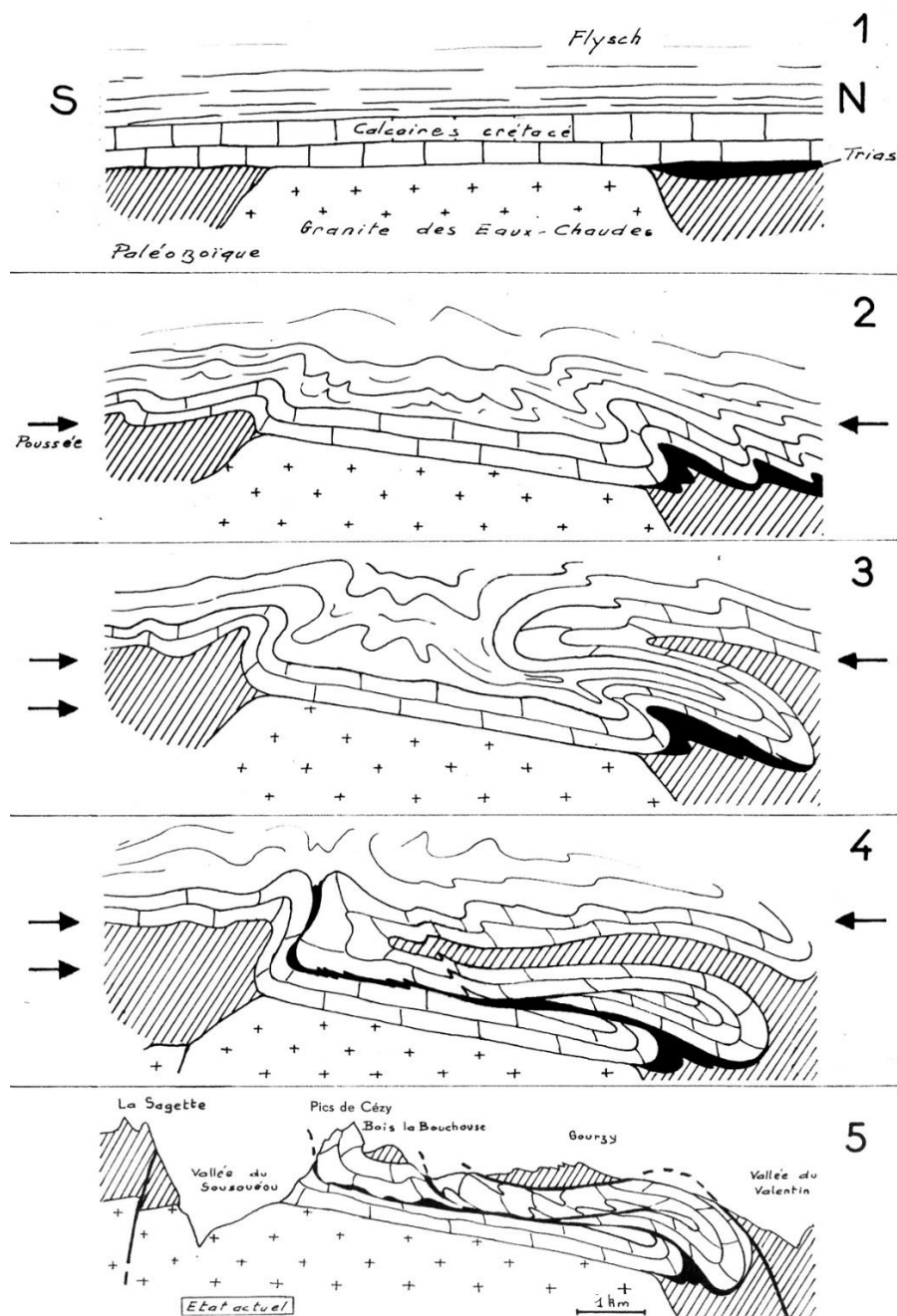


**Fig. 1.6.** Schematic evolution of the western Eaux-Chaudes massif from the granite basement sector (modified from Ternet, 1965). Recumbent fold structure and duplexing is proposed within upper Triassic in between.

Concerning the area represented by deformable basement (b) Ternet proposed another restitution scheme in three steps (Fig. 1.7) with a trend of sinuous basement-involved folds separated by vertical faults preserving Keuper silvers coming from an interpreted Triassic basin in between the Paleozoic and Mesozoic unconformity. A noteworthy aspect from detailed cross-sections of this area is the “ductility” emphasized by tight folds in the Upper Cretaceous limestones containing Paleozoic metasediments in the antiformal cores (Fig. 1.7).

The sections by Ternet (1965) are fairly consistent with the outcropping geology and not unrealistic considering the limited knowledge of the varied expressions of salt tectonics half a century ago. However, the source of the Triassic silvers will be discussed in chapter 4.

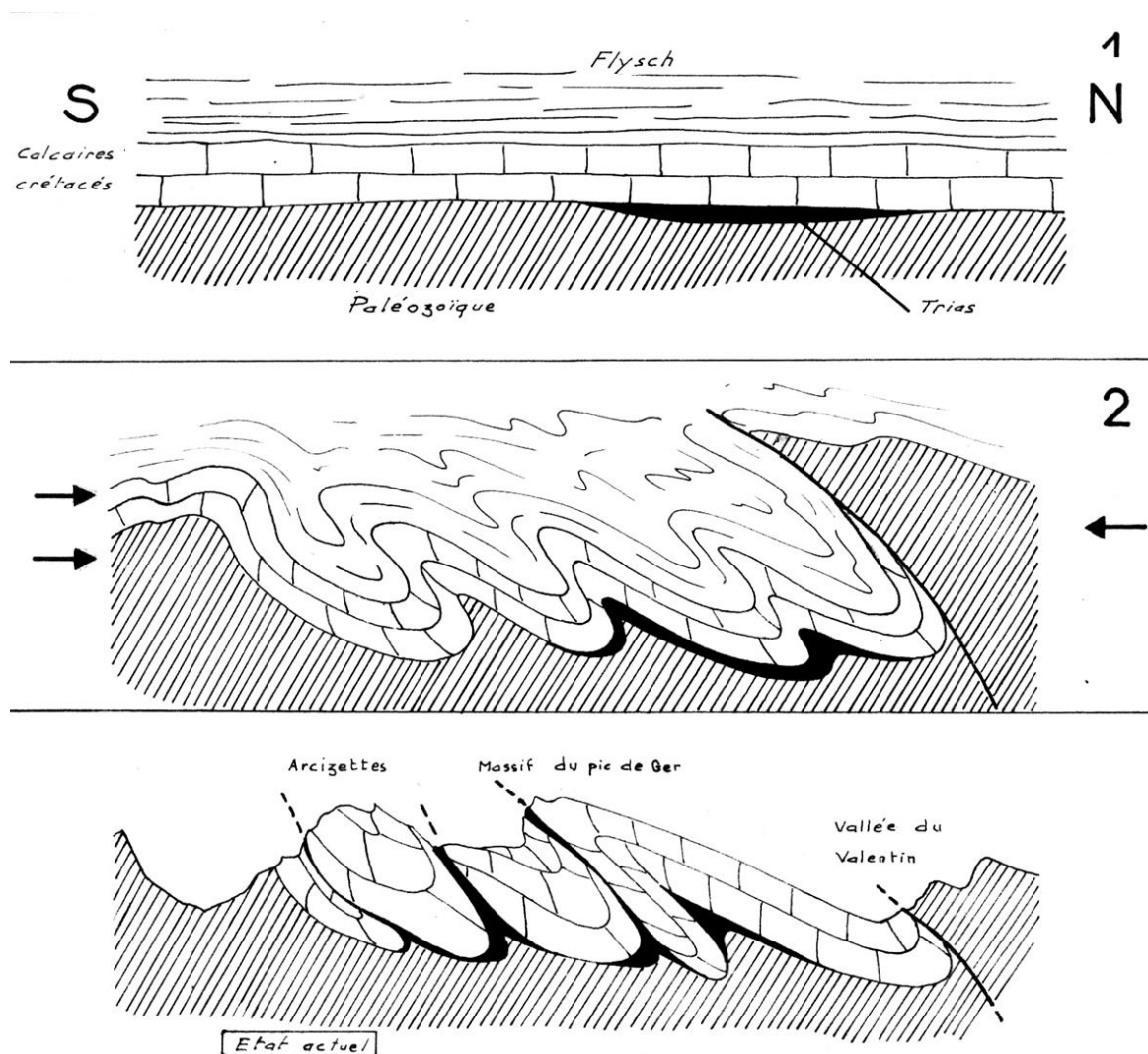


**Fig. 1.7.** Schematic restitution modified from Ternet (1965) of the eastern Eaux-Chaudes massif where basement is formed by the Paleozoic metasediments. A fold-thrust system with squeezed Triassic bodies is developed instead of large duplex structures or occasional recumbent fold.

The proposal of Ternet (1965) and Ternet et al. (2004) is reinterpreted in this thesis by supportive material, such as structural data, field images and sketches, microstructural analysis and paleothermal records from the upper Cretaceous of the ECM, which are indicative of the Alpine deformation occurred during the Mesozoic collision in the hinterland of the west-central Pyrenees.

#### 1.4. Motivation of the study

As reported in the introduction, the classic interpretation of the structural development for the western Pyrenean hinterland was considered brittle, even the ductile features in the cross-sections proposed by Ternet (1965). It has been perpetuated for more than 50 years although the recognizable ductility at large-scale. The source for the ophite and Muschelkalk rocks, related to Keuper, is inferred to be autochthonous, in between the Paleozoic basement and the Mesozoic cover.

In the last decade, the comprehension of the syn-rift processes has rapidly evolved from the field and structural interpretations, and paleothermal study of the Mesozoic metasediments. The knowledge of the post-rift collision, although it is quite constrained for the detached former rift and basement cover, is still poorly known for the orogenic hinterland.

The preservation of the upper Cretaceous limestone's in the Eaux-Chaudes massif gives key clues to the understanding of the deformation conditions during the Pyrenean orogeny on its interiors and deeper levels.

The specific objectives of this project can be summarized as follows:

- Unravelling the Eaux-Chaudes massif deformation from the Alpine collision, to understand which processes and conditions led to the ductility observed in the massif.
- Related to the previous point, to determine the maximum plaeotemperature values recorded in the carbonaceous material from the upper Cretaceous limestones, to constrain the metamorphic grade during the main deformation event.

- From the structural point of view, to identify and characterize the suspected large-scale recumbent fold of the western sector of the massif and its evolution to the east, where the exposed geology drastically changes.
- To understand the relationship between the Eaux-Chaudes massif, the upper Paleozoic nappes and the overlying Jurassic and lower Cretaceous rocks.
- To understand the origin and behaviour of the upper Triassic facies (Keuper and ophite) rocks in the Alpine deformation from the small slices pinched in between the upper Cretaceous limestones, and in between the limestones and the upper Paleozoic nappes.
- At the small-scale, to perform a microstructural analysis to characterize the mechanisms and intensity of deformation in the domains of high strain, and to obtain paleopiezometric information.
- To understand the influence of secondary mineral phases, such as dolomite and quartz, in the grain-scale deformation.
- To propose a structural sequential restoration for the upper margin of the Iberian plate since the post-rift phase, capturing the main stages of the orogenic deformation.

## 1.5. Thesis structure

The organization of this thesis is performed in a classic format. However, part of the results has been published in a scientific journal (Terranova) and chapter 4 is part of a manuscript which will be submitted soon into another scientific journal (Tectonics).

- **Chapter 2** contains the stratigraphy of the three main groups of rocks: 1) Paleozoic metasediments, 2) the upper Triassic facies and 3) the upper Cretaceous limestones.
- **Chapter 3** summarizes the methodology used in for successfully achieving the objectives. A combination of classical fieldwork and large-scale structural study together with laboratory analysis were used.



- **Chapter 4** extends the large-scale structural study focused on the Eaux-Chaudes massif and interpreting the sequential evolution during the Alpine collision for the uppermost Iberian margin.
- **Chapter 5** provides the paleothermal data obtained from the carbonaceous material contained in the Cretaceous sediments and from the calcite-dolomite geothermometer.
- **Chapter 6** shows the first calcite aggregates results of the microfabric analysis for the upper Cretaceous of the Pyrenees, accounting for deformation mechanisms and piezometry.
- **Chapter 7** corresponds to the diagenetic inspection from cathodoluminescence for the calcite and dolomite phases in the pre-, syn- and post-tectonics stages.
- **Chapter 8** presents a general discussion integrating the results presented in the previous four chapters.
- **Chapter 9** presents the conclusions of this work.
- **Chapter 10** contains a list of the references cited.
- **Appendix I** includes the first publication of this thesis in Terra Nova journal showing the preliminary structural, paleothermal and microfabrics results.
- **Appendix II** includes a figure of a spectra from each analysed sample by Raman Spectroscopy of Carbonaceous Material and a simplified 3D figure of the structure of the Eaux-Chaudes Massif.

## **Chapter 2: Stratigraphy of the Eaux-Chaudes massif and surroundings**

### **2.1. Paleozoic basement and lower Triassic**

The Axial Zone of the Pyrenees is composed by the Paleozoic rocks from the Upper Proterozoic to the Carboniferous, previously deformed by the Variscan orogeny, such that they are normally referred to as “basement” with respect to the Mesozoic and Cenozoic geology. The pre-Mesozoic basement around the ECM belongs to the Upper Paleozoic and consists of sedimentary or low-grade metasedimentary rocks (Fig. 2.1). The oldest unit in the area corresponds to Silurian black slates (Mirouse, 1962). This unit is considered regionally a detachment level for Paleozoic of the Axial Zone (e.g. García-Sansegundo et al., 2011, and references therein), being not an exception for the study area. Above this unit, an approximately 400 m thick succession of pelites, limestones, sandstones and quartzites of Devonian age is observed, followed by turbidites and limestones (Culm facies, Delvolvé, 1987) of Carboniferous age. These rocks host an intrusive granitic body known as the Eaux-Chaudes pluton, which is late Carboniferous in age (301 +/- 9, Guerrot, 2001).

Discontinuous Buntsandstein conglomeratic and sandy facies are occasionally found unconformable over the Paleozoic basement. In the ECM, pre-Cretaceous erosion removed a vast volume of Buntsandstein, but some pods have been preserved as rounded conglomerates or graded sandstones mainly quartzitic. They conform useful markers to constrain boundaries of stratigraphic nature and polarity relationships between the Upper Cretaceous and Devonian limestones, especially useful for the recognition of the large-scale structure in the Eaux-Chaudes massif.

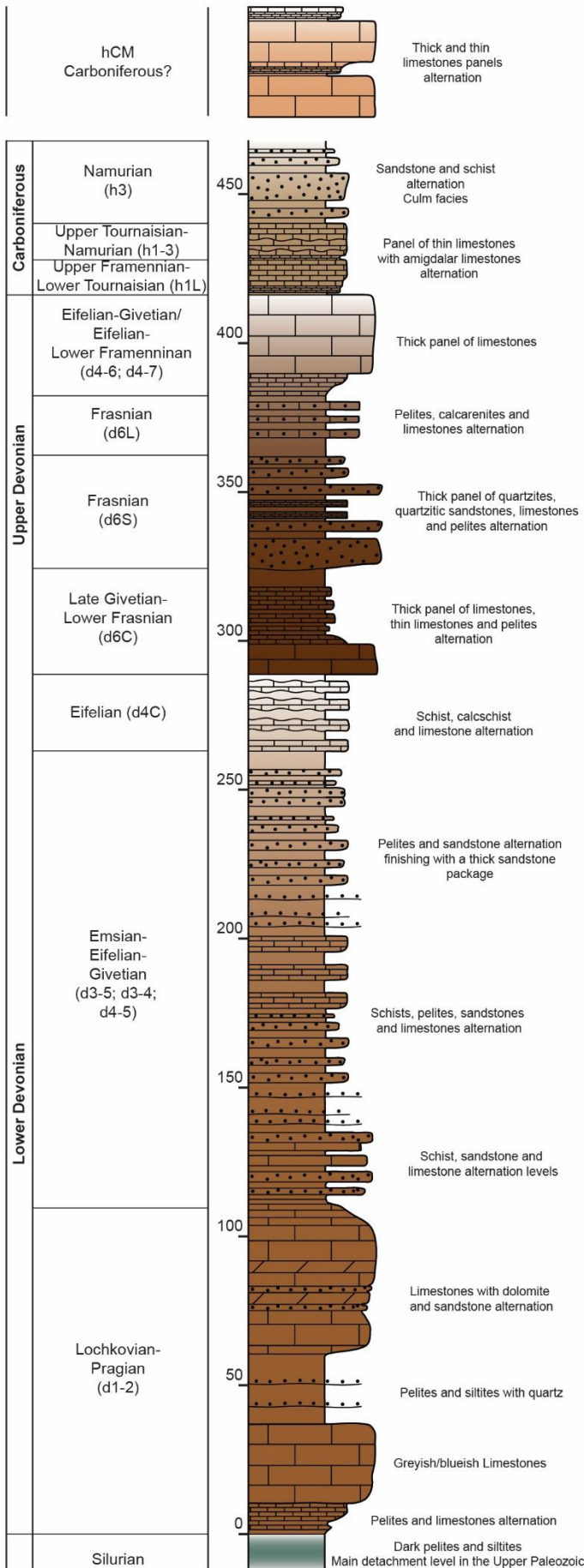


**Fig. 2.1.** Synthetic stratigraphic log of the Paleozoic rocks of the Eaux-Chaudes massif compiled from the previous works (e.g. Ternet, 1965; Ternet et al., 2004).

## 2.2. Allochthonous Keuper sheet

The middle-upper Triassic Keuper in the ECM was reported overlying or encased in the Upper Cretaceous of the Eaux-Chaudes massif and surroundings (Ternet, 1965, and Ternet et al., 2004, Fig. 2.2). It consists of a melange of claystones, cagneules, Muschelkalk limestones, and ophites. Evaporites are not observed at the surface but are well documented elsewhere in the subsurface in the Pyrenees and adjacent basins (Biteau et al., 2006; Ortí et al., 2017; Soto et al., 2017). The Keuper is not found along the main unconformity between the Paleozoic basement and the Upper Cretaceous carbonates of the ECM but forms an allochthonous sheet emplaced over the Upper Cretaceous by the Lakora thrust system.

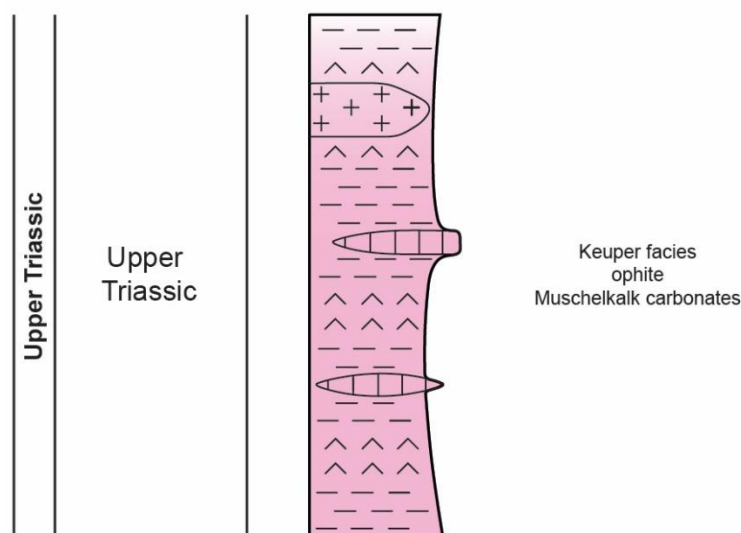


**Fig. 2.2.** Synthetic stratigraphic log of the upper Triassic rocks of the Eaux-Chaudes massif compiled from the previous works (e.g. Labaume & Teixell, 2020).

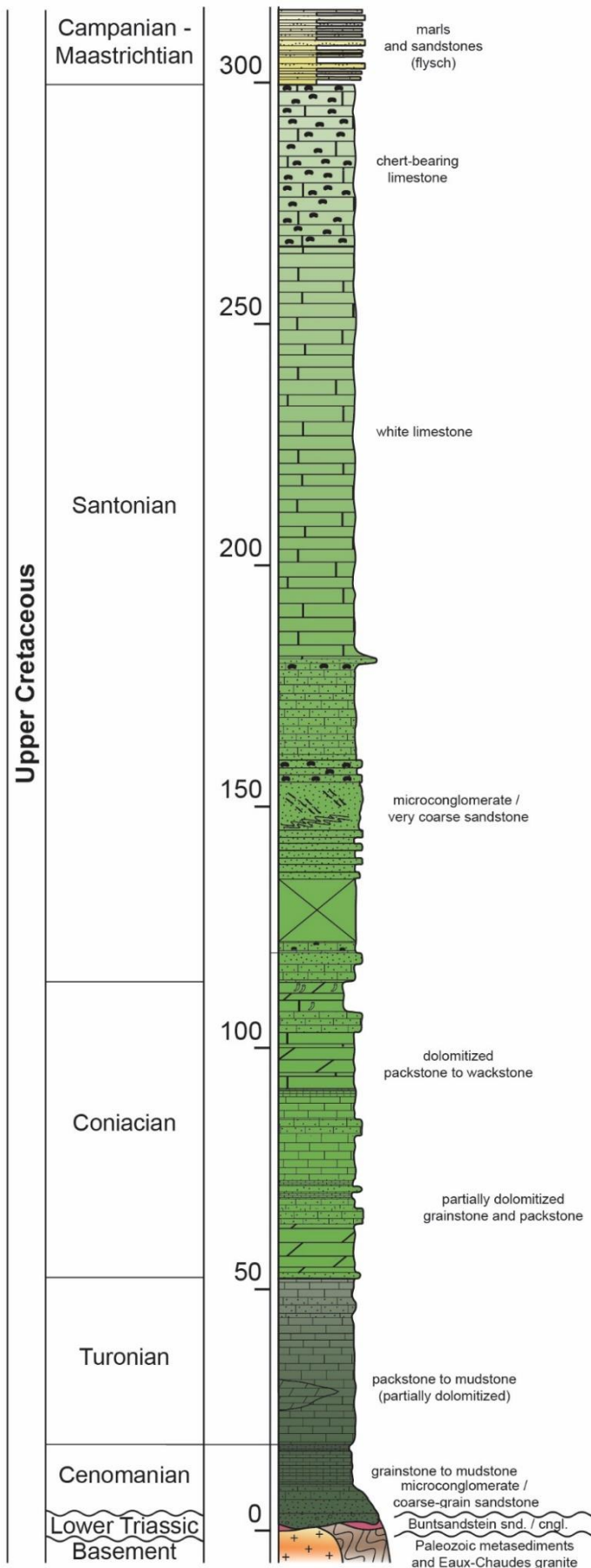
## 2.3. Upper Cretaceous

The autochthonous Cretaceous succession of the Eaux-Chaudes massif has been investigated in prior research (e.g. Casteras, 1956; Casteras & Souquet, 1964; Ternet, 1965; Alhamawi, 1992). It is conditioned by the final stages of the Cretaceous rifting (post-rift phase) and first steps of its tectonic inversion. The succession is characterised from bottom to top by shallow platform carbonates (Cenomanian to Santonian) passing to a synorogenic flysch sequence (essentially Campanian-Maastrichtian) (Fig. 2.3). The massif features huge carbonate ridges and canyons, so the limestones

are currently known as “Calcaires des Cañons”, a nomenclature used for the first time on the western part of Aspe Valley and the Pierre-Saint-Martin area by Fournier (1905), and, forming the late Mesozoic cover of the western Axial Zone (see also Souquet, 1967 and Teixell, 1992).

At the base, the Cenomanian, with maximum thickness of ca. 25m (Ternet, 1965) is unconformably lying on the Paleozoic basement (Silurian to Carboniferous, including late-Paleozoic granite), or the Buntsandstein. Occasionally, it begins with a quartz-rich microconglomerate or coarse-grained sandstone, followed by a succession of lime grainstones to mudstones and wackstones with *Praealveolina* and *Pseudocyclamina*. The transition to Turonian is highlighted by continued packstone to mudstone deposits featuring *Chrysalidina* and *Nezzazata* fossil content. *Pithonella*, debris of echinoderms, *Halimeda ellioti* and *Globotrunca helvetica bolli* are also characteristic of this unit (Conard & Rioult, 1977). The Turonian limestone shows varying thickness, with maximum of ca. 80m (Alhamawi, 1992). This thickness variation hampers the recognition of the transition to the Coniacian along the massif, although it is commonly highlighted by partially dolomitized grainstones and packstones with a thickness of ca. 40m (Ternet et al., 2004). Dolomitization is dominant at the base, as well as debris of *Hippurites*, polypers, gasteropods and foraminifera (Alhamawi, 1992). To the top, there is a succession of packstones to wackstones with benthic foraminifera, rudists, oysters, and polypers. At the southern flank of the Arcizettes mountains (Fig. 1.4 for location), a ~40 m thick panel of dark dolomitized limestones is well-developed at the base of the Cretaceous sediments and is recognizable along 2 km laterally as a reference horizon.

The Santonian is a white-colored, massive limestone unit with a thickness up to 250m (Ternet, 1965), widespread and forming the tallest reliefs of the ECM. It begins with microconglomerate or very coarse sandstone cemented by calcite and containing rounded quartz grains. The dominant white limestone contains decimetric levels of slightly sandy packstones with high content of *Lacazina* and bivalve debris. The end of the Santonian is characterized by a 6 to 30m layer of limestone with chert nodules, a characteristic key level in the western Axial Zone cover (Souquet, 1967) (Fig. 2.3), easy to recognize in the field. In some areas the Santonian limestones are followed by a 10 to 15m of calcareous shales with a wide variety of microfauna and fossils as echinoids, benthic and pelagic foraminifers. The top



of the Upper Cretaceous sedimentary record of the Eaux-Chaudes massif is composed of an alternance of marls and turbiditic sandstones known as the Campanian flysch, to several hundred metres thick (younger deposits are not preserved). Sandstones present grain-size gradation and/or cross-stratification by quartz grains and muscovite slats (Ternet et al., 2004) with resedimented benthic microfauna in the sandstone (e.g. *Orbitoides media*, *O. tissoti*, *Nummofallotia cretacea*), and pelagic microfauna in the marls (e.g. *Globotruncata elevata*, *G. rosetta*).

The Upper Cretaceous limestones represent a post-rift shelf in the upper Iberian margin (Teixell et al., 2016). Relatively stable episodes of regression and transgression determined its facies deposition over time. The uppermost Cretaceous clastic deposits mark an abrupt flexural deepening of the margin in the early steps of the Pyrenean orogeny (Teixell, 1996).

**Fig. 2.3.** Synthetic stratigraphic log of the upper Cretaceous rocks of the Eaux-Chaudes massif from the autochthon Upper Cretaceous in the Petite Arcizette.

## Chapter 3: Methodology

To contribute to the knowledge of the hinterland deformation in the western Axial Zone of the Pyrenees during the Alpine orogeny different methodologies were used in this study, combining classical field and structural approaches (e.g. cartography, cross-sections, microscopy, etc.) with recently developed instrumental techniques (e.g. Raman Spectroscopy of Carbonaceous Material, SEM-EBSD).

### 3.1. Field work

To better approach the aims of this thesis, conscious and methodical field campaigns along the Eaux-Chaudes massif and nearby areas were necessary. An area of approximately 168 km<sup>2</sup> was covered from the Montagnon d'Iseye structural unit to Petite Pêne Médée peak in west-east orientation, and from Arcizettes peaks to Cinq-Monts unit in N-S trend (Fig. 3.1). The accessibility to the study area by car, apart from the main roads (e.g. Ossau Valley), is quite restricted due to the strong relief and the leafy forests. There exist only 5 forest tracks that can be used with prior permission of the municipality, making it possible to access to elevated areas in the massif. Nevertheless, the main field work consisted of covering long distances by hiking to reach remote points to sampling, photographing and or recognizing the cropping geology. Due to the weather conditions and especially the prevalence of snow between the months of November to June, those campaigns were developed during the summer season in 12 different stages divided into periods from five to twelve days.



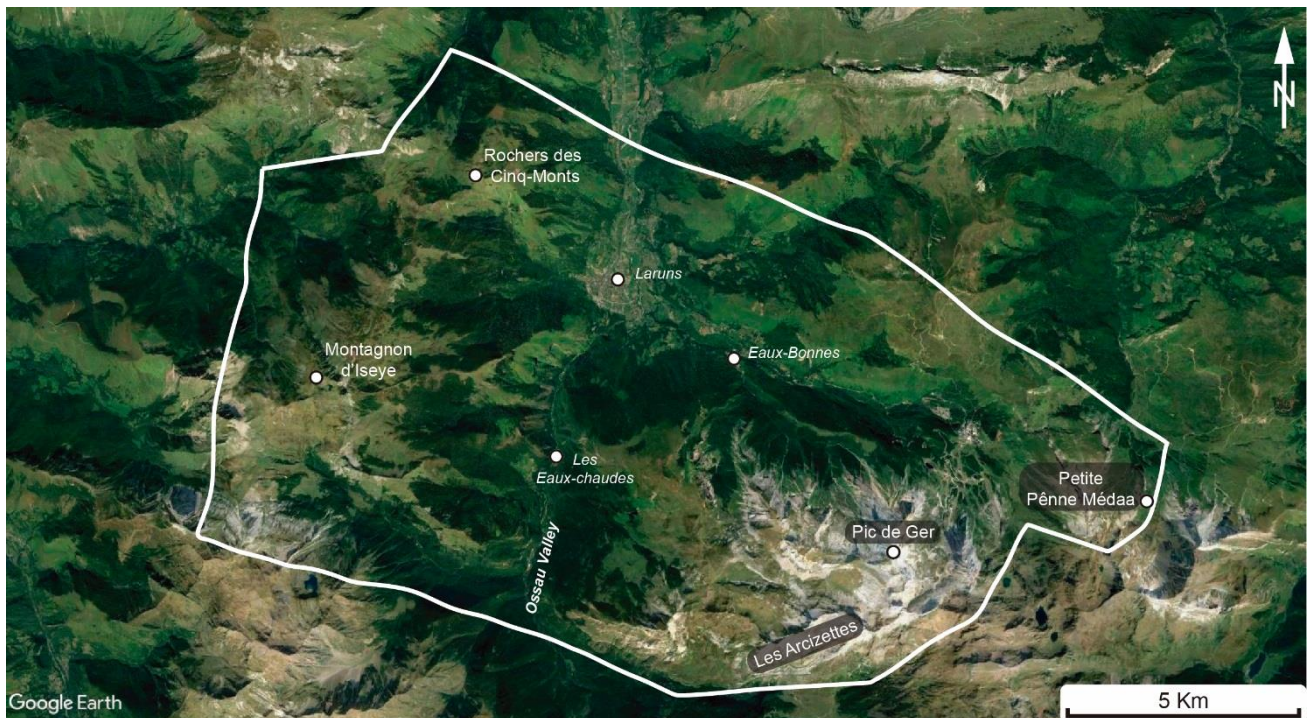


**Fig. 3.1.** Study area delimited by the white polygon on the ortophotography from Google Earth. Toponyms of villages and mountains used in the description of the study area are indicated.

Field structural analysis and mapping were combined with in-situ cross-section construction. As the Eaux-Chaudes massif is characterized by high relief (Fig. 3.2), field observations combined with schematic drawing and picture collection have been very valuable for the understanding of the structure and its rapid lateral evolution. The revision and improvement of the geological map have been a continuous mission even when the previous ones from Ternet (1965) and Ternet et al. (2004) were fairly accurate. The acquisition of structural data has been focused on bedding dips, foliation, stretching lineation and fold axes. Published geological maps from nearby areas have been used to complete the geology of the Paleozoic and Mesozoic from the upper thrust sheets and the Chaînons Béarnais Belt (e.g. Bannère et al., 1980; Ternet et al., 2004; Labaume & Teixell, 2020). Also, a representative stratigraphic column was constructed from the autochthonous upper Cretaceous in the southern part of the ECM. Finally, sampling was a main task during the fieldwork. The main purpose of sampling, centred on the upper Cretaceous carbonates, was to study the micro-scale deformation imprint along the Eaux-Chaudes massif and the paleotemperature record.





**Fig. 3.2.** Panoramic image of the carbonate Eaux-Chaudes massif during the field campaign performed in October 2019. The pictures are taken from the western edge of the massif looking to the east.

### 3.2. Petrography and microstructure from thin sections

A total of approximately 200 thin sections were done from the 235 collected samples, mainly from the upper Cretaceous rocks but also a few from the Triassic (Buntsandstein, Muschelkalk and ophites) and Paleozoic metasediments. Some samples have been cut in multiple orientations for structural analysis, or from specific regions of interest of the samples (e.g. porphyroclasts, microscale folds). For the petrographic recognition, thin sections from deformed samples were performed normal to the foliation and parallel to the stretching lineation (if visible), i.e. the XZ planes, in order to study fabrics and symmetry. Undeformed samples were cut perpendicular to stratification whether identifiable.

Petrographic study allowed us to recognise the bulk facies of the Upper Cretaceous and the recording of diagenetic, metamorphic, and tectonic processes. A systematic study on facies recognition/identification has been not performed in detail, just to confirm or slightly improve the descriptions made by Alhamawi (1992) and Ternet et al. (2004) from the stratigraphic record. A first recognition of the samples was necessary for the paleothermal and microstructural analysis. The focus was to recognize elevated content of carbonaceous material for Raman spectroscopy, and to qualitatively identify the presence or not of the second-phase content for microfabric inspection, particularly dolomite and quartz mineral phases, which are the more common in the massif.

### 3.3. Geological mapping and cross-section construction

Outcropping geology of the Eaux-Chaudes massif had been mapped out in concise detail for the preceding works. For the purpose hereof, geological mapping is based on the revision of the previous maps emphasizing the most controversial areas due to map inconsistencies or difficulties in explaining the mapped structures. This process was performed in detail (scale of approximately 1:25000) during all the field campaigns and thoroughly focused on clarifying the specific areas which conform the key points for the understanding of regional structures, and to better constrain their stratigraphic and tectonic relationships. Even though, the proposed maps in this work are performed on larger scales, 1:100000 for the regional and 1:50000 for the detailed one (shown in the following chapter). Stratigraphic polarity, not always easy to recognize due to the abundant limestone facies in Paleozoic and Mesozoic rocks, and clue for structural comprehension, was constricted by some small preserved Buntsandstein pods in between.

To describe the lateral structural variation along the ECM, numerous local and regional cross-sections, along with restitution diagrams and field image interpretations have been developed. For the acquisition of structural data in the field, the Field Move (Petroleum Experts) application was used in a tablet device (IPAD model Air A1566) and sometimes supported by the analogue compass. In the office, the Move programme (with an academic license provided by Petroleum Experts) was used for the treatment of this database, managing the geological map and the cross-section profiles in both 2D and 3D.

Six structural cross-sections with N-S trend cover the whole upper Cretaceous massif. One crustal-scale section has been constructed to place the Eaux-Chaudes structure in the framework of the Pyrenean hinterland. One more section, oriented W-E, further illustrates the lateral variation and complexity of the massif. Finally, two schematic restorations in sequential steps were performed as a proposal for the inversion tectonic processes that occurred in the upper Iberian margin from the post-rift stage to the present day. Feedbacks from this procedure have served to continuously improve the geological map and the cross-sections.

### 3.4. Paleothermometry

#### 3.4.1. Raman Spectroscopy of Carbonaceous Material (RSCM)

Raman spectroscopy of carbonaceous material (RSCM) is an analytic technique widely used in recent years for the analysis of the structural organization of the carbonaceous material (CM) (Wopenka & Pasteris, 1993) contained in rocks. The structural organization, directly related with the maturity of the CM, is conditioned by diagenetic and/or metamorphic processes experienced by the rock and is considered non-sensitive to retrograde transformations. The technique consists of the acquisition of the inelastic diffusion occurring by the interaction of a laser beam with the carbonaceous material. As a result, the CM may absorb or emanate light resulting in a Raman spectra (Raman shift) (Fig. 3.3) that, according to its shape, enables to calculate of the peak temperature experienced by the rock ( $T_{max}$ ).

37 samples enriched in carbonaceous material of upper Cretaceous sedimentary rocks; two from the Paleozoic basement of the Gavarnie nappe; and one from the allochthonous Keuper facies of the Eaux-Chaudes massif and surroundings around the western termination of the Axial Zone were analysed with this technique, in order to retrieve paleotemperatures to gain insight into the burial and deformation conditions of the study area. The acquisition was performed at the Bureau des Recherches Géologiques et Minières labs (Orléans, France) under the supervision of Abdeltif Lahfid using a diode-pumped solid-state laser source excitation of 514.5 nm on polished, standard thin sections. The laser power reaching the sample surface, through the 100x objective of a Leica DM2500 microscope, did not exceed 1 mW. Before each measurement session, the spectrometer had to be calibrated using a silicon standard with 520.5  $\text{cm}^{-1}$  line. Raman spectra are composed in the first region (1100-1800 $\text{cm}^{-1}$ ) (Tuinstra & Koenig, 1970; Nemanich & Solin, 1979) by the graphite band (G) and defect bands ( $D_{1-4}$ ) (Fig. 3.3). The spectra composing the 180-350°C range is decomposed by up to the four mentioned defect bands (Fig. 3.3) and the spectra of 330-650°C just by the two ( $D_1$  and  $D_2$ ). The paleotemperature value was estimated from the fitted spectrum (Fig. 3.3) following the calibration procedures described by Beyssac et al. (2002) for samples resembling the shape of the

one from 17NC26 and Lahfid et al. (2010) from samples like spectra from TC-0801. These procedures are adapted to the temperature ranges of 320-650°C and 150-320°C respectively.

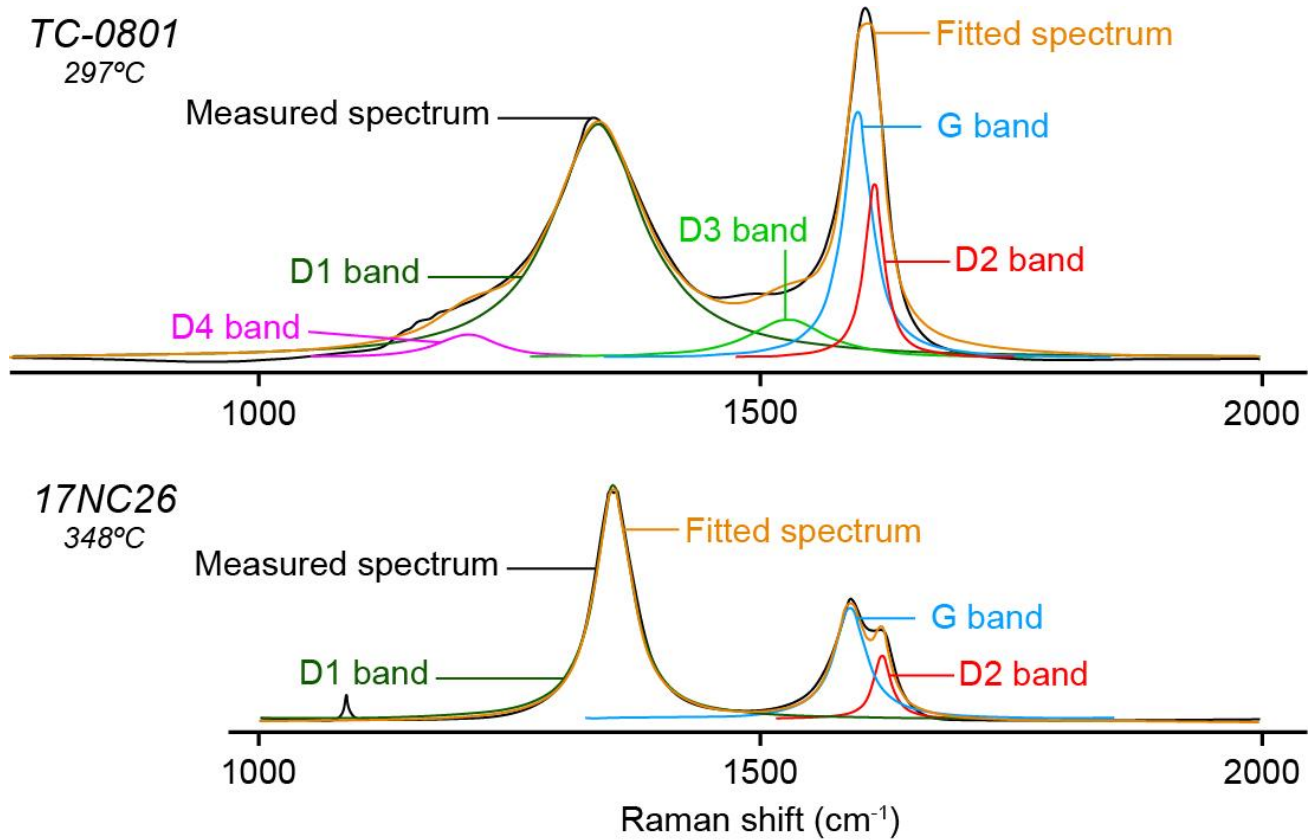


**Fig. 3.3.** TC-0801: Sample Raman spectra decomposition during the fitting procedure of disordered carbonaceous material from a low-grade metamorphic rock (TC-0801) of the Belagua area (Roncal valley, 30 km west of the ECM) in a range of 260-310°C. 17NC26: Sample Raman spectra decomposition during the fitting procedure of slightly ordered carbonaceous material from a low-grade metamorphic rock of the Eaux-Chaudes Mesozoic in a temperature >330°C. All the defect bands (D<sub>1-4</sub>) and G band, composing the spectra, were identified, and used to obtain the fitted spectrum from which the  $T_{max}$  was obtained.

### 3.4.2. Electron Microprobe analysis (EMPA)

While the Raman spectroscopy provided the bulk of the paleotemperature data obtained in this work, additionally paleotemperatures were calculated using the calcite-dolomite geothermometer. The absolute cation contents (Mg, Mn, Fe) of calcite grains coexisting with dolomite on five samples were analysed using a microprobe analyser (EMPA) JEOL JXA-8230 coupled with Energy Dispersive

Spectroscopy at the “Serveis Científic i Tecnològics” of the Universitat de Barcelona. The acquisition conditions were a focussed beam of 20kV accelerating voltage in approximately 11s count time.

Calcite-dolomite geothermometry is a common technique used for samples affected by relatively low-grade metamorphism. It depends on the magnesium solubility in calcite in the assemblage calcite-dolomite. We used the two geothermometers described by Powell et al. (1984) and Covey-Crump & Rutter (1989), both are focused on the equilibrium between calcite and dolomite phases. The first geothermometer takes into account the molar fraction of dolomite ( $X_{MgCO_3}$ ) in calcite using equation (1).

**Eq (1)**  $T (K) = 1000 / (0.5528 - 0.2996 \ln (2X_{MgCO_3}))$  for  $X_{MgCO_3} < 0.07$

$$T (K) = 1000 / (0.6693 - 0.2397 \ln (2X_{MgCO_3})) \text{ for } X_{MgCO_3} > 0.07$$

The experiments from Powell et al. (1984) comprise the molar fraction of iron ( $X_{Fe}$ ) in the dolomite phase versus the molar fraction of magnesium ( $X_{Mg}$ ) in the calcite phase, assuming the equilibrium in an assemblage between calcite-dolomite-siderite. To reveal the paleotemperature of the cationic exchange closure, the values of the molar fraction are plotted in the proposed diagram by Powell et al. (1984) (Fig. 3.4) containing the curves from 300°C to 550°C obtained from the empirical experiments for equilibrium between those three carbonate phases.

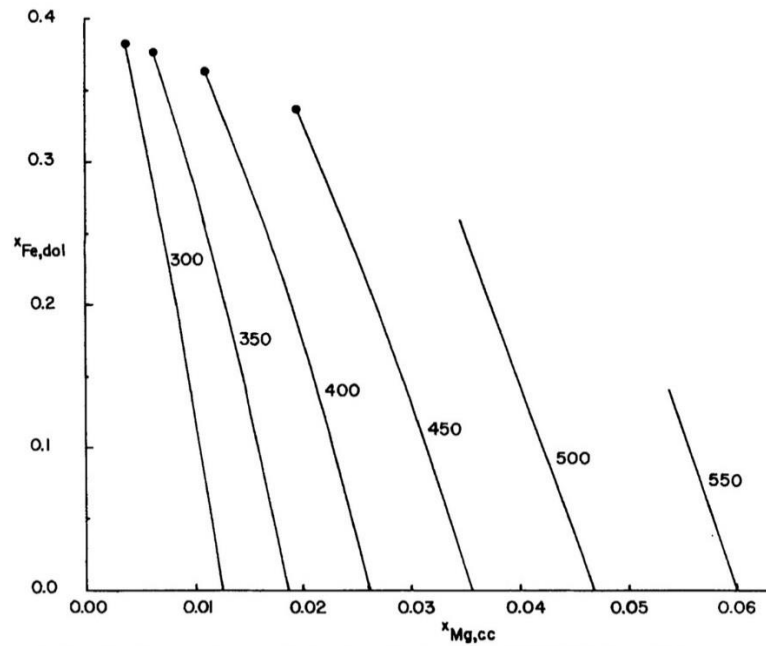


**Fig. 3.4.** Plot from Powell et al. (1984) of  $X_{Fe,dol}$  against  $X_{Mg,cc}$  with the predicted temperature curves for equilibrium between calcite-dolomite.

### 3.5. Micro-scale fabric: SEM-Electron Backscattered Diffraction (EBSD)

Electron Backscattered Diffraction maps were collected to study microfibrics (e.g. grain-size, grain shape and crystallographic preferred orientation) of deformed rocks to gain insight into deformation mechanisms and recrystallization processes. Energy Dispersive Spectroscopy (EDS) was coupled to index the chemistry of mineral phases previously identified by petrography. EBSD maps were performed on 23 thin-sections at the University of Montpellier (France), with a CamScan X500-FE CrystalProbe SEM-EBSD equipped with the Oxford NordlysNano EBSD detector. Operating conditions were an acceleration voltage of 20kV and a working distance of around 25mm under low vacuum conditions (-5 Pa). Differing from the common EBSD detector, it works with the electronic tube inclined at 70°, which allows the sample to be kept horizontal during the analysis. This allows for acquisition of larger areas and increases its quality. There is only one other example of this type of SEM-EBSD in the world, in Liverpool. Local maps have been constructed with step sizes varying between 1 and 9  $\mu\text{m}$ , depending on the resolution intended to constraint microfibrics features. Sampling was mainly focused on structural domains displaying moderate ductile deformation,

although samples from low-strain domains were analysed to characterise the initial microstructure and/or late brittle-ductile deformations. This technique is highly dependent on polishing, diamond paste often causes mechanical damage, such as scratches, which considerably reduce the quality of mineral indexing. To prevent from that a suspension of colloidal silica was used as a polishing agent and the obtained indexing ratios ranges from 70 to 97%. Non-indexed pixels are due to fractures, voids, or to non-specified mineral phases during the pre-acquisition.

The AZtecHKL software of Oxford Instruments was used to index the acquired EBSD patterns and to apply several correction filters of data such as mineral phase corrections (using the EDS data), and reduction of misindexing errors and noise. Further, postprocessing and analysis of microfabrics (e.g. grain-size calculations, IPF and PF plots) were performed using the MTEX toolbox v5.8 (Fig. 3.5) to constraint the fabric strength of the deformed samples and to identify deformation mechanisms and deformation domains along the ECM. The analysis of grain distribution, shape and subgrains boundaries are key to identifying mechanisms of deformation (i.e. dislocation creep, grain boundary sliding).

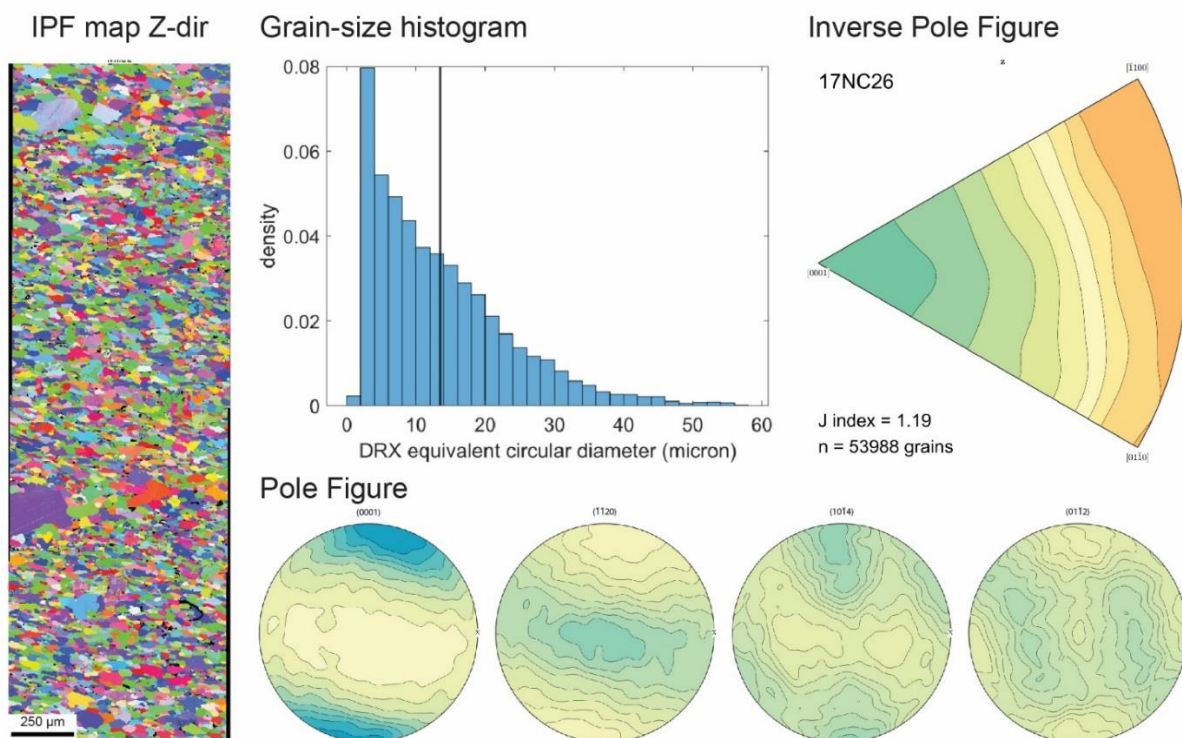


**Fig. 3.5.** Example of IPF map in Z-direction of crystallographic orientation, grain size distribution and fabric strength (from Inverse Pole Figure (IPF) and Pole Figure (PF)) data obtained from the EBSD analysis.

### 3.6. Sample preparation for EBSD and SEM analysis

Thin sections used for these analyses have been replicated from the original samples due to the specifications imposed by the EBSD analyser. They were mechanically polished to thin sections with a thickness of about 30  $\mu\text{m}$ . For microstructure analysis, they were additionally polished with an alkaline colloidal silica suspension to avoid scratching. Previously to be inserted into the analysed they were sprayed due to clean the surface and all the edges were covered by a small and thin metal sheet to enhance the electron conductivity. Deformed samples were cut in the XZ plane of the finite strain, which is perpendicular to the main foliation and parallel to the stretching mineral lineation (Fig. 3.6), where the deformation features may be well-identified. Undeformed samples were cut more or less randomly but intended to be perpendicular to the stratification or weak foliation, if possible to identify.

Samples used for SEM analysis were cut and mechanically polished to thin sections with a thickness of around 30  $\mu\text{m}$ . Metallographic polishing was applied to reduce the surface irregularities. To improve the acquisition conditions all samples were also cleaned and coated by carbon to improve the electron conductivity.

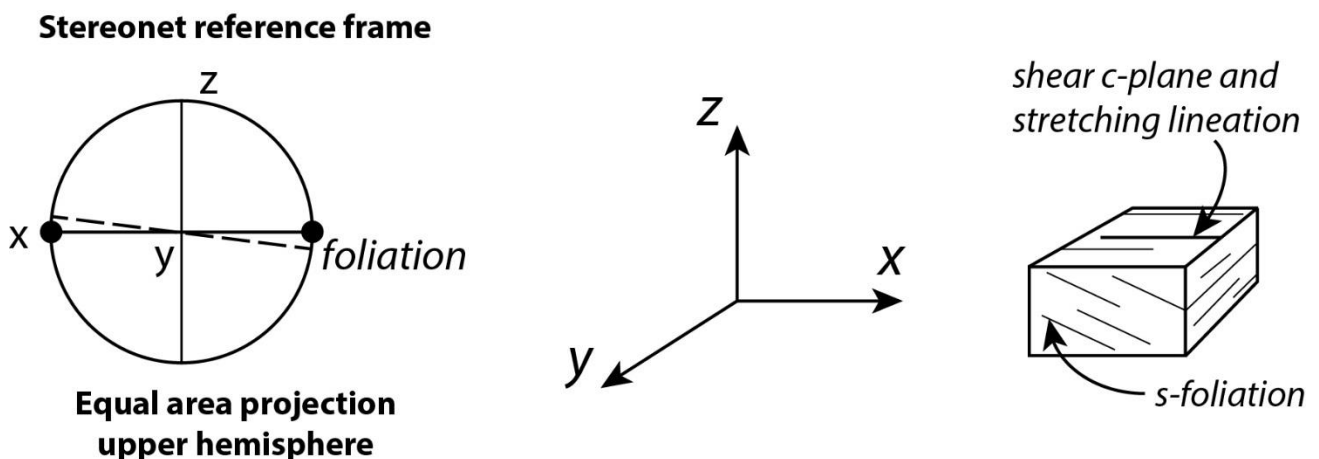


**Fig. 3.6.** Crystal coordinate reference frame for the deformed samples in the pole figures from the EBSD analysis and representative orientation of the foliation.



### 3.7. Cathodoluminescence analysis

Cathodoluminescence petrography (CL) is a useful tool commonly applied to identify dolomitization and recrystallization processes, as well as diagenetic relationships in carbonates (e.g. Fairchild, 1983; Purser et al., 1994; Choquette & Hiatt, 2008). Selected thin sections were analysed by cold cathodoluminescence microscopy, to decipher different families of calcite and dolomite, and paragenetic processes (such as replacements, recrystallization, etc.) of the upper Cretaceous carbonates of the ECM, from their luminescent response. The analyses were performed using a Technosyn Cold Cathode Luminescence model 8200 MkII at Universitat de Barcelona (Spain), with operating conditions of 15-18kV and gun current of 300-350  $\mu$ A. Dolomite textures recognition was based on the combined Gregg & Sibley (1984) and Sibley & Gregg (1987) dolomite textural classification, which focuses on the grain-size, crystal shape and matrix portion. Cathodoluminescence colours are indicative of the chemical composition of parental fluids and give information on diagenetic processes. Warm colours such as yellow, orange or red are usually related to meteoric fluids, while dull-dark luminescence refers to burial fluids (Fig. 3.7). Recrystallization processes (i.e. dynamic recrystallization or dedolomitization) may be recognized by this technique, which helps in supporting the results obtained by EBSD.

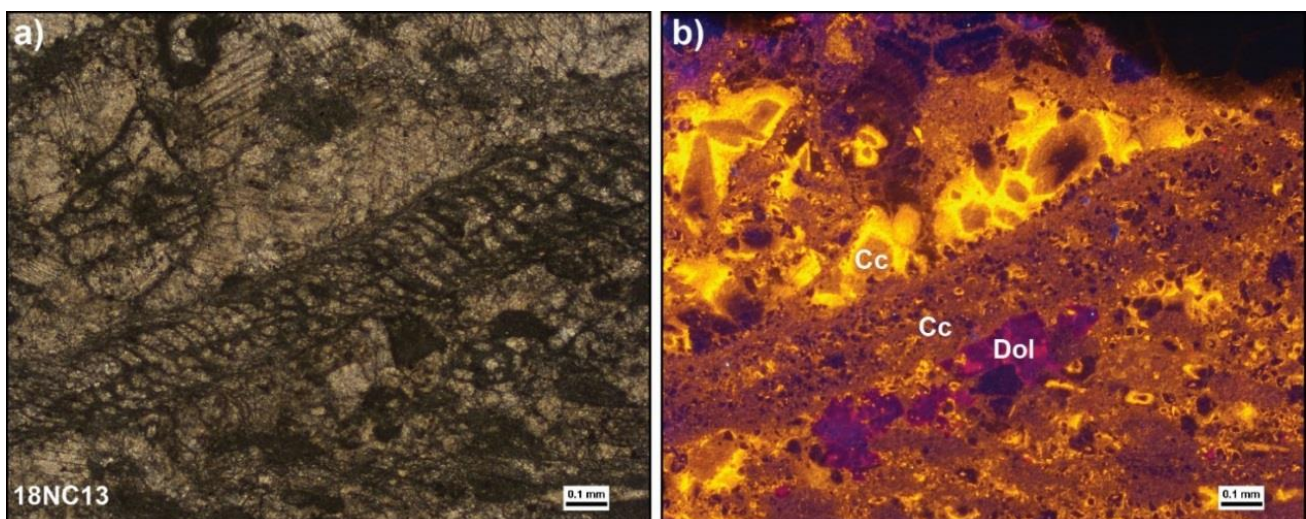


**Fig. 3.7.** Transmitted (left) and cathodoluminescence (right) light of a sample from autochthon upper Cretaceous of the Eaux-Chaudes massif. Dolomite is identified by violet and magenta colours while calcite is characterized by yellow colours.

## **Chapter 4: Macroscale structure of the Eaux-Chaudes massif (ECM) and implications for the deformation of the Pyrenean hinterland**

Paleotectonic reconstructions place the upper Cretaceous platform carbonates of the ECM in the upper margin of the Iberian plate during the Mesozoic post-rift stage (e.g. Teixell et al., 2016 and references therein, Labaume & Teixell, 2020). These carbonates later became sandwiched between Paleozoic rocks during the Pyrenean convergence, where we define a new structural profile featuring an unexpected large-scale ductile structure involving alike the Cretaceous and the Paleozoic rocks, firstly proposed in Caldera et al. (2021). It consists of a south-verging ~5km-long recumbent fold nappe cored by folded Silurian-Devonian metasediments with a near-horizontal axial plane and a large sheared overturned limb (Fig. 4.1a). The Paleozoic core shows a heterogeneously distributed foliation developed during both, the Variscan and Alpine deformation episodes, and minor-scale folds with horizontal axial planes parallel to the large structure. The overturned limb is in thrust contact over an autochthonous panel of weakly deformed upper Cretaceous carbonates with occasional remnants of Keuper and ophiolites along it as observed in the cropping geology (e.g. Fig. 4.2). This unique Pyrenean structure is fairly comparable to the lower Helvetic Morcles-Doldenhorn nappes of the Alps (Fig. 4.1b), which feature recumbent folds with long overturned limbs involving low-grade Mesozoic metasedimentary rocks (e.g. Ramsay, 1981; Burkhard, 1988; Escher et al., 1993; Pfiffner, 1993; Casey & Dietrich, 1997; Herwegh & Pfiffner, 2005). The regional plunge of the western Axial Zone to the west is also recognized in the Eaux-Chaudes recumbent structure, which hence disappears laterally under overlying thrust sheets. East of the Ossau valley the Eaux-Chaudes fold nappe (ECFN) is largely eroded, so the valley area provides a unique opportunity to observe the proposed structural relationships. The aim of this chapter is to provide sufficient structural data and field images to extend and further complement the hypothesis proposed in the first publication of the thesis work (Caldera et al., 2021).

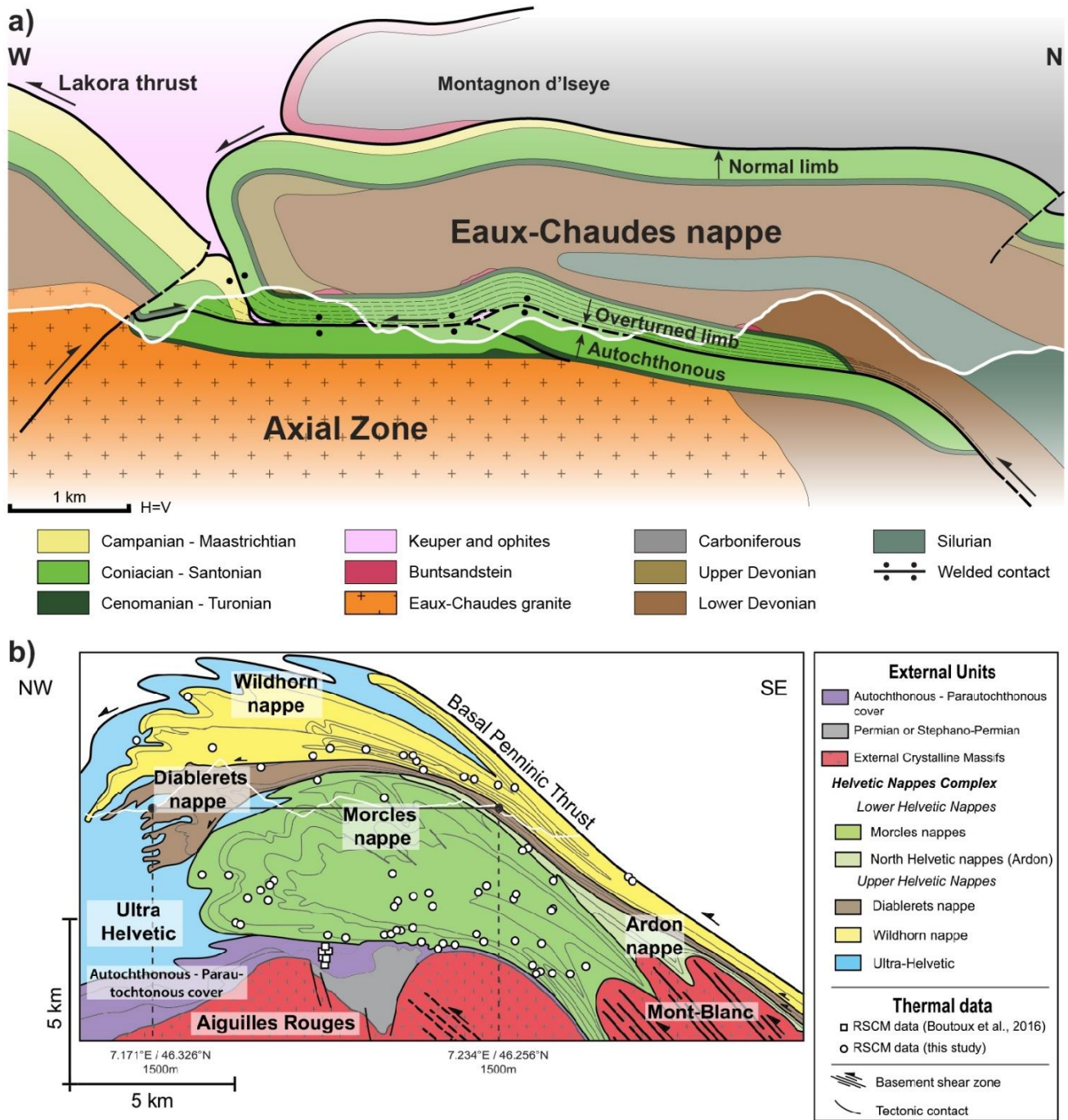


**Fig. 4.1.** a) Cross-section of the Eaux-Chaudes fold nappe in the western side of the Ossau valley as proposed in Caldera et al. (2021). Section trend is equivalent to S2 in Fig. 4.2. b) Cross-section of the Helvetic Morcles nappe from Girault et al. (2020). The Eaux-Chaudes and Morcles nappes show both large-scale and sheared overturned limbs, near-horizontal axial planes, overlie strong basements, and are in turn overlain by upper nappes.



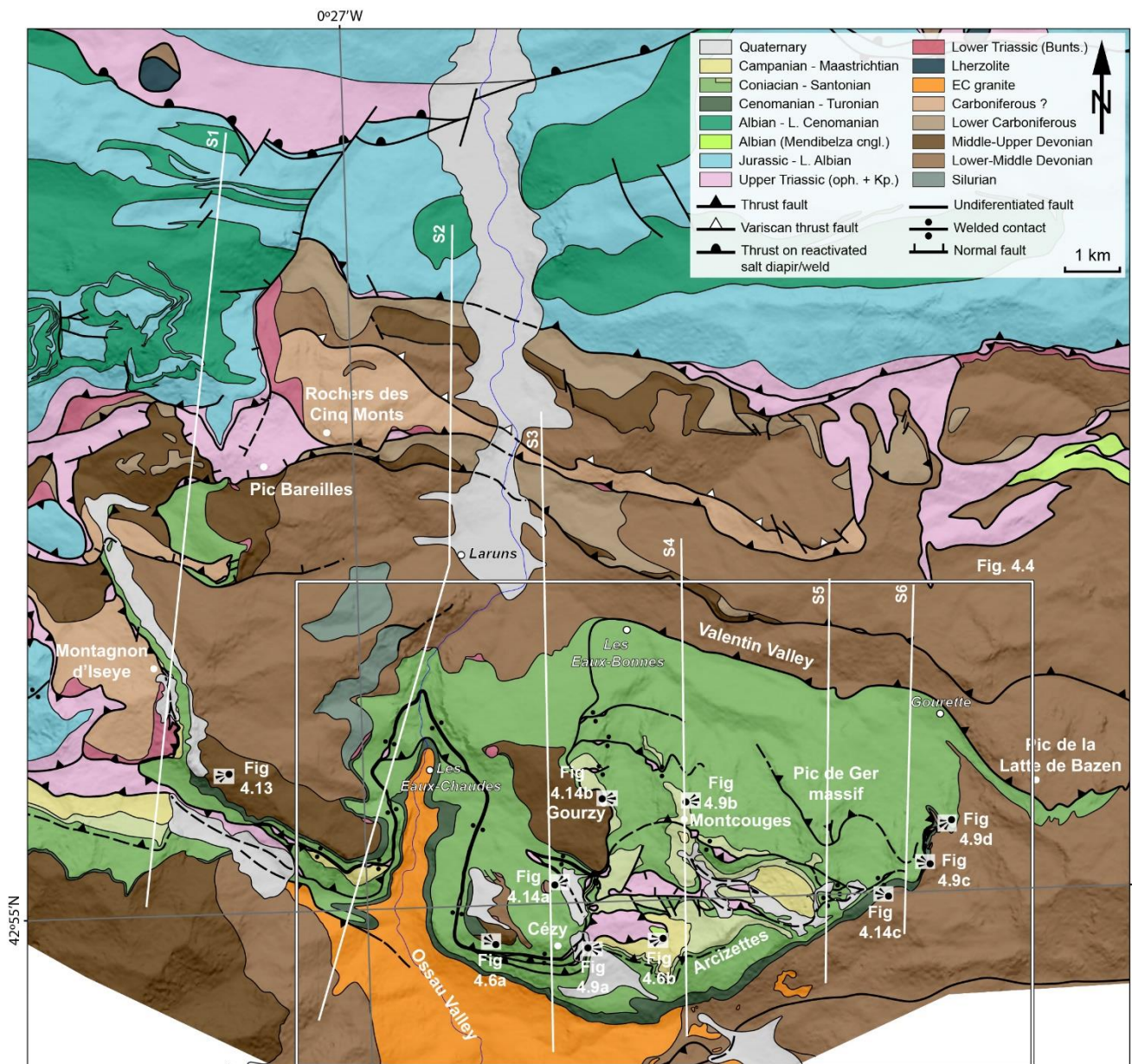


**Fig. 4.2.** Updated geological map of the Eaux-Chaudes massif and surrounding areas. Data compiled from published maps (Ternet, 1965; Ternet et al., 2004; Labaume & Teixell, 2020; Caldera et al., 2021), and own field observations. The white frame indicates the mapped area amplified in Fig. 4.4. S1 to S3: cross-sections in Fig. 4.5. S4 to S6: cross-sections in Fig. 4.8. Indicated in the legend with a question mark is an azoic succession of limestones and slates attributed tentatively to the Carboniferous by Ternet et al. (2004). The locations of figures with interpreted landscapes are also indicated.

## 4.1. Structural units in the study area

The stratigraphic record of the ECM, described in chapter 1, is well-constrained after Ternet et al. (2004) which has been clue in the recognition of structural features, especially the polarity of the strata. The tectonic configuration is based in four main tectono-sedimentary units (Fig. 4.3) arranged from bottom to top as:

- 1) The Gavarnie nappe, with upper Cretaceous carbonate rocks unconformable on the Paleozoic metasediments and granite, and with scarce Buntsandstein remnants in between (Fig. 4.2).
- 2) The Eaux-Chaudes nappe, with upper Cretaceous rocks and Paleozoic metasediments involved in complex folding. This unit is divided into two sectors: western and eastern. The first corresponds to the Eaux-Chaudes Fold Nappe (ECFN) and the latter features a simple thrust structure as the continuation of the recumbent fold structure to the east, the change of which will be discussed below.
- 3) The Paleozoic-bearing thrust sheets overlying the ECM, comprising metasedimentary basement rocks with local Buntsandstein pods and Keuper. Three large nappes are differentiated: Montagnon d'Iseye Nappe (MIN), Montagne Verte Nappe (MVN) and Cinq-Monts Nappe (5MN),
- 4) The system formed by the assemblage of the allochthonous Keuper (upper Triassic) thrust sheet from the Bedous unit (Lower Lakora thrust), overlying all the units described above (cf. Fig. 1.1c), and the Chaînons Béarnais Belt of the North Pyrenean Zone, consisting of a Jurassic and Lower Cretaceous succession detached on the Triassic Keuper (Lakora thrust *sensu lato*) and affected by thermal metamorphism inherited from the Cretaceous rift to post-rift stages.



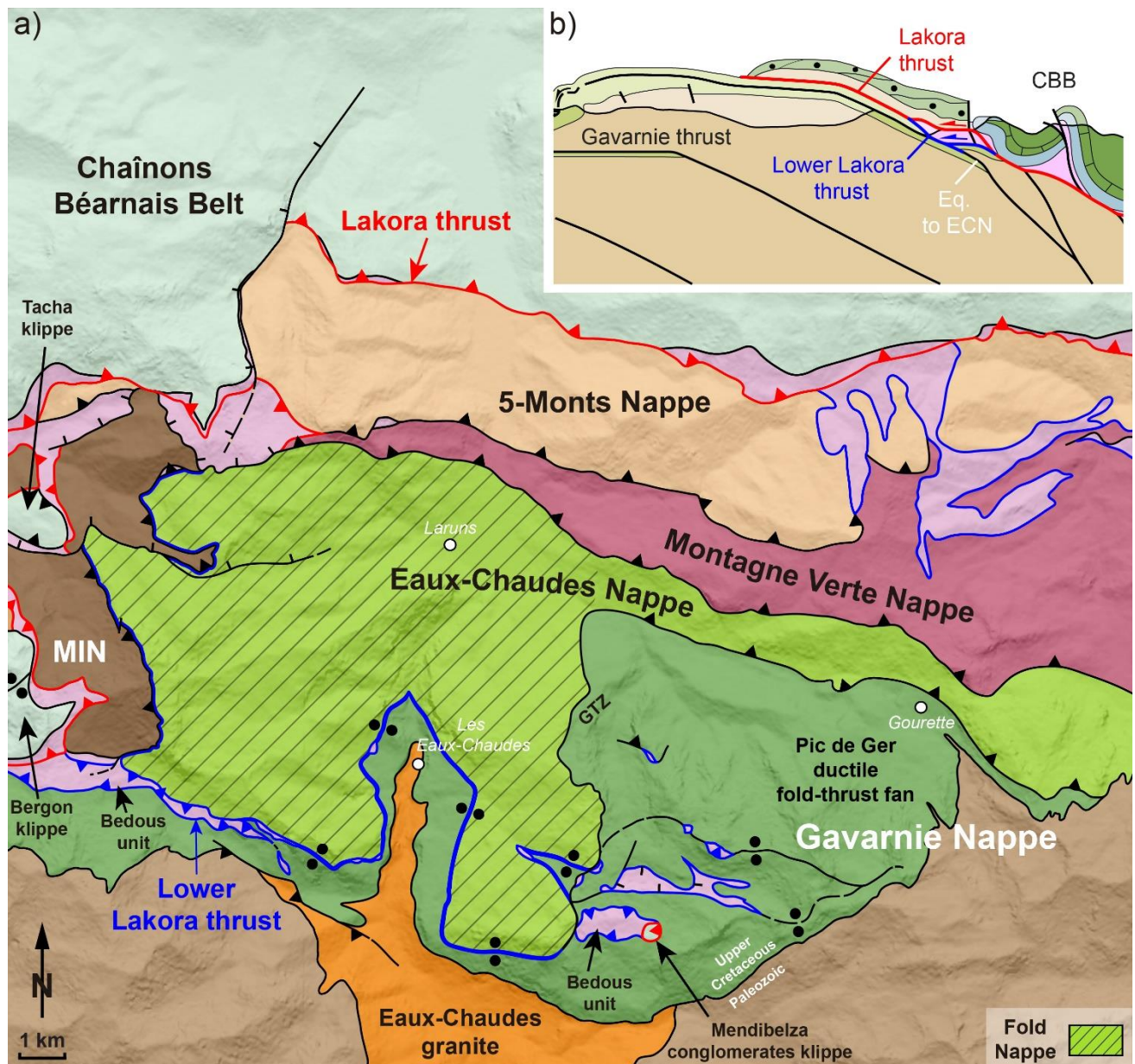


**Fig. 4.3.** (a) Simplified tectonic map of main structural units of the Eaux-Chaudes massif and southern edge of the Chaînons Béarnais Belt. The Bedous unit corresponds to the upper Triassic carried by the Lower Lakora thrust. MIN: Montagnon d'Iseye Nappe; GTZ: Gourzy Transfer Zone. (b) Detail of the regional cross-section in Fig. 1.1b (cf. chapter 1) from the Gavarnie nappe and its overlying tectonic units indicating the structural position of the Lower Lakora thrust and Lakora thrust sensu lato. The small thrust duplicating the upper Cretaceous would be equivalent to the Eaux-Chaudes nappe described in this thesis (Eq. to ECN).

#### 4.1.1. The Eaux-Chaudes Nappe (ECN)

The western sector of the ECN comprises the ECFN, firstly described in Caldera et al. (2021), well-identified on both sides of the Ossau Valley (Fig. 4.2). The eastern sector shows a simple thrust

largely eroded, which corresponds to the classical Eaux-Bonnes thrust (e.g. Bresson, 1903). The fold nappe involves the upper Cretaceous carbonates and the upper Paleozoic succession that occupies the fold core. It directly rests above the low deformed and sub-horizontal autochthonous upper Cretaceous carbonates (Gavarnie unit) by a sharp contact. In the autochthonous and in the normal limb of the nappe, sedimentary textures are well preserved, with small-scale brittle faults, and spaced pressure-solution-cleavage. Generally, fossils are unstrained apart from solutions seams, and ductile deformation at the grain scale is not observed. The contact that is usually mapped as the Eaux-Chaudes thrust in the Ossau valley (e.g. Ternet et al., 2004) is here reinterpreted as an overturned stratigraphic boundary between Paleozoic and upper Cretaceous carbonates, supported by (1) the occurrence of overturned Buntsandstein pods along the contact, (2) a folded Paleozoic stratigraphy cored by Silurian slates, and (3) the recognition by Ternet (1965) of overturned Paleozoic and Cretaceous rocks at the Cézy peak and nearby (cf. Fig. 1.5a). Features of strong ductile deformation that obliterates the primary sedimentary textures and the fossil content, such as pervasive mylonitic foliation and stretching lineation have been identified along the carbonates from the overturned limb, both plunging to the north (Caldera et al., 2021). Large-scale recumbent folds with kilometric overturned limbs have not been previously reported for the Alpine Pyrenees, while they were reported for the Variscan deformation in developed in the Paleozoic metasediments (Aerden & Malavieille, 1999; Matte, 2002, and references therein; Bastida et al., 2014). The autochthonous upper Cretaceous carbonates of the Gavarnie nappe continue to the west as a simple north-dipping monocline and eventually folded limiting the western termination of the Axial Zone (cf. Fig. 1.1a, b).

To the east, the Eaux-Chaudes nappe passes laterally to a tentatively interpreted simple hanging-wall anticline through a relatively narrow transfer zone, here named the Gourzy transfer zone, located between the Pic du Gourzy and Montcouples, and passing by Les Eaux-Bonnes village to the north (e.g. Figs. 4.2, 4.3, 4.4). It consists of a high-angle, west-dipping tear fault system, which accommodates a displacement reduction of the Eaux-Chaudes allochthon, passing from the far-reaching fold nappe in the west to a simple thrust in the Valentin valley by which Paleozoic rocks overlie upper Cretaceous carbonates with normal stratigraphic polarity (the Eaux-Bonnes thrust

recognized by Bresson, 1903) (Fig. 4.4). In this latter area, the upper Cretaceous of the hanging wall and the possible fold structure that it defined has been eroded, while the Cretaceous of the footwall, in the Pic de Ger massif and surroundings, is intensely deformed by an imbricate, ductile fold-thrust fan that (Fig. 4.3a) is described in section 4.2.

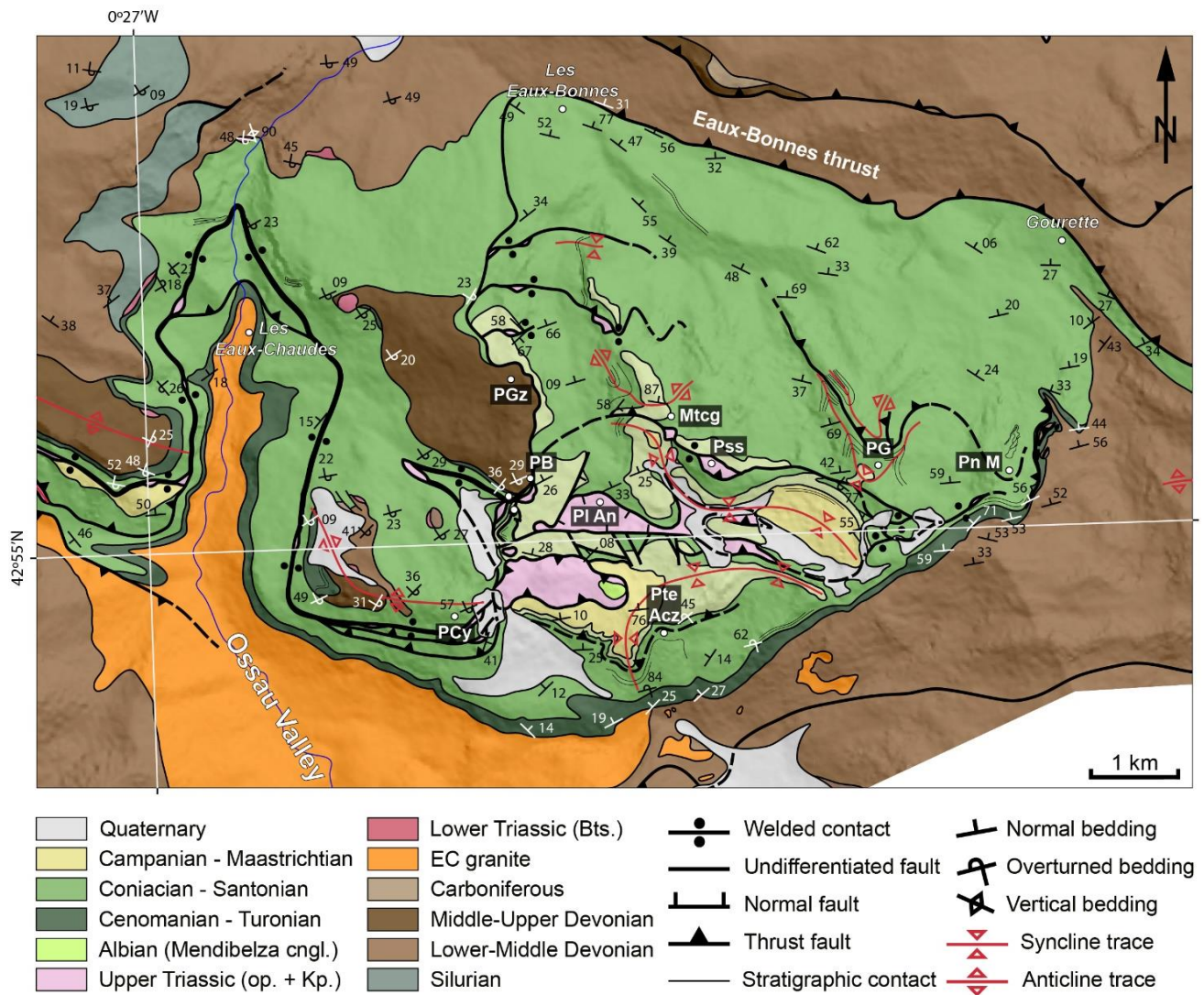


**Fig. 4.4.** Detailed map of the Eaux-Chaudes massif (based on Fig. 4.2) showing further structural data and the situation of the main localities referred to in the text. PCy: Pic de Cézy; PGz: Pic du Gourzy; PB: Pic de Breque; Pl An: Plateau d'Anouilh; Pte Acz: Petite Arcizette; Mtcg: Montcoges; Pss: Pambassibé; PG: Pic de Ger; Pn M: Pêne Médaa.



### 4.1.2. *The Paleozoic nappes over the ECFN*

The ECFN is overlain by a stack of basement-involved thrust sheets (e.g. Fig. 4.3), first reported by Majesté-Menjoulas (1968) and later mapped by Ternet et al. (2004). Three units are described below, from bottom to top in the pile (as discussed in section 4.3), with a definition that differs from the previous reports. The first unit overlying the ECFN is the Montagnon d'Iseye fold nappe (MIN), outcropping on the western edge of the massif (Labaume & Teixell, 2020; Caldera et al., 2021). The southern part of this unit consists of a south-verging recumbent fold with a ~2 km-long overturned limb outlined by the Lower Triassic Buntsandstein facies and cored by Carboniferous rocks in the southern region while comprises Devonian and Carboniferous in the northern part. Late normal faults cut both the MIN and the Cretaceous of the ECFN (Fig. 4.2).

The second thrust nappe corresponds to the Montagne Verte Nappe (MVN) (Fig. 4.3), formed by upper Devonian to Lower Carboniferous metasediments surrounded by discontinuous Buntsandstein pods. From west to east, this unit widens cartographically and reaches ~3.5 km wide in the extreme east of the study area (Fig. 4.3). There is no identified overturned limb in this unit. The uppermost basement unit is the Cinq Monts nappe (5MN) (Fig. 4.3). Similarly to the ECFN and MIN, it also contains an overturned limb at the front of the structure, although slightly smaller than that of MIN, defined by the Buntsandstein beds intermittently eroded. As common in the Paleozoic units its interior preserves a Variscan thrust structure sealed by the Buntsandstein, and previously mapped by Ternet et al. (2004) (Fig. 4.2).

### 4.1.3. *The Lakora thrust system and the Chaînons Béarnais Belt*

The Eaux-Chaudes massif and the Paleozoic-bearing thrust sheets are overlain by the Lakora thrust system (red and blue lines in Fig. 4.3). The Lakora thrust system was firstly attributed to the inversion of the Iberian rifted margin since the latest Cretaceous (Teixell, 1993, Teixell et al., 2016). The main Lakora thrust *sensu lato* (as proposed by Teixell, 1993) in the study area carries the Jurassic-Lower Cretaceous sedimentary rocks of the Chaînons Béarnais Belt (CBB) from the North Pyrenean Zone

(NPZ). It is accompanied by a thick Keuper thrust horse at its bottom (the Bedous Triassic unit of Labaume & Teixell, 2020) (Fig. 4.3b), whose sole thrust is here referred to as the Lower Lakora thrust (LwLT; blue lines in Fig. 4.3). The CBB is interpreted a salt-detached fold-and-thrust system made of Middle Triassic to Lower Cretaceous rocks from the former rift axis (Labaume & Teixell, 2020). Two outliers of the CBB are preserved above the western termination of the Montagnon d'Iseye nappe (MIN) (the Tacha and Bergon klippe; e.g. Fig. 4.3a). The characteristic shortcut of the Paleozoic in the leading edge of the Lakora thrust sheet, firstly reported in the Iguntze massif (Teixell, 1993), is lacking in the study area. In contrast to this, small remnants of siliciclastic conglomerates, attributed to the Albian Mendibelza formation (Ternet, 1965), have been preserved over the Triassic Keuper or directly on the footwall over the upper Cretaceous (Fig. 4.2).

## 4.2. Structural cross-sections of the Eaux-Chaudes massif

To describe the structure of the Eaux-Chaudes massif and its lateral variation from west to east, six new cross-sections were constructed (Figs. 4.5, 4.8), and supported by field data and several interpreted outcrop images or panoramas (Figs. 4.6, 4.9). The sections are oriented approximately N-S, perpendicular to the dominant structural trend. They have been constructed from original field work (geological map, structural data and observations) complemented by compiled data from previous works (e.g. Ternet, 1965, Ternet et al., 2004, Labaume & Teixell, 2020, Caldera et al., 2021). The Move software (Petroleum Experts) was used for the managing of map data and to constrain surfaces and geolocation of structural data in 3D.

The description of the sections is divided into two parts, west and east of Les Eaux-Bonnes village (e.g. Fig. 4.2), attending to the different structural characteristics of the ECM. While in the western sector (Ossau Valley), the general structure of the ECM is a large-scale, basement-involved allochthonous fold nappe (Figs. 4.3, 4.5), the eastern sector (Pic de Ger massif) is characterized by a fold-thrust fan developed in the autochthon upper Cretaceous (Figs. 4.3, 4.8). The geometry and structures of the Chaînons Béarnais Belt shown in S1 are based on Labaume & Teixell (2020), where

constraints are more reliable. To the east they are not represented due to their higher erosion. Similarly, the projection of the 5MN nappe in section S3 is speculative (blurred to white in the figure).

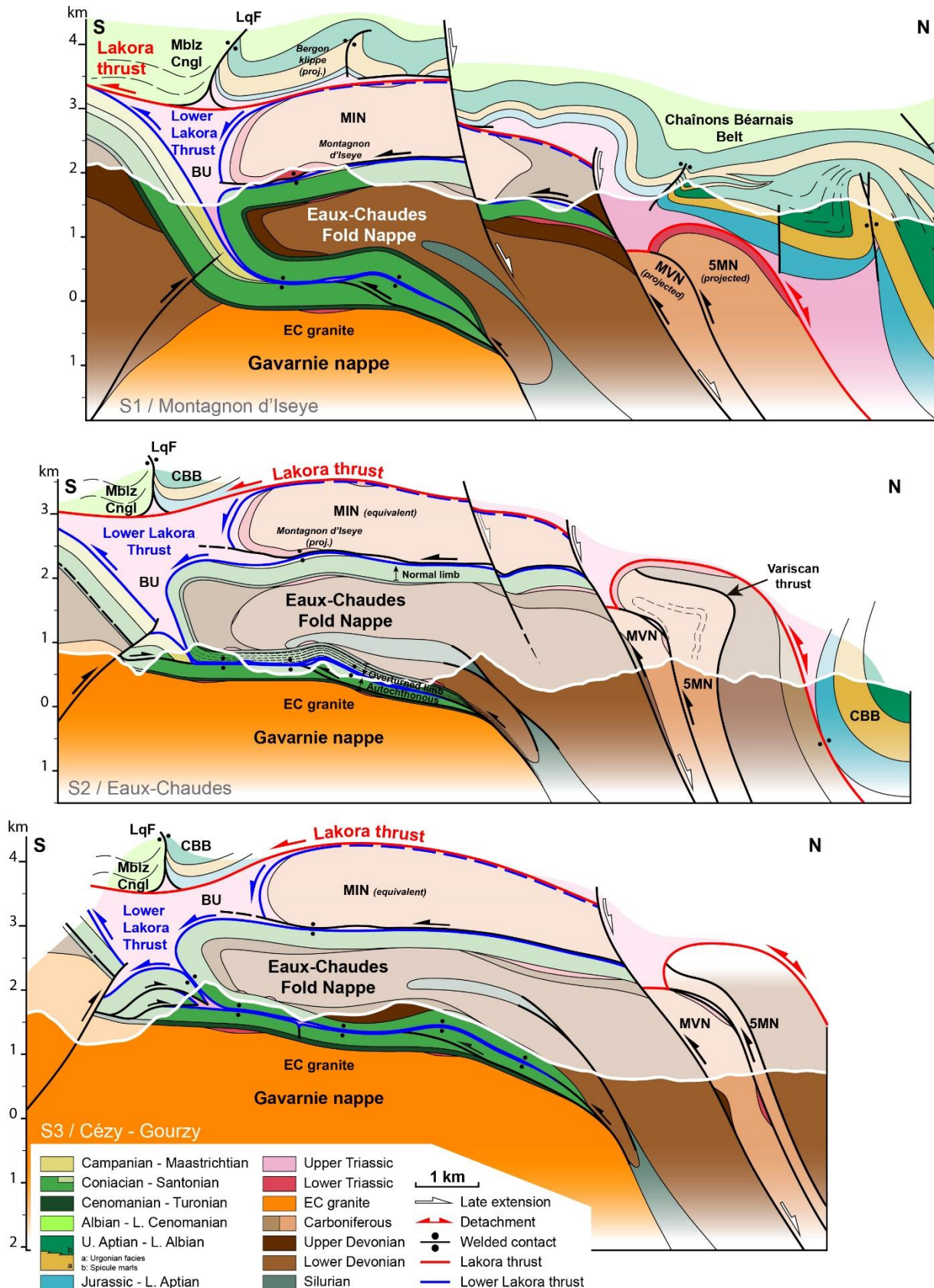


**Fig. 4.5.** Geological cross-sections of the western sector of the Eaux-Chaudes massif (Ossau Valley) presenting the lateral variation of the Eaux-Chaudes fold nappe from west to east (S1 – S3), and the overlying tectonic units (see location in Fig. 4.2). Section S2 is the update from Caldera et al. (2021) shown in Fig. 4.1. Mblz Cngl: Mendibelza Conglomerates; LqF: Licq Fault; MIN: Montagnon d'Iseye Nappe; 5MN: Cinq Monts Nappe; MVN: Montagne Verte Nappe; CBB: Chaînons Béarnais Belt; BU: Bedous Unit (carried by the Lower Lakora thrust). White line corresponds to the topography and the above geology is interpreted.

#### 4.2.1. Western sector (Ossau Valley): The Eaux-Chaudes Fold Nappe (ECFN)

The general structure of the ECM has been classically interpreted as a duplex with a roof thrust carrying Paleozoic rocks over the upper Cretaceous (Ternet, 1965; Déramond et al., 1985; Dumont et al., 2015; Cochelin et al., 2017). Just a small, overturned fold limb was reported by Ternet (1965) in the front of the structure without continuity to the north. Caldera et al. (2021) proposed recently a reinterpretation of this structure in the western sector consisting of a km-scale, south-vergent recumbent fold nappe with a large, overturned limb (Caldera et al., 2021; Fig. 4.1a). Here, the cross-section presented in Caldera et al. (2021) is updated in the profile S2 (Fig. 4.5). Due to a general westward plunge of the structure, the geological constraints for the upper thrust sheets, today extensively eroded, are stronger to the west, while larger uncertainties arise to the eastern sections.

The autochthonous upper Cretaceous (i.e. the Mesozoic cover of the Gavarnie nappe, Figs. 4.2, 4.4) lies unconformably on the Eaux-Chaudes granite and remains mostly unstrained (Ternet, 1965; Caldera et al., 2021) under the ECFN. Its succession is not always complete but locally preserved up to the Campanian flysch (e.g. below the Montagnon d'Iseye thrust in S1 cross-section). Features observed in the upper Cretaceous carbonates of the overturned limb, such as stretching mineral lineation and mylonitic foliation, indicate top to the south shearing developed under ductile conditions and relatively moderate temperatures (315°C-360°C; Caldera et al., 2021). Evidence examples of this ductility at large and small scales are S-C composite fabrics, mylonitic foliation at a low angle to stratification, and asymmetric kinematic indicators (i.e. crystal-shape, dolomite porphyroclasts). These structures are further documented in chapter 6.

The Eaux-Chaudes fold nappe plunges to the west following the general trend of the western Axial Zone. Although there exist some small differences in the fold shape across the west-east trend in the three sections (Fig. 4.5), the overall geometry is fairly consistent. The overturned stratigraphy has been identified by the presence of Buntsandstein pods along the contact between Paleozoic and upper Cretaceous rocks of the fold core. As mentioned before, the clastic rocks of the Buntsandstein show way-up criteria (crossbedding, grain-size grading) indicating an inverted position. It is worth mentioning the strong thinning of the upper Cretaceous in the overturned limb from section S1 to section S3 (Fig. 4.5).

The hinge zone of the recumbent fold is box-shaped featuring strong ductile deformation in the Cretaceous rocks by intense stretching of fossils, folding and grain recrystallization. Great amount of fluid circulation along the unconformity between the Paleozoic and upper Cretaceous is evidenced by a complex network of calcite and quartz veins, sometimes crossing from the Paleozoic to the Mesozoic rocks. The emplacement of the ECFN is linked in depth with the classically named Eaux-Bonnes thrust (e.g. Bresson, 1903, Ternet et al., 2004), well-traced in the Valentin valley (“accident du Valentin” in Ternet, 1965) (Figs. 4.2, 4.4). Several ophite bodies remain trapped in between the overturned limb of the ECFN and its autochthon (Figs. 4.2, 4.4). They are remains of the allochthonous Keuper sheet of the overlying Lakora unit pinched in the synformal zone between both limbs (Fig. 4.7) (i.e. a tertiary type weld *sensu* following Jackson & Hudec, 2017) (Caldera et al., 2021). In the Paleozoic core of the fold, inherited Variscan structures such as folds and foliations can be recognized (light grey lines in Fig. 4.6).

South of the recumbent fold, the autochthonous upper Cretaceous features small steep north-vergent back-thrust structures (Caldera et al., 2021) (Figs. 4.5, 4.6), associated with the tilting of the northern Axial Zone. These thrusts are visible on the western side of the Ossau Valley, where they offset the basement and the upper Cretaceous alike (section S1 in Fig. 4.5 and Fig. 4.6a; Caldera et al., 2021). The number and complexity of these structures increase from west to east, evolving from a simple back-thrust (S1) to a small antiformal stack (section S3 in Fig. 4.5 and Fig. 4.6b). On the eastern side of the Ossau Valley, on the southern slopes of the Pic du Cézy, the back thrusts cause repetitions of



the upper Cretaceous and Keuper sheet (Sections S2 and S3 in Fig. 4.5 and Fig. 4.6b). Ophite bodies are also pinched between the hinge of the ECFN and the imbricate back thrusts.

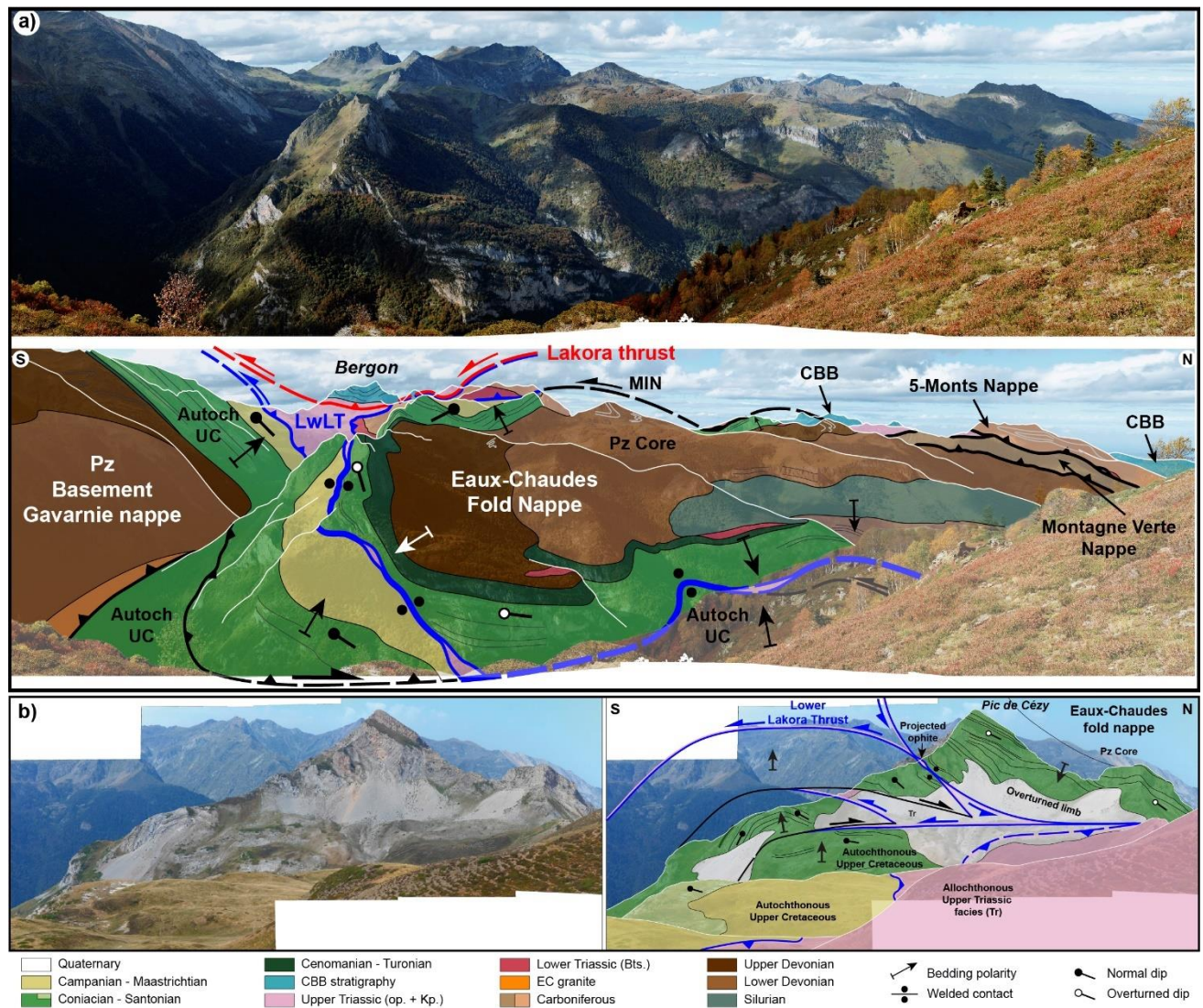


**Fig. 4.6.** (a) Interpreted panorama of the Eaux-Chaudes recumbent fold and overlying tectonic units (MIN, Lower Lakora and Lakora thrusts, 5MN, CBB, MVN) in the Ossau Valley from an eastern viewpoint. (b) Interpreted panorama of the Pic de Cézy from an eastern viewpoint. It corresponds to the southern termination of the recumbent fold in section S3. The system of late back thrusts (black) is overprinting the Lower Lakora thrust (blue), which is marked by Keuper and ophite bodies. See the location of the views in Fig. 4.2.

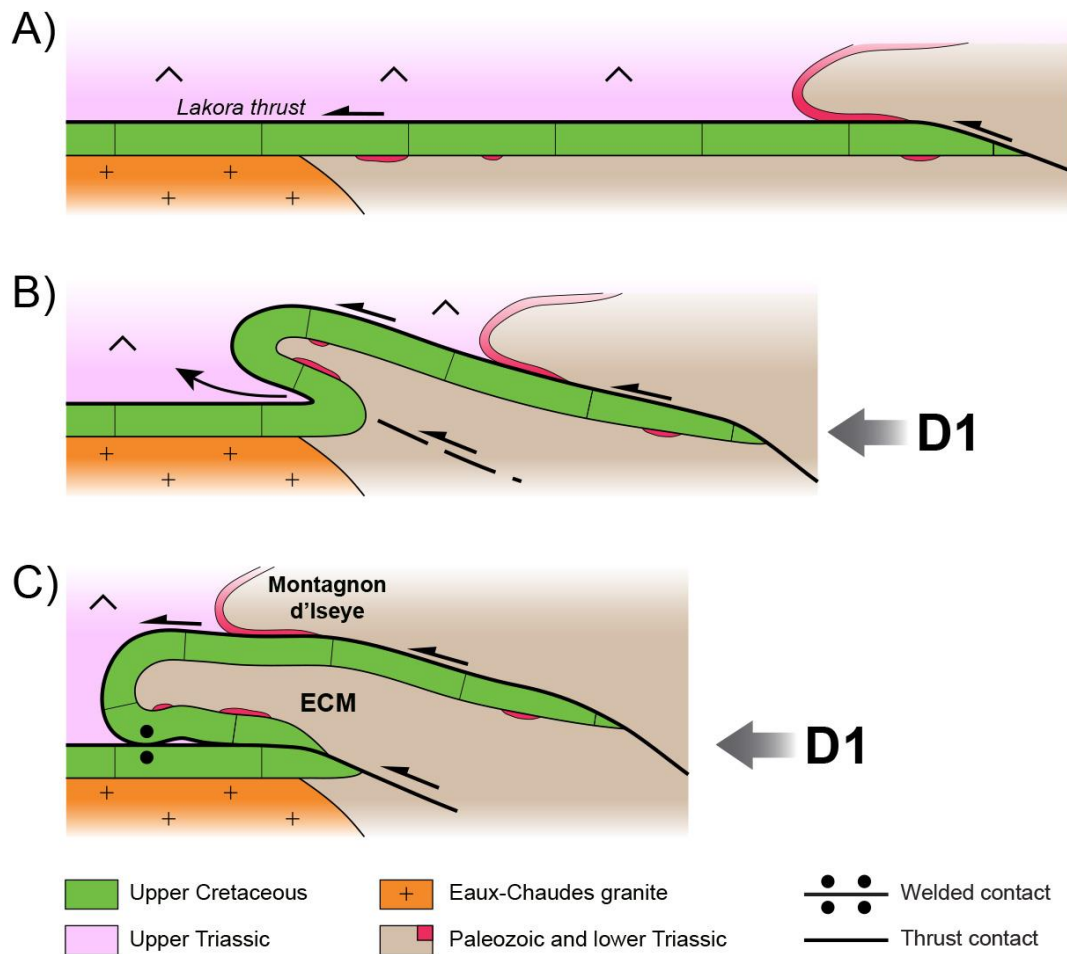


**Fig. 4.7.** Simplified sketch illustrating the evolution of the ECFN during the main compressional event of the Pyrenean orogeny (D1) (Caldera et al., 2021). In (c) there are shown the relicts of Keuper and ophites in between the overturned limb and the autochthon, during extrusion related to the Eaux-Chaudes fold nappe emplacement. The thickness of evaporites (upper Triassic) and subsequent units (i.e. MIN) are poorly constrained.

The Paleozoic stratigraphy entrained in the fold core also displays the anticlinal geometry, but inherited structures determine more complex features (e.g. Fig. 4.6), i.e. Silurian slates are locally touching the overturned upper Cretaceous (see S2 section), and to the north, they become pinched by the Devonian limestones accommodating top-to-the-south shearing.

The projection, in cross-sections, of the Paleozoic-bearing upper thrust sheets reported over the ECFN (i.e. MIN, MVN and 5MN) is constrained from the cropping geology on the normal limb (i.e. Montagnon d'Iseye) or to the north of the Laruns village and Valentin Valley (Montagne Verte and Cinq Monts area). The MIN and 5MN show strongly overturned fold limbs defined by the



Buntsandstein. Frequently, Keuper pods from the Bedous unit are locally pinched between the MIN and normal limb of the ECFN, likewise than observed in between the pinched syncline of the ECFN (e.g. Fig. 4.7). Those pods derive from the overlying Lower Lakora thrust sheet. The Lakora *s.l.* carries, over its basal Keuper, the whole stratigraphy of the Chaînons Béarnais Belt together with Mendibelza conglomerate (e.g. Figs. 4.3, 4.5, 4.8), that is interpreted to be separated by the Licq fault, in a similar way than was observed more to the west by Labaume & Teixell (2020).

#### *4.2.2. Eastern sector (Pic de Ger massif): The ductile fold-thrust system*

The cross-sections and field-interpreted images from the eastern sector are shown in Figs. 4.8 and 4.9. In this area, the majority of the upper thrust sheets are eroded, and constraints are scarce, except for a klippe of Keuper and Mendibelza conglomerates carried by the Lakora thrust system on top of the upper Cretaceous (cropping out south of Plateau d'Anouilhas, Fig. 4.4 for location). Although intensely folded, as reported by Ternet (1965), the upper Cretaceous is broadly in a right-way-up attitude, and in contrast with the western sector, a long-overtaken panel is not observed.

The eastern continuation of the reverse limb of the ECFN is done through the Eaux-Bonnes thrust, a structure that brings the Paleozoic on top of the autochthon upper Cretaceous in the Valentin valley (Figs. 4.2, 4.4, 4.8). The justification for the tentative structure in the hanging-wall drawn in the sections will be addressed in the discussion chapter. Contrary to what it was observed in the western sector, the autochthon upper Cretaceous in the eastern is notwithstanding affected by strong ductile deformation. Cross-sections S4 to S6 and field images (Figs. 4.8, 4.9) illustrate a strain gradient in the autochthonous rocks that increases from west to east and from south to north by increasing the number of structures and their accompanying strain.

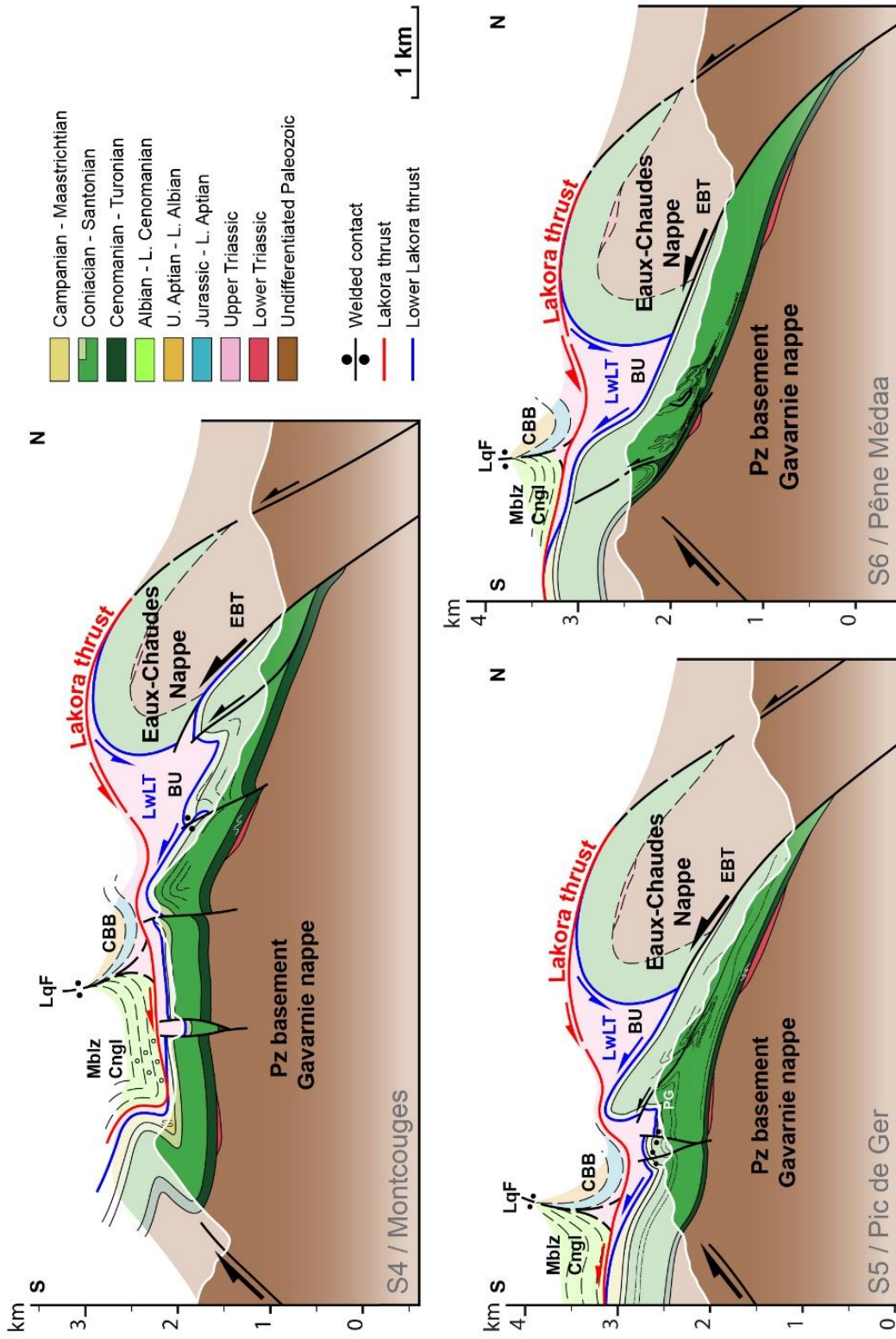


**Fig. 4.8.** Geological cross-sections of the eastern sector of the Eaux-Chaudes massif featuring the strong ductile deformation in the upper Cretaceous in the footwall of the Eaux-Chaudes nappe. See location in Fig. 4.2. Mbiz Cngl: Mendibelza Conglomerates; LqF: Licq Fault; CBB: Chaînons Béarnais Belt; LwLT: Lower Lakora thrust; BU: Bedous Unit (carried by the Lower Lakora thrust); EBT: Eaux-Bonnes Thrust; PG: Pic de Ger in S5. The Eaux-Chaudes fold nappe is tentatively interpreted to be replaced in these transects by a simple thrust-related ramp anticline, whereas much of the deformation is transferred to its footwall. White line corresponds to the topography and the above geology is interpreted.



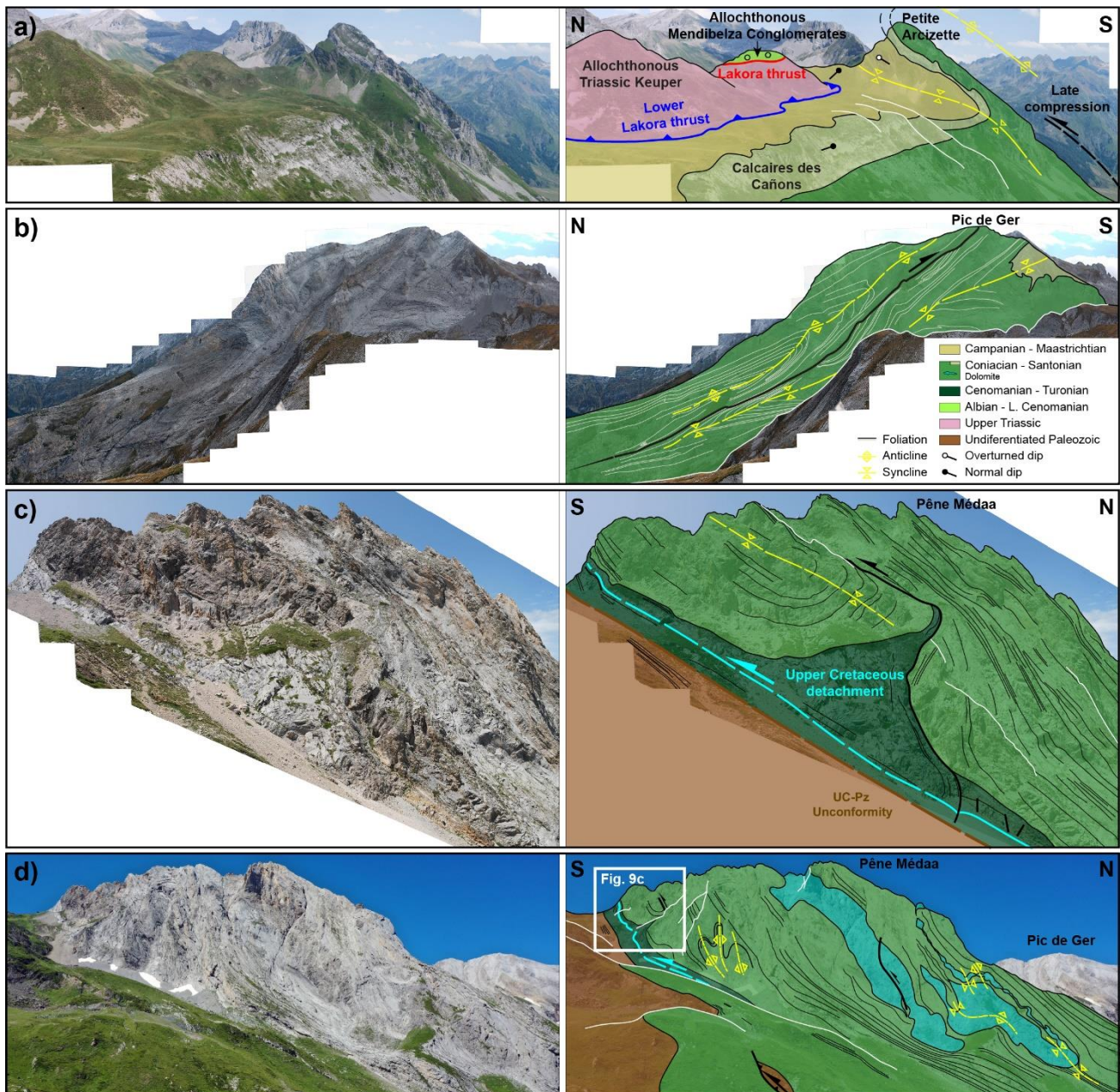


**Fig. 4.9.** Interpreted panoramic views showing different examples of deformation in the upper Cretaceous of the eastern part of the Eaux-Chaudes massif (location of views in Fig. 4.2). (a) View from the west of the Petite Arcizette north-verging syncline. The blue line corresponds to the Lower Lakora thrust carrying the allochthonous Keuper and the red line to the Lakora thrust carrying Mendibelza conglomerates. See text for explanation. (b) View from the west of the Pic de Ger. A large-scale isoclinal anticline-syncline pair with an intervening thrust attest for a strong ductile deformation in the upper Cretaceous. A view of the syncline on the eastern slope of the Pic de Ger is in Fig. 4.14c. (c) View from the east of the Pêne Médäa showing an intra-Cretaceous detachment at the level of the Cenomanian. Ductile deformation led to the folding and squeezing of the lower limestone units. (d) View from the east of the northern slope of Pêne Médäa showing large-scale dolomitic bodies affected by boudinage, folding and thrusts evidencing intense deformation in this area. Widespread mylonitic foliation in the host limestones is indicated by black lines. Small thrusts affect the basal unconformity.

Describing the section S4 from south to north, the first main structure recognized is a north-vergent syncline in the Mesozoic rocks of the Petite Arcizette peak (Fig. 4.9a) (peak location in Fig. 4.4; Pte. Acz.), with strongly deformed Campanian flysch rocks in its core. This structure trends E-W but is rapidly damped to the east. To the north, a subhorizontal or gently north-dipping kilometric-scale panel of upper Cretaceous is affected by hectometre-scale south-vergent folds and cut by a steeply dipping set of normal faults (Fig., 4.8a). An asymmetric E-W trending graben in Plateau d'Anouilh (location in Fig. 4.4) preserves Keuper facies, mostly represented by ophites, which are allochthonous over the upper Cretaceous. A few hundred meters to the west of section S4, two larger klippe are observed. One of them is carrying the Triassic and the other the Mendibelza conglomerates (Ternet, 1965) (Figs 4.3, 4.4, 4.8a), both proposed to be carried by the Lakora thrust system (Fig. 4.3).

Further to the east (e.g. S5 in Fig. 4.8) in the Pic de Ger, the folding of the upper Cretaceous becomes more intense and develops a fold-thrust fan (Fig. 4.3; namely "Pic de Ger fold-thrust fan"). It corresponds to the footwall of the ECN, accommodating large amount of strong ductile deformation. Two large-scale south-vergent similar folds (the anticline-syncline pair shown in Fig. 4.9b) are beautifully exposed on the western slopes of Pic de Ger, and separated by a complex north-dipping fault obliterated to the north by a penetrative schistosity. The axial planes are inclined to the north by  $\sim 30^\circ$  degrees (Figs. 4.8b, 4.9b). The limbs of the isoclinal folds are strongly stretched, the hinges are thickened, and a penetrative axial plane foliation is well-developed. Mylonitic foliation and mineral stretching lineation, as well as intrafolial folds, are widely developed along this area. South-vergent internal detachments within the upper Cretaceous are locally observed. They are schematically drawn in the S6 section from Fig. 4.8 and interpreted from the field images in Figs. 4.9c, d. The ductility of the basal facies of Cretaceous rocks (Cenomanian) is envisaged by triangular-shaped structures shown in Fig. 4.9c recording the plasticity and the squeezing of limestones. Asymmetric disharmonic folds are recognized north of the exposed detachment as well as folded, stretched, imbricated and boudinaged dolostone levels within the strained limestones (Fig. 4.9d), evidencing a large amount of shortening. As in the overturned limb, penetrative foliation, stretching lineation and tight folds are well-

developed at all scales. Foliation wraps around the large dolostone bodies, which occasionally resemble large porphyroclasts (Fig. 4.9d).

Several steep faults cutting the upper Cretaceous and Paleozoic rocks contain pinched bodies of Keuper facies and ophites, resembling salt welds (e.g. southern border of Pic de Ger, section S5 in Fig. 4.8). These unusual structures, which origin is discussed below, are observed preferentially in the upper part of the fault tracts and were reported by Ternet et al. (2004) (e.g. Figs. 4.4, 4.10). An example is the large ophite body located south of Pic de Breque (Fig. 4.10; Fig. 4.4 for location) and the continuous “weld” structure passing through the Montcouges-Pambassibé peaks and Pic de Ger massif (Figs. 4.2, 4.4, 4.10). To the east, they rapidly fade and are not observed in S6. Finally, small south-vergent imbricate thrusts, which probably started as extensional structures (i.e. normal faults), and were subsequently inverted, affect the unconformity between Paleozoic and Mesozoic rocks involving the upper part of Devonian and the Cenomanian under the main intracretaceous detachment level (S6 in Fig. 4.8 and Fig. 4.9d).

Fig. 4.10 show the structural complexity of mainly south-vergent inverted former extensional structures, involving allochthonous upper Triassic Keuper, developed in the autochthon upper Cretaceous where Paleozoic basement is represented by Devonian metasediments. The transition in between both domains is led by the Gourzy transfer zone (GTZ) (orange line). The Lakora thrusts is represented by the small remnant of Mendibelza conglomerates on top of the Keuper sheet located in between the Plateau d’Anouilhas and the Petite Arcizette. The Eaux-Bonnes thrust appears to the top-left border, represented by Paleozoic metasediments, and structures related to the late Gavarnie thrust emplacement are tentatively shown by a dashed black line featuring the retrodeformation that performed the north-verging Petite Arcizette syncline.



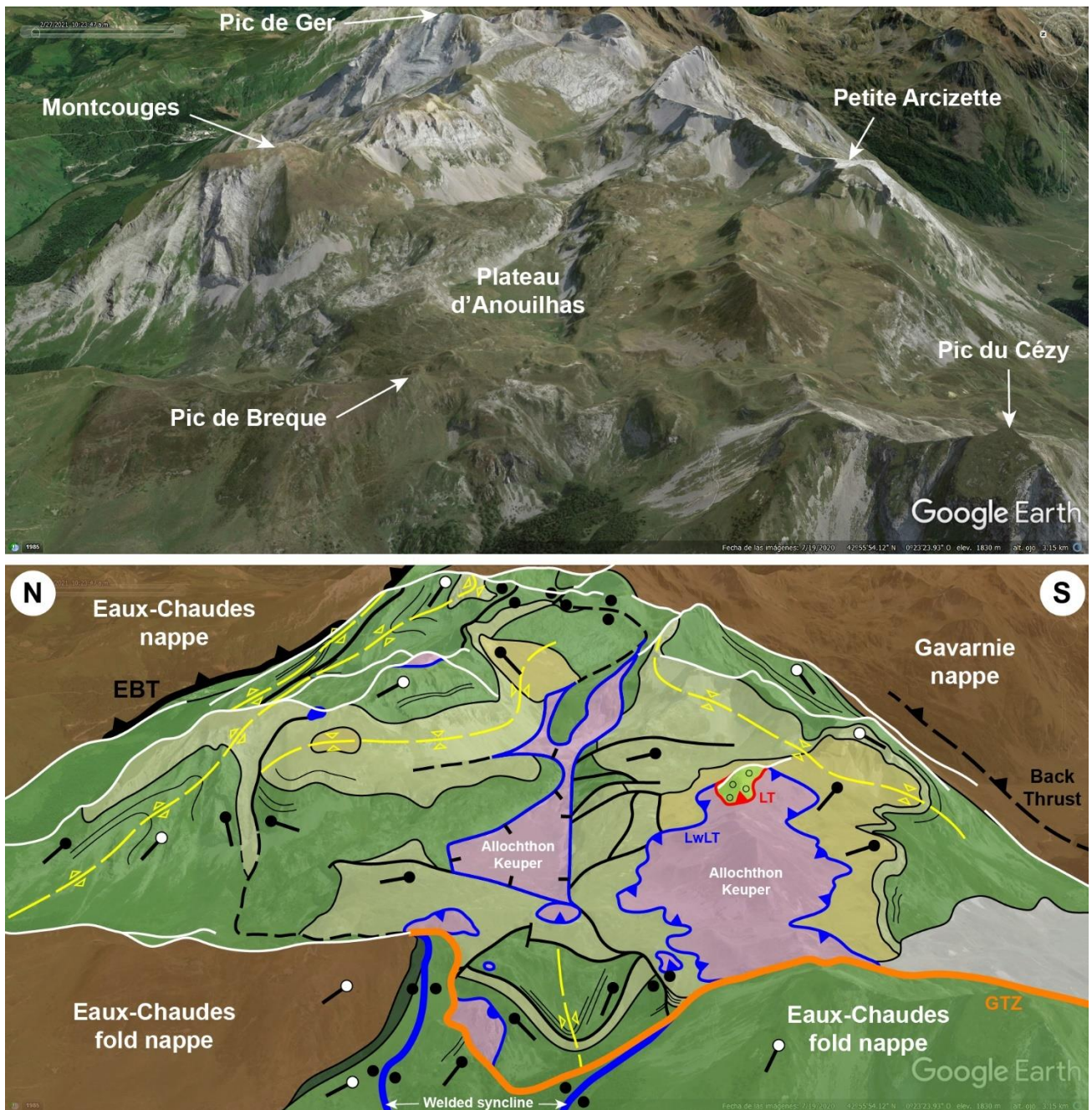


**Fig. 4.10.** Image interpretation of the transition from the ECFN to the autochthon domain eastwards, through the Gavarnie Transfer Zone, and showing the structural complexity of the autochthon upper Cretaceous and the upper Triassic Keuper involved in the deformation by multiple and varied type of inverted former extensional structures. EBT: Eaux-Bonnes Thrust; GTZ: Gourzy Transfer Zone; LwLT: Lower Lakora Thrust; LT: Lakora Thrust. For the colour code of the stratigraphy confer Fig. 4.2.

## 4.3. Discussion

### 4.3.1. *On the variation of the tectonic style*

Field observations and the cross-sections of the ECM indicate a complex ductile deformation of the Iberian margin during the Pyrenean collision. A marked difference in tectonic style is observed between the eastern and western sectors of the massif: from a large-scale recumbent fold nappe in the west to a fold-thrust system eastward. The fold nappe is characterized by high strain in the overturned limb, while in the fold-thrust fan the large amount of internal deformation is accommodated in the right way-up Cretaceous succession, which is autochthonous with respect of the ECN. Several factors may have contributed to the complex structure depicted in the cross-sections: 1) the structural inheritance of the Variscan basement, 2) the geometry and thermal gradient of the Iberian margin due to the Mid-Cretaceous hyperextension, 3) the mechanical stratigraphy of both the Mesozoic and Paleozoic strata and (4) the tectonic burial history by the upper thrust sheets. During the inversion of the margin, the structural inheritance of the basement and sedimentary cover induced the reactivation of ancient structures and triggered several detachment levels (Silurian, Keuper and intra-Cenomanian). The discussion is focused on two major key questions: 1) the factors influencing the lateral variation of the tectonic style of the ECM and 2) the time evolution of the ECM and overlying thrust units illustrated by qualitative restoration of two representative sections, S1 and S4 (Figs. 4.16, 4.17, from the west and east sectors, respectively).

### 4.3.2. *What caused the structural contrast between the fold nappe and the fold-thrust domain? Constraints from the recumbent fold*

As stated by Bastida et al. (2014), the development of large recumbent folds with moderately dipping axial surfaces requires specific conditions: low or medium metamorphic context accompanied by intense simple shear deformation.



During the past years, the importance of inherited extensional structures from the hyperextension (Chevrot et al., 2018) and of crustal-scale transfer zones (Saspiturry et al., 2022), has been highlighted to explain the structural non-cylindricity of the northern Pyrenees. For example, N-S trending transfer faults segment the Paleozoic-bearing upper thrust sheets in the western parts of the Ossau valley (i.e. the Ossau thrust of Canérot, 2008) (Figs. 4.2 and 4.3). The lateral structural variation in the ECN is quite sudden and occurs in a relatively narrow zone, located between the Pic du Gourzy and Montcouges, and passing through Les Eaux-Bonnes village located to the north. This lateral structure is interpreted as a transfer zone and here is named as the Gourzy transfer zone (Figs. 4.2, 4.3, 4.4). It is a high-angle, west-dipping tear fault system, which causes a recess of the Eaux-Chaudes allochthonous unit, passing from the far-reaching fold nappe to the west to the Eaux-Bonnes thrust (Fig. 4.11), by a relative displacement of approximately 4 km to the south by the fold nappe. The Cretaceous of the hanging wall has been completely eroded and the Paleozoic metasediments from its core override the autochthonous upper Cretaceous (Figs. 4.2, 4.4). Interestingly, the fold nappe domain actually coincides with the existence of the Eaux-Chaudes granite pluton under the autochthon Mesozoic (Fig. 4.3).

It is inferred that the Gourzy transfer zone accommodates a structural variation (Fig. 4.11), where the development of the recumbent fold to the west was thus favoured by the nature of the footwall basement, coupled with the existence of mechanically weak layers that favoured the development of a lower and an upper detachment level (i.e. the Silurian of the fold core and the allochthonous Keuper emplaced over the Upper Cretaceous).

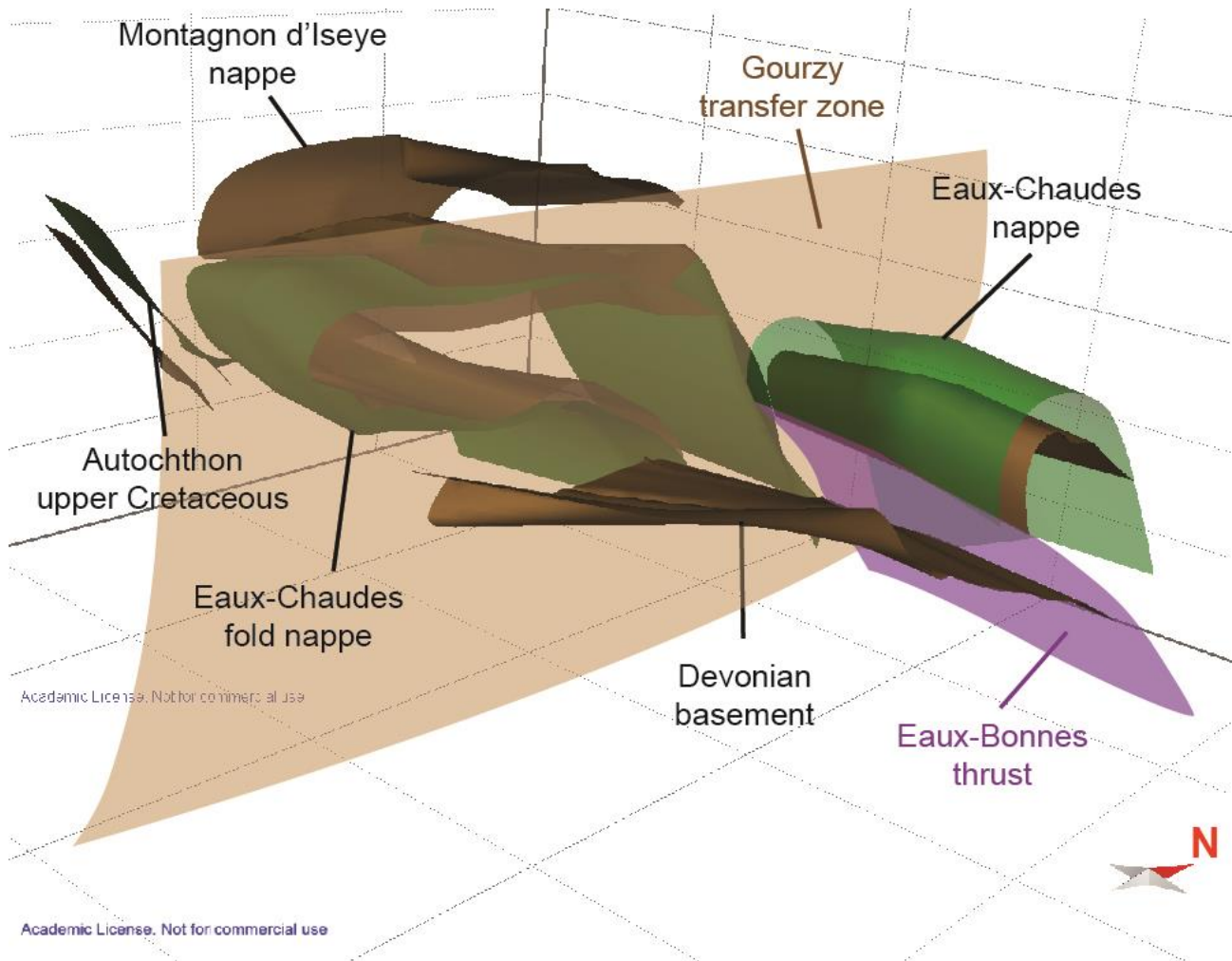


**Fig. 4.11.** 3D schematic structure of the Gourzy transfer zone (from the Move software) and its structural relationship with the two sectors of the ECM. To the west the far-travelled ECFN overlain by the MIN and bounded by the tilted-to-the-north autochthon upper Cretaceous of the Gavarnie nappe. Eastwards the ECM is located more to the north with smaller displacement through the Eaux-Bonnes thrust and with the deformable Paleozoic metasedimentary basement in the autochthon domain (Gavarnie nappe). Cf. appendix II for 3D view of this model.

### *Granitic vs non-granitic basement*

The Paleozoic basement underlying the ECM is constituted by two clearly differentiated lithological units: the upper Paleozoic metasediments and the Carboniferous granite pluton (Figs. 4.2, 4.4, 4.5). While the recumbent fold largely prevails over the Eaux-Chaudes pluton, the eastern fold-thrust fan overlies the softer Devonian rocks (interlayered slates and limestones) (Figs. 4.2, 4.5, 4.8). The Eaux-Chaudes granite is very little strained, occasionally affected by minor back-thrust faults (e.g. Fig. 4.5).

On the other hand, the Paleozoic rocks show strong ductile deformation expressed by pervasive folding from minor to large scale with southern vergence. The age of folding (i.e. Variscan vs. Alpine) has not been unequivocally attributed for each structure, but it is observed that the Paleozoic rocks have experienced superposed shortening from both orogenic cycles. A good example of that is the Alpine foliation imprint, which is identified in both the upper Cretaceous and Paleozoic rocks, refracted from each other as seen in Fig. 4.12.

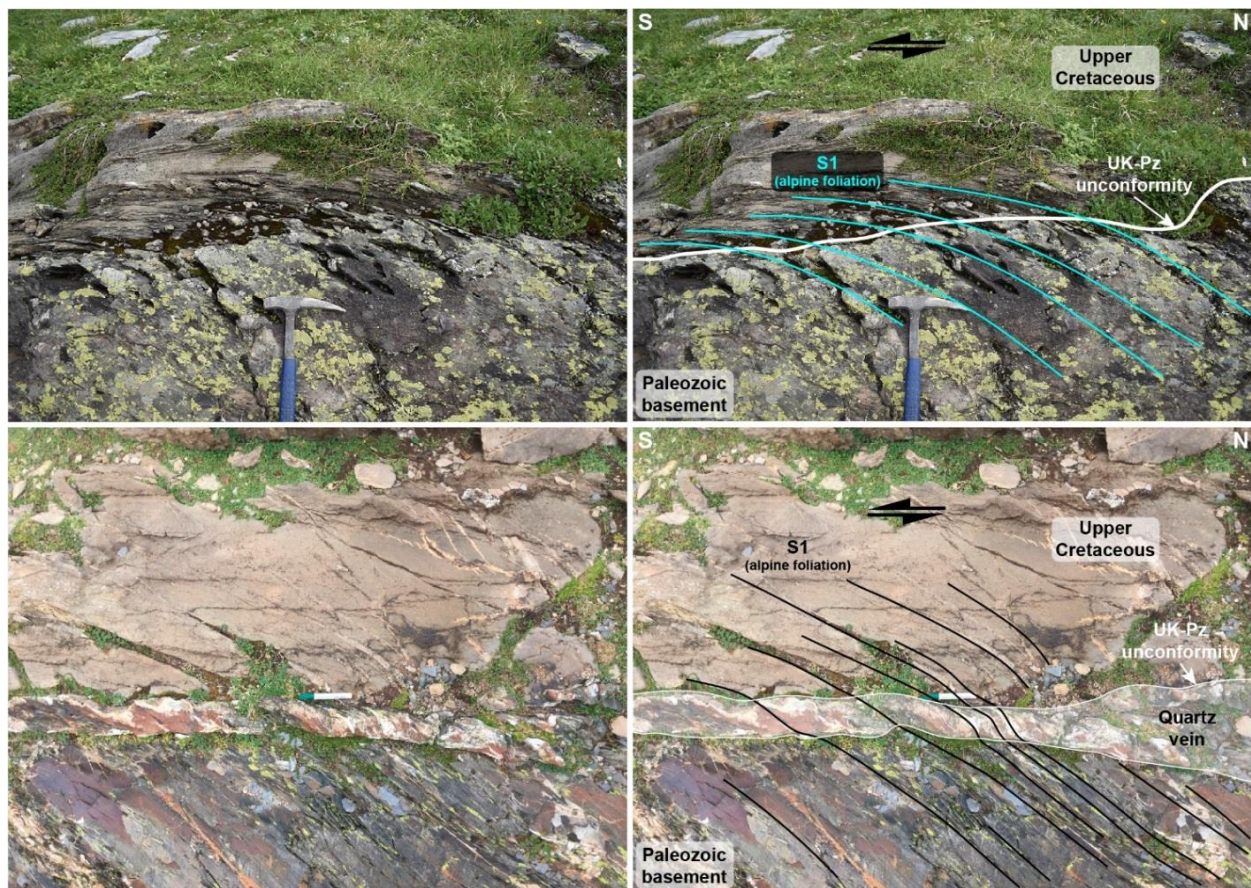


**Fig. 4.12.** Original (left) and interpretation (right) of two detailed examples of top-to-the-south Alpine foliation refraction from Paleozoic basement to the upper Cretaceous cover (difference in colour is due to easy visualization). Refraction laws are followed accounting for the viscosity contrast in between quartz and schists or limestones.

Therefore, the granite pluton may have acted as a localized strong body imposing a buttressing effect leading the extrusion of the Silurian and a strain forestop enabling the transport of the fold nappe southwards entraining the Paleozoic metasediments originally north of the granite. It is worth pointing



out that Bresson (1906) already invoked the role of the basement granites for the nucleation and preservation of thrust nappes in the area.

The unconformity between Paleozoic and Cretaceous strata is reactivated, accounting for flexural slip kinematics, and favour the localization of shearing and little decoupling, which are enhanced by the fluid circulation witnessed by the abundance of veins across the contact. In the hinge zone kinematic indicators such as S-C structures account for a top-to-the-south shearing between the Paleozoic and Cretaceous sediments (Fig. 4.13) resulting from the relative shear of both sedimentary units.

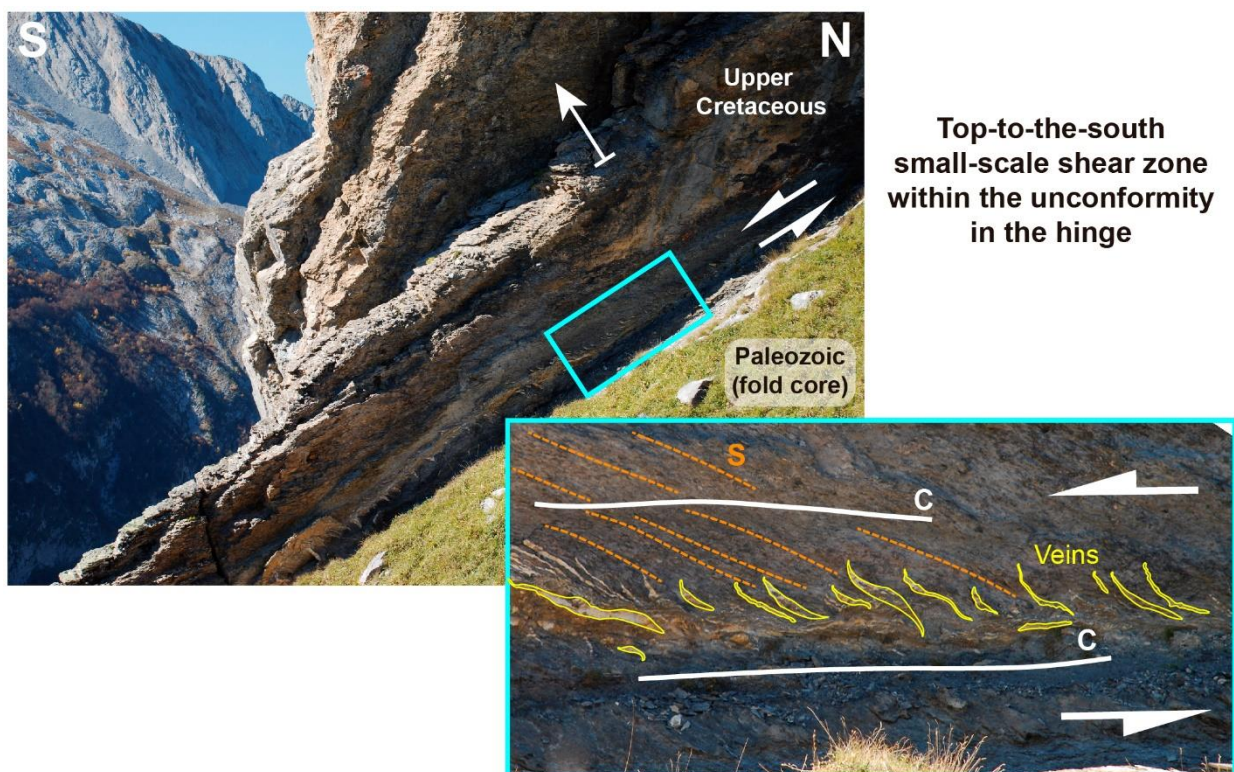


**Fig. 4.13.** Detail from the top-to-the-south small-scale brittle-ductile zone developed in between the upper Cretaceous of the ECFN normal limb and its Paleozoic core near the hinge of the recumbent fold. S-C foliation and shear structures provide kinematic evidence for flexural shear. The en-echelon veins are not consistent with this kinematics, and must represent a late deformation event (probably a shear reversal).

### *The mechanical role of weak units: the underlying Silurian and overlying Keuper*

The recumbent fold poses the question of the mechanical behaviour of the Paleozoic “basement” located in the tight core of the structure. The bulk of these rocks is rich in phyllosilicates, i.e. slates with limestone and sandstone intercalations of Devonian age, and graphitic Silurian slates

interbedded with thin-black limestones at its bottom. Mapping suggests that the ECFN was bounded by two weak units, the Silurian black slates and the allochthonous Keuper evaporites and shales from the Bedous unit on top of the structure, both acting as lower and upper ductile levels, respectively. The Silurian detachment allowed extrusion of a relatively thin upper Paleozoic section to be entrained in the fold core by a top-to-the-south shearing as proposed in Fig. 4.5, which in turn enabled the recumbent folding. The Silurian slates, reported as well as the basal detachment of the Gavarnie thrust (Bresson, 1903; Séguret, 1972), have also been proposed to be effective detachment eastwards of MVN during the Alpine orogeny in the Chiroulet and Lesponne domes (Cochelin et al., 2021). The upper Paleozoic thrust sheets (MIN, MVN, 5MN) can also be interpreted to be detached in the upper part of the Silurian slates.

The allochthonous Keuper sheet, which probably contained a large proportion of evaporite on its origin, was also key in causing the decoupling of the upper Cretaceous from the overlying thrust sheet systems. This unit was attributed to the infill of a former Triassic graben later inverted (Teixell, 1993, Labaume & Teixell, 2020), but also it can be interpreted as an olistostrome (Stevaux & Zolnai, 1975; Lagabrielle et al., 2010) or as an extruded salt sheet (García-Senz et al. 2019). In this work, it is interpreted to be carried by the Lakora thrust on top of the upper Cretaceous limestones before the activation of the Eaux-Chaudes folds and thrusts. Indeed, the Keuper on the upper Cretaceous limestones was crucial in enabling recumbent folding of the ECFN, being expelled from the underlying faulted syncline as attested by few pinched remnants (Fig. 4.7). The combination of two detachments (the Silurian in the upper Paleozoic and the allochthonous Keuper) with the Eaux-Chaudes granite buttress effect, account for the intense top-to-the-south shear leading to the development of the Eaux-Chaudes recumbent fold that characterizes the eastern part of the massif.

Finally, it is questionable the interpretation by Ternet (2004) of the Keuper outcrops in between the Pic du Cézy and Petite Arcizette in the southern part of the ECM (Fig. 4.4). Here, a quaternary mass gliding is proposed for the chaotic and mixing exposure of Keuper rocks, which comes from the allochthonous sheet located on the Santonian and Campanian sediments from the Plateau d'Anouillas (Fig. 4.4) and extends 1 km to the south with a tongue-like geometry.

### *4.3.3. Weld structures within the Upper Cretaceous*

Pinched pieces of Triassic ophiolites, Keuper shales and carbonates appear within the upper Cretaceous limestones in two occurrences: 1) in the pinched syncline between the overturned limb of the ECFN and its relative autochthon (e.g. Fig. 4.7), and 2) in steep fault zones cutting the right-way up succession of the eastern part of the massif (Ternet et al., 2004; Fig. 4.14).

A first approximation of the origin of these features can be done by invoking salt tectonics, assimilating the structures that host the Triassic slivers to salt welds after the Keuper evaporites. There is no evidence of Keuper rocks under the upper Cretaceous of the Eaux-Chaudes massif, which always remains unconformable over Paleozoic rocks or small Buntsandstein remnants. This observation is irreconcilable with any interpretation considering that the weld-like geometries observed in the massif derive from the squeezing of regular diapirs that originally pierced the Cretaceous succession from below, as previously interpreted by Ternet (1965) and Dumont et al. (2015). On the contrary, they rather must be considered as tertiary welds originated from the allochthonous Keuper transported by the overlying Lower Lakora thrust. In Caldera et al. (2021), the Keuper and ophiolite slivers in the sheared, isoclinal synform between the overturned limb of the ECFN and its autochthon are interpreted by the expulsion of the Triassic sheet located at the core fold (Fig. 4.7). Similarly, in the steep welds of the eastern part of the ECM, the Keuper and ophiolite bodies are observed in the upper part of the faulted upper Cretaceous limestones (Fig. 4.14). These faults may show normal or reverse offsets, which it is interpreted to document the shortening of former extensional faults. These faults post-dated the emplacement of the Lakora thrust sheet, as observed in the Anouilh graben (Fig. 4.4). The faults often show drag folds on both walls, which can be described as a-type flanking folds according to the classification by Passchier (2001), consistent with extensional slip. The origin of these extensional faults is unclear, but they may be attributed to flexure associated with the emplacement and load change of the overlying thrust sheets to the north, down-dropping the allochthonous Keuper facies sheet the flanking folds associated to the faults. Subsequent shortening led to fault steepening and tightening of the flanking folds, expelling the Keuper and ophiolites, which were locally pinched forming the observed weld-like structures (Figs. 4.9, 4.14, 4.15).



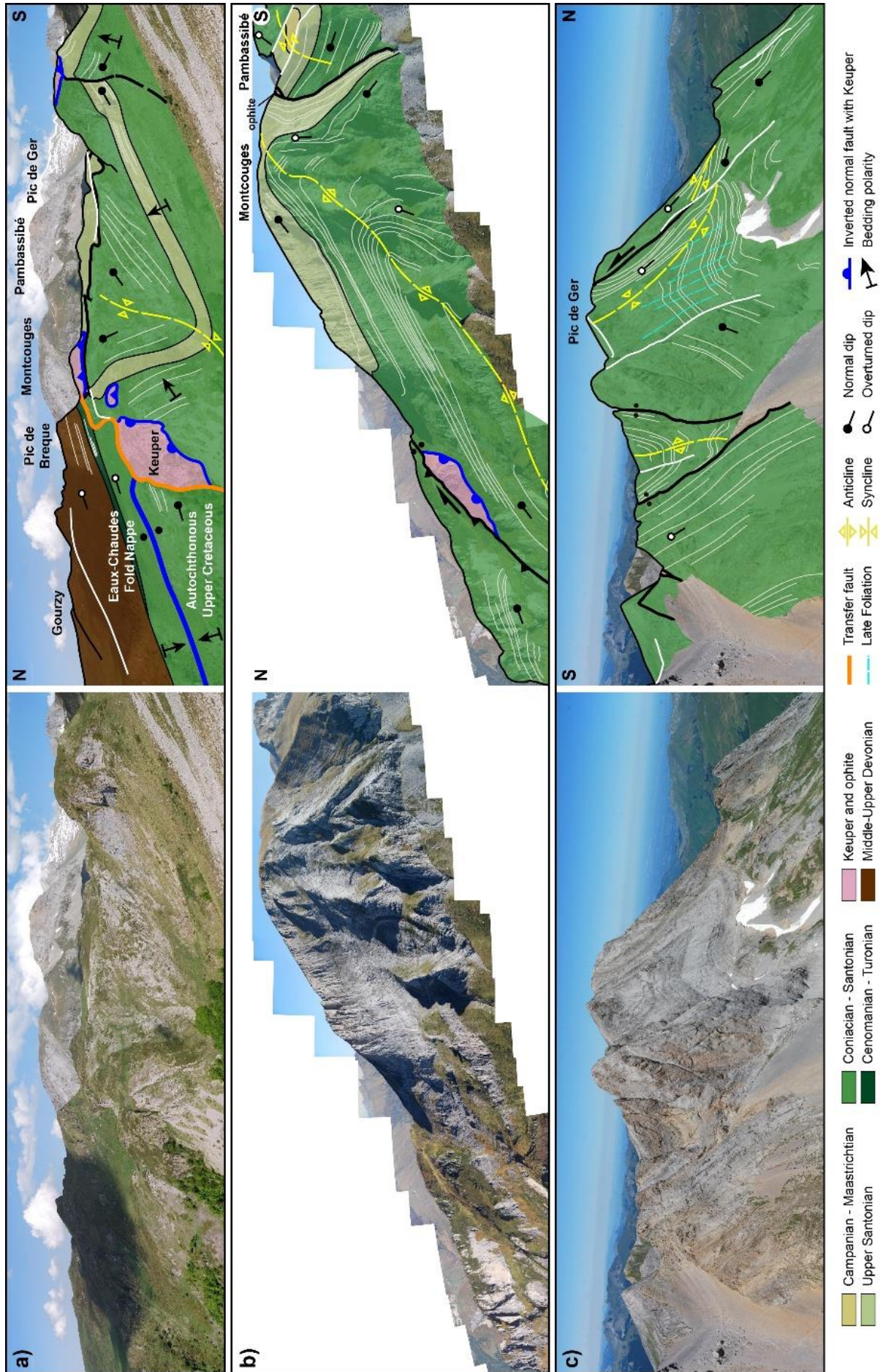




**Fig. 4.14.** Interpreted panoramas of salt weld-like structures in the eastern Eaux-Chaudes massif (see location of pictures in Fig. 4.2). Weld structures are marked by ophite or Keuper shale slivers enclosed in the upper Cretaceous limestone. (a) View from the west of the Pic de Breque to the large ophite body in the autochthon of the ECFN. The autochthon is deformed by the inversion of an extensional small graben which originally cut the Lower Lakora thrust (see text for explanation). (b) View from the west of the Montcougues and Pambassibé mountains, showing a large, detached anticline limited to the north and south by former extensional faults tectonically inverted. Ophite rocks are pinched in faults, witnessing their compressional tightening. The tightening of the fold is accompanied by foliation in the carbonates. (c) View from the east of the Pic de Ger ridge showing the prominent syncline imaged in Fig. 4.9b and faulted contacts to the south that are marked by Triassic slivers. Strong ductility is evidenced by the penetrative mylonitic foliation which is folded by the syncline. A vertical foliation (blue dashed lines), which is oblique to the axial plane of the fold developed during a later deformation episode.

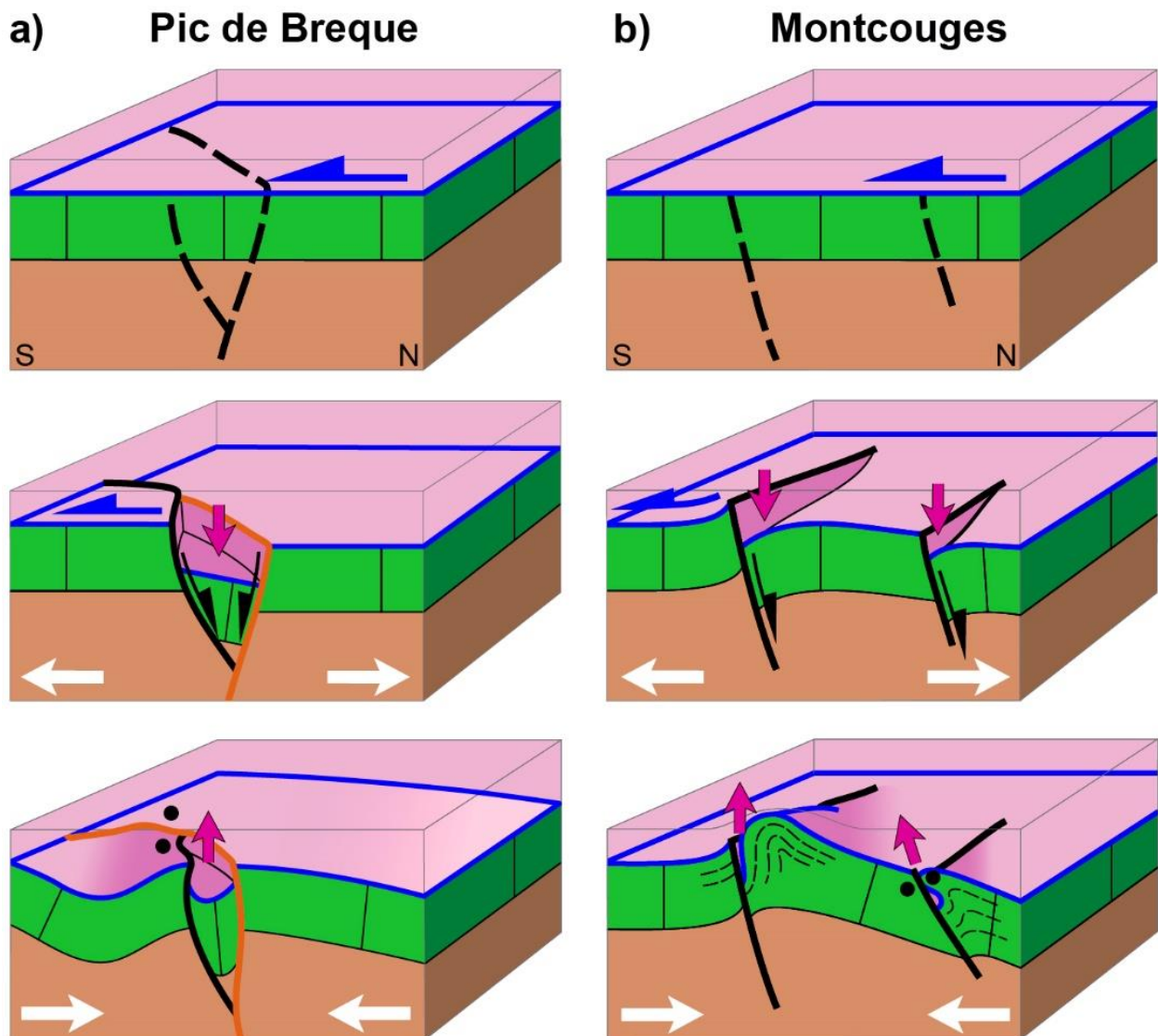


**Fig. 4.15.** *Simplified sketches explaining the occurrence of pinched Keuper and ophite bodies in the upper Cretaceous carbonates of (a) the Pic de Breque and (b) the Montcouges (see location in Fig. 4.14). In the first step, the Lower Lakora thrust emplaced the Keuper sheet over the upper Cretaceous. In a second step, normal faults were formed by the flexure associated with the thrust loads, resulting in the mobilisation of the Keuper rocks into depressed areas. Finally, during renewed shortening, welded structures were formed when small bodies of upper Triassic were trapped in the core of the previous extensional structures deformed by flattening and inversion. In a) the orange line corresponds to the Gourzy Transfer Zone. The ECFN is not represented to simplify the illustration.*

#### 4.4. Sequential evolution of the upper Iberian margin: the Eaux-Chaudes fold nappe and the eastern Eaux-Chaudes fold-thrust system

Restorations of sections S1 and S4 are shown in Figs. 4.16 and 4.17. A sequential tectonic evolution is proposed for both sectors of the ECM. They begin at the immediate pre-orogenic stage (mid-Santonian) of the upper Iberian margin. The reconstruction is based on compiled data from field observations, structural cross-sections and previous works on the west-central Pyrenees from Teixell et al. (2016) and Labaume & Teixell (2020).

The evolution of the western section is shown in 7 steps (Fig. 4.16), while the eastern section is in 4 steps (Fig. 4.17), the latter encompassing the last three from the western evolution. Dashed lines indicate the trace of the future structures in the next step. Red arrows on the right border of the pictures illustrate the compressional stage while blue arrows indicate the post-orogenic exhumation.

##### 4.4.1. Sequential evolution of the Eaux-Chaudes fold nappe (Fig. 4.16)

a) Expansive shallow carbonate platforms (i.e. Calcaires des Cañons) dominated the upper Iberian margin landform during the mid-Santonian (post-rift times). The Paleozoic basement of the future ECM was covered by the upper Cretaceous platform carbonates, while to the north, the Paleozoic basement was covered by both the Keuper of the Bedous unit and the overlying upper Cretaceous (future Paleozoic nappes: Montagnon d'Iseye (MIN); Montagne Verte (MVN); and Cinq Monts (5MN)).

The boundaries between these units are interpreted as extensional faults inclined to the north.

The shelf edge limited the Bedous unit to the slope rupture of the Iberian platform. Northwards in the basin, the Mendibelza conglomerates onlap the Paleozoic basement on the necking zone of the continental margin, bounded more to the north by large diapiric structures which will become the future Licq fault and correspond to the southern limit of the Chaînons Béarnais Belt (CBB). The CBB is interpreted as representing the lower margin and the rift axis of the hyperextended basin (Labaume & Teixell, 2020).

b) First syn-orogenic deposits appear at the early stages of the Pyrenean orogeny by the Campanian-Maastrichtian flysch. They mark a deepening of the upper Cretaceous shelf. The inversion of the basin axis started with the transport to the south of the salt-detached fold-and-thrust system of Chaînons Béarnais Belt by the thin-skinned Lakora thrust (red line) (Teixell et al., 2016, Labaume & Teixell, 2020).

c) Near synchronous with the Lakora *s.l.* thrust, the Lower Lakora thrust (blue line) initiates its movement by emplacing most of the Bedous Keuper unit over the future ECM, in a horse-like structure. During or immediately after this stage, the sole detachment on the Silurian of the 5MN was active and started to override the southern segment of the Bedous basement.

d-e) Progressively, the northern Paleozoic thrust sheets (MIN, MVN and 5MN) were emplaced from north to south, in a piggyback sequence, by a propagating basement-involved thin-skinned (Piffner, 2017) thrust system. The latter structure to be activated was the Eaux-Chaudes fold nappe, the deepest in the stack. The key element then was the EC granite pluton, which faced opposition to the progressive deformation, being transmitted upwards and to the rear. This triggered the nucleation of the antiformal fold cored by Silurian slates and Devonian layered metasediments. The persistent shortening kept the progression of the structure to a fold nappe by the hinge migration mechanism.

The uppermost part of the Silurian, which constitutes a broad and diffuse weak level on the upper Paleozoic, favoured the detachment of the whole of these thrust sheets of the stack. The relatively high temperature induced by the tectonic burial, or the inherited high geothermal gradient (Bellahsen et al., 2019) or a combination of both (Caldera et al., 2021), favoured the dominant ductile deformation associated with the ECFN.

The allochthonous Keuper sheet transported by the Lower Lakora thrust is folded by the stacking of the Paleozoic units and the ECFN. The progressive growth of the overturned limb and tightening of the synclines resulted in the Keuper expulsion (Caldera et al., 2021).

It has been proposed that the Lakora and the Eaux-Chaudes nappes remained active up to Mid Eocene times (Labaume et al., 2016), by the system propagating in a broad piggy-back sequence.

f) The south-directed displacement and development of the ECFN and Paleozoic units were followed from the Late Eocene by the emplacement of the Gavarnie nappe. It induced a change in the style of deformation by the accretion of a footwall sequence of thick-skinned thrusts resulting in the Axial Zone antiformal structure (Teixell, 1996; Jolivet et al., 2007; Labaume et al., 2016; Teixell et al., 2016; Labaume & Teixell, 2018) (cf. Fig. 1.1b). This stage is inferred to correspond to the full crustal collision between the Iberian and European plates which developed from the Late Eocene to Early Miocene (Teixell et al., 2016). The previous structures were uplifted and arched resulting in tilting to the north, and the formation of the northern limb of the Axial Zone antiform. Linked with that, local structures of the Eaux-Chaudes massif, such as north-verging back-thrust systems, back-folds, and sub-vertical foliation were related to the Gavarnie nappe emplacement.

g) Further uplift of the ECM and adjoining areas by the Guarga thrust are constrained by thermochronology during the Late Eocene-Miocene (Bosch et al., 2016). Consequently, a large amount of recycled, earlier syn-orogenic deposits and Axial Zone rocks were shed into both the Jaca (Puigdefàbregas, 1975; Labaume et al., 2016; Roigé et al., 2016) and Aquitaine basins (Biteau et al., 2006) (cf. Fig. 1.1a). Large extensional faults affected the whole stack of the ECM up to the CBB during the post-orogenic stage of the Axial Zone. These faults down-dropped the 5MN and MVN to the north to a lower structural elevation than the MIN and were probably initiated in the final steps of Gavarnie-related arching (Teixell, 1996), and reactivated in Quaternary times by readjusting of isostatic effects induced by erosion (e.g. Lacan, 2008; Lacan & Ortuño, 2012; Dumont et al., 2015).

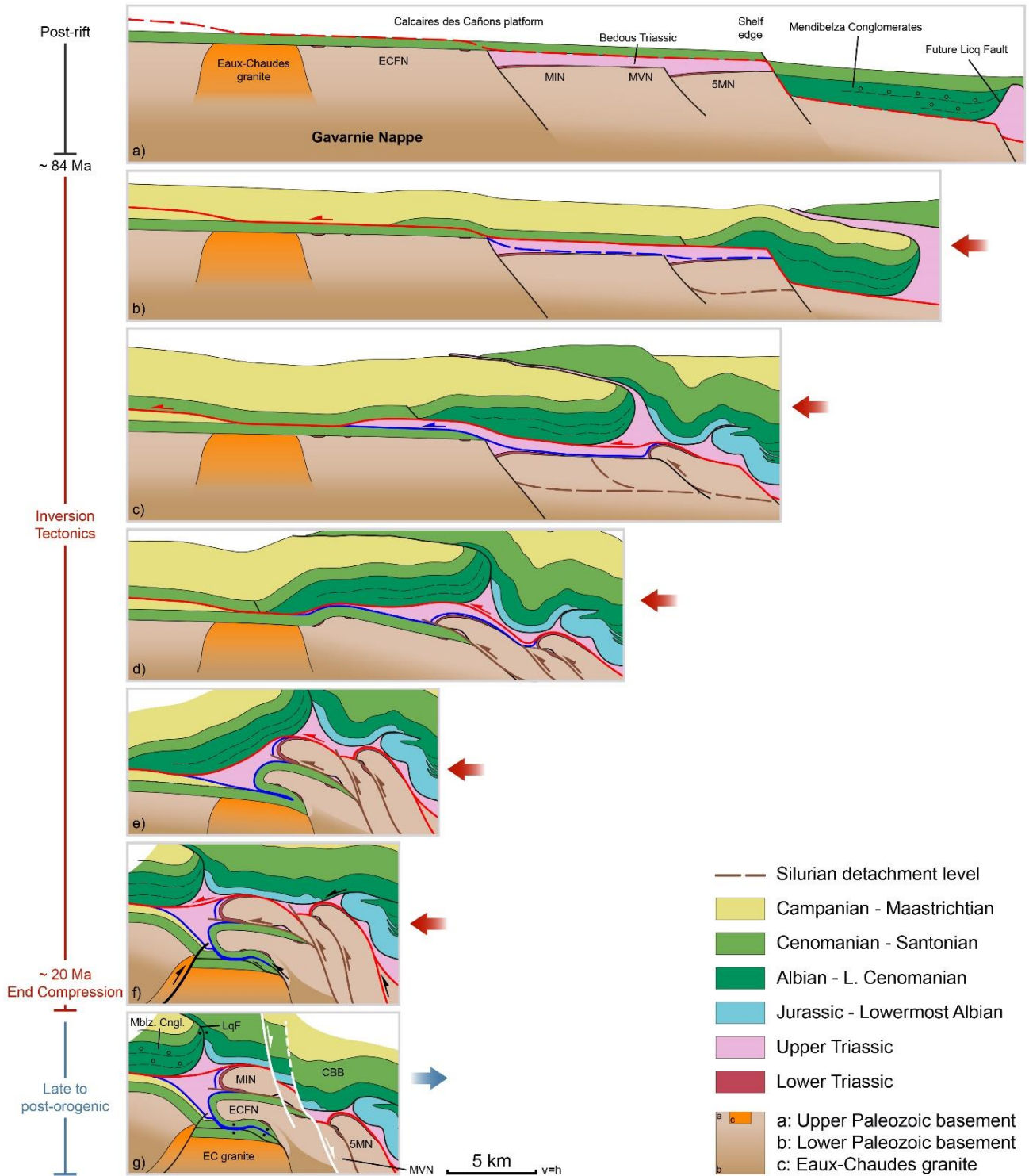


**Fig. 4.16.** Cartoon illustrating the proposed sequence for the compressional inversion of the upper Iberian margin in the western Eau-Chaudes massif, including the structural stacking of the upper thrust units. Red line corresponds to the Lakora thrust carrying the detached CBB and Mendibelza conglomerates. Blue line corresponds to the branch of the Lakora thrust carrying the allochthonous Keuper sheet (horse) on the ECFN. Dashed lines show the location of future faults in the following steps. The structure of the pre-inversion stage (a) is modified from the model of hyper-extension of Teixell et al. (2016). The last stage (f) is based on the cross-sections S1 and S2 from Fig. 4.5 for the ECFN, MIN, 5MN and MVN. The kinematic evolution of the CBB is



taken from Labaume & Teixell (2020). ECFN: Eaux-Chaudes Fold Nappe; MIN: Montagnon d'Iseye Nappe; 5MN: 5 Monts Nappe; MVN: Montagne Verte Nappe; CBB: Chaînons Béarnais Belt; Mblz. Cngl: Mendibelza Conglomerates.

#### 4.4.2. Sequential evolution of the eastern Eaux-Chaudes fold-thrust imbricate fan (Fig. 17)

The most important differences from the western sector are highlighted in the evolution proposed in Fig. 4.16. The eastern sector is characterized by the deeper erosion of the Paleozoic-bearing thrust units north of the ECN, and of the Cretaceous cover of the latter. The roots of the MVN and 5MN remain outcropping to the north, making their complete restoration speculative. For the purpose of simplicity, the post-rift stage shows a shorter Bedous basement, only represented by the future MVN and 5MN. The volume of the Upper Triassic Keuper is interpreted to conform the Bedous Unit as in the western sector, on the basis of the present-day klippe observed in the eastern ECM.

During the orogenic stages, deformation was spread into the autochthonous Mesozoic and Paleozoic rocks south of the eastern ECM, due to the softer basement because of the absence of granitic plutons. Extensional structures were created in relation to flexure affecting the whole stratigraphic succession and the leading edge of the already-emplaced Lower Lakora thrust, dropping down the allochthonous Keuper sheet. The leading edge of the ECN is not preserved and is speculatively interpreted as a simple hanging-wall anticline, with a moderately developed overturned limb in the upper Cretaceous. Indeed, at variance to the western part, the autochthon upper Cretaceous in the eastern sector is strongly ductile deformed, indicating that a large part of the deformation was transmitted into the footwall of the Eaux-Chaudes allochthonous structure.

The back-thrust systems associated with the Gavarnie nappe emplacement to the east evolve into a fault-propagation fold structure resulting in north-verging syncline in the Petite Arcizette (S4 in Fig. 4.8). Further east, the steep attitude of the basement-upper Cretaceous unconformity, south of i.e. Pêne Médaa (Figs. 4.8, 4.9), is also attributed to back-folding of the Gavarnie nappe.

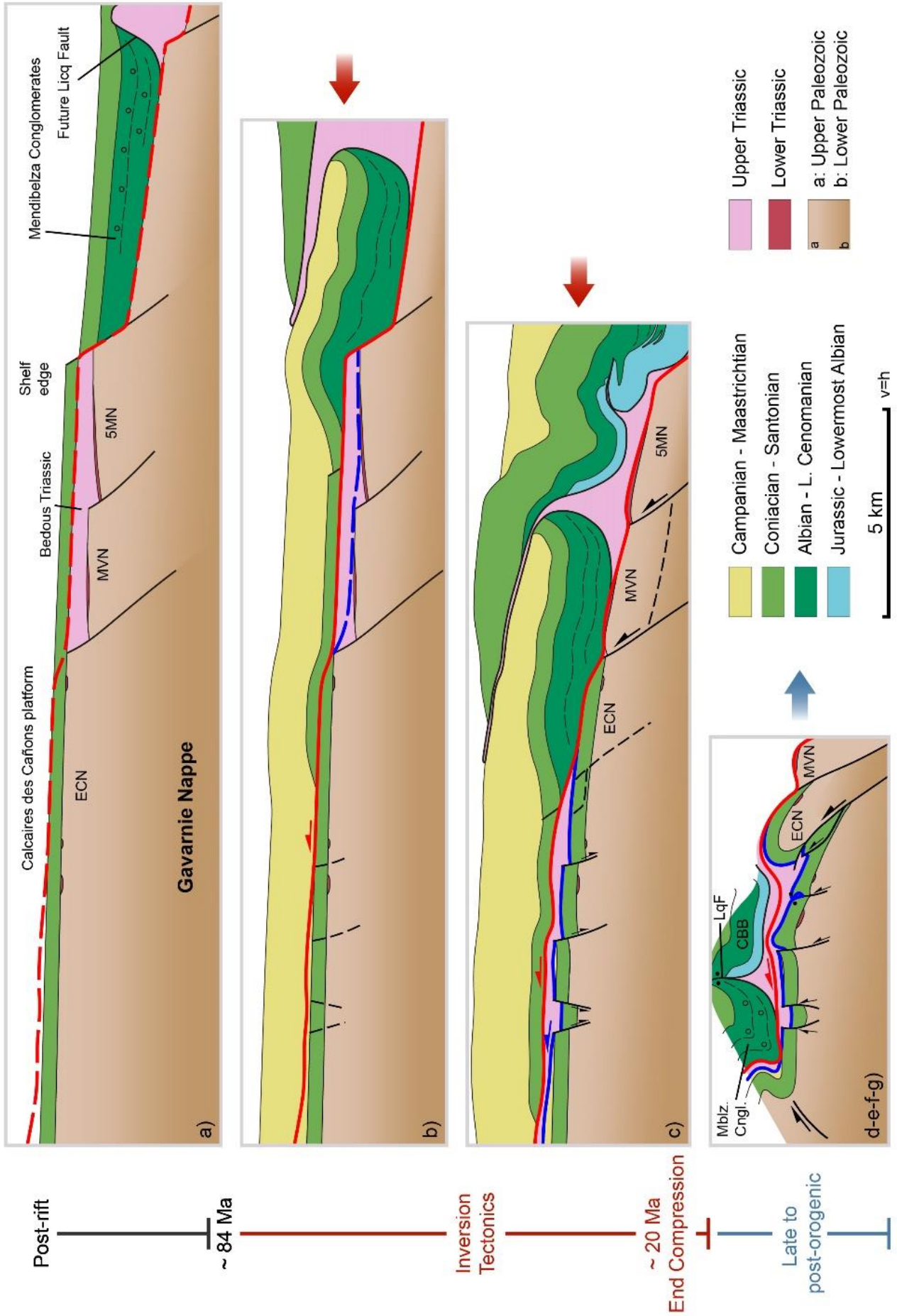


**Fig. 4.17.** *Cartoon illustrating the proposed sequence for the inversion of the upper Iberian margin in the eastern Eaux-Chaudes massif. It features the deformation of the footwall upper Cretaceous rocks in conjunction with the underlying Paleozoic metasediments and the overlying allochthonous Keuper sheet. Red line corresponds to the Lakora thrust carrying the detached CBB and Mendibelza conglomerates. Blue line corresponds to the branch of the Lakora thrust carrying the allochthonous Keuper sheet on the ECN. Dashed lines show the location of future faults in the following steps. The structure of the pre-inversion stage (a) is modified from the model of hyper-extension of Teixell et al. (2016). The last stage (d-e-f) is based on the cross-sections S4 from Fig. 4.8 for the ECN, MVN and 5MN. The kinematic evolution of the CBB is taken from Labaume & Teixell (2020). For explanation of acronyms, refer to the legend of the previous figure.*

## 4.5. Implications on the collision of the Iberian margin during the Pyrenean orogeny

Two types of tectonic structures characterize the alpine Pyrenees: 1) thick-skinned thrusts (e.g. Gavarnie, Guarga, Rialp, Orri) detached in depth and increasing the structural relief along the belt, and 2) thin-skinned thrusts (e.g. Lakora, Larra, Monte Perdido, Cotiella, Boixols, Montsec, Serres Marginals) with shallower detachments in the Mesozoic cover or in the upper Paleozoic (basement short-cuts, e.g. Teixell 1993), but being able to carry sheets over long distances (i.e. over dozens of km).

Brittle to brittle-ductile conditions are assumed to deform the Axial Zone of the Pyrenees during the Alpine orogeny, resulting in a modest internal strain. From our study of the ECM, we conclude that the Pyrenean hinterland of this region is formed by a stack of a series of “ductile” thin-skinned basement-involved nappes (nomenclature by Pfiffner, 2017), with the development of recumbent fold nappes (ECFN and MIN). This implies an intense ductile simple shear deformation regime during early-middle stages of the Iberian margin collision and active detachment along levels of the upper Paleozoic (i.e. Silurian). Likewise in the ECFN, the basement units MIN, MVN and 5MN are also detached on the Silurian, and occasionally feature recumbent folds on their front with intense ductile shearing in the overturned limb. This tectonic style has not been reported thus-far in the Alpine Pyrenees, evidencing basement-involved, ductile thin-skinned folding and thrusting. Similar ductile

alpine structures may have been unperceived so-far in other parts of the Paleozoic basement of the Axial Zone.

#### 4.6. Conclusions from the macroscale structural study

The Axial Zone of the Pyrenees is regarded as an antiformal stack of basement units buried and deformed during the Cenozoic at temperatures, in general, <300°C (e.g. Fitzgerald et al., 1999; Jolivet et al., 2007; Metcalf et al., 2009; Abd Elmola et al., 2017; Bellahsen et al., 2019). This work shows for the first-time evidence of ductile, basement-involved thin-skinned deformation (*sensu* Pfiffner, 2017) by km-scale recumbent fold and thrust nappes in the Pyrenees, affecting the upper Paleozoic metasediments and the overlying Mesozoic sedimentary rocks, which bear similarities with the fold nappes of other orogenic domains as the lower Helvetic Alps.

The six cross-sections proposed in this work pose the scope of the remarkable along-strike structural variability within the Eaux-Chaudes upper Cretaceous massif, laterally from west to east. The western large-scale ductile recumbent fold rapidly evolves into an imbricate, ductile fold-and-thrust fan to the east, separated by the Gourzy transfer fault. The rheology of the Paleozoic basement underlying the upper Cretaceous strongly constrains this abrupt change in the deformation style. The Eaux-Chaudes granite leads the localization of deformation on top of it locating the recumbent fold nappe, while in the upper Paleozoic metasediments (Devonian limestones and schists) the deformation is distributed along the stratigraphic pile.

As far as there is no evidence of autochthonous Keuper remnants in between the unconformity of Paleozoic basement and the Cretaceous rocks, the occurrence of these rocks is attributed to the remains of an allochthonous sheet, emplaced on the upper Cretaceous rocks by a horse-like Lower Lakora thrust in the beginning of the Pyrenean tectonic inversion. The allochthonous Keuper acted as an upper detachment for the ECFN and facilitate the hinge migration and tightening of the recumbent fold. Moderately deep detachment in Silurian slates was also key in the initiation of the recumbent fold, allowing the upper Paleozoic to be entrained in the fold nappe core. Detachment in

the Silurian is also inferred for the basement-involved thrust sheets that overlie the Eaux-Chaudes structure (Montagnon d'Iseye, Montagne Verte, Cinq Monts). Small intracretaceous detachments and along the unconformity with the Paleozoic metasediments enhanced the shearing within the large-scale.

Unusual tertiary weld-like structures, marked by ophite and claystone pinched slivers, attest for the allochthonous Keuper sheet. Unlike common tertiary welds, these are formed within tight synforms of the upper Cretaceous subsalt rocks, from which the bulk of the salt sheet was expelled. Those structures also formed where slivers of the allochthonous Keuper sheet were pinched along former normal faults during their inversion.

The Eaux-Chaudes Fold Nappe is not the sole structure evidencing Alpine ductile deformation in this segment of the Pyrenean hinterland. Moderately large and overturned limbs are developed in the front of the Paleozoic basement units of Cinq Monts and Montagnon d'Iseye, being delineated by post-Variscan, lower Triassic rocks. The deformation observed in the Cretaceous rocks is consistent with the moderate paleotemperatures recorded (>300-360°C) (see chapter 5). The nappe stacking at Eaux-Chaudes and surroundings represents a tectonic style reported for the first time in the Alpine Pyrenees, evidencing relatively deep burial and/or high inherited thermal gradients during deformation, and basement-involved thin-skinned thrusting. This tectonic style characterizes the inversion of the previous Cretaceous rift during the early stages of the Pyrenean orogeny, at variance to the thick-skinned fan which structured the Axial Zone of the central Pyrenees during the subsequent continental collision. It also warns on so-far unperceived alpine ductile deformation in the basement of the Pyrenean hinterland.



## Chapter 5: Paleotemperature of the Eaux-Chaudes massif

Paleotemperature analysis of the Eaux-Chaudes massif were motivated by the ductile features (i.e. mylonitic foliation, stretching mineral lineation, intrafolial folds and asymmetric porphyroclasts) recognized in the upper Cretaceous limestones during the field campaigns. Mylonitic foliation in calcite aggregates and dolomite porphyroclasts are well-developed in both the micro- and macro-scale, attesting for persistent moderately high temperatures during the main deformation event performed in the Alpine orogeny. Paleotemperature data, although abundant for the Chainons Béarnais Belt (e.g. Clerc, 2012; Cloix, 2017; Corre, 2017; Izquierdo-Llavall et al., 2020) and the rest of the North Pyrenean Zone, was inexistent for the ECM.

The reason why Raman Spectroscopy of Carbonaceous Material (RSCM) (see chapter 3) was primarily used was the nature of the rocks to be analysed, in that case carbonate-rich rocks as limestones of the lower part of the succession (Cenomanian to Santonian) and marls from the flysch in the upper part of the sequence (Campanian), which both usually contain elevated fractions of carbonaceous material affected by the thermicity occurred during the Alpine collision. I also used the calcite-dolomite geothermometer by Electron Microprobe Analysis (EMPA), previous to the Raman analysis, to get a first approach to the expected maximum temperature values for the carbonates in the ECM. They provided equilibrium temperatures from the element trace relationship between calcite and dolomite.

The paleotemperature analysis was extended beyond the Eaux-Chaudes massif to the upper Cretaceous rocks that crop out around the western termination of the Axial Zone (i.e. Internal Sierras, Pierre-Saint-Martin and Aspe Valley). The results allowed to produce the first  $T_{max}$  map of this part of the Pyrenees altogether with the compiled temperatures from the contribution of the previous works in the nearby areas (i.e. Jaca basin or Iguntze massif) by Raman spectroscopy. As will be discussed further in this chapter, it exists a heating effect to the hinterland of the west Prenees (i.e. the Eaux-Chaudes massif), where the strongest deformation has been developed.

## 5.1. Raman Spectroscopy results

The geothermometry of RSCM was obtained from a total number of 40 samples, 32 of them from the upper Cretaceous of the Eaux-Chaudes massif (Fig. 5.1 and Table 5.1). Two samples came from the Paleozoic basement of the Gavarnie nappe (easternmost sector of the ECM) and one from the allochthonous upper Triassic rocks (Muschelkalk limestone) sampled from the klippe located south of Plateau d'Anouillas.

To unravel the paleotemperature along the Mesozoic Iberian shelf enclosing the western Axial Zone, and in addition to data previously obtained by Labaume et al. (2016) and Saspiturry et al. (2020), eight other samples have been analysed. One taken from the Balaïtous upper Cretaceous limestones just above of the unconformity with the upper Paleozoic basement, and 7 others from the Internal Sierras and Zuriza area south of the Axial zone, the Pierre-Saint-Martin area (west of the Axial Zone), and from the Aspe Valley, south of Bedous. Samples were also taken from the upper Cretaceous limestones (Fig. 5.2). Given the deficiency in carbonaceous content of some specimens, the minimum analysed points for an acceptable statistical study were not achieved in 3 of those 7 samples. Up to five spots have been obtained for sample TC0305 (from the Internal Sierras), and just one for samples TC0704 and TC050108T from the Aspe valley and east of Zuriza, respectively (Fig. 5.2). They are not statistically feasible but qualitatively representative from the regional paleothermal pattern.

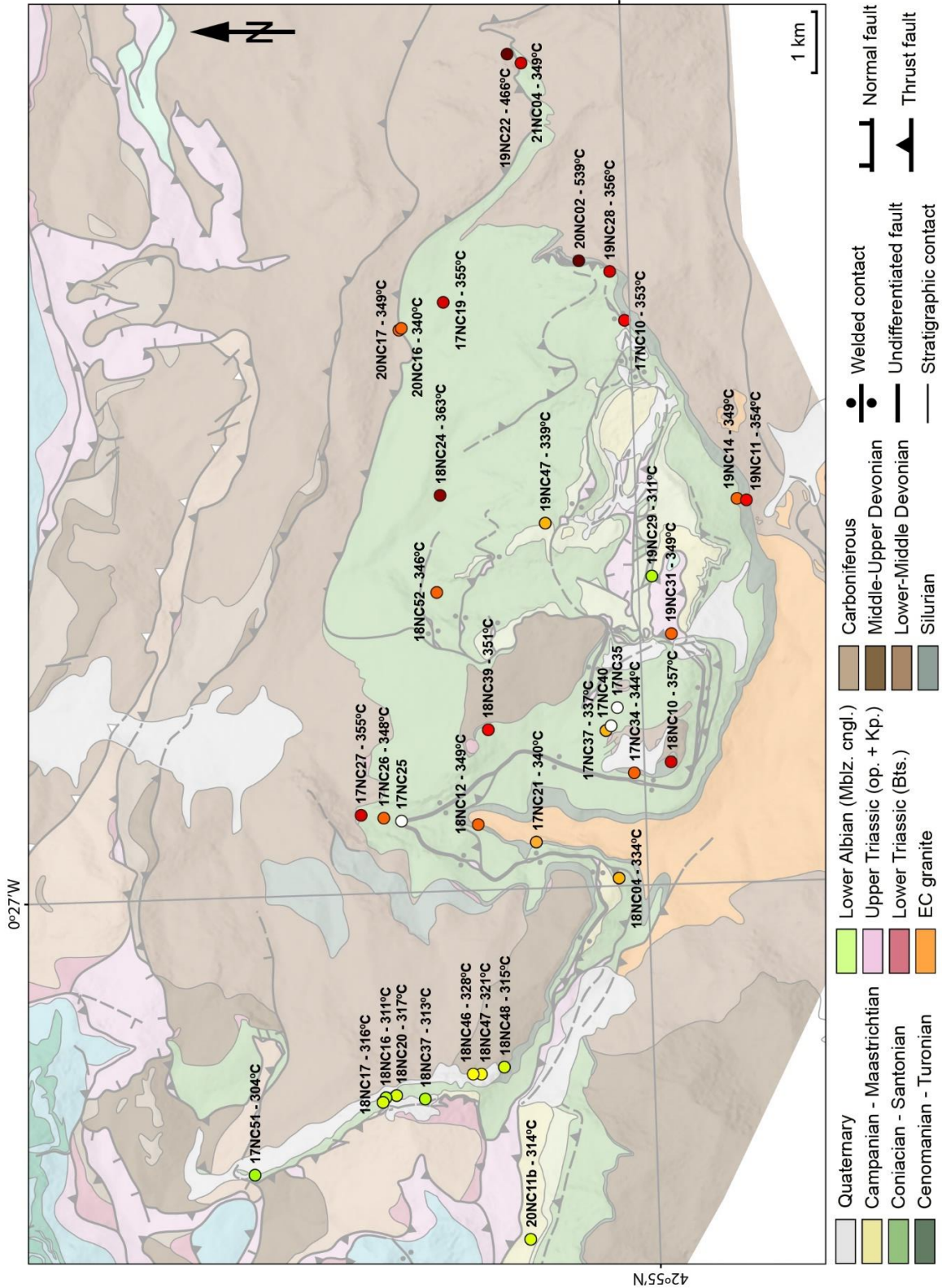


Figure 5.1. Location of samples analysed by Raman spectroscopy and paleotemperatures acquired in the Eaux-Chaudes massif. Colour code from points correspond to the temperature value obtained by this technique: yellow-green (310-330°C); orange (331-340°C); red (341-360°C); dark-red (>360°C). White spots correspond to the samples only used in the calcite-dolomite geothermometer which temperature values are rather lower (290-320°C) than the obtained by Raman analysis.

TABLE 5.1. RESULTS OF RSCM

Sample	Latitude N	Longitude W	Zone	RA2 parameter		RA1 parameter		N <sup>o</sup> of spectra	T <sub>max</sub> (°C)	SD
				Mean	SD	Mean	SD			
17NC10	42° 55' 50.31"	0° 20' 35.49"	Au	0.65	0.02	-	-	15	353	8
17NC19	42° 57' 23.85"	0° 20' 17.61"	Au	0.64	0.03	-	-	7	355	11
17NC21	42° 56' 44.69"	0° 26' 39.45"	Au	0.67	0.03	-	-	17	340	8
17NC26*	42° 58' 3.27"	0° 26' 20.03"	OL	0.65	0.02	-	-	16	348	8
17NC27*	42° 58' 14.39"	0° 26' 17.28"	OL	0.64	0.02	-	-	22	355	7
17NC34*	42° 55' 52.68"	0° 25' 52.96"	OL	0.66	0.02	-	-	21	344	6
17NC37*	42° 56' 7.22"	0° 25' 22.92"	OL	0.68	0.02	-	-	18	337	8
17NC51	42° 59' 13.80"	0° 30' 27.30"	NL	-	-	0.60	0.06	8	304	27
18NC04	42° 56' 2.59"	0° 27' 7.40"	Au	0.68	0.03	-	-	15	334	7
18NC10	42° 55' 34.67"	0° 25' 46.75"	OL	0.64	0.02	-	-	16	357	9
18NC12	42° 57' 14.14"	0° 26' 25.28"	Au	0.66	0.01	-	-	23	349	4
18NC16	42° 58' 5.81"	0° 29' 36.55"	NL	-	-	0.62	0.01	14	311	10
18NC17	42° 58' 6.62"	0° 29' 37.71"	NL	-	-	0.63	0.01	10	316	15
18NC20	42° 58' 0.87"	0° 29' 34.21"	NL	-	-	0.63	0.01	13	317	7
18NC24	42° 57' 28.71"	0° 22' 33.39"	Au	0.63	0.02	-	-	9	363	7
18NC37	42° 57' 46.53"	0° 29' 37.65"	NL	-	-	0.63	0.01	10	313	15
18NC39	42° 57' 7.67"	0° 25' 19.53"	OL	0.66	0.01	-	-	19	351	6
18NC46	42° 57' 19.84"	0° 29' 21.50"	NL	0.70	0.02	-	-	15	328	5
18NC47	42° 57' 17.08"	0° 29' 21.61"	NL	0.72	0.01	-	-	12	321	4
18NC48	42° 57' 5.41"	0° 29' 17.86"	NL	-	-	0.63	0.01	12	315	13
18NC52	42° 57' 32.77"	0° 23' 41.92"	Au	0.66	0.02	-	-	14	346	8
19NC11	42° 54' 50.45"	0° 22' 44.17"	Au	0.64	0.02	-	-	12	354	8
19NC14	42° 54' 55.29"	0° 22' 43.38"	Au	0.66	0.02	-	-	10	349	9
19NC22**	42° 56' 46.86"	0° 17' 26.26"	Pz	0.4	0.06	-	-	8	466	25
19NC28	42° 55' 58.81"	0° 20' 0.30"	Au	0.64	0.01	-	-	16	356	6
19NC29	42° 55' 42.03"	0° 23' 35.89"	Au	-	-	0.62	0.01	11	311	8
19NC31	42° 55' 32.45"	0° 24' 15.77"	Tr	0.66	0.02	-	-	12	349	10
19NC47	42° 56' 35.50"	0° 22' 57.01"	Au	-	-	0.65	0.01	15	339	14

<b>20NC02</b>	42° 56' 13.83''	0° 19' 53.76''	Pz	0.23	0.05	-	-	15	539	23
<b>20NC11b</b>	42° 56' 54.33''	0° 31' 18.25''	Au	-	-	0.63	0.01	9	314	16
<b>20NC16</b>	42° 57' 47.29''	0° 20' 38.11''	Au	0.67	0.01	-	-	16	340	3
<b>20NC17</b>	42° 57' 47.29''	0° 20' 38.11''	Au	0.66	0.01	-	-	12	349	6
<b>21NC04</b>	42° 56' 39.43''	0° 17' 33.71''	Au	0.66	0.03	-	-	12	349	11
<b>Balaïtous</b>	42° 50' 18.21''	0° 17' 23.54''	Au	-	-	0.64	0.01	14	332	10
<b>TC0219</b>	42° 46' 51.64''	0° 34' 02.31''	SI	-	-	0.60	0.01	14	284	12
<b>TC0224</b>	42° 46' 50.70''	0° 34' 02.63''	SI	-	-	0.62	0.01	11	295	8
<b>TC0801</b>	42° 57' 18.97''	0° 42' 54.65''	PSM	-	-	0.61	0.01	11	297	14
<b>TC9046T</b>	42° 44' 07.41''	0° 31' 23.94''	SI	-	-	0.58	0.01	17	258	11
<b>TC0305</b>	42° 46' 49.56''	0° 34' 03.29''	SI	-	-	0.61	0.01	5	298	11
<b>TC0704</b>	42° 57' 39.03''	0° 36' 32.87''	Asp	-	-	0.63	-	1	320	-
<b>TC050108T</b>	42° 51' 34.20''	0° 44' 21.37''	Zur	-	-	0.59	-	1	266	-

**Table 5.1.** Raman paleotemperature results from the Eaux-Chaudes massif, western termination of the Axial Zone and Balaïtous peak. The number of analysed points is shown for each sample, as well as the standard deviation of the temperature values. R2 parameter correspond to Beyssac (2002) procedure and R1 to the Lahfid et al. (2010). Au: autochthon; OL: overturned limb; NL: normal limb; Pz: Paleozoic; Tr: Triassic; SI: Internal Sierras; PSM: Pierre-Saint-Martin; Asp: Aspe valley south of Bedous; Zur: Zuriza.



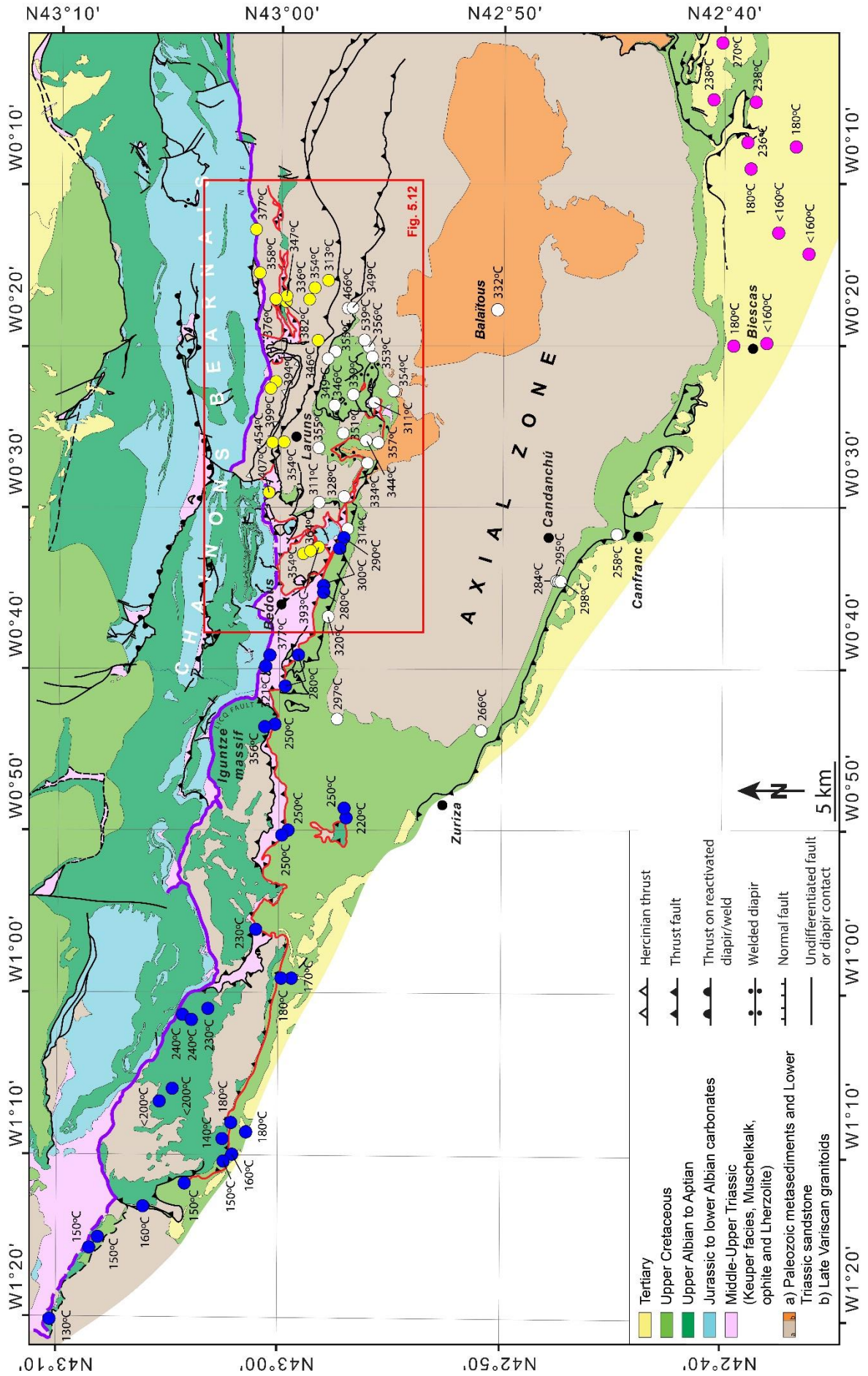


**Fig. 5.2.** *Compiled Raman paleotemperatures for the western Axial Zone cover from published works and new data from this thesis: Labaume et al. (2016) (violet spots); Corre (2017) and Izquierdo-Llavall et al. (2020) (yellow spots); Saspiturry et al. (2020) (blue spots) and results from this thesis (white spots). Lakora thrust (red line); Boundary between the preorogenic rift axis (CBB and Mauléon basin of the North Pyrenean Zone) and the necking zone and Iberian shelf to the south (Iguntze-mendibelza massifs, Axial Zone) (violet lines).*

### 5.1.1. Paleothermometry of the Mesozoic of the Eaux-Chaudes massif

As listed in table 5.1, the maximum temperature reached by the Mesozoic rocks during the alpine orogeny is in the lower greenschist facies, with values around 350°C and a standard deviation of 10-15°C. Considering the structural units described in the previous chapter, it exists a difference in the temperature between the overturned limb and the autochthon upper Cretaceous with respect to the normal fold limb. Representative Raman spectra from the basal beds of the autochthonous unit and the entire overturned limb show intensity differences by a D<sub>1</sub> band slightly more intense than the G band (Fig. 5.3). This indicates qualitative temperature estimates >340°C. The quantitative values obtained for those samples are in a range of 340°C to 365°C. On the contrary, in samples from the upper part of the succession (i.e. Santonian or Campanian flysch) and from the complete succession of the normal limb of the recumbent fold (in the whole upper Cretaceous stratigraphy), both D<sub>1</sub> and G bands show a very similar intensity or even higher intensity of G band (Fig. 5.3), accounting for a qualitative temperature estimate <330°C. After the fitting of spectra, the resulting temperature values are characterized by a range of 310°C to 330°C for this domain. In contrast with the basal facies of the Cretaceous sediments, the upper part of the stratigraphic pile and the normal limb of the ECFN present such a decrease in T<sub>max</sub> values with a less than straightforward interpretation that will be discussed below.

The microstructural features observed at ECM are consistent with the RSCM estimates. Occasionally, deformation twins of type III-IV are recognized in coarser grains from thin section observations in different samples, which are indicative of temperatures >250°C (Ferrill et al., 2004). Complete recrystallization of calcite, also identified, is commonly reported at temperatures >300°C (Weber et

al., 2001), and incipient bulging recrystallization in quartz (occurred at some areas) is documented for the range 300-400°C (Stipp et al., 2002a).

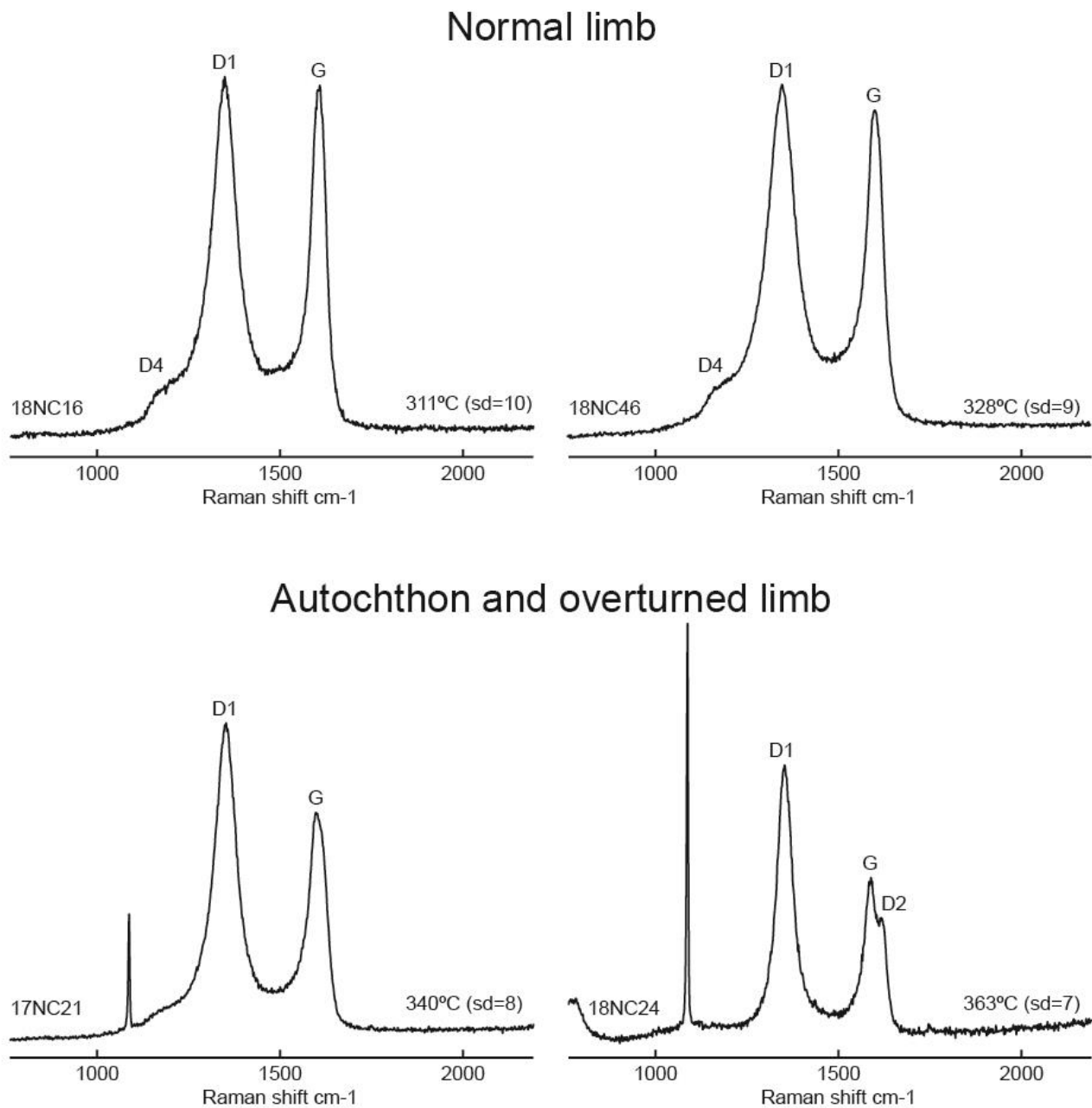


**Fig. 5.3.** Representative Raman spectra from the Eaux-Chaudes massif in both domains (normal limb and autochthon in combination with the overturned limb). Spectra of the lowermost analysed temperature of the range to the left and spectra of the highest analysed temperature of the range to the right.

### *5.1.2. Paleothermometry of Paleozoic rocks and the allochthonous Keuper sheet*

In order to compare the thermometry of the upper Cretaceous with its polydeformed basement, two samples from the Raman analysis performed in this work are from this domain. One corresponds to the Gavarnie nappe (20NC02), taken in between the Pêne Medáa and Pêne Sarriere, and the other to the Eaux-Bonnes hanging-wall (19NC22). Both are located at the eastern sector of the Eaux-Chaudes massif, in the limit of the study area (Fig. 5.1). Definitely, the Paleozoic thermal imprint is heterogeneous as shown by the results provided from Izquierdo-Llavall (2020) and Corre (2017) (yellow points in Fig. 5.2), with paleotemperatures in range from 313°C to 454°C.

According to the single paleotemperature value of 354°C for the Paleozoic core of the Eaux-Chaudes recumbent fold, it experienced similar  $T_{max}$  than the autochthon and overturned limb whether reached just in the Pyrenean orogeny or also in the Variscan times. The MVN is also characterized by moderately high paleotemperature values from 313°C to 354°C, similar to the observed for the Cretaceous. The 5MN preserves the highest thermal record of the Paleozoic stack in the study area with values from 394°C to 454°C (values published by Corre, 2017 and Izquierdo-Llavall et al., 2020). This unit to the east features a hanging wall anticline with overturned carboniferous strata in the southern limb, thrusting Albian rocks, and keeping a slightly colder thermal imprint with a range of 358°C to 376°C (data from Izquierdo-Llavall et al., 2020). Our results from two analysed Paleozoic samples show a temperature higher than that obtained in the mentioned works: 537°C for the sample of the autochthon Gavarnie nappe (in between the Pêne Medáa and Pêne Sarriere), and 466°C for the sample in the hanging-wall of the allochthonous Eaux-Chaudes nappe. The spectra obtained is singular and characteristic of the high ordered carbonaceous material (according to Beyssac et al., 2007 and references therein) with the G band very well-developed and a strongly reduced  $D_1$  and  $D_2$  bands (Fig. 5.4).

## Paleozoic from the EC and Gavarnie Nappes

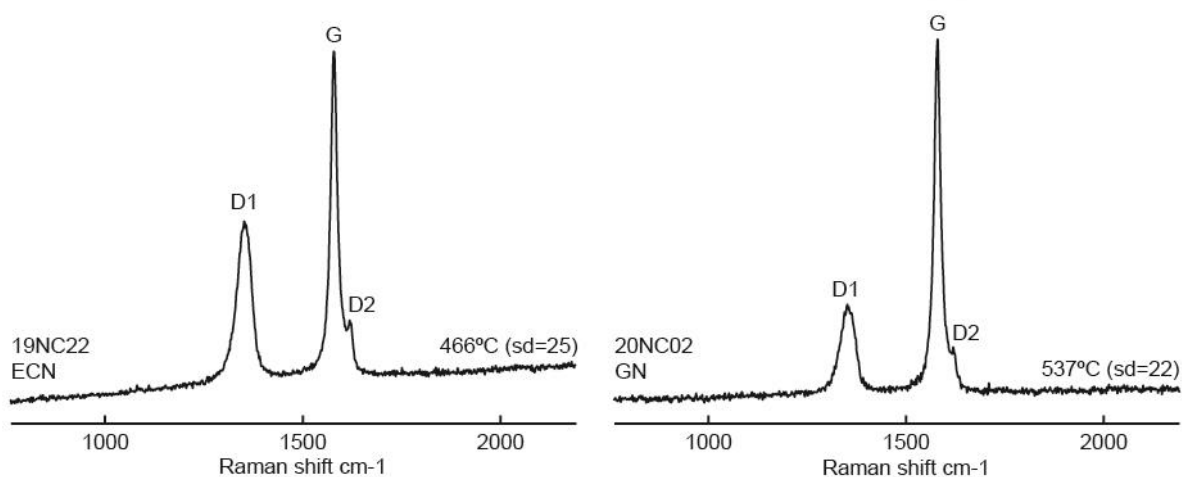


**Fig. 5.4.** The two Raman spectra obtained from the Paleozoic basement from the EC and Gavarnie Nappes.

As for the allochthonous Keuper sheet emplaced by the Lower Lakora thrust, embedded Muschelkalk limestone located south of Plateau d'Anouilhas yielded a  $T_{max}$  value of 349°C, very similar to the basal upper Cretaceous autochthon, the overturned limb and the Paleozoic of the ECFN core and MVN.

### 5.1.3. Paleothermometry around the western termination of the Axial Zone

From a larger point of view, in the Cretaceous rocks that form the closure of the western Axial Zone paleotemperatures are progressively lower west- and southwards than in the Eaux-Chaudes massif (Fig. 5.2). The five analysed samples corresponding to the south- and western borders of the Axial Zone (Sierras Interiores and Pierre-Saint-Martin and Aspe Valley areas, respectively) follow this trend: the values of  $T_{max}$  are in a range of 255-300°C at Sierras Interiores to 300-320°C at Pierre-Saint-Martin and Aspe Valley areas. Providing that, paleotemperatures from the Mesozoic facies decrease significantly to the west due to the pronounced western inversion of the Axial Zone which, definitely, induces the preservation of shallower stratigraphic levels. In the Jaca Basin the tertiary sediments are even shallower than the previously mentioned and it is reflected in the temperature range of 160-270°C.



From the preserved upper Cretaceous limestone in the Balaïtous peak (Fig. 5.2) we obtained a  $T_{max}$  value of around 332°C, similarly to the ones obtained in the upper part of the Cretaceous sediments in the ECM or in the normal limb of the ECFN. Those temperature values are consistent with the partial reset proposed for this area by Bosch et al. (2016) from ZHe thermochronology analysis obtained in the Eaux-Chaudes and Balaitous-Panticosa igneous bodies.

A conscious thermal study of the upper Paleozoic metasediments from the Aragón-Béarn Basin (south-western Axial Zone), just north of the Canfranc village, in the Candanchú area (Fig. 5.2), was carried by Cantarelli et al. (2013). Different geothermometers have been used, such as clay-mineral based geothermometers, homogenization temperatures from fluid inclusions from the host rock quartz-cements and vitrinite reflectance. Samples were taken under a thick pile of 500 to 1000m of Permian-Triassic sediments. Temperatures reported from deepest samples are approximately 170-220°C, while shallower Paleozoic rocks show colder values, from 100 to 150°C. They interpreted anomalous high values of mean vitrinite reflectance, 4.7% to 2.9% (from bottom to top in the stratigraphy, respectively), to be registered during different magmatic events by contact metamorphism processes. A comparison of %Ro values with burial temperatures have been proposed by many authors (e.g. Burnham & Sweeney, 1989; Barker & Goldstein, 1990). As a result, temperatures estimated for values of Ro higher than 2.4 are considered higher than 230°C or than 280°C. Price (1983) proposed a conversion of %Ro values to temperature, by his correlation anomalous values >2.9% may be higher than 300°C. Thermal analysis performed in this thesis account for values in the Mesozoic rocks higher than 260°C for their basal levels. The relative difference in  $T_{max}$  may be explained due to the standard deviation induced by the technique.

## 5.2. Electron Microprobe results

Measurements of Electron Microprobe Analyser were made to obtain the bulk Mg content of calcite coexisting with dolomite in thin sections from five selected different dolomitized samples in the overturned limb of the ECFN (Table 5.2).

TABLE 5.2. RESULTS OF EMPA

Sample	Crystal	Phase	MgO	SrO	FeO	MnO	CaO	total
17NC25	1	<i>Dolomite</i>	19.900	0.027	0.527	0.021	31.130	51.604
			20.090	0.000	0.496	0.006	31.390	51.982
		<i>Calcite</i>	0.609	0.000	0.071	0.000	55.080	55.760
			0.513	0.000	0.042	0.005	56.570	57.130
			0.352	0.000	0.052	0.018	56.430	56.852
	2	<i>Dolomite</i>	20.060	0.020	0.418	0.000	31.550	52.048
			20.200	0.000	0.415	0.000	31.140	51.755
		<i>Calcite</i>	0.497	0.000	0.040	0.015	56.170	56.721
			0.417	0.000	0.113	0.034	56.520	57.083
			0.624	0.000	0.056	0.000	56.710	57.390
			0.611	0.000	0.056	0.024	56.290	56.980
			0.654	0.000	0.044	0.032	56.010	56.740
	3	<i>Dolomite</i>	19.790	0.028	0.329	0.031	32.090	52.267
			20.740	0.012	0.233	0.000	31.640	52.625
			18.190	0.000	2.480	0.015	31.780	52.465
		<i>Calcite</i>	0.373	0.007	0.067	0.000	56.680	57.127
			0.646	0.034	0.062	0.000	56.430	57.172
			0.627	0.032	0.052	0.000	56.000	56.711
			0.616	0.035	0.067	0.000	56.210	56.927
			0.682	0.000	0.062	0.000	56.080	56.823
	4	<i>Dolomite</i>	19.340	0.000	1.890	0.040	30.670	51.940
			18.020	0.000	1.800	0.062	32.360	52.242
		<i>Calcite</i>	0.403	0.000	0.047	0.019	56.850	57.319
			0.569	0.000	0.059	0.000	56.510	57.138
0.650			0.008	0.054	0.013	56.420	57.144	
0.561			0.000	0.066	0.000	56.370	56.996	
1	<i>Dolomite</i>	20.360	0.006	0.224	0.008	31.790	52.388	
		20.340	0.000	0.205	0.029	31.860	52.435	
	<i>Calcite</i>	0.579	0.003	0.185	0.041	53.360	54.168	
		0.504	0.004	0.012	0.041	55.930	56.491	
		0.511	0.000	0.003	0.000	56.260	56.774	
		0.582	0.046	0.000	0.000	56.400	57.028	
		0.511	0.000	0.003	0.000	56.260	56.774	
	2	<i>Dolomite</i>	20.230	0.012	0.224	0.020	31.970	52.455
			18.950	0.000	0.129	0.006	34.740	53.824
		<i>Calcite</i>	0.602	0.000	0.005	0.000	56.380	56.987
			0.625	0.000	0.000	0.040	56.650	57.315
			0.561	0.000	0.024	0.013	55.820	56.418
			0.632	0.000	0.000	0.028	56.670	57.330
	3	<i>Dolomite</i>	19.550	0.000	0.171	0.002	32.150	51.873
			19.980	0.004	0.210	0.024	31.800	52.018

		<i>Calcite</i>	20.530	0.033	0.196	0.000	32.440	53.199
			0.542	0.000	0.018	0.012	56.650	57.221
			0.447	0.004	0.000	0.004	56.510	56.964
			0.581	0.032	0.031	0.040	56.550	57.233
<b>17NC37</b>	1	<i>Dolomite</i>	20.040	0.033	0.627	0.027	31.610	52.337
			19.900	0.015	0.504	0.043	31.550	52.011
		<i>Calcite</i>	0.470	0.027	0.019	0.082	56.430	57.028
			0.617	0.000	0.000	0.000	56.360	56.977
			0.601	0.000	0.048	0.008	55.280	55.937
			0.559	0.000	0.043	0.000	56.110	56.712
	2	<i>Dolomite</i>	20.840	0.000	0.376	0.010	30.240	51.466
			21.280	0.022	0.374	0.032	30.420	52.129
		<i>Calcite</i>	0.546	0.024	0.000	0.018	55.130	55.719
			0.499	0.000	0.035	0.060	56.360	56.954
			0.514	0.055	0.023	0.008	56.750	57.350
			0.515	0.000	0.028	0.000	55.580	56.122
	3	<i>Dolomite</i>	20.060	0.000	0.439	0.039	31.540	52.078
			21.180	0.001	0.219	0.035	30.920	52.355
		<i>Calcite</i>	0.545	0.000	0.022	0.028	55.700	56.294
			0.519	0.000	0.026	0.000	55.590	56.135
0.426			0.000	0.030	0.019	56.500	56.975	
0.410			0.000	0.029	0.025	55.930	56.394	
<b>17NC35</b>	1	<i>Dolomite</i>	17.97	0.000	0.4434	0.0365	34.65	53.100
			18.56	0.000	0.7105	0.0832	33.19	52.544
		<i>Calcite</i>	0.3588	0.0651	0.183	0.0183	55.79	56.415
			0.4308	0.02	0.0533	0.0166	56.36	56.881
	2	<i>Dolomite</i>	0.3096	0.000	0.0963	0.0129	56.87	57.289
			20.08	0.0234	0.5089	0.0433	32.41	53.066
		<i>Calcite</i>	18.21	0.000	1.35	0.0452	33.28	52.885
			0.6125	0.039	0.2789	0.0281	55.71	56.669
			0.4806	0.000	0.0321	0.0276	56.7	57.240
			0.4965	0.000	0.1652	0.0322	55.93	56.624
	3	<i>Dolomite</i>	19.64	0.0181	0.7194	0.03	32.3	52.708
			16.76	0.000	0.5096	0.0591	35.79	53.119
		<i>Calcite</i>	0.5079	0.0329	0.2491	0.0327	55.86	56.683
			0.6002	0.000	0.0917	0.000	56.36	57.052
	4	<i>Dolomite</i>	0.6116	0.0449	0.4988	0.0398	54.01	55.205
			18.34	0.045	0.0541	0.000	35.38	53.819
			16.3	0.025	3.12	0.029	33.74	53.214
			17.55	0.000	1.2706	0.1346	33.02	51.975
		<i>Calcite</i>	17.14	0.0358	1.49	0.1995	33.2	52.065
			0.5392	0.0045	0.3305	0.000	55.09	55.964

			0.5123	0.000	0.1159	0.0434	56.23	56.902		
			0.6043	0.000	0.2959	0.0105	55.6	56.511		
			0.4961	0.0274	0.2946	0.0112	55.44	56.269		
	5	<i>Dolomite</i>		17.94	0.000	0.3823	0.0254	34.27	52.618	
				18.08	0.000	0.3569	0.0174	34.33	52.784	
		<i>Calcite</i>		0.5171	0.000	0.3689	0.0101	54.82	55.716	
				0.51	0.000	0.261	0.000	55.6	56.371	
				0.5534	0.000	0.3043	0.0244	55.53	56.412	
	6	<i>Dolomite</i>		19.53	0.000	1.48	0.177	31.24	52.427	
				17.6	0.000	0.3014	0.2332	34.14	52.275	
				16.78	0.000	3.55	0.0224	32.47	52.822	
				18.14	0.0166	0.0401	0.0025	35.37	53.569	
				18.14	0.0271	0.1203	0.000	34.62	52.907	
		<i>Calcite</i>		2.36	0.0371	0.1783	0.000	51.44	54.015	
				0.4608	0.0098	0.2281	0.0023	55.78	56.481	
				0.5284	0.023	0.2492	0.0353	55.21	56.046	
	17NC40	1	<i>Dolomite</i>		19.66	0.000	0.5978	0.0298	31.15	51.438
					19.68	0.0084	0.5775	0.0005	30.67	50.936
<i>Calcite</i>				0.4792	0.000	0.0466	0.0173	55.74	56.283	
				0.5365	0.000	0.054	0.0329	55.16	55.783	
				0.451	0.000	0.0529	0.000	55.68	56.184	
2		<i>Dolomite</i>		0.2603	0.000	0.0345	0.019	55.79	56.104	
				20.85	0.000	0.4291	0.003	31.18	52.462	
		<i>Calcite</i>		19.93	0.000	0.4784	0.0622	31.28	51.751	
				0.4729	0.000	0.0374	0.0371	55.76	56.307	
				0.5965	0.000	0.0512	0.0361	55.97	56.654	
				0.5736	0.000	0.0519	0.0106	55.99	56.626	
3		<i>Dolomite</i>		0.5252	0.000	0.0428	0.0017	55.73	56.300	
				20.66	0.000	0.5887	0.0457	31.12	52.414	
		<i>Calcite</i>		19.73	0.000	0.602	0.0661	31.47	51.868	
				0.311	0.000	0.0351	0.0312	56.37	56.747	
				0.3202	0.0019	0.048	0.0076	56.47	56.848	
4		<i>Dolomite</i>		0.5114	0.000	0.0387	0.0034	56.26	56.814	
				0.5444	0.0385	0.0319	0.0069	55.73	56.352	
		<i>Calcite</i>		20	0.000	0.505	0.0325	32	52.538	
				19.9	0.000	0.5477	0.0176	31.17	51.635	
				0.4201	0.000	0.1593	0.0322	56.65	57.262	
				0.5339	0.000	0.0633	0.0449	56.07	56.712	
5		<i>Dolomite</i>		0.5428	0.000	0.0257	0.000	55.72	56.289	
			0.4568	0.0613	0.0467	0.000	56.09	56.655		
		<i>Dolomite</i>		19.63	0.000	0.5227	0.085	32.04	52.278	
				19.27	0.000	0.5578	0.0577	32.23	52.116	

			1.2533	0.02	0.009	0.000	55.41	56.692
			0.6257	0.0102	0.0622	0.0181	55.33	56.046
		<i>Calcite</i>	0.4704	0.000	0.0496	0.000	56.2	56.720
			0.564	0.000	0.0592	0.000	56.18	56.803
			0.5466	0.000	0.0294	0.000	56.12	56.696

**Table 5.2.** Results of electron microprobe analysis of coexisting calcite and dolomite phases from the five dolomitized samples in the overturned limb of the recumbent fold.

The Mg content in calcite coexisting with dolomite can be used to obtain metamorphic temperatures (Goldsmith, 1983; Bucher & Grapes, 2011). The effect of  $\text{FeCO}_3$  was studied by Powell et al. (1984) and Anovitz & Essene (1987). In the samples of this thesis 3 to 7 analyses per grain were made, distributed near the border of the calcite crystals close to the dolomite contacts (Fig. 5.5).

In this work, I have tested two geothermometers prior the systematic analysis using the RSCM method. A first method from Powell et al. (1984) is based on a diagram which plots the  $X_{\text{Fe,dol}}$  vs  $X_{\text{Mg,cc}}$  containing empirical predicted curves of 300°C to 550°C for calcite-dolomite equilibrium (Fig. 5.6). This diagram resulted from analytical experiments focusing on the solubility of magnesium in calcite assemblage with dolomite in the mineral system of  $\text{CaCO}_3$ - $\text{MgCO}_3$ - $\text{FeCO}_3$  at different temperature conditions. A second, from Covey-Crump & Rutter (1989) is based on  $X_{\text{MgCo}_3}$  of calcite co-existing with dolomite following the eq (1) previously exposed in chapter 3.4. Our EMPA results were averaged per analysed grains for the Powell et al. (1984) geothermometry, but not for the Covey-Crump & Rutter (1989) procedure. In the latter, the content of both Fe (<0.3wt %) and Mn (<0.5wt %) was dismissed due to its lower representativeness and, consequently, with no significant effect in the thermal values.

The paleotemperature record for the overturned limb by Powell et al.'s geothermometer is in a range between the predicted curves of 300°C and 350°C (Fig. 5.6), roughly consistent with the RSCM results. Some data are plotted below the first curve and just one exotic point overrides the curve of 350°C.



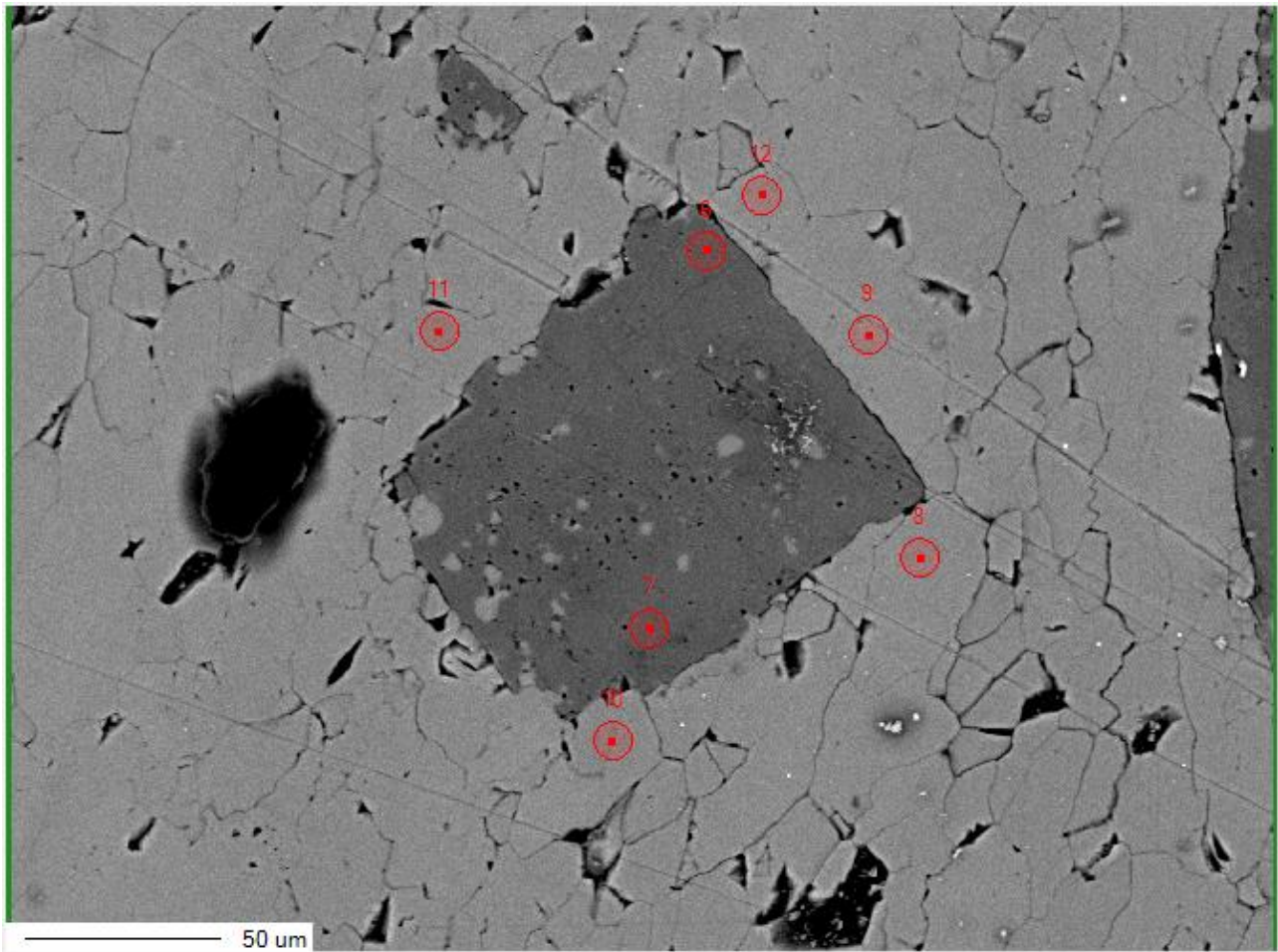


**Fig. 5.5.** SEM image of the EMPA acquisition from a dolomite crystal (dark grey) embedded in a calcite matrix. Two spots were acquired in the border of the dolomite crystal, and five other spots in five different calcite crystals in contact with dolomite.

The results from Covey-Crump & Rutter's geothermometer also are consistent with the  $T_{max}$  values obtained by RSCM. The three intervals of frequency that account for the 85% of the total amount of the resultant data are in a range between 320°C and 350°C. There are data of below 300°C and above 350°C, but not in a representative ratio (Fig. 5.7).

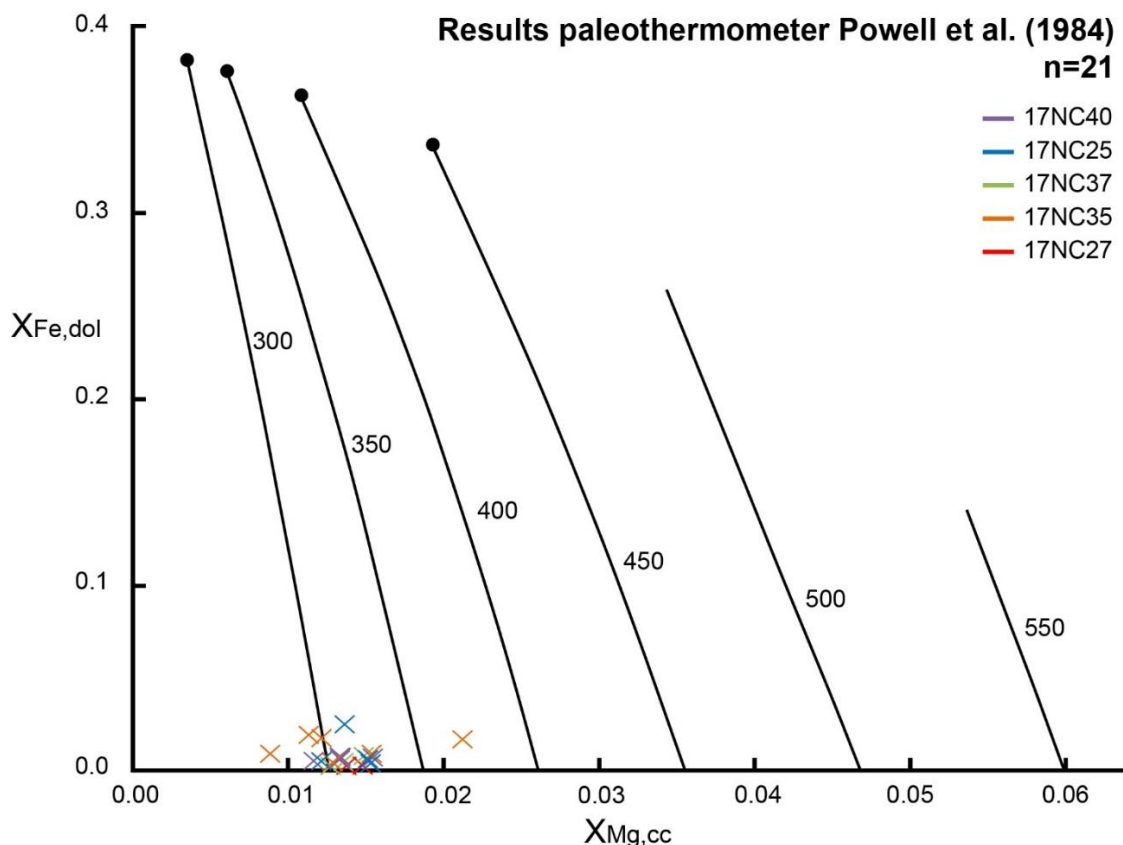


**Fig. 5.6.** Projected data obtained from EMPA analysis of samples of the Eaux-Chaudes massif in Powell et al.'s (1984) plot with predicted curves of 300°C to 550°C, for equilibrium accounting for  $X_{Fe}$  in dolomite vs.  $X_{Mg}$  in calcite (location of samples in Fig. 5.1).

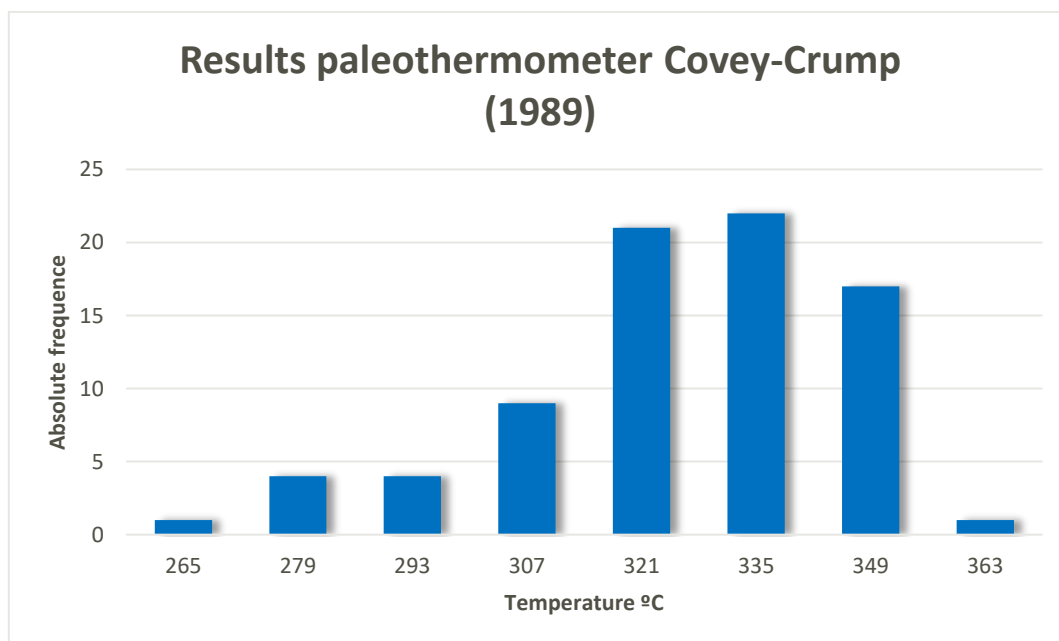


**Fig. 5.7.** Paleotemperature obtained by Covey-Crump (1989) paleothermometer from the ECM samples analysed by EMPA. Total values of temperature obtained are 79 and they are compiled in 8 absolute frequency intervals showing the great number of values in between 320 and 350°C with a bell-like distribution.

### 5.3. Paleothermal implications

#### 5.3.1. *Thermal record in the Eaux-Chaudes massif*

In the Eaux-Chaudes massif, the paleothermal record of the upper Cretaceous rocks exhibit unexpected relatively high temperatures, not reported previously, due to its shallow position of the carbonate platforms at the post-rift stage (Fig. 1.1), from where paleotemperatures should be much lower than the analysed. Providing that, the origin of the high thermal imprint for the upper Cretaceous must be invoked to the Alpine orogeny. Compressional tectonics entails a relative deep burial by the stacking of thrust units in a combination with complex processes of fluid circulation which could turn into hydrothermal by the occurrence of their deep origin and/or circulation. Up to this point and considering what exposed in the chapter 4, those hypotheses are plausible to explain the heating of the Cretaceous sediments. These rocks show the highest values of the Iberian Mesozoic with an average of 350°C, especially near the unconformity and from the overturned limb of the ECFN. Nonetheless, temperatures from the Montcuges peak and from the south of Plateau d'Anouilhas (Fig. 5.8, revise location in Fig. 4.4), in the upper levels of the Cretaceous sediments, are in a range of 339 to ~310°C, respectively, much lower than the deeper samples. Those values have been obtained from rocks separated vertically ~300m from which this highlighted difference confers a local geothermal gradient of approximately 60 to 120 °C/km. Looking at the normal limb of the ECFN, below the Montagnon d'Iseye (Fig. 4.2 for location), a decreasing gradient of 20°C from bottom to top (in 300m) is also observed (S1 in Fig. 5.8). In addition, paleotemperatures from the autochthon of the ECFN, lying over the Paleozoic of the Axial Zone in the western sector, define a highest gradient of approximately 45°C from the basal levels of Cenomanian up to the shales from Campanian flysch (e.g. S1 in Fig. 5.8), again in approximately 300m in a vertical profile. Even though, the lower temperatures obtained by Raman spectroscopy (between 310-328°C) remain high compared to the Mesozoic of the Iberian margin which do not correspond to the ECM.

This high thermal record, even unexpected, is rather consistent with the ductility appreciated by field observations and structural study. Although, the microdeformation is very-dependent from the strain-

rate, temperature have a great impact on intra and intercrystalline evolution. Calcite is able to develop dynamic recrystallization processes, such as grain boundary migration (GBM) or intracrystalline plasticity by twins, at rather low temperatures (150-250°C, according to Kennedy & White, 2001). Stretching mineral lineation and mylonitic foliation are the more prominent features of these processes recognized in the field, as reported in the previous chapter, especially accounting for plastic calcite deformation. On the other hand, dolomite, requires more energy to activate intracrystalline deformation (twins), at least 300°C (e.g. Barber & Wenk, 2001), and behaves more rigidly than calcite. Dolomite porphyroclasts are described as sign of ductility and well-exemplifies the differences in deformation between the two carbonate phases. On the other hand, quartz phase, which is not dominant in those limestones is slightly ductily deformed. It requires higher temperatures to develop strong ductility. Otherwise, weak intracrystalline deformation as undulous extinction and very rare bulging have been identified, by the petrographic observations, as postulated as the common structures for low-grade conditions (e.g. Stipp et al., 2002a).

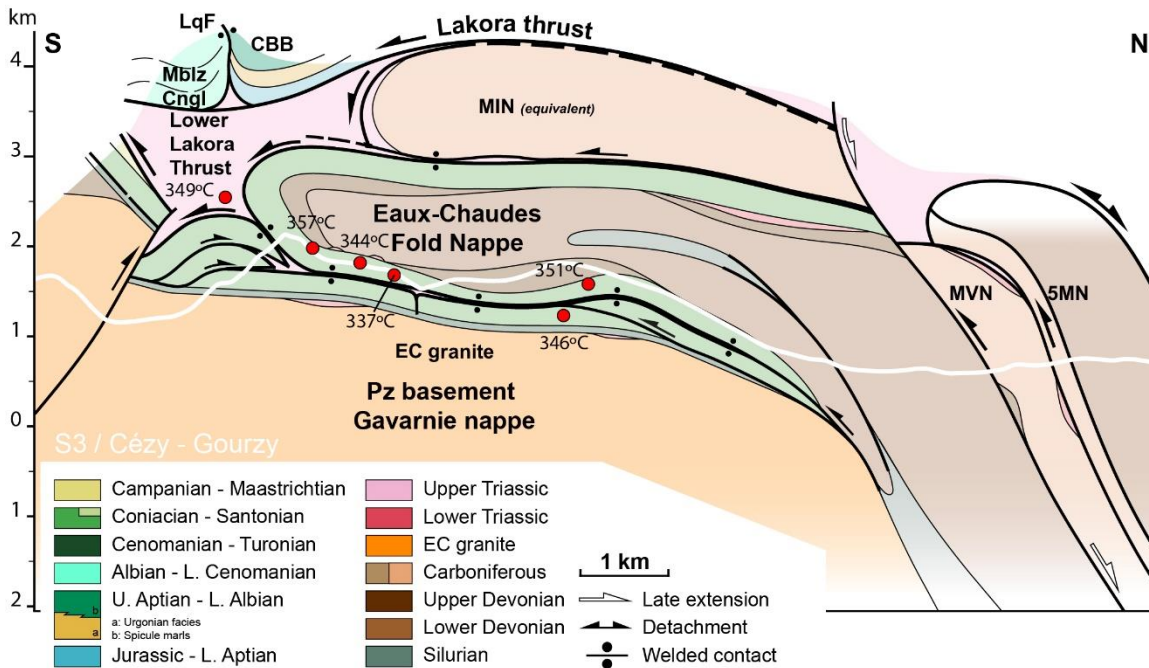
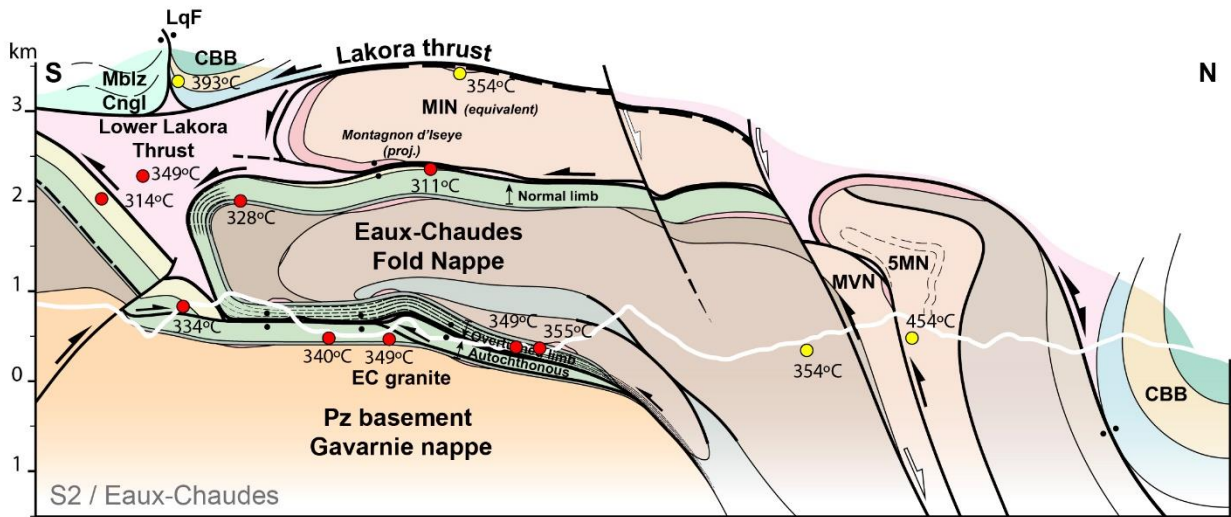
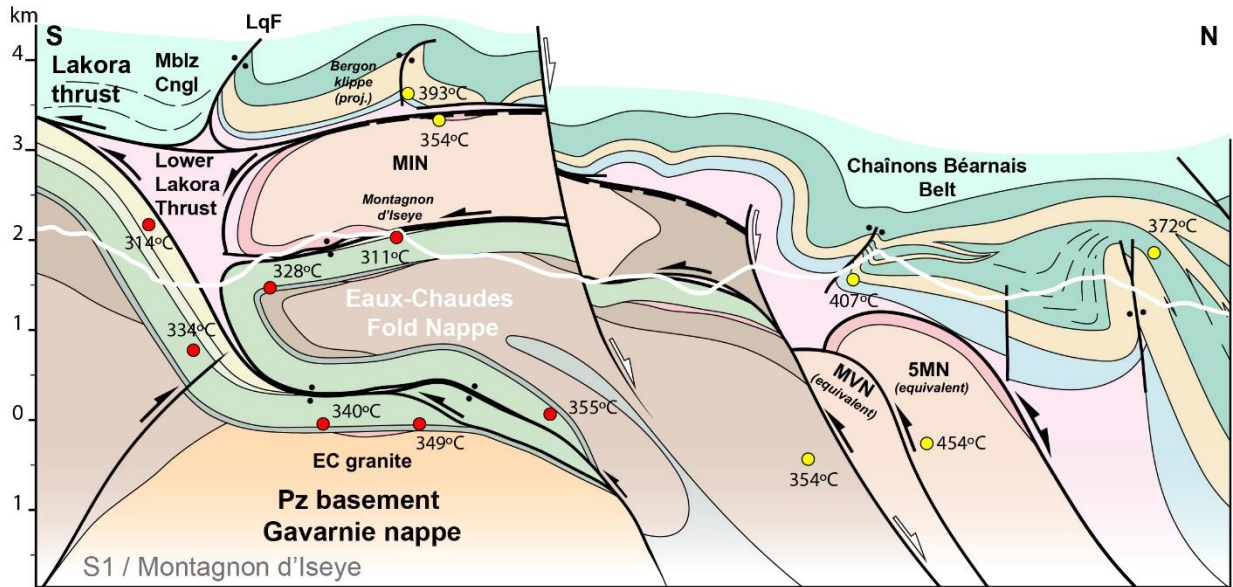




**Fig. 5.8.** *Paleotemperatures obtained in this work (red points) and from the previous authors (yellow points) by RSCM, projected in the structural cross-sections of the western sector of the ECM (cf. Fig. 4.5). They show the thermal imprint of different structural units and, especially, along the upper Cretaceous carbonates from the basal facies to the uppermost ones. Internal thermal gradients have been identified within the autochthonous from its bottom on the EC granite to the top in the flysch facies or inside the normal limb (i.e. section S2). Normal limb and the southern autochthonous are relatively colder than the overturned limb and the autochthon over the EC granite. Paleozoic core and MIN show similar temperatures than the upper Cretaceous while 5MN keep much higher value from inherited metamorphism. Allochthonous unit of CBB show elevated inherited temperatures from the low-mid Cretaceous hyperextension.*

The explanation for the thermicity of the Eaux-Chaudes massif, which is undoubtedly higher than the observed in the Mesozoic rocks of the Alpine Pyrenees (e.g. Labaume et al., 2016; Saspiturry et al., 2020) is challenging. Comparing the paleothermal results of the Eaux-Chaudes with similar tectonic stacks elsewhere, the first approach was tested with the analogue Helvetic nappes of the Swiss Alps, where the high paleotemperatures recorded from 220 to 360°C (e.g. Girault et al., 2020 and references therein) are explained by the burial of more than 15 km stacking pile conformed by the Penninic and Austroalpine nappes (Dietrich & Casey, 1989; Pfiffner et al., 1997; Herwegh & Pfiffner, 2005; Nibourel et al., 2018). Such burial is difficult to assume for the case study of the Pyrenean hinterland in view of the much thinner overlying thrust pile that can be estimated (e.g. Teixell, 1998; Bellahsen et al., 2019).

Caldera et al. (2021) focused on the western sector of the ECM, especially on the fold nappe structure by analysing samples from the three domains (autochthonous, overturned limb and normal limb). With the first results, Caldera et al. (2021) tentatively proposed a geothermal gradient to firstly approach a hypothesis for the explanation of the unexpected high Cretaceous paleotemperatures. To achieve that, the thermal gradient required inside the fold nappe, between the normal and overturned limbs, which today are separated approximately 1 km vertically. The result exhibits a decrease of ~30°C/km from the overturned to the normal limb. This hypothesis for the thermal variation is very much similar to the one proposed by Saspiturry et al. (2020) of 34°C/km for the European conjugate margin. However, and considering this estimated gradient, a total burial of ~11 km is deduced for the observed  $T_{max}$  values in the ECM, which is hard to envisage from the proposed crustal-scale restorations where

thin-skinned tectonics is the main structural style of deformation for the structures concerned to the study area (e.g. Teixell, 1998; Labaume & Teixell, 2020, and Figs. 4.16 and 4.17). On the other hand, in the thermochronology-assisted restoration of the Iberian margin to the late Eocene published by Labaume et al. (2016), ~8 km of stratigraphic burial is estimated over the ECM. Merging this proposal with the provided paleotemperature results, a gradient of 120°C/km is inferred. Bellahsen et al. (2019) account for a persistent high geothermal gradient from the Mesozoic thinning along the Iberian paleomargin to the Axial Zone in his study from the Bielsa Mesozoic cover (Gavarnie nappe). His proposal fits the geological scheme of reasonable burial proposed by Labaume et al. (2016). The structural evolutive restorations proposed in the previous chapter (Figs. 4.16 and 4.17) could be consistent with the combination of both effects: 1) a moderate burial by the stack of Paleozoic and CBB units, coupled with 2) an elevated geothermal gradient persistent from the Cretaceous hyperextended rift.

The second step was to extend the thermal study to the whole ECM by RSCM which provided key information to test this argument and to consider alternative scenarios. Regarding the strong vertical difference in the obtained temperatures for the autochthonous upper Cretaceous below the fold nappe (up to 45°C in approximately 300 m of Mesozoic stratigraphy), the hypothesis of an inherited and relatively high gradient could be supported. The maximum paleotemperatures calculated for the Cretaceous rocks are located in the basal facies from the Cenomanian-Turonian, near the unconformity with the Paleozoic basement, being progressively lower to the top of the stratigraphy.

The field work led to the recognition of evidence of fluid circulation in the uppermost Paleozoic strata and along the unconformity with the Mesozoic facies. Large quartz veins have been identified locally in the Devonian carbonates and occasionally crossing to the Cenomanian limestone (i.e. south of Pêne Medáa; Fig. 5.9, see Fig. 4.4 for location). It is known that hydrothermal fluids could become heat sources by metamorphic contact and/or heat diffusion, inferring HT-LP metamorphism as testified in other areas of the Pyrenees i.e. by Clerc et al. (2015). Moreover, the heating of the basal upper Cretaceous succession favoured its ductility and, consequently, the development of intra-

Cenomanian detachments (e.g. Figs. 4.9, 5.10) widely observed along the Pêne Medáa and Pic de Ger massif, performing features of squeezed limestones (Fig. 5.10).

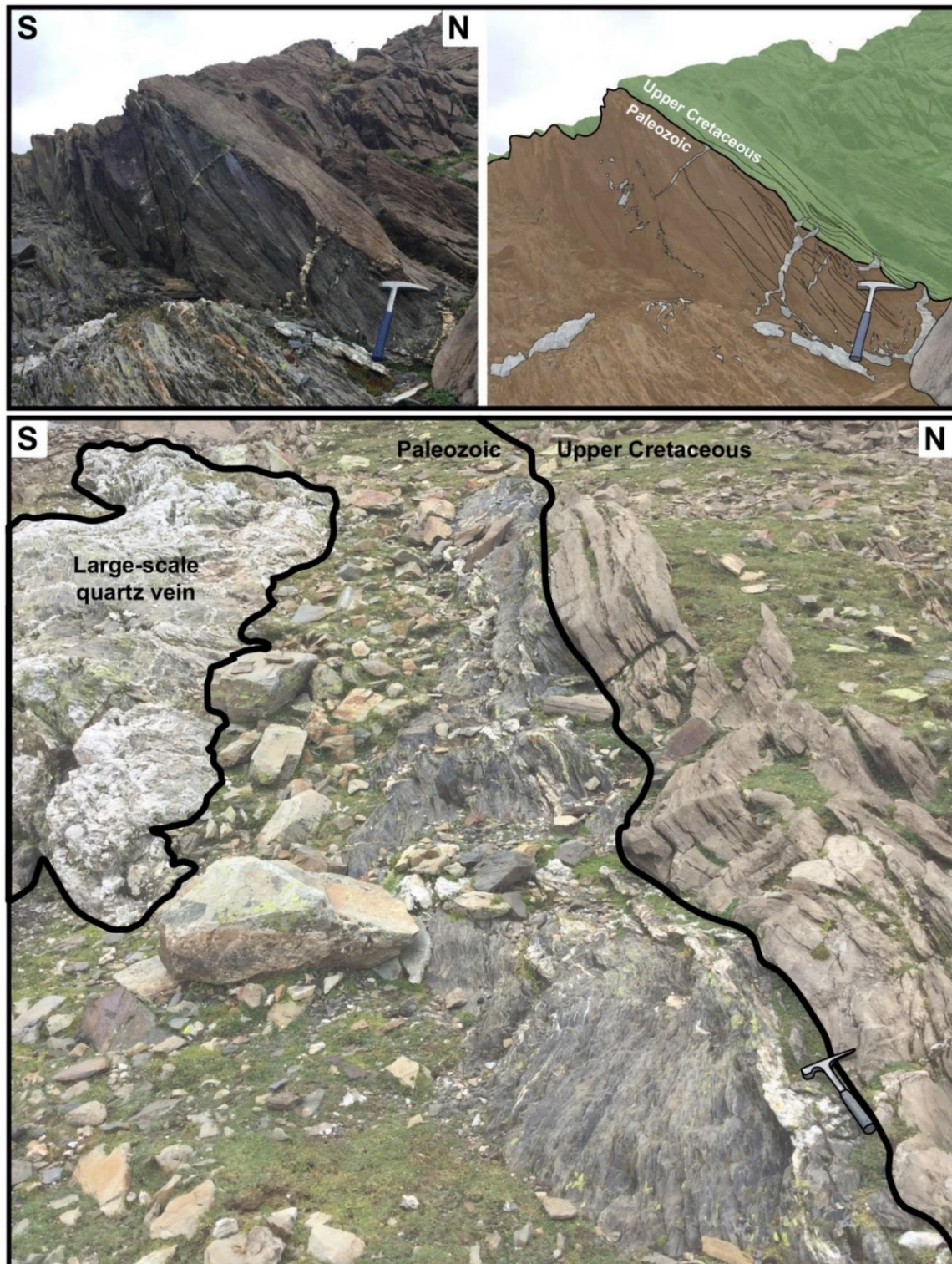


**Fig. 5.9.** Examples of large and small-scale quartz veins near and cross-cutting the Paleozoic-Cretaceous unconformity (near Pêne Medáa, eastern sector of the Eaux-Chaudes massif) and acting as a heat source for the basal Mesozoic limestones.



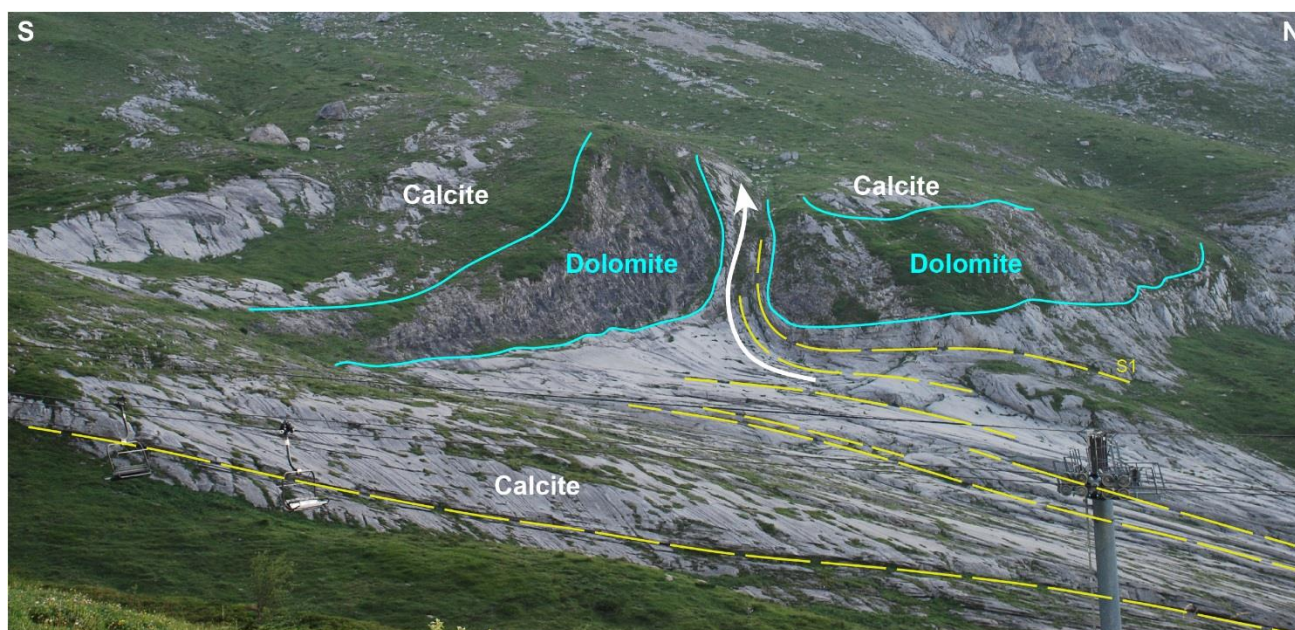


**Fig. 5.10.** Example of limestone squeeze in between two stronger bodies of dolomite east of Pic de Ger. Alpine foliation S1 (dashed yellow lines) is also affected by the squeezing being folded in the narrow zone. Dolomite is poorly deformed.

Due to the inefficient thermal conductivity of the carbonaceous material-rich sediments (Blackwell & Steele, 1989) as limestones (1.26 to 1.33 W/mk; Bergman et al., 1990) and marbles (2.07 to 2.94 W/mk, Holman, 1990), the abnormal high gradient referred above (60-120°C/Km) may be explained by the retention of the heat and depriving its transfer to the overlying facies by the process known as the thermal blanked (e.g. Blackwell & Steele, 1989; Pollack & Cercone, 1994; Nunn & Lin, 2002) in the upper Cretaceous limestones (Fig. 5.11), especially for the Cenomanian and Turonian sediments. In view of this, large amount of burial is not required but could be supportive. The areas where basement is also represented by limestones (Devonian) or by low quartz-vein content the temperature in the upper Cretaceous is relatively lower (328-311°C, i.e. normal limb of the ECFN). Focusing on the large-scale (upper Iberian margin), and considering this hypothesis, the decrease in temperature of the upper Cretaceous facies could be explained by the increase in limestone thickness west- and southwards. The inefficiency of thermal conductivity increases and, consequently, the recorded  $T_{max}$  is more related to burial effects (e.g. 150 °C in Saspiturry et al., 2020; Fig. 5.2).

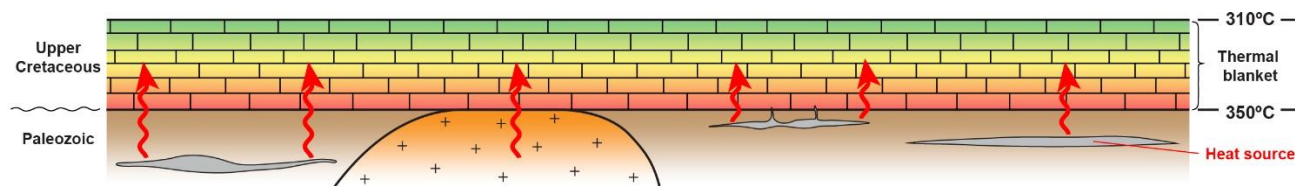


**Fig. 5.11.** Scheme of heating and inefficient thermal conductivity across the upper Cretaceous limestones of the ECM by the thermal blanket effect. Colour gradient from red to green represent the heat retaining near to the unconformity and hampering the heat transfer to the top.

Specifically, temperatures obtained in this work for the Paleozoic basement of the Gavarnie nappe are much higher than those previously reported (e.g. Corre, 2017; Izquierdo-Llavall et al., 2020) (violet spots from Figs. 5.2, 5.12). As proposed for the upper Cretaceous, high temperature fluid circulation during strong deformation events may affected those rocks by ordering its carbonaceous material to graphite phase. This affection is strongly localized and quick but sufficient to raise the temperature.

Maximum temperatures for the southern basement of the western Axial Zone (Cantarelli et al., 2013) are very similar to those from its Mesozoic cover where deformation is less intense and hydrothermal activity fairly reduced as it occurs far from the hinterland with complex structural inheritance.

### *Thermal history of the North Pyrenean Zone: the rift axis*

In the vicinity of the study area, the paleothermal record of the Jurassic-Lower Cretaceous rocks from the Chaînons Béarnais Belt is in range of 300°C to almost 500°C (e.g. Clerc et al., 2015; Corre, 2017; Cloix, 2017; Izquierdo-Llavall et al., 2020). However, these paleotemperatures are attributed to the HT-LP metamorphism (Golberg 1987; Golberg & Leyreloup, 1990; Lagabrielle et al., 2010; Clerc & Lagabrielle, 2014) that occurred during the Cretaceous episode of crustal hyperextension in the core of the Pyrenean rift (e.g. Jammes et al., 2009; Lagabrielle et al., 2010; Saspiturry et al., 2020; Ducoux et al., 2021b).

The allochthonous syn-rift Mesozoic (Jurassic and lower Cretaceous) in the vicinity of the Eaux-Chaudes massif is preserved along the southern edge of the Chaînons Béarnais belt, i.e. in the



Bergon klippen on top of the MIN and in the Lauriolle area further north (Fig. 5.12). Temperature values show a moderately high thermal record (Corre, 2017; Cloix, 2017; Izquierdo-Llavall et al., 2020). Temperatures from all contributors have been synthesized in the figure for a cleaner display.

The explanation for the high paleotemperature record of the CBB is quite straightforward invoking the crustal and lithospheric thinning in the Pyrenean rift, largely discussed in the literature (e.g. Lagabrielle et al., 2010; Clerc et al., 2015 and references therein; Izquierdo-Llavall et al., 2020; Labaume & Teixell, 2020; Saspiturry et al., 2020; Ducoux et al., 2021a).

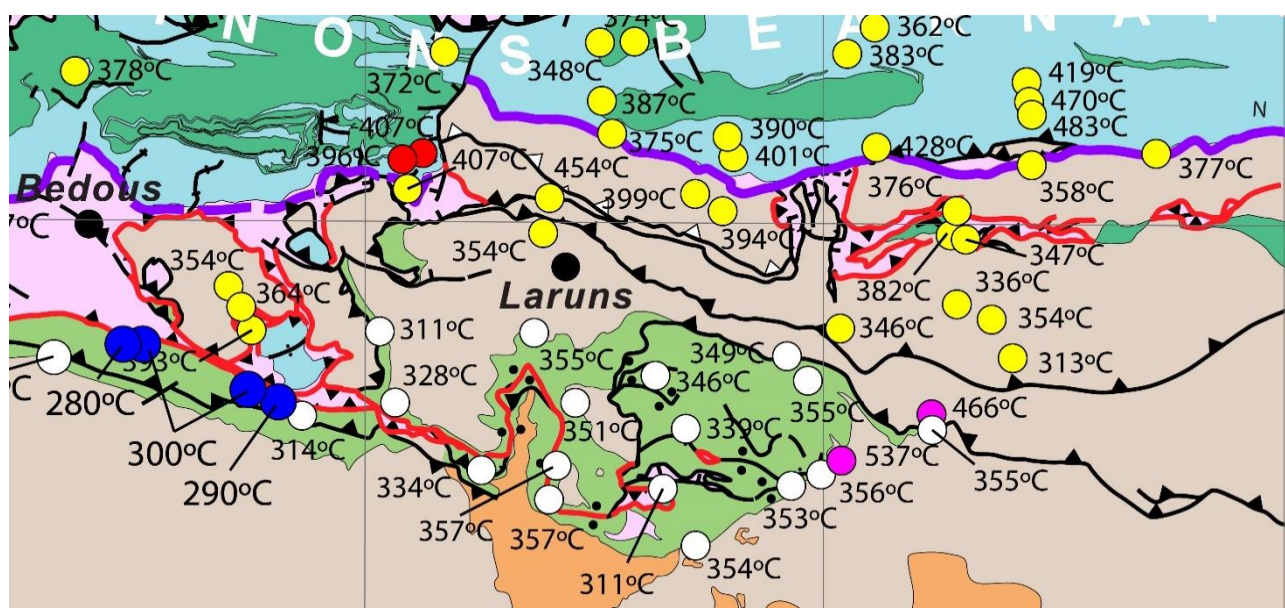


**Fig. 5.12.** Detailed map from figure 5.2 with synthesized paleotemperatures from southern CBB and ECM. Red colours correspond to temperatures from Cloix, 2017; for the rest of the colour code cf. Fig. 5.2.

### *Thermal history of the northern Iberian margin during the Pyrenean collision*

As mentioned before and reported by Labaume et al. (2016) and Saspiturry et al. (2020), paleotemperatures in the Upper Cretaceous progressively decrease to the south and to the west, as observed in the Jaca Basin and the southern domain of the Mauléon Basin, respectively. From the compilation of all data from the northern border of the Mesozoic Iberian margin, we propose a qualitative heat map (Fig. 5.13) showing this paleothermal pattern, decreasing away from a maximum centred in the ECM. This peak of temperature has been developed during and because of the

Pyrenean orogeny in the Alpine collision. The proximity to the necking zone of the Iberian margin conditioned its evolution to the hinterland of the Pyrenees where strong and deepest deformation have occurred. The progressive stacking of detached thrust sheets increased the burial of the ECM and enhanced the shearing in between the units, probably stimulating the fluid circulation. Furthermore, the structural inheritance of the Paleozoic basement should favour and intensified this process, maybe inducing deeper circulation and conferring to the fluid hydrothermal characteristics. The intrinsic inefficient thermal diffusion of the carbonates (thermal blanket effect) resulted in anomalous intracretaceous high thermal gradients (20-40°C in ~300m vertically). On the other hand, west and southwards in the Iberian platform, where deformation became weaker, and those processes are severely reduced. Indeed, the thickness of Cretaceous facies increase and therefore the sedimentary pile exposed nowadays is from more recent sediments or farther from the unconformity with the Paleozoic rocks, resulting in a lower recorded temperature (Fig. 5.13).

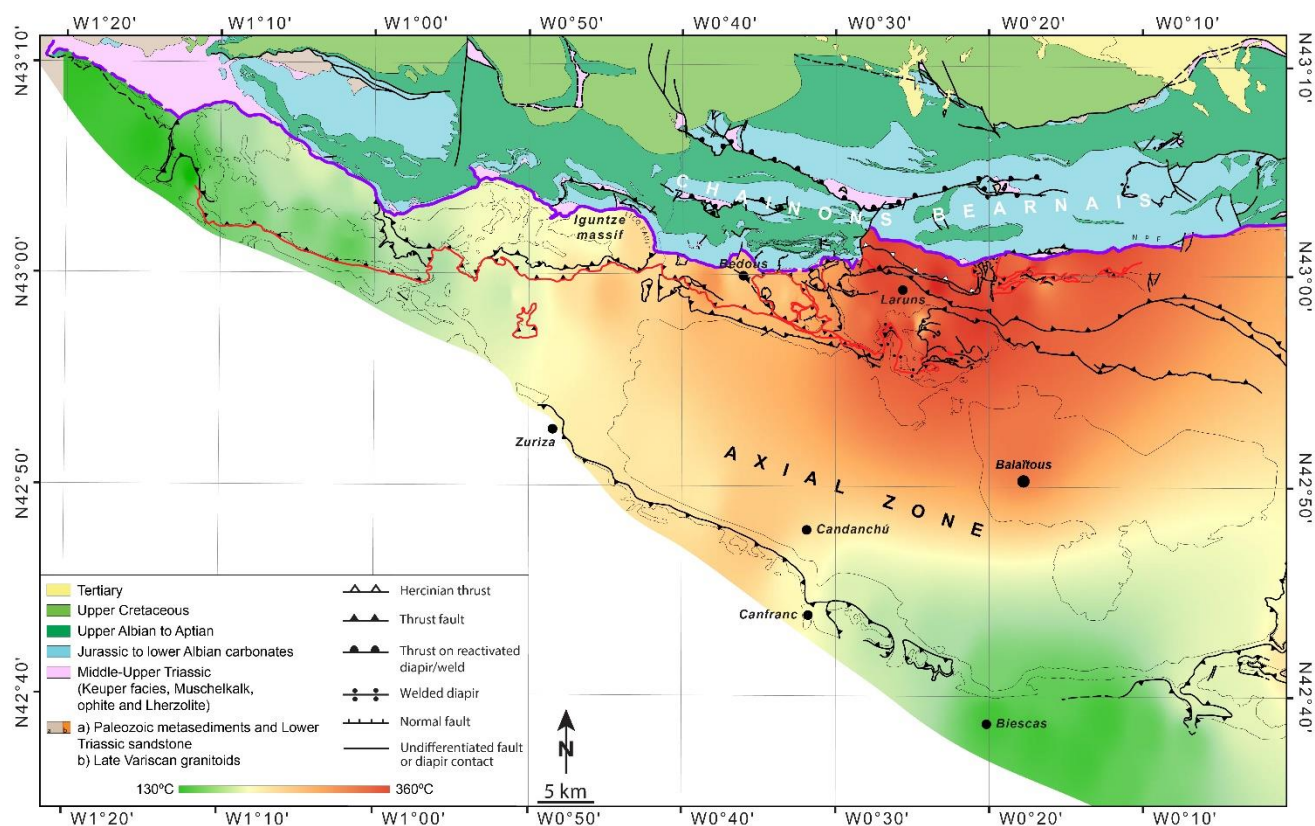


**Fig. 5.13.** Heat map based on the paleotemperature record of the Mesozoic rocks of the upper Iberian margin. Violet line: boundary between the preorogenic rift axis (CBB and Mauléon basin of the North Pyrenean Zone) and the necking zone and Iberian shelf to the south (Iguntze-mendibelza massifs, Axial Zone).

## 5.4. Conclusions of the paleothermal work

The thermicity of the upper Cretaceous rocks of the western Axial Zone of the Pyrenees may be considered low from the recognized fragile structures, widely developed in brittle conditions (i.e. thrusts and fault-related fold). Indeed, paleotemperatures reported for these rocks along the upper Iberian margin are lower than 300°C (e.g. Labaume et al., 2016 and Saspiturry et al., 2020; and temperatures from this thesis). The unexpected ductility identified in the upper Cretaceous carbonates of the Eaux-Chaudes massif (i.e. from mylonitic foliation, stretching mineral lineation, intrafolial folds, dolomite porphyroclasts) led to unravel conditions of deformation in the lower green-schist metamorphic facies, of around 320°C to 360°C, not reported hitherto for the Alpine collision.

The moderately high temperature reported by RSCM and calcite-dolomite geothermometer, and deformation style observed for the western sector of the ECM (the ECFN) account for a deep structural setting during the Pyrenean collision, which has been contrasted by the tectonic proposal (i.e. chapter 4). Nonetheless, much thinner than the burial proposed for the Helvetic nappes. In view of the above and in order to explain the recorded elevated temperatures, it was firstly suggested a combination of a persistent high geothermal gradient from the hyperextension event in a combination with moderate burial effect (Caldera et al., 2021), accounting for the hypothesis of Labaume et al. (2016) for the flexure of the margin.

Extending the thermal study to the whole ECM has emphasized that those high temperatures of the Cretaceous rocks (350°C) remain constant through the facies near to the unconformity with the Paleozoic basement (especially in the Cenomanian-Turonian levels). From the evidence of a large amount of fluid circulation in the uppermost Paleozoic facies and within the unconformity a second hypothesis becomes more reliable, instead. We can account for those fluids (hydrothermal) to represent the heat source which warm and soften the basal Upper Cretaceous facies, enabling the development of the intracenomanian detachments and limestone squeezing. The lower thermal conductivity of carbonates provokes a heat entrapment by the thermal blanket effect avoiding its dissipation to the top of the Mesozoic stratigraphy inducing gradients of temperature from 30 to 45°C

in approximately 300m in a vertical trend within the limestone succession. The thickness of upper Cretaceous pile increases west- and southwards along the upper Iberian margin and the maximum paleotemperatures reported for these areas (i.e. south of the Mauléon Basin and Jaca Basin) are much lower than in the ECM. Two main factors account for this reason: 1) the increase in thickness of the sedimentary pile, which results in higher gradients from the Paleozoic basement. 2) The more plausible, the remoteness with the Pyrenean hinterland (ECM) and the significant west tilting to the west, where deep and strong deformation have not been developed. Instead, true-thin skinned tectonics occurred in low-grade or brittle conditions.

Finally, temperatures obtained in this thesis for the Paleozoic basement (RSCM technique) are such higher than the previously reported nearby of the ECM. The hypothesis is in accordance with the circulation of hydrothermal fluids as a much-localized heat source, affecting small and specific areas. To the south of the Axial Zone, temperatures reported by Cantarelli et al. (2013) are much lower but in the line of those from the upper Cretaceous, inferring a coetaneous maximum heating, at least, during the Mesozoic collision.

## Chapter 6: Microstructure and fabric

The field observations of strong deformation in the post-Paleozoic rocks (e.g. mylonites) of the ECM have prompted the study and understanding of microfabrics and microstructural processes that occurred during the Alpine deformation by electronic microscope using the Electron Backscatter Diffraction analysis (SEM-EBSD). This is a technique widely chosen for microstructural analysis of deformed polymineralic and polycrystalline aggregates (e.g. Prior et al., 1999, 2009; Valcke et al., 2006, 2014). As reported in the two previous chapters, complex tectonic processes were highly influenced by the structural inheritance of basement, and subjected to persistent moderate temperatures. Last is evidenced by extensive ductile deformation of the Mesozoic rocks (upper Cretaceous carbonates) and temperatures recorded. Large-scale deformation is strongly linked and controlled by microstructural evolution, which is conditioned by the physico-chemical conditions such as temperature or strain rates (e.g. Regenauer-Lieb & Yuen, 2003; Herwegh & Berger, 2004). The aim of this chapter is to unravel the characteristics of microfabrics related to deformation processes to determine different domains of strain, its intensity and the deformation mechanisms that operated during the Alpine orogeny. The limit between the overturned limb and the autochthonous domain is not always evident from the overall structural observations. For example, polymineralic limestones usually display structures indicating strong deformation at outcrop-scale, which sometimes are not evident at the microscale. To account for that, this chapter focuses on the quantitative microstructural and textural analysis of the deformed rocks of the upper Cretaceous, with the goal to identify the main rock mineral composition, the structural context of samples, fabric strength, flow stresses, among others and supported by field structural data.



## 6.1. Deformation of the Cretaceous carbonates

In the autochthon and normal limb of the ECFN, generally, the sedimentary structures are preserved, and fossils remain unstrained, despite small-scale brittle faults and spaced pressure-solution cleavage. Ductile deformation at grain scale is not evident and EBSD analysis show random distribution of calcite crystallographic axes. Features of strong ductile deformation have been identified in the overturned limb of the ECFN and in the eastern autochthonous upper Cretaceous (in the Pic de Ger massif; cf. Fig. 4.2; e.g. Fig. 6.1). The overturned limb is characterized by strong ductile deformation that obliterates fossil content and recrystallizes the calcite matrix. Schistosity to mylonitic foliation, subparallel to bedding at the mesoscale, and stretching mineral lineation are commonly developed in this domain, and both are inclined to the north (Fig. 6.1a, b). Microfabrics are controlled by the rheological behaviour of the mineral phases. Crystal-plastic deformation processes were inferred as dominant in calcite-rich layers also in the eastern sector conditioning the evolution of the matrix and displaying S-C fabrics at all scales (e.g. Fig. 6.1c, d, e). Dolomite-rich layers are observed in some samples showing moderate plastic deformation with occasional fold streaks, and asymmetric porphyroclasts or large boudinaged bodies in outcrop-scale (e.g. Fig. 6.1f, g, h). Microdeformation, as will be discussed at the end of this chapter, is strongly influenced by the content of second phases, which may deeply condition the strain localization and/or favour grain growth/reduction processes.



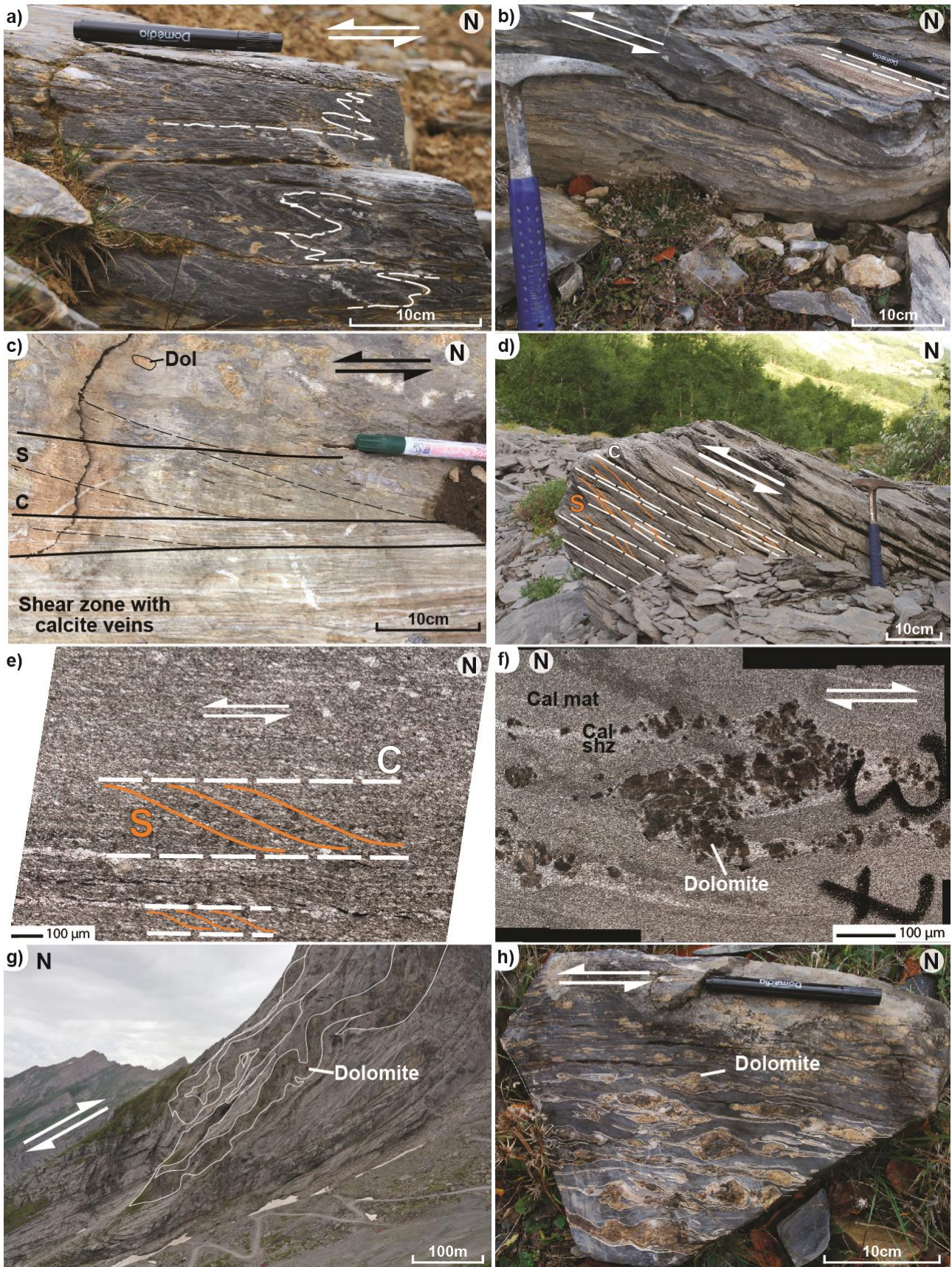




**Fig. 6.1.** Examples of ductile features recognized in the field and thin section. a, b) Intrafolial folds and stretching lineations (indicated by dashed white lines) on sheared carbonates in Cambeihl area. Arrows indicate shear direction. c) Small-scale shear zone characterized by a progressive shear increase and multiple calcite veins subparallel to the foliation (from area between Pic de Ger and Pêne Médaa). S-C structures are developed just above the calcite veins and dolomite porphyroclasts show low strain and reoriented parallel to foliation. d, e) meso-scale and thin section S-C fabrics in calcite-rich layers (from the overturned limb in the southeast of Pêne Médaa). f) Folded dolomite-rich thin bed showing strongly rotated asymmetric reverse limb from the overturned limb. Note extensional fractures and pinched shadow zones (cal shz) with calcite grains showing larger grain-size than in the matrix (cal mat). g, h) Folded and stretched dolomite bodies in large-scale (west of Pêne Médaa) and sample-scale (Cambeihl area), respectively. All the asymmetrical structures show a top-to-the-south sense of shear.

### 6.1.1. Domains of strain in the Eaux-Chaudes massif

Attending for the previously described structural units (cf. chapter 4) four main strain domains are proposed for the ECM during the Pyrenean orogeny (Fig. 6.2): 1) the normal limb of the ECFN, 2) the overturned limb of the ECFN and the hanging-wall of the Eaux-Bonnes thrust, 3) the weakly and 4) strong deformed autochthonous of upper Cretaceous of the eastern sector of the ECM. The limits between these domains are fairly constrained according to the obtained microstructural data and in some places those domains do not exactly correspond with the large structures defined in chapter 4.

It is also interesting to point out the limit between the two domains in the autochthon of the ECN. It coincides with the transition between the recumbent fold nappe and the Eaux-Bonnes thrust accommodated by the Gourzy transfer zone (cf. chapter 4) and the end of the EC granite. However, the limit between the overturned limb and its autochthon is straight and generally follows the structural setting.

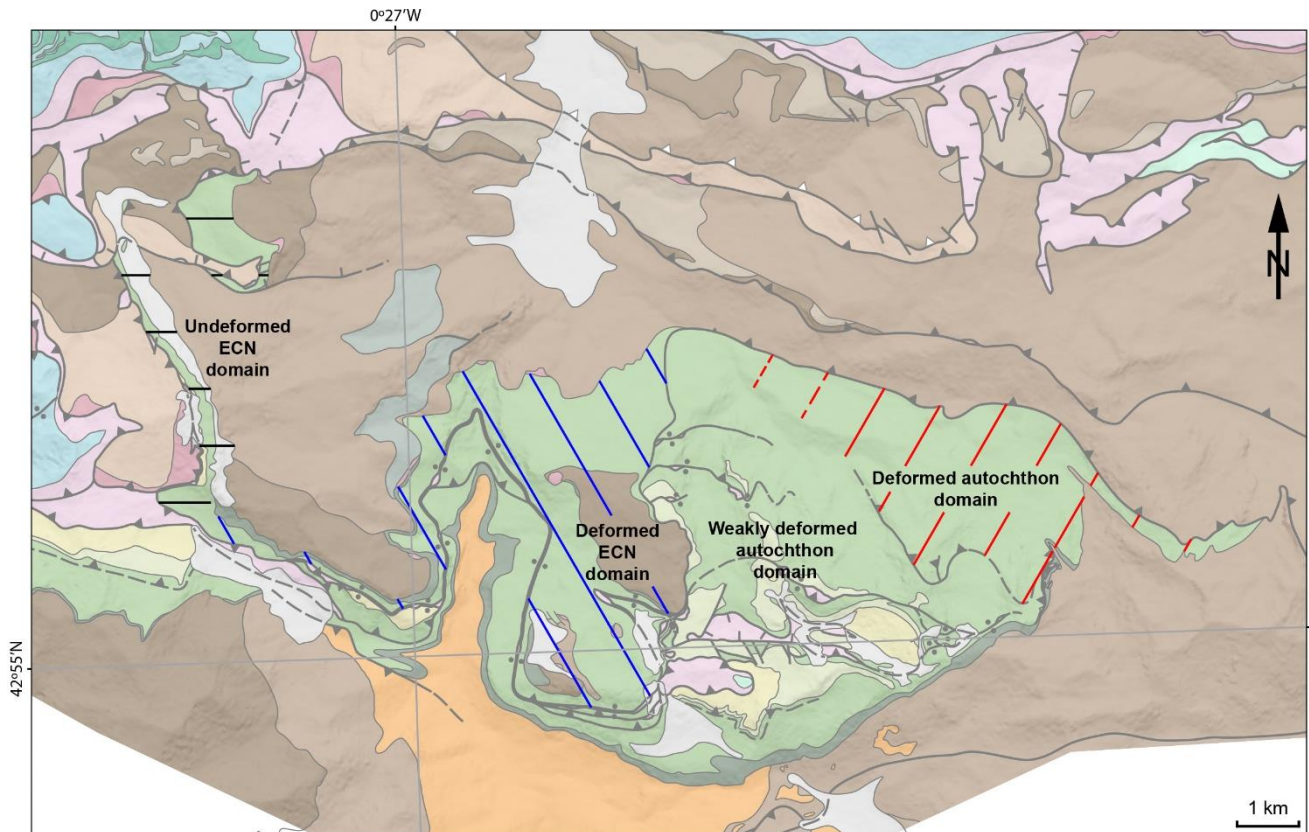


**Fig. 6.2.** Strain domains proposed for the ECM. Note that strain domains do not coincide exactly with the boundaries of macrostructures.

### 6.1.2. Field structural data in relation to the strain domains

The main orientation of foliation and lineation are displayed in Fig. 6.3 according to the four domains. The general trend of dip of the main foliation is to the north, with moderate dip values. In some domains, especially the overturned limb and in the weakly deformed autochthon domain, some anomalous orientations have been detected (right projections in each pair of circles) where the irregular distribution of the foliation is more evident. As a result, verticalization and a deviation to the N-S trend of the strike in cleavage are commonly developed. On the other hand, in the deformed autochthon domain the cleavage dips moderately to the north-west, apart from some exotic values. Lineation data (mainly stretching lineation) is restricted to the overturned and deformed autochthon domains due to their higher strain, and there also exist some irregular distributions in each area (right plots). Concerning the deformed ECN domain, lineation is commonly inclined to the north with a very

gently plunge. Anomalous orientations to the north or south-west or sub-horizontal are also observed. On the contrary, the deformed autochthon domain is characterized by a common orientation of the lineation to the north-east with a gently to moderate plunge. As in the overturned limb, the irregularities are inclined to the north-west. The dip of both cleavage and plunge of lineation is discussed below.

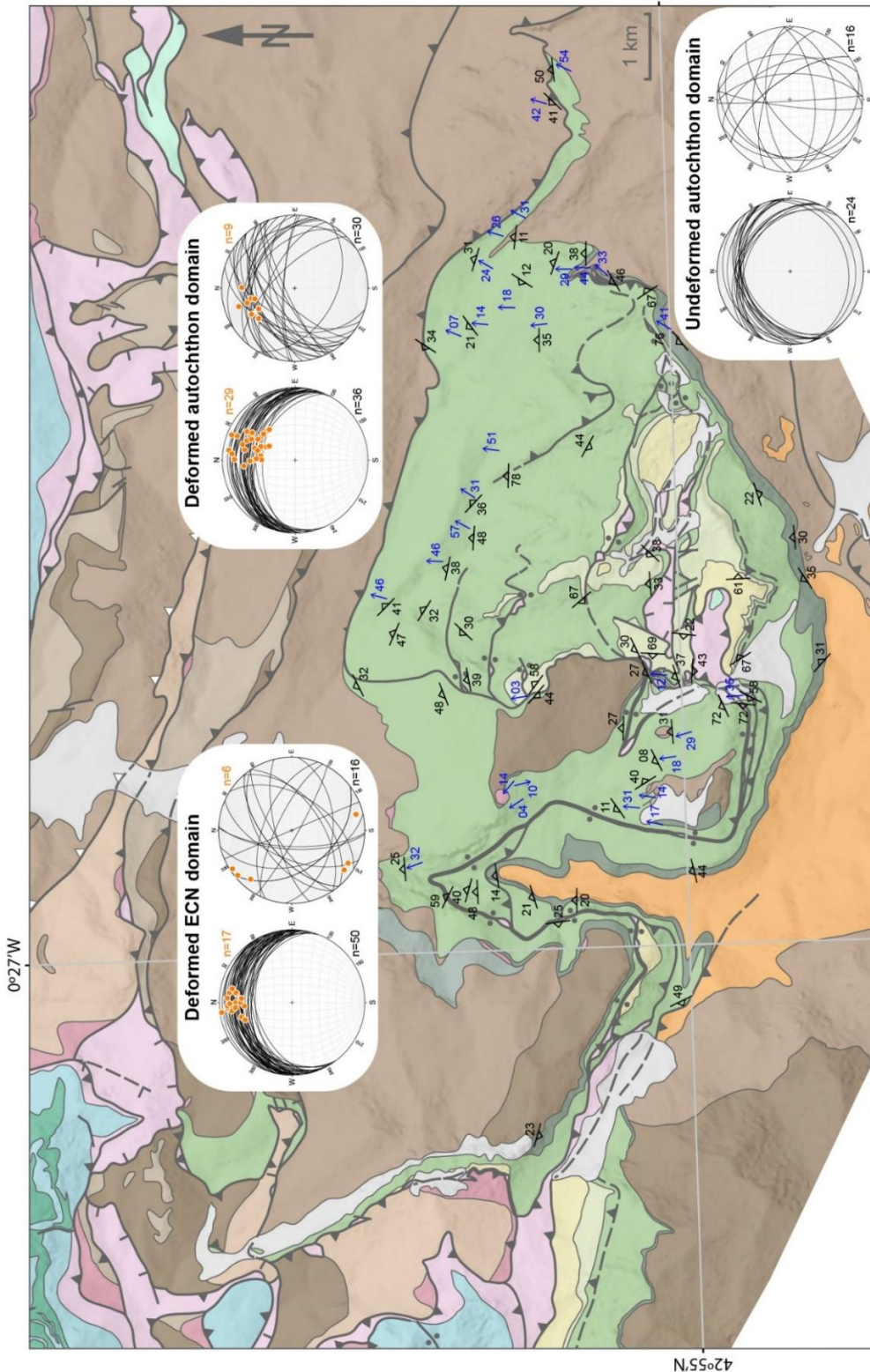


**Fig. 6.3.** Geological map of the ECM showing a summary of foliation and lineation data in upper Cretaceous rocks. Projections of cleavage (black) and lineation (blue) data are grouped by deformation domains and from where they have been acquired. Right projections correspond to the irregular orientations of both cleavage and lineation (if there exist). Note the variations in orientation of the structural data, especially in the overturned limb of the ECN and in the easternmost sector.



## 6.2. Microstructures from petrographic microscopy

Petrographic observations have been valuable for the initial identification of the main mineral phase content, such as calcite, dolomite, and quartz in the upper Cretaceous limestones, as well as for the microstructural features. Dolomite grains are extensively observed along the ECM, identifying zones with intense and poorly developed and/or dispersed in the matrix. Sometimes conform parallel bands intercalated between calcite-rich layers or as dolomite asymmetrical rods and large-boudinaged bodies. Quartz-rich layers are observed in the upper Santonian and correspond to chert nodules (cf. chapter 2) and poorly constrained and heterogeneously distributed stratabound silicifications. They are mainly located along the Plateau d'Anouilhas. The rest of the upper Cretaceous stratigraphy contains small, detrital grains of quartz dispersed in the calcite matrix.

In thin section, ductile deformation is identified mainly by the calcite grains and their textural variations surrounding second phases or fossil fragments. In the hinge of the ECFN, the deformation was moderately intense, but not so strong as to completely transpose and recrystallize the whole rock. In that case, fossils are still preserved, sometimes strongly stretched (Fig. 6.4a) but usually only affected by solution-seams. Along the massif, calcite pressure shadows are well-developed around large crystals of other stronger mineral phases, such as quartz, dolomite, or even fossils (Fig. 6.4b, c). In general calcite grain size is fine and does not display twins, but is possible to observe type III-IV calcite twins (Ferrill et al., 2004) in larger grains (Fig. 6.4d, e). Small-scale folds and multiple twins are not uniquely developed in the dolomite grains but also in the calcite veins or in layers of coarser host grains. As explained later, they are also detected by EBSD maps (Fig. 6.4f). Quartz and phyllosilicate-rich layers (e.g. Bundsandstein and Cretaceous clastic limestones) are characterized by brittle-to-ductile behaviour discussed later in this chapter.

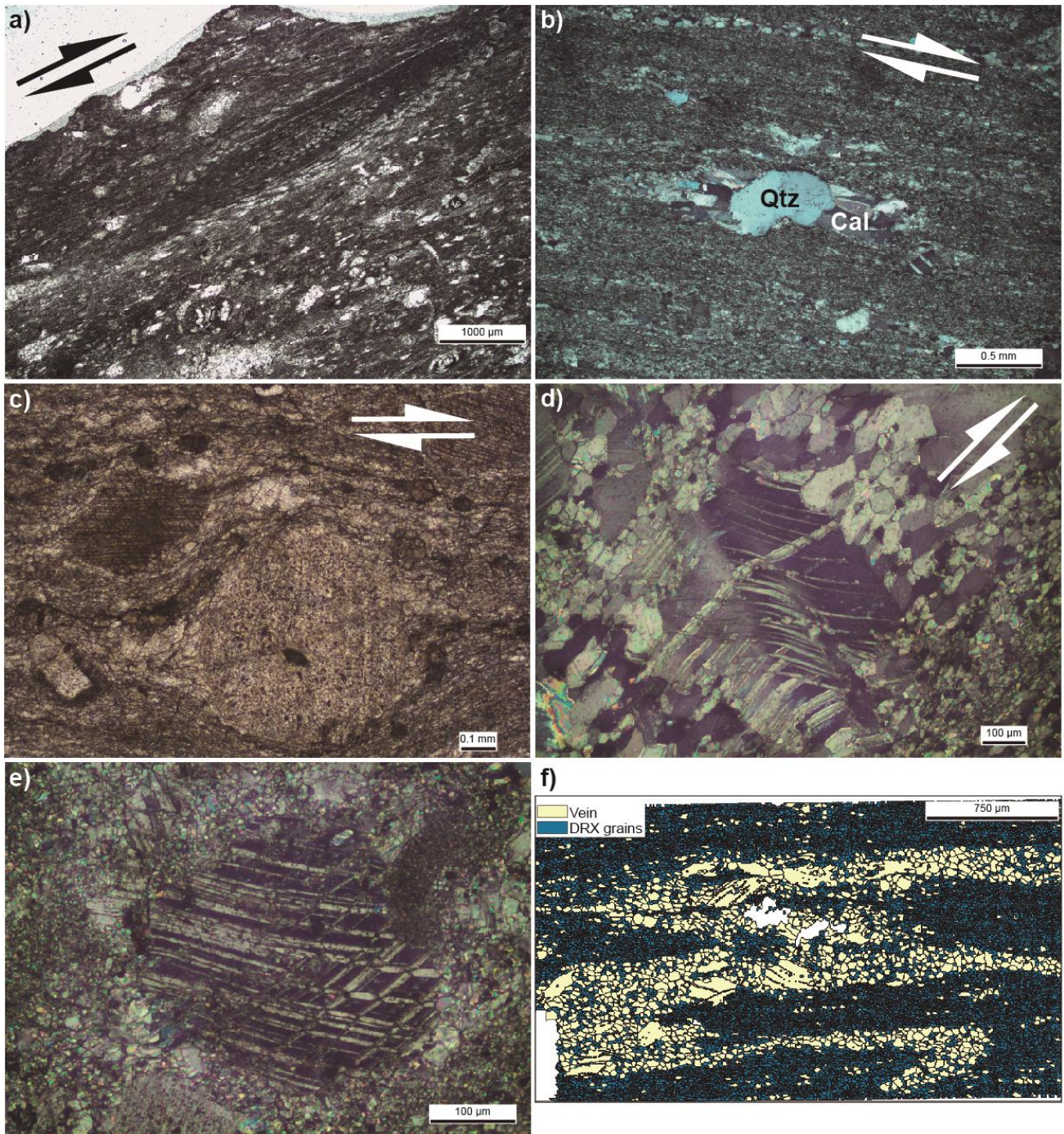


**Fig. 6.4.** Microstructures from petrographic observations. a) Strongly stretched foraminifera in the hinge zone of the ECFN (cf. Fig. 4.2). b) Shadow tails by elongated calcite crystals on both sides of quartz grains displaying weak undulose extinction from late back-thrusts (cf. S2 from previous chapter). c) Large calcite, probably fossils fragments, with asymmetric tails and mylonitic foliation around them. Sample taken at Eaux-Bonnes village (hinge of the ECFN syncline), d, e) III-IV type calcite twins attesting for relatively high temperature deformation in the autochthon of the eastern sector. Note the deformation affecting the twins indicates dextral sense of shear respect to layering. f) EBSD map of large host calcite grain aggregates conforming calcite folded veins in the hinge zone of Pic de Cézy (cf. Fig. 4.2). Small calcite matrix grains oriented according to the main foliation.

*Small grains are attributed to recrystallized grains, while large relict grains to be inherited from coarse calcite veins. Coarser grains contain deformation twins.*

### 6.3. EBSD analysis

Attending large- to meso-scale field observations, a total number of 23 samples were strategically selected from the different strain domains of the Eaux-Chaudes massif. Samples were taken as close as possible to the structural cross-sections (Fig. 6.5) with the goal to constrain the fold nappe geometry, characterizing high strain regions and the transition between the fold nappe and the thrust nappe (i.e. the Gourzy transfer zone). Critical areas correspond to the limit between the overturned limb and the autochthonous, the normal limb, the weakly deformed western autochthon, and the deformed autochthon from the eastern sector (Fig. 6.5). In some places, the boundary between normal and overturned limbs in the welded syncline is not always evident by the occurrence of upper Cretaceous limestone superpositions and the absence of upper Triassic facies, challenging the stratigraphic polarity recognition. In that case, deformation intensity may be helpful considering the localization of the strong deformation in the overturned limb.

The selected samples cover the whole spectrum of the massif, from strongly deformed up to almost undeformed Cretaceous limestones. The easternmost sample (19NC22 in Fig. 6.5) corresponds to Paleozoic metacarbonates of the hanging-wall of the Eaux-Bonnes thrust (Figs. 6.5, 6.6). High ductile deformation is identified at large scale by large boudinaged quartzitic layers, embedded in thicker limestone panels (Fig. 6.6), and resembling the ductile structures observed in the Cretaceous carbonate mylonites from the ECM.



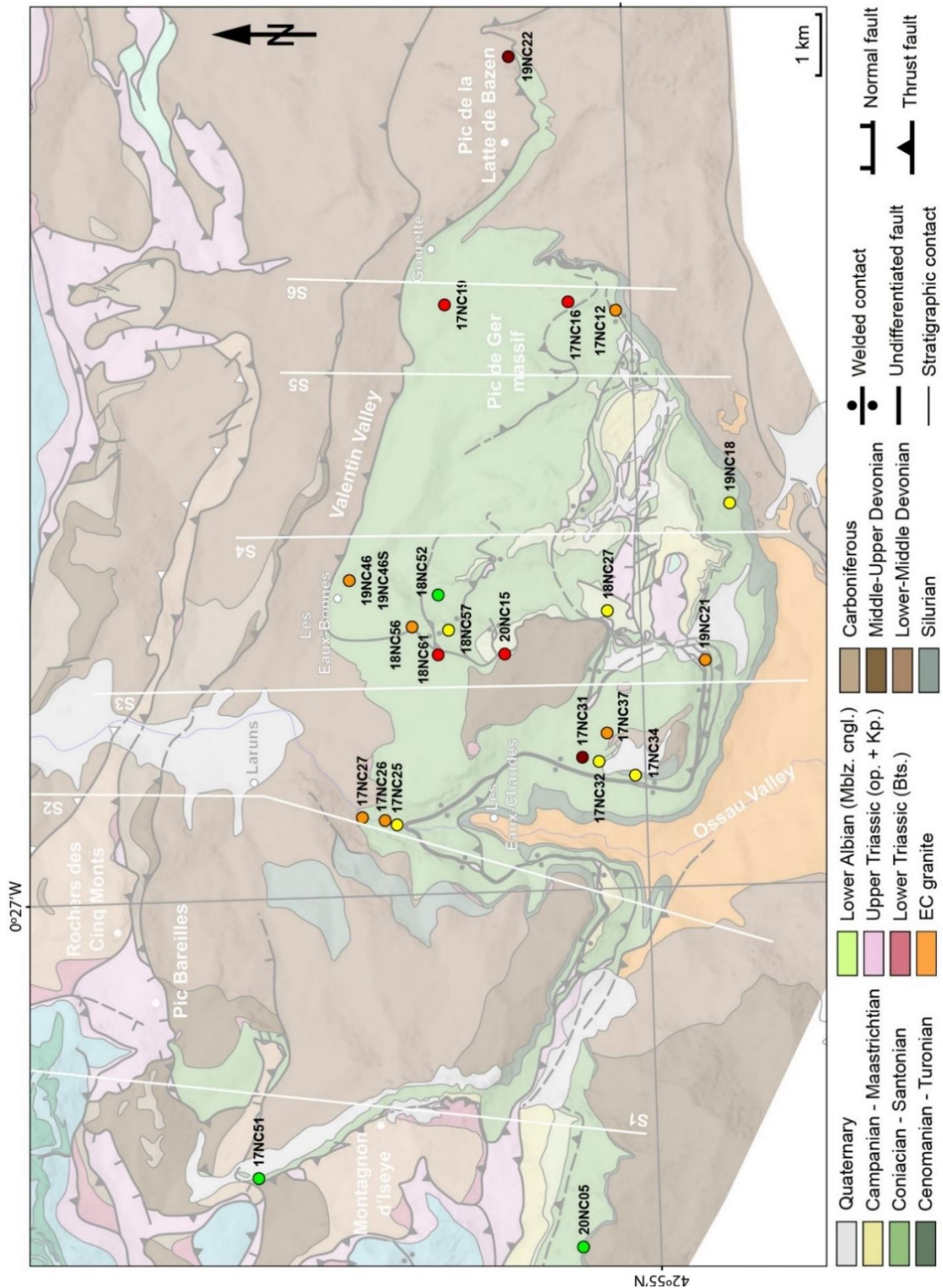


**Fig. 6.5.** Location of samples analysed by EBSD in the Eaux-Chaudes massif. Colour code corresponds to the fabric strength (according to the intensity of *c*-axis in the pole figures, expressed by multiple of uniform distribution (*m.u.d.*); cf. Table 1 for quantitative values): green to dark red colours indicate transition from low to high fabric strengths.



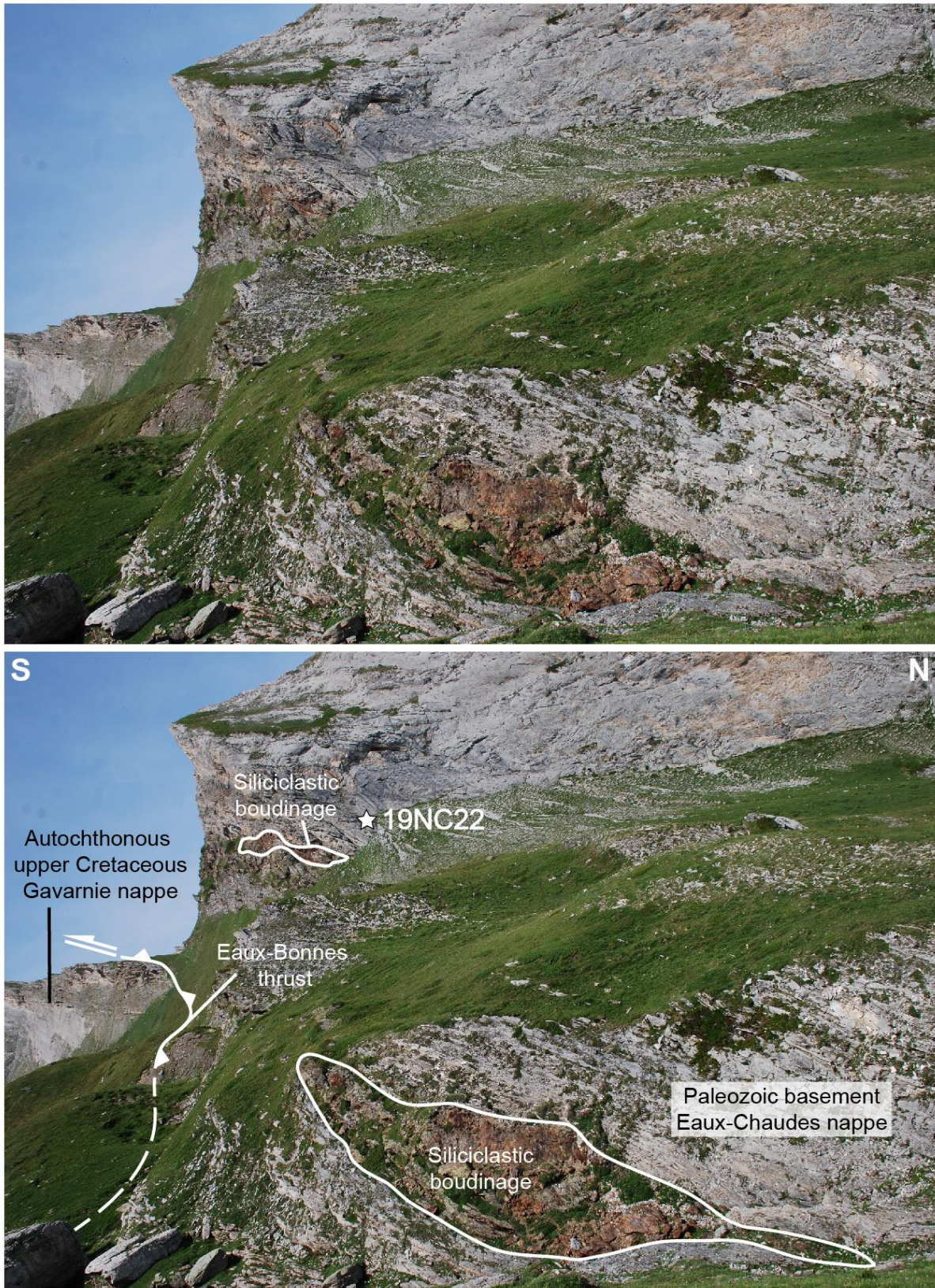


**Fig. 6.6.** Large-scale ductile deformation identified by siliciclastic boudins in the Paleozoic rocks from the hanging-wall of the ECN, in the eastern sector of the ECM (East of Pic de la Latte de Bazen, cf. Fig. 6.5). The Paleozoic basement overrides the upper Cretaceous autochthon, which is also strongly deformed and stretched, especially near the contact.



### 6.3.1. Textural analysis of the upper Cretaceous carbonates

#### Phase content

From the phase composition of the analysed samples (Table 6.1), four types of limestones are considered for the microfabric study attending the relative phase contents (Fig. 6.7): 1) pure calcite limestones; 2) calcite + dolomite limestones; 3) calcite + quartz limestones and 4) calcite + dolomite + quartz limestones. Almost all samples show white spikes in the phase maps corresponding to non-indexed mineral phases, voids or scratches produced during the polishing process.

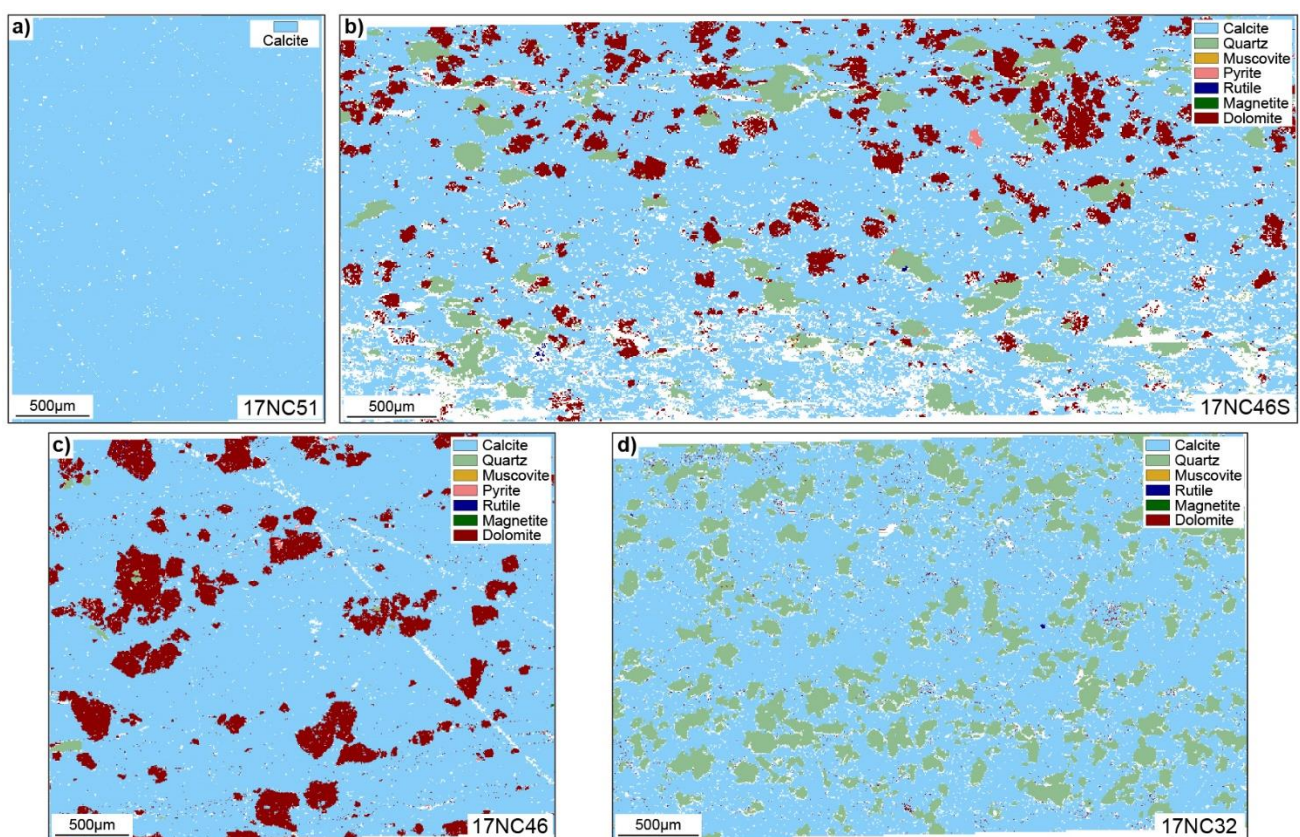


**Fig. 6.7.** Phase map of the four types of limestone considered for the EBSD analysis: a) pure calcite limestone; b) calcite + dolomite + quartz limestone; c) calcite + dolomite limestone; d) calcite + quartz limestone.

Samples with large amount of dolomite (almost completely dolomitized) have not been considered for the microstructural analysis but for a cathodoluminescence study and described in the following chapter. Deformation and/or metamorphic histories of rocks can be interpreted using microstructure observation from mono- and poly-mineralic rocks (e.g. Ramsay, 1967; Means, 1976; Fischer &

Woodward, 1992; Vernon, 2004). An especially important parameter is grain size analysis, considered to be key to infer deformation mechanisms and flow stresses during the deformation of rocks (e.g. Twiss, 1977; Frost & Ashby, 1982; Walker et al., 1990; de Bresser et al., 2001; Freund et al., 2001; ter Heege et al., 2002; Austin & Evans, 2007, 2009; Platt & Behr, 2011). Other interesting parameters to interpret the kinematic of the deformation are fabric strength, obtained from the crystallographic preferred orientation (CPO) and quantified using the J-index, or shape preferred orientation of grains.

TABLE 6.1. RESULTS OF EBSD

Sample	Latitude N	Longitude W	Step size (µm)	Max m.u.d.		DRX grains (µm)	J-index (DRX)	% of 2 <sup>nd</sup> phases			
				IPF	PF			Cal	Dol	Qtz	NI
17NC12	42° 55' 54.23"	0° 20' 32.03"	1.25	1.50	2.07	6.77	1.23	78	2	-	19
17NC16	42° 56' 20.21"	0° 20' 19.94"	5	1.43	2.51	-	1.20	70	-	2	28
			5	1.46	-	24.24	1.18				
			2.5	-	-	14.28	1.06	67	-	3	31
17NC19	42° 57' 23.85"	0° 20' 17.61"	6	1.52	2.85	34.34	1.39	86	-	-	14
17NC25	42° 57' 55.72"	0° 26' 23.24"	9	1.16	1.89	28.6	1.09	71	25	-	1
17NC26	42° 58' 3.27"	0° 26' 20.03"	7	1.41	2.22	-	1.19	88	3	-	8
			1	-	-	13.47	-				
17NC27	42° 58' 14.39"	0° 26' 17.28"	7.5	1.37	2.86	31.5	1.44	96	2	-	-
				1.24	2.17	29.49	1.18				
17NC27-ROI			-	-	-	26.31	-	74	20	-	-
17NC31	42° 56' 20.27"	0° 25' 39.44"	3	1.56	3.37	15.49	1.51	91	2	-	7
17NC32	42° 56' 11.86"	0° 25' 42.68"	4.5	1.36	1.83	17.18	1.07	67	-	20	12
17NC34	42° 55' 52.68"	0° 25' 52.96"	6-7	1.20	1.61	22.27	1.05	94	-	-	6
17NC37	42° 56' 7.22"	0° 25' 22.92"	6	1.37	2.45	-	1.23	84	14	-	2
			5	1.33	2.12	-	1.14	68	28	-	4
17NC37 HR			1	-	-	12.44	-	-	-	-	-
17NC37 ROI			5	-	-	19.09	-	-	-	-	-
17NC51	42° 59' 13.80"	0° 30' 27.30"	8.5	1.07	1.26	25.32	1.01	95	-	-	5
18NC27	42° 56' 4.57"	0° 23' 58.13"	7.5	1.27	1.90	45.76	1.06	18	4	55	23
18NC52	42° 57' 32.77"	0° 23' 41.92"	6	1.15	1.57	-	1.01	66	2	19	13

			3.6	-	-	18.51	-	66	4	18	13
18NC56	42° 57' 45.72''	0° 24' 3.95''	4.5	1.17	2.17	-	1.14	79	-	2	19
			2.7	-	-	23.75	-	80	-	8	12
18NC57	42° 57' 27.49''	0° 24' 7.41''	3.5	1.22	1.80	16.31	1.07	95	-	-	5
18NC61	42° 57' 32.99''	0° 24' 23.59''	5	1.71	2.82	36.78	1.35	78	-	2	20
19NC18	42° 55' 0.56''	0° 22' 44.12''	4	1.30	1.76	21.34	1.07	79	4	-	17
19NC21	42° 55' 15.17''	0° 24' 32.57''	3.5	1.28	2.31	12.76	1.18	92	-	1	7
19NC22	42° 56' 46.86''	0° 17' 26.26''	3	1.56	3.18	15.56	1.43	87	3	2	8
19NC46	42° 58' 17.75''	0° 23' 27.24''	5	1.26	1.81	18.94	1.07	78	15	-	5
19NC46S	42° 58' 17.75''	0° 23' 27.24''	6	1.25	2.06	25.17	1.12	64	11	7	18
20NC05	42° 56' 28.14''	0° 31' 23.13''	2.5	1.11	1.37	11.48	1.01	92	-	-	7
20NC15	42° 56' 59.29''	0° 24' 24.59''	3	1.88	3.06	25.76	1.47	88	-	-	12

**Table 6.1.** EBSD results of the 23 samples analysed with fabric strength values of *m.u.d* (maximum intensity of the contoured pole figures from crystallographic preferred orientations) and *J-index* (a measure of fabric strength obtained from the inverse pole figure of one point per analysed grain), and % of second mineral phases and non-indexed (NI) minerals or fractures. Step size confers to the resolution of area analysed, lower values indicate higher resolution and smaller areas and vice versa. *Cal*: calcite; *Dol*: dolomite; *Qtz*: quartz; *DRX*: recrystallized

## Grain size

In general, samples show homogeneous to highly heterogeneous grain size distributions (e.g. Table 6.1). Relict and recrystallized grains were differentiated using the average misorientation angle and the presence of subgrains and twins. In general, grains with a high content of subgrain structures, twins or large grains, with sizes 10 to 15 times higher than the average grain size, were interpreted as relicts. Recrystallized calcite grains show a varied range of grain size from 6.77 to 45.76  $\mu\text{m}$ , with a mean value of 21.3  $\mu\text{m}$  and a standard deviation of 9  $\mu\text{m}$ . The smallest grain size (6.77  $\mu\text{m}$ ) is observed from the deformed autochthon domain and the highest one (45.76  $\mu\text{m}$ ) from the weakly deformed autochthon domain. If we look in detail at the size distribution for each domain, those results arise: the deformed ECN domain shows a range of 12-26  $\mu\text{m}$  with an average of  $\sim 18 \mu\text{m}$ . The weakly

deformed autochthon is in the range of 11-22  $\mu\text{m}$  with an average of  $\sim 16 \mu\text{m}$ . The deformed autochthon shows a range of 6-25  $\mu\text{m}$  with an average of 15  $\mu\text{m}$ .

The original grain size for the Cretaceous carbonates before deformation is usually unknown from the lack of relict crystals and the intense processes of recrystallization. In comparison with surrounding regions not affected by alpine deformation, we can assume heterogeneous grain size, from micritic to fine limestones with a relative important content of fossils or second mineral phases (cf. chapter 2).

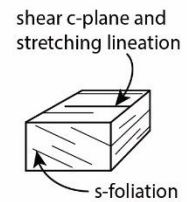
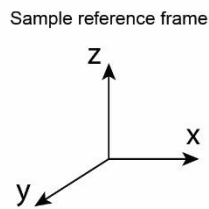
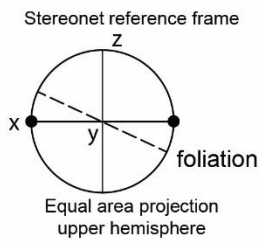
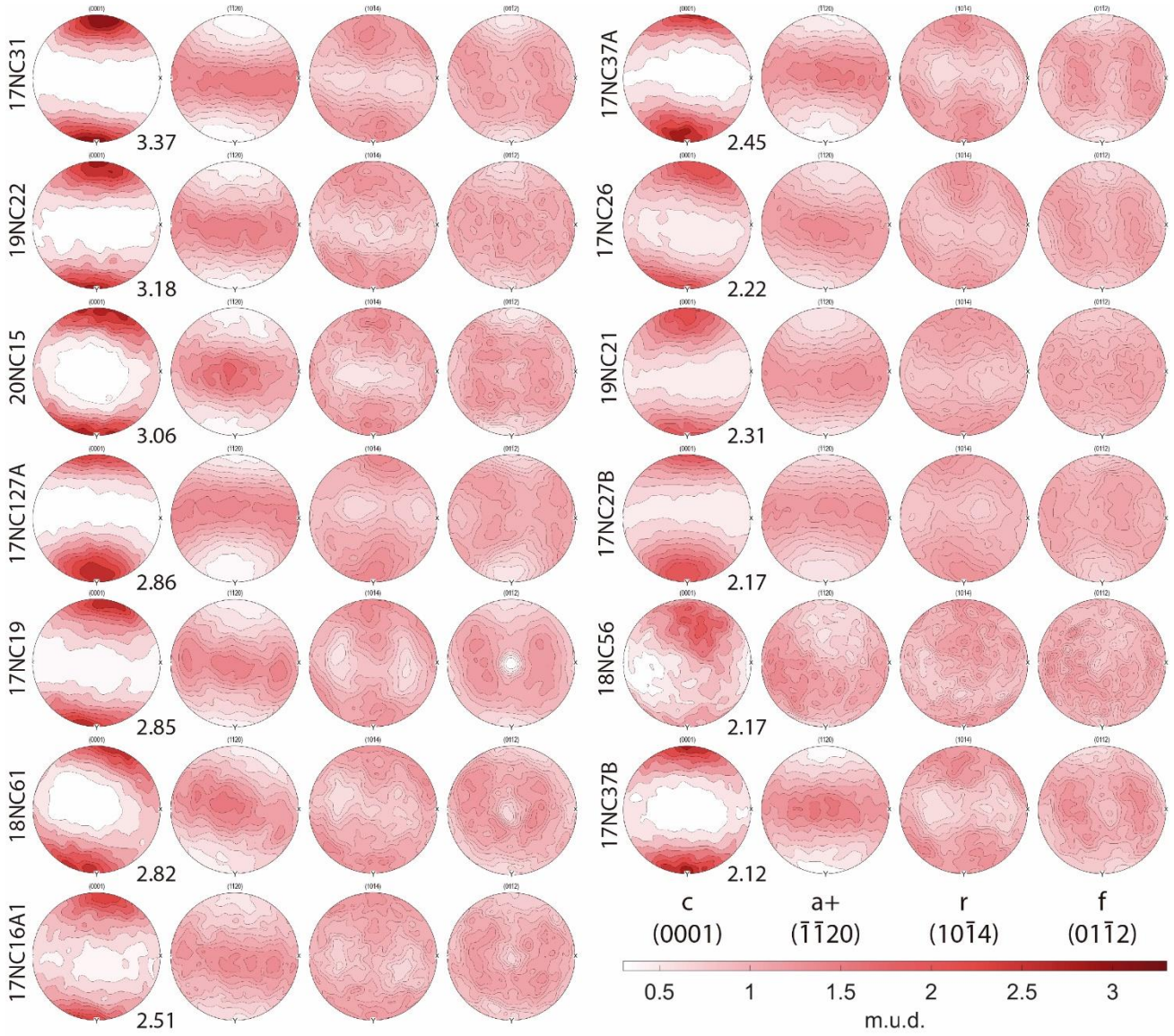
### *Fabric strength*

The intensity of fabric strength was calculated using two different approaches. In the first one, the fabric strength was estimated using the maximum value observed in the pole figures (PF) of calcite c-axes distribution. Pole figure is a stereographic projection in sample reference system of the frequency and orientation of a particular crystal axis. Normally the frequency is represented in multiples of uniform distribution (m.u.d.). The second approach is based on the J-index (e.g. Skemer et al., 2005), a parameter used to estimate the second moment of an orientation distribution function (ODF) and extendedly applied in the material science literature (e.g. Mainprice & Silver, 1993; Ismail & Mainprice, 1998). The J-index is obtained from the inverse pole figure (IPF), a “stereographic” projection relative to the crystal reference system, and very sensitive to smoothing correction and the number of measured grains (Matthies & Wagner, 1996; Wenk, 2002). We used one point per grain for the analysis and all the detected grains (avoiding segmentation at the limits of the sample). Data in PF are displayed in equal-area projections also using one point per grain (Fig. 6.8)

The CPOs of the recrystallized matrix of the Eaux-Chaudes samples (from PF results; Fig, 6.8) are characterized by a single c-axis maximum normal to the main foliation plane and parallel to the maximum shortening Z-axes (axis normal to the foliation plane in the sample; Fig. 6.8). CPO intensity range from 1.26 to 3.37 m.u.d. (Table 6.1). The a- and m-axes are widely distributed along the foliation defining a girdle parallel to the deformation XY plane (i.e. foliation plane; Fig. 6.8).

The stronger fabrics were obtained from the deformed ECN and deformed autochthon domains, especially the Paleozoic sample from the hanging-wall of the Eaux-Bonnes thrust (cf. chapter 4 structural setting), while the weakest fabric from the undeformed ECN domain (normal limb of the ECFN). There are some samples (i.e. 17NC12, 18NC27, 18NC57) showing a disturbed orientation of c-axes with respect to the general trend (Fig. 6.8), the significance of which will be discussed further in this chapter. The J-index also shows a certain range of distribution from 1.01 to 1.51 (Table 6.1, Fig. 6.10) but, in general, much weaker than the c-axes distribution intensity in pole figures. In both cases, values close to 1 indicate random fabric, while elevated values account for preferential orientations and higher fabric strength. The correlation between them is quite well-adjusted by polynomial and linear relation (Fig, 6.9).







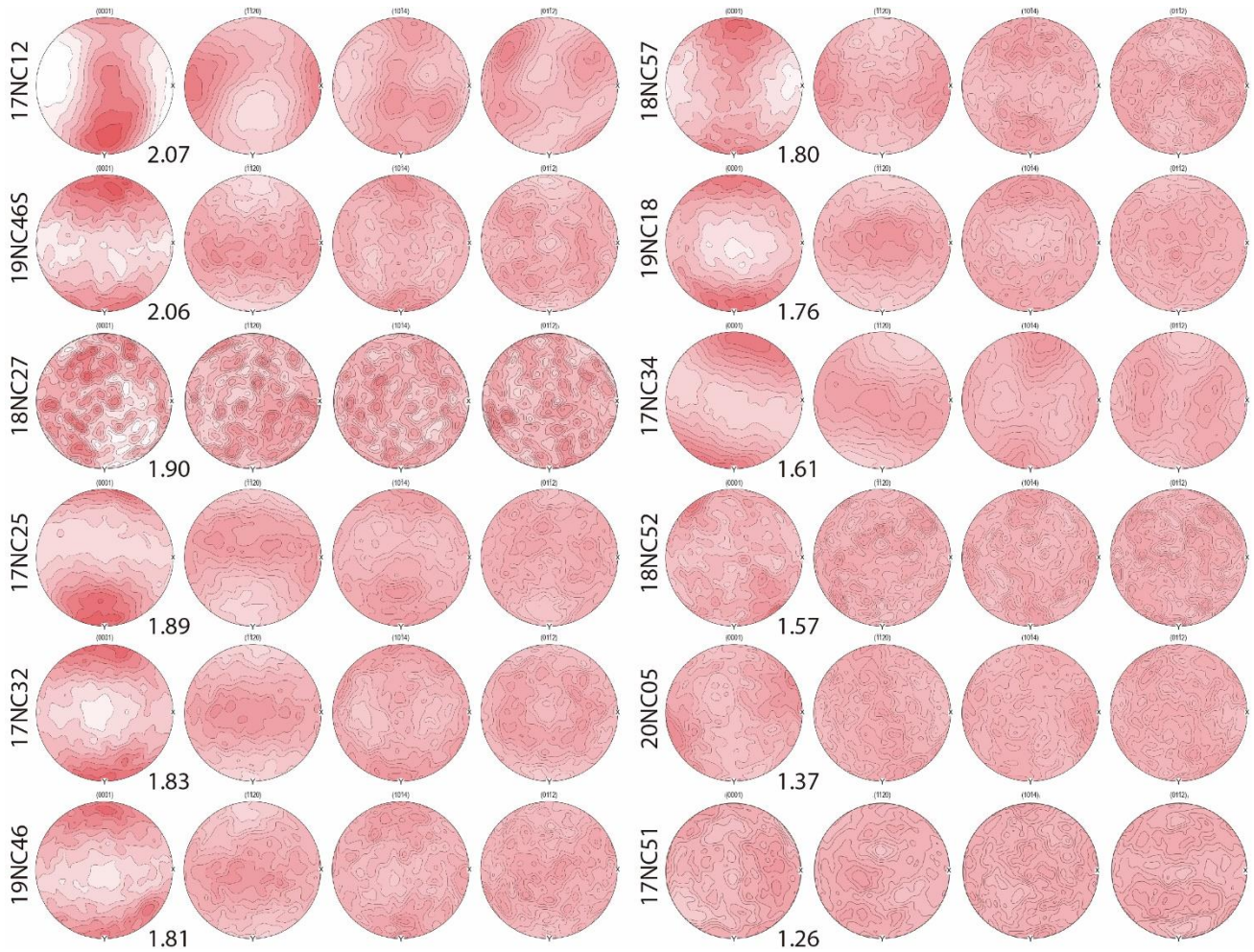


**Fig. 6.8.** Plots of the crystal-preferred orientations (CPO) for calcite c-axis [0001], a-axes {1120}, r-vector {1014} and f-vector {0112}. Pole figures of all samples are displayed from the strongest to the weakest deformed one. Values shown in between the first and second pole figure correspond to the c-axis m.u.d., which is indicative of the fabric strength. Sample reference frame is indicated respect to the deformation XYZ axes.

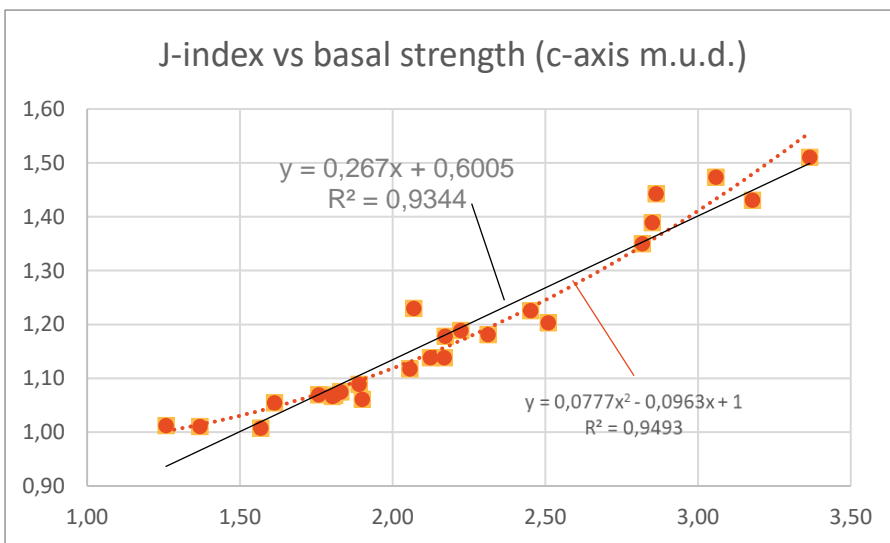


**Fig. 6.9.** Linear and polynomial relation of J-index and basal strength (c-axis m.u.d. in pole figures) from the analysed samples.

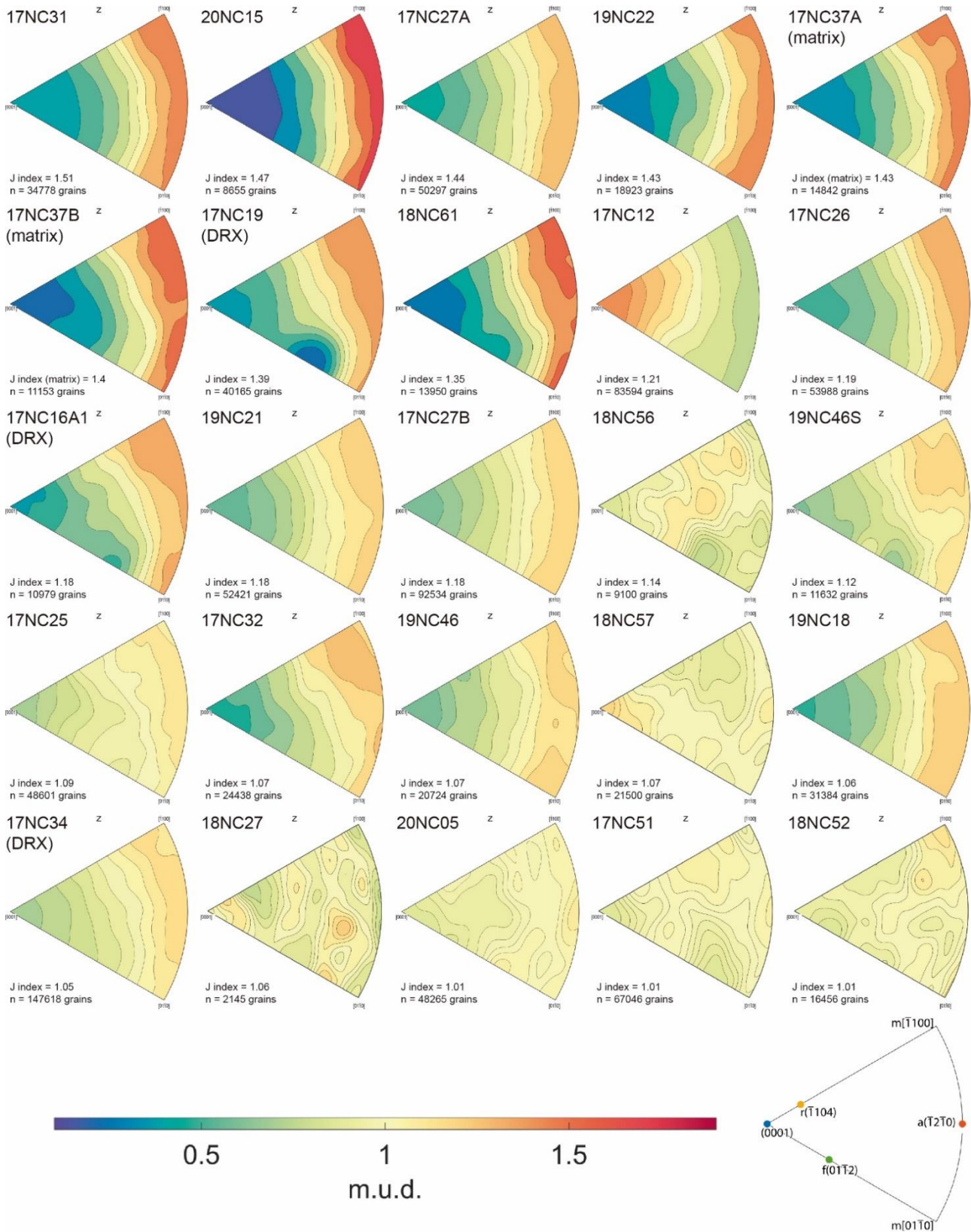


**Fig. 6.10.** Inverse pole figures of all samples analysed and ordered from the strongest deformed to the weakest deformed one. Values of J-index are also indicative of the fabric strength. In general, the maximum intensity is oriented parallel to a-axis and slightly tilted to m-slip direction indicating a dominant slip direction parallel to a- and m-axes.

Misorientations between or inside the calcite grains are represented by the rotation angle required to turn one orientation into another (e.g. Wheeler et al., 2001). The bulk results are usually plotted by the distribution of the misorientation angle and compared with the expected for a theoretical sample with random misorientation distribution (Fig. 6.11). From some samples more than one histogram has been obtained due to the acquisition from different regions of interest. Most of the samples fit the measured distribution with the theoretical random distribution, especially for samples from low deformation regions. Otherwise, the most intense deformed samples tend to show a bell-like geometry with a maximum peak of distribution located at  $60^\circ$  (e.g. first row of Fig. 6.11). With the increase of the CPO, the misorientation distribution differs from the theoretical random curve. In almost all the samples, this curve is much higher than the analysed for the range of 60 to  $90^\circ$  misorientation angles. Anomalous distribution for angles near twin orientations are in general not observed (e.g.  $60^\circ$  for {11-22} twin planes or  $80^\circ$  for {10-12} twins). On the other hand, it is lower in the range below  $60^\circ$ . It is worth mentioning that misorientation distribution of a sample from very low deformed domains (20NC05) fits particularly well with the theoretical random distribution. The Paleozoic sample (19NC22), strongly stretched, shows a bell geometry with a distinctive peak at  $80^\circ$  corresponding to the {10-12} calcite twins, developed in large host grains and not removed in the preliminary treatment to its analysis. The histogram from sample 18NC27 is not plotted due to the low representativeness of the calcite phase in the matrix, which is lower than 20%. The two samples with the weakest fabric obtained by the inverse pole figures, 17NC51 and 18NC52, show a higher deviation from the theoretical random curve of low angle misorientations (from 10 to 40 degrees) Similarly to this, occurs in the sample 17NC32, which has stronger fabrics.



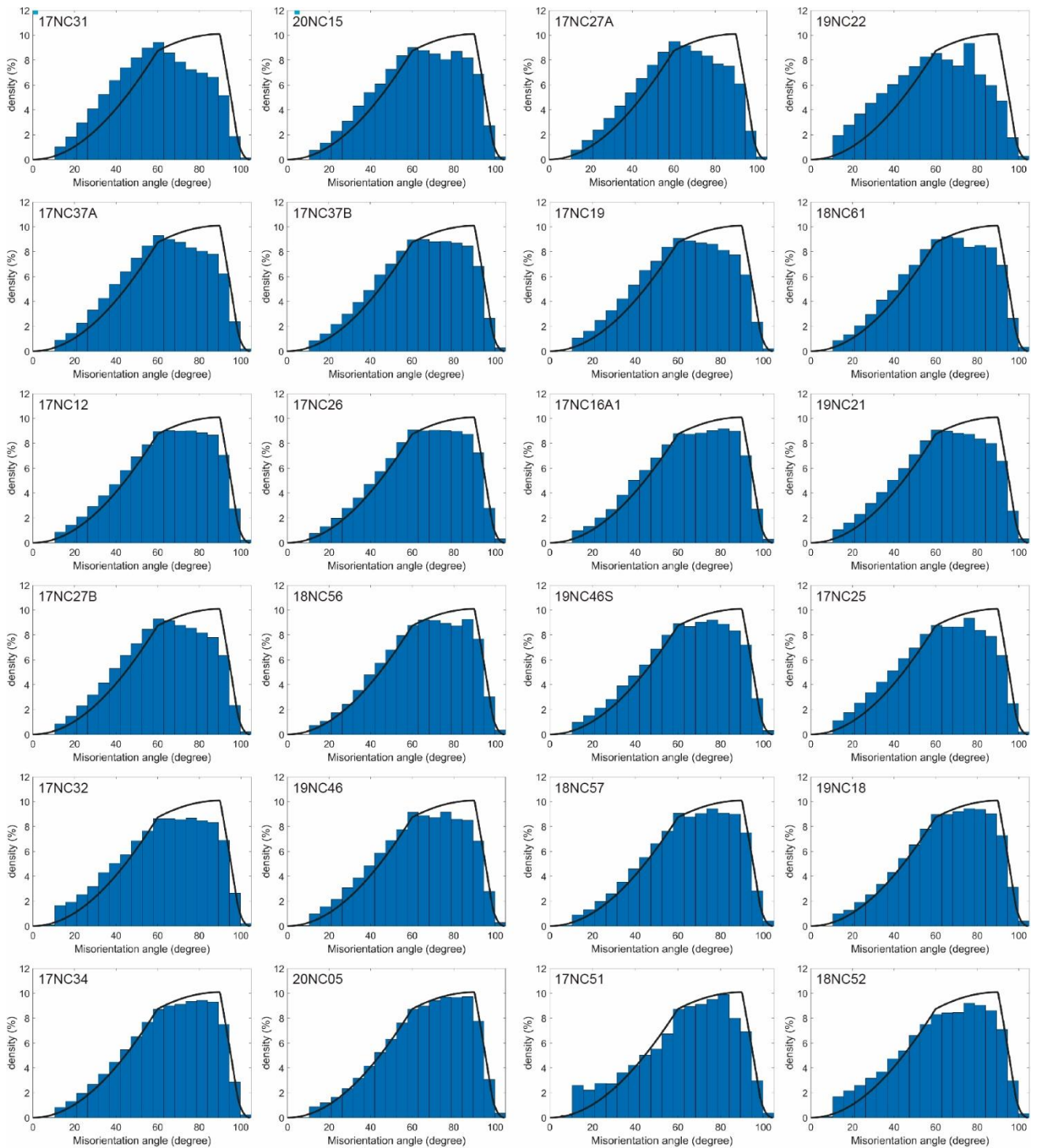


**Fig. 6.11.** Misorientation angle histograms equally ordered as in Fig. 6.8. Generally, a bell-like geometry is developed in samples with strong fabric (specifically the first row) and the random distribution is best fitted in the weakest deformed samples (i.e. 17NC34, 20NC05).



From the inverse pole figure maps of crystal orientations (IPF with respect to the z-direction), there exists a contrast in microstructure between the regions with recrystallized calcite grains (small grains, low internal misorientation) and calcite relicts or porphyroclasts from other phases, such as dolomite grains (Figs. 6.12, 6.13). Again, for calcite-rich mylonites very well-developed shape- and crystallographic-preferred orientations are observed, mainly defined by recrystallized grains and following the macroscopic foliation. On the other hand, the shape of recrystallized calcite in polymineralic samples, or those containing large relict calcite grains or veins, show weaker shape-preferred orientations and are much more isotropic. Dolomite-rich domains, such as porphyroclasts and banded layers, display a randomly or low CPO, with any clear preferred orientation. Sometimes, extensional fractures following the dolomite grain boundaries are observed, indicating extension parallel to layering coetaneous to ductile deformation (e.g. Fig. 6.13). Intragrain misorientations are rarely developed in the calcite recrystallized grains from the matrix and are only observed in some larger host calcite grains characterized by a large amount of intracrystalline heterogeneities. A good example is in sample 17NC31 with anomalous large host calcite grains, occasionally very close to 1mm of the long axis (Fig. 6.14). The recrystallized matrix displays very low intracrystalline deformation and relatively small grain size. Moreover, there are different domains of matrix recrystallization intensity, especially in polymineralic rocks (e.g. Figs. 6.12, 6.13). Triple-grain junctions are generally observed along calcite grains sometimes at  $120^\circ$ , while four-grain junctions prevail in areas faintly strained and/or with smaller grain sizes (e.g. Fig. 6.12b). Sample 20NC05 keeps a vast number of large host calcite grains with abundant twin content and a moderately developed SPO, featuring slight S-C fabrics.

Assuming dynamic equilibrium conditions, crystal plastic deformation dominates in the high strain domains evidenced by strong CPOs in the calcite matrix, which usually features small grain sizes and well-development of crystal faces. The tendency with increasing deformation to preferred orientations of c-axis normal to the foliation and a-axis and m-axis parallel to the shear direction led to suggest that deformation mainly occurred under dislocation creep by glide and climb probably dominated by slip along the  $\{1-120\}$  (0001) slip system. The moderate fabric strength of all samples and temperature

are coherent with the activation of climb dislocation. The similarity between CPO in regions with fine and large grain size, does not evidence for dominant grain-size dependent mechanisms, although diffusion creep and grain boundary sliding probably were active as a complementary deformation mechanism, (for example evidenced by four-grain junctions and very small grain sizes).

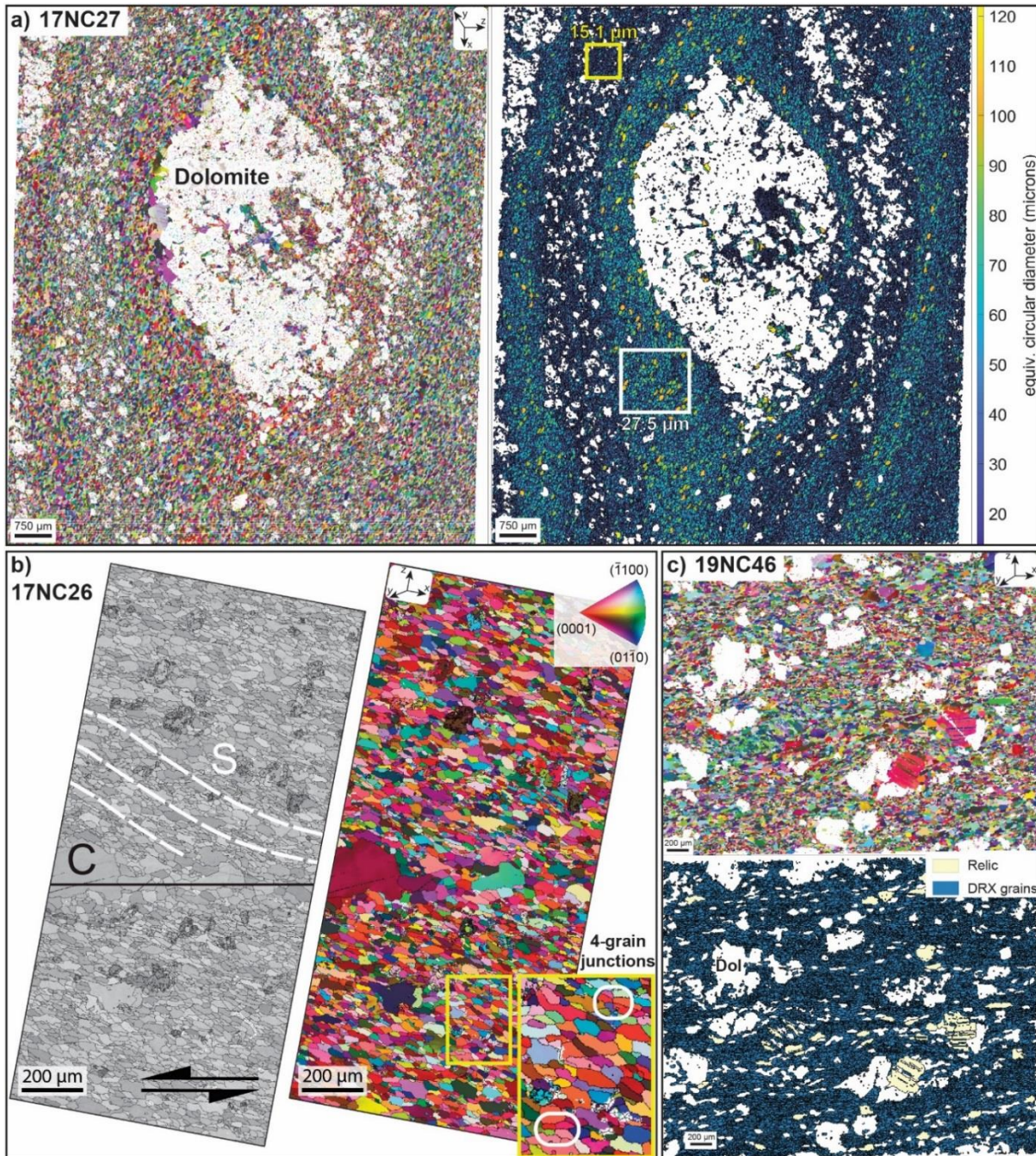


**Fig. 6.12.** a) Maps of CPO coloured using IPF respect to z-direction, as indicated in the figure, and relict/recrystallized grains map of sample 17NC27. Smaller calcite grains are located in between the aligned dispersed dolomites (yellow frame), while higher calcite grains are in between this alignment and the big porphyroclasts (white frame). b) Maps of sample 17NC26 from phase and CPO coloured using IPF respect to



*z-direction* In, as indicated in the figure. S-C fabrics is well-identified by the alignment of small calcite grains (S) and the large crystals conforming C planes. Four-grain junctions are highlighted in the detail of IPF map. c) Maps of CPO coloured using IPF respect to *z*-direction, and relict/recrystallized grains map of sample 19NC46. The effect of dolomite in deformation is more complex due to the large heterogeneity of its distribution. Large calcite relicts show twins as evidence of initial grain size reduction processes.

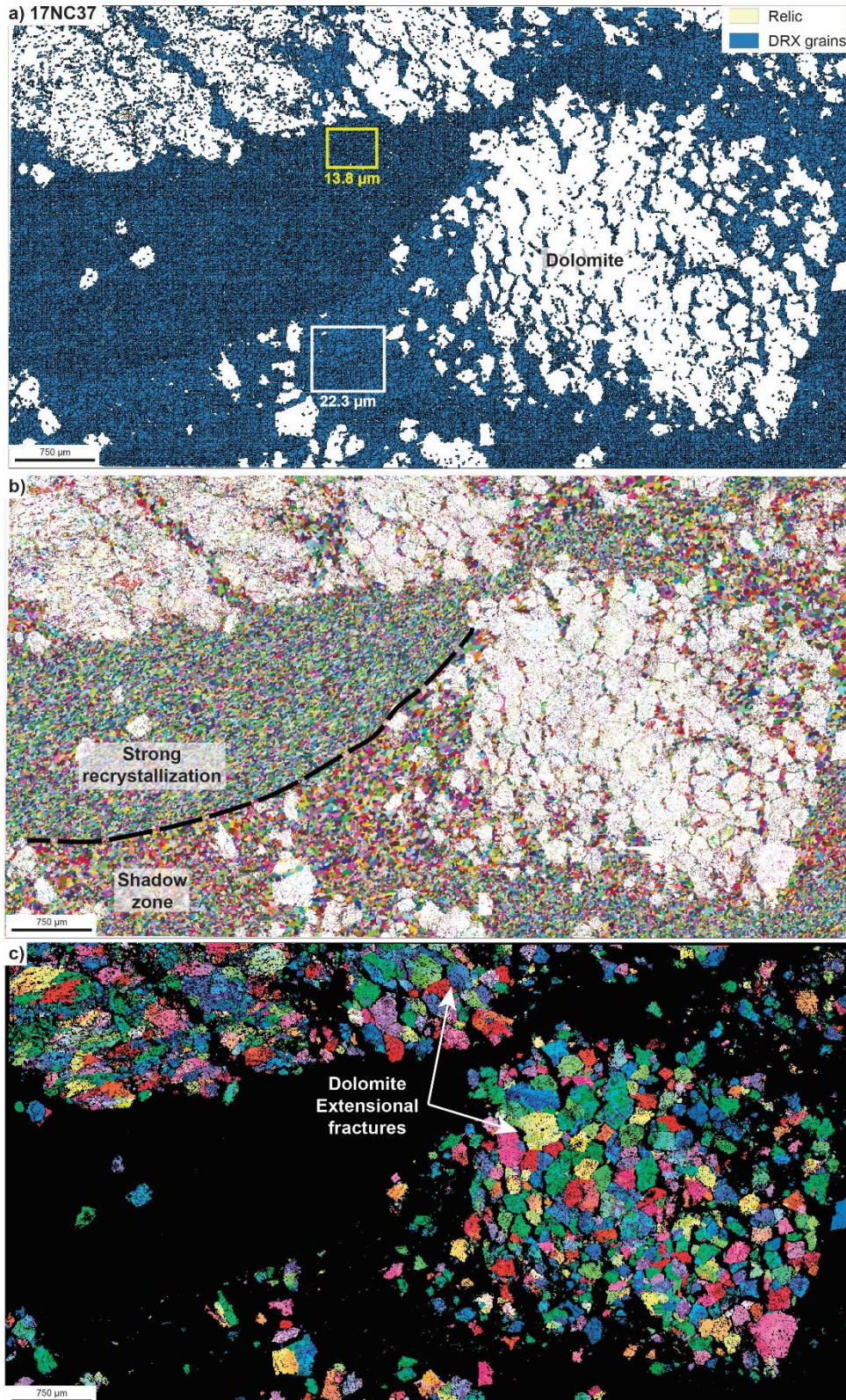




**Fig. 6.13.** a) Coloured calcite phase with grain boundaries showing different domains of grain size according to the Zener effect. Larger sizes are located in between the dolomite crystals (“shadow zone”) and smaller sizes correspond to the larger spaces in between dolomite bodies. b) IPF map with respect to z-direction of calcite. Green and blue colours are in the strongly recrystallized area while red and violet in the “shadow zone”. c) IPF with respect to z-direction of dolomite. Although this phase remains almost undeformed or very little deformed, and its orientation is poorly conditioned by deformation, extensional fractures in between grains are developed in an orientation orthogonal to the main deformation.

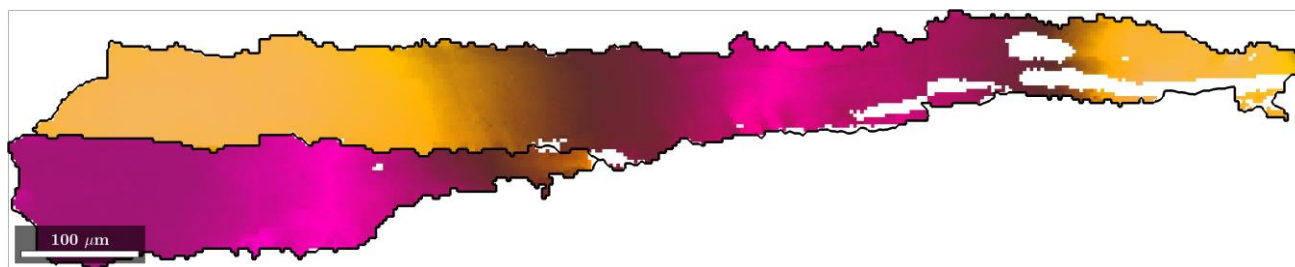


**Fig. 6.14.** Large host calcite grain from 17NC31 sample obtained from the IPF map in z-direction, with moderate fraction of intracrystalline misorientations shown in darker nuances of the different colours from the crystallographic orientation code.

### 6.3.2. Paleopiezometry and mechanisms of calcite deformation

Quantification of calcite grain size average and distribution allows for an estimate of the paleostress during deformation using different empirical and experimental piezometers (e.g. Twiss, 1977, 1986; Mercier et al., 1977; Etheridge & Wilkie, 1979, 1981; Schmid et al., 1980; Hacker et al., 1990, 1992; van der Wal et al., 1993; Rutter, 1995; Stipp & Tullis, 2003). For calcite mylonites, the assumption of a steady state of the dynamic recrystallized matrix grains seems reasonable, attending to fine grain size, absence of internal heterogeneities in grains or development of sharp grain boundaries. The grain sizes measured in the ECM are displayed in Table 6.1 and were used to calculate the differential (or flow) stresses during the Alpine deformation. Several calcite paleopiezometric relationships and deformation mechanism maps were used from the literature (Schmid et al., 1980; Rutter, 1995; Austin & Evans, 2007; among others) and the results are shown in Fig. 6.15. Considering all the different paleopiezometer and without limitations due to the dominant recrystallization process, the range of the differential stress is between 20 to ~120 MPa. Nonetheless, extensive grain boundary migration

is not observed in our samples and the grain intraheterogeneities observed in relict grains indicate subgrain recrystallization (SGR) as the dominant recrystallization process. Therefore, the Schmid et al. (1980) and Rutter (1995) piezometers based on subgrain recrystallization look the more coherent (Calcite-SGR). For this case, the range of flow stress is between 20 to 60 MPa. An additional step is to constrain the strain rate from the piezometer assuming the temperature of deformation from RSCM results. If we assume an average temperature of 350°C and the range of differential stress between 20 to 60 MPa, the range of potential strain rate is between  $10^{-12}$  and  $10^{-10}$  s<sup>-1</sup> (Fig. 6.15b, based on the deformation plot from Giuntoli et al., 2020). The range spans two orders of magnitude, but the higher strain rate seems perhaps uncoherent attending the general observation of few brittle structures coetaneous to ductile deformation.

An alternative to the piezometers is the paleowattmeter proposed by Austin & Evans (2007). In this approach, the dynamic equilibrium of grain size is proportional to the work done during the deformation and not only to the differential stresses is assumed in the approaches based on piezometers. Attending the temperature data obtained in the area using RSCM (and cc-dol geothermometer), the application of the paleowattmeter can be done in two different approaches: 1) assuming the temperature from RSCM of the samples or 2) using strictly the paleowattmeter and independent of our measured temperatures. The calcite deformation mechanism map at  $10^{-12}$  s<sup>-1</sup> for a range of temperature between 250-400°C is displayed in Fig. 15c, d. The Austin & Evans paleowattmeter and the other main piezometers are also indicated. For the first approach, with temperature from RSCM data, the range of differential stresses are between 6 to 20 MPa (Fig. 15c) and clearly ECM data are in the diffusion creep field. For the second approach the range of stresses increase between 10 and 70 MPa. For this case, the equilibrium grain-size is in the transition between dislocation and diffusion creep mechanisms, and the expected temperatures for deformation are approx. between 270°C and 350°C, average approx. 320°C.

The highest paleostress values have been acquired for the Pic de Ger fold-thrust fan (cf. Fig. 4.3 for location), due to the small grain size of the calcite matrix observed in sample 17NC12 (e.g. Table 6.1). The lowest stress value is related to the almost undeformed and silicified sample 18NC27 from the



Plateau d'Anouilhas (e.g. Table 6.1) (cf. Fig. 4.4 for location). For the last sample and some other in low deformation domains, the assumption of dynamic equilibrium of the recrystallized grain size do not seem valid, or at least questionable.

Concerning the deformation mechanisms, dislocation creep becomes dominant as is indicated from the moderate strength of microfibrils (CPOs analysis) and probably was assisted by diffusion mechanisms and grain boundary sliding (grain size dependent mechanisms) as shown in Fig. 6.15c.

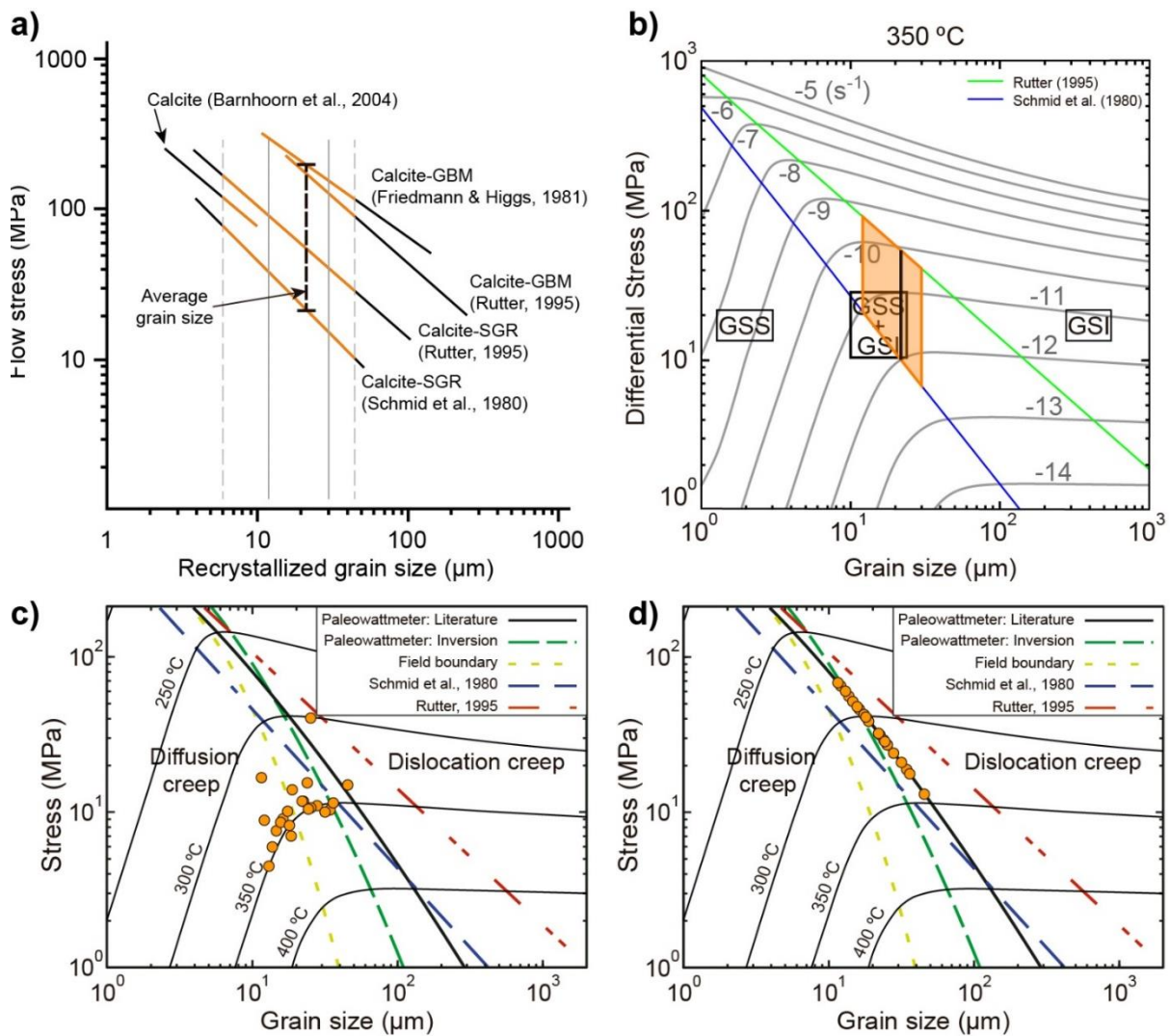


**Fig. 6.15.** a) Recrystallized grain size and differential stress relationship for calcite phase of indicated paleopiezometers in the plot. b) Deformation mechanism map for calcite at 350°C with the relationship between recrystallized grain size and differential stress (from Giuntoli et al., 2020). Two different paleopiezometers are plotted. GSS and GSI = grain size sensitive and insensitive creep, respectively. c) Deformation mechanism map (from Austin & Evans, 2007) at strain rate of  $10^{-12} \text{ s}^{-1}$  for calcite with grain size and stress relationship from paleowattmeter, empirical paleopiezometers and field boundary hypothesis of de Bresser et al. (1998, 2001). d) Data from c) projected in the paleowattmeter line (literature) indicating a range of stresses much higher.

## 6.4. Deformation of quartz in the Eaux-Chaudes massif

Up to this point, the results have been focused on the carbonate mineral phases (calcite and dolomite), which tend to be ductile (dislocation creep) in the domains with higher strains, while brittle and pressure-solution are dominant in lower strain areas. The content of detrital quartz is relatively common in certain levels. In general, quartz shows brittle to slightly ductile structures. Brittle-to-ductile transition of quartz is produced at higher temperatures ( $>400^{\circ}\text{C}$ ) (e.g. Hirth & Tullis 1992; Lloyd & Freeman 1994; Stipp et al., 2002a). General studies indicate that in low green-schist facies, brittle fracturing, undulose extinction and kink bands can be observed (e.g. Nishikawa & Takeshita, 1999). In strongly deformed grains, bulging recrystallization may also exist for these conditions (e.g. Stipp et al., 2002a).

In layers with large content of quartz, such as chert bodies from the upper Santonian in the Plateau d'Anouilhas, deformation structures resembling domino-type bookshelf by porphyroclasts embedded in a strongly stretched carbonate mylonite have been identified (Fig. 6.16a). It is necessary to point out that ductile deformation of quartz (Fig. 6.16b) is identified near the large ophite body from Pic de Breque (cf. Fig. 4.4 for location) in the weakly deformed autochthon upper Cretaceous domain (cf. Fig. 6.2). Even peak temperature reached during the Alpine orogeny in the ECM is around  $350^{\circ}\text{C}$ , and the temperature for quartz to be ductile deformed is  $400^{\circ}\text{C}$ , some chert nodules of the Santonian unit have been strongly folded and stretched in the direction of shear. Slightly folded quartz veins cross-cutting main foliation are abundant in upper Cretaceous rocks near the main unconformity between Paleozoic and Mesozoic cover (cf. chapter 5). In general, they are restricted near basement rocks and quartz veins above the intracretaceous ductile detachments were not observed. In thin section, serrated grain boundaries (e.g., Fig. 6.16) are abundantly observed. They are interpreted to be emplaced synchronously to the main ductile deformation event as they are cross-cutting foliations, but also folded and deformed.



**Fig. 6.16.** Deformation of the quartz phase in the ECM. a) Rigid bookshelf-type chert porphyroclasts embedded in carbonate mylonite attesting for antithetic rotation. b) Ductile deformation of chert nodules and quartz veins by small-scale folding. c) Undulose extinction of small quartz grains in dolomitized sample. d) Undulose extinction of quartz grains and slight bulging recrystallization. Serrated grain borders are identified.

## 6.5. Results for deformation domains from the EBSD analysis

### 6.5.1. Undeformed Eaux-Chaudes Fold Nappe domain (normal limb)

This domain is restricted to the normal limb of the ECFN. Even though it is just represented by only one analysed sample (17NC51), deformation identified by petrographic observations in the other collected samples from this domain are consistent with the EBSD microstructural features. 17NC51 shows the weakest fabric of the entire ECM. Small-scale brittle faults and almost undeformed fossils with pressure shadows and solution seams, observed with the petrographic microscope, argue for a



sparse deformation in the normal limb of the ECFN (e.g. Fig. 6.17). Calcite veins are heterogeneously distributed along the normal limb, although abundant in some samples.

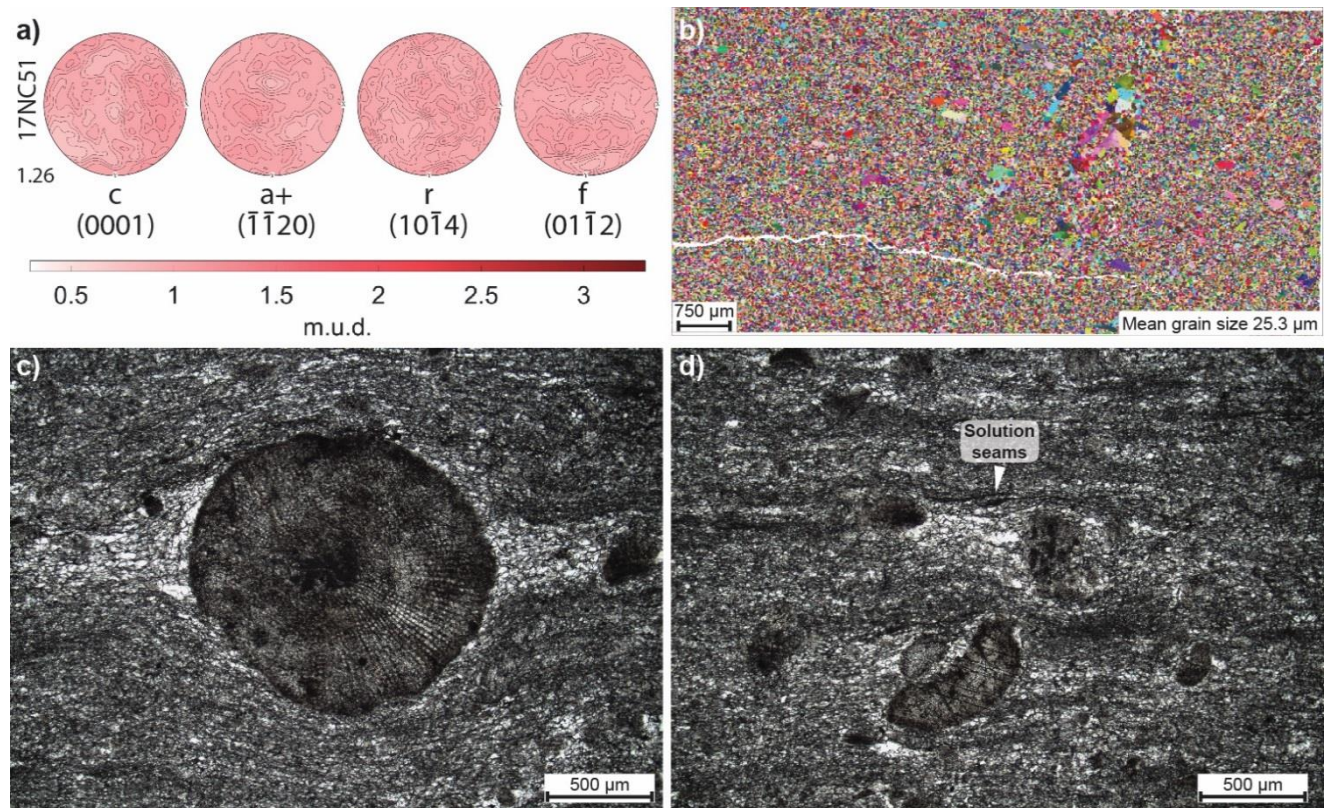


**Fig. 6.17.** Pole figures of crystal preferred orientation in the undeformed domain a), IPF map b) and deformation features c, d) from sample 17NC51 from the normal limb of the ECFN. Random distribution of c-axis evoke for weak strength of the fabric. Solution seams and small pressure shadows attest for the dominant pressure-solution mechanisms in this domain.

### 6.5.2. Deformed Eaux-Chaudes Fold Nappe domain (overturned limb and hinge area)

It is represented by the overturned limb and hinge zone of the ECFN. Eight of the analysed samples are located in this domain with the stronger microfabrics of the analysed samples. The overturned limb is characterized by strong ductile deformation identified at all scales by i.e. mylonitic foliation subparallel to bedding at the mesoscale, stretching lineation, and asymmetric features such as S-C fabrics, dolomite porphyroclasts and intrafolial folds.



### *6.5.3. Weakly deformed autochthon domain*

This domain extends from the eastern border of the overturned limb of the ECFN and at least up to the Arcizette region and Pambassibé peak (cf. Fig. 4.4 for location), eastwards. To the east, the limit is not well-constrained. The fabric strength of this domain is dominantly weaker than in the ECFN domain. Features of strong deformation are not identified and fossil content together with sedimentary textures are well-preserved. All kinematic indicators are in line with a top-to-the-south shear sense.

It exists a relative strong contrast in the deformation intensity between the overturned limb of the ECFN and the autochthon domains as will be discussed further in this chapter.

### *6.5.4. Deformed eastern autochthon domain*

The easternmost domain of the study area includes the strongly deformed autochthon carbonates of the ECM in the Pic de Ger area and surroundings. Three samples aligned in the Pêne Medáa section (S6 in Fig. 4.8) are from the upper Cretaceous autochthon limestones and the 19NC22 is from the Paleozoic basement of the Eaux-Bonnes thrust hanging-wall. In this domain, and similarly to the ECFN overturned limb, features of strong deformation are also developed at all scales, such as stretching mineral lineation, intrafolial folds or asymmetric dolomite porphyroclasts. Outcrop-scale shear zones have been identified in an area dominated by calcite veins (e.g. Fig. 6.1c).

These domains of deformation highlight the heterogeneous strain distribution along the massif, from west to east and from north to south as proposed from the large-scale field observations. Especially, deformation is localised in the overturned limb of the km-scale recumbent fold and in the fold-thrust fan of Pic de Ger, which is the footwall of the allochthon Eaux-Chaudes Nappe. The hypothesis for that is extended in the tectonics chapter, mainly led by the presence/absence of the EC granite, which infers strong localization of deformation in the overturned limb and allows its distribution along the stratigraphic pile to the fold-thrust fan. In the northern edge of the fold-thrust fan, near the Eaux-Bonnes thrust, relatively thick calcite veins have been emplaced (Fig. 6.18) following the foliation

plane, probably formed during late stages of deformation and displaying brittle-ductile conditions. Small-scale folds are observed in veins indicating top-to-the-south shearing.



**Fig. 6.18.** Examples of folded calcite veins in the fold-thrust fan of Pic de Ger displaying late brittle-ductile deformation.

## 6.6. Discussion

### 6.6.1. Fabric strength from Crystallographic-Preferred Orientations

#### *Monomineralic mylonites*

Near half of the analysed samples from the ECM can be considered “pure” calcite mylonites accounting for the low content of second-phase elements (Table 6.1). The presence of second-phase elements exerts a control on the microstructural evolution of calcite-rich mylonites, even in low content (e.g. Herwegh et al., 2011). According to Ebert et al. (2007), for polymineralic mylonites dominated by second phases (50 vol%), the matrix grain size could decrease to half size with respect to monomineralic mylonites, and strongly weaken the strength of CPOs.

Calcite mylonites are usually affected simultaneously by different deformation mechanisms and grain size reduction processes, such as brittle deformation or twinning (Vernon, 1981; Rutter, 1995), subgrain rotation (SGR), or diffusion creep, among others. Some other processes produce grain boundary migration or annealing processes, such as dynamic recrystallization which seeks to minimise the internal free energy of the system. Each mechanism is dominant according to the specific physical conditions of deformation, commonly enhanced by temperature and/or strain rate conditions (e.g. Hirth and Tullis, 1992; Gleason et al., 1993; Stipp et al., 2002a, b; Herwegh et al., 2005).

Upper Cretaceous carbonates of the ECM, from undeformed limestones to mylonites, account for different processes of deformation according to the wide range of strain reported by the results of the fabric strength (Table 6.1, Fig. 6.8). Given that deformation conditions may be assumed to have been fairly homogeneous along the ECM, such as temperature and strain rate, some other features must have been clue in the localization of deformation (e.g. basement rheology, second phase content and/or detachment levels) and consequently in the activation of different mechanisms of deformation. Well-developed crystallographic preferred orientation (CPO) in the calcite matrix, accounting for strong microfabrics, is recorded and identified by c-axes, oriented normal to the foliation and slightly inclined to the north. Foliation plane is defined by a girdle of a- and m-axes in sub horizontal slightly inclined to the north (Fig. 6.8). Strong shape preferred orientations (SPO) are also identified in the strongly deformed samples. Those features account for dislocation creep deformation mechanism, which is dominant in monomineralic calcite mylonites in relatively moderate temperature conditions (e.g. Schmid & Handy, 1991; Kohlstedt et al., 1995). Dislocation glide occurs on r- and f-slip planes with the rotation axis oriented perpendicular to the slip direction (de Bresser, 1991). The basal <a> slip is considerably activated and dominates the deformation (Schmid et al., 1987; de Bresser & Spiers, 1993, 1997; Barnhoorn et al., 2004). Considering the observations, CPOs and IPFs diagrams, the dominant deformation process for these rocks is dislocation creep, probably assisted by diffusion and grain boundary sliding (GBS).

Local misorientation maps reveal intragranular deformation within large host calcite grains (Fig. 6.14), but not on the small calcite matrix, which indicates low differential stresses acting during the deformation and that steady-state conditions were reached. GBS process perhaps was also activated, due to the observation of four-node junctions (e.g. Fig. 6.12). Normally, GBS produces an increase of intergranular misorientation due to the grain rotation (e.g. Bestmann & Prior, 2003; Svahnberg & Piazzolo, 2010), and induces a weakening of the strength of the fabrics (e.g. 17NC51, 18NC52). For example, moderate values of interparticle misorientation angles in the range of 10 to 40 degrees (e.g. Fig. 6.11) are observed in fine grain-size layers. Slightly deformed samples from the normal limb of the ECFN or from the autochthon domain in between the fold nappe and the fold-thrust fan, show weak fabrics (e.g. Fig. 6.8) and sometimes preserve a portion of large relict grains containing twins (e.g. Fig. 6.12c). Those structures together with pressure-solution seams are inferred to be developed during the initial steps of ductile deformation at lower temperatures, sometimes overridden by the increase of deformation intensity or by dislocation creep affection.

### *Polymineralic mylonites*

The main second phases observed in samples are dolomite and quartz in low to moderately high content, but there exist some others in the analysis, such as non-indexed minerals. Dolomite deforms slightly differently than calcite due to its relatively higher strength. Twinning occurs at temperatures  $>300^{\circ}\text{C}$  and on f-planes. It is commonly affected by basal  $\langle a \rangle$  slip at low to moderate temperatures. (Barber & Wenk, 2001). Ductile deformation of quartz normally occurs at higher temperatures ( $>400^{\circ}\text{C}$ ) than those reported for the ECM. The volume occupied by the second-phase content is crucial: just a volume fraction of 0.1% is required to induce a pinning effect in half of the matrix grain boundaries (Herwegh et al., 2011). The interparticle spacing in between the second phase crystals is crucial in the localization of strain. In areas with a high volume content of second phases, the low interparticle distance localizes the deformation in the calcite edges by the pinning processes (e.g. Drury & Urai, 1990; Olgaard, 1990; Krabbendam et al., 2003; Herwegh & Berger, 2004; Ebert et al., 2008; Linckens et al., 2011) in which second-phases contribute to raise differential stresses in the



borders of the matrix grains inducing viscous granular flow deformation (e.g. diffusion-assisted granular flow, according to Paterson, 1995) instead of dislocation creep. For example in sample 17NC27 (Fig. 6.12a), layers with different content of dolomite also have differences in the average grain size, indicating a contrast to the differential stresses between these layers. For this particular case, the calcite-rich layer has approx. a double grain size that of the layer with dolomite (27.7  $\mu\text{m}$  vs. 15  $\mu\text{m}$ , respectively), indicating, at least locally, a contrast of the differential stress by a factor of two (20 MPa vs. 40 MPa, if strain rate is considered constant) between both layers. In other situations, such as surrounding large dolomite porphyroclasts, shadow zones are observed, and typically in these zones, calcite grain sizes are relatively higher than in the matrix. Here, the difference in grain sizes between regions accounts for differences in strain rate and, therefore, changes in the dynamic recrystallization processes (grain growth vs. grain size reduction). Stronger CPOs are developed in specimens with low content of second phases.

Temperature is a key factor in the grain growth processes by promoting the enlargement of the mean grain sizes in both matrix and second phases. Therefore, the increase of interparticle spacing and of distance between second-phase interparticles enhance the effective grain boundary mobility (Herwegh et al., 2011 and references therein). On the other hand, deformation is not strictly dependent only on the temperature. Initial grain size of calcite matrix is even more decisive in the development of deformation processes.

The interaction between grain growth and grain size reduction processes is dependent on the microstructure dissipation energy, the so-called paleowattmeter (Austin & Evans, 2007, 2009; Austin et al., 2008; Ricard & Bercovici, 2009). It is proposed that the energy dissipation from these processes can account for determining the dominant in the preservation of a steady-state grain size, in the competition between the mechanisms involved in the grain enlargement and those responsible for the grain size reduction (e.g. Herwegh & Handy, 1996).

### 6.6.2. Calcite grain size distribution

The evaluation of grain-size from EBSD analysis is highly dependent on the acquisition step size. The range used in the microstructural inspection was between 1 and 9  $\mu\text{m}$ . For some samples, more interested into analyse large areas (e.g. for crystal preferred orientation or grain shape analysis), the step size was too large, producing an overestimation of the grain size values. Due to that, we optically estimated sizes from thin section images obtained by calcite grains drawing from transmitted and polarized light images (e.g. Fig. 6.19). Grain size results are indicated on the left bottom of every drawn sample with the main value, standard deviation and the shape factor of calcite crystals. In all the samples, the values obtained are slightly lower than those from the EBSD results. It is important to consider the human error of drawing from the interpretation of calcite grain edges in the images. Grain elongation and shape preferred orientations are well-developed in the deformed samples.

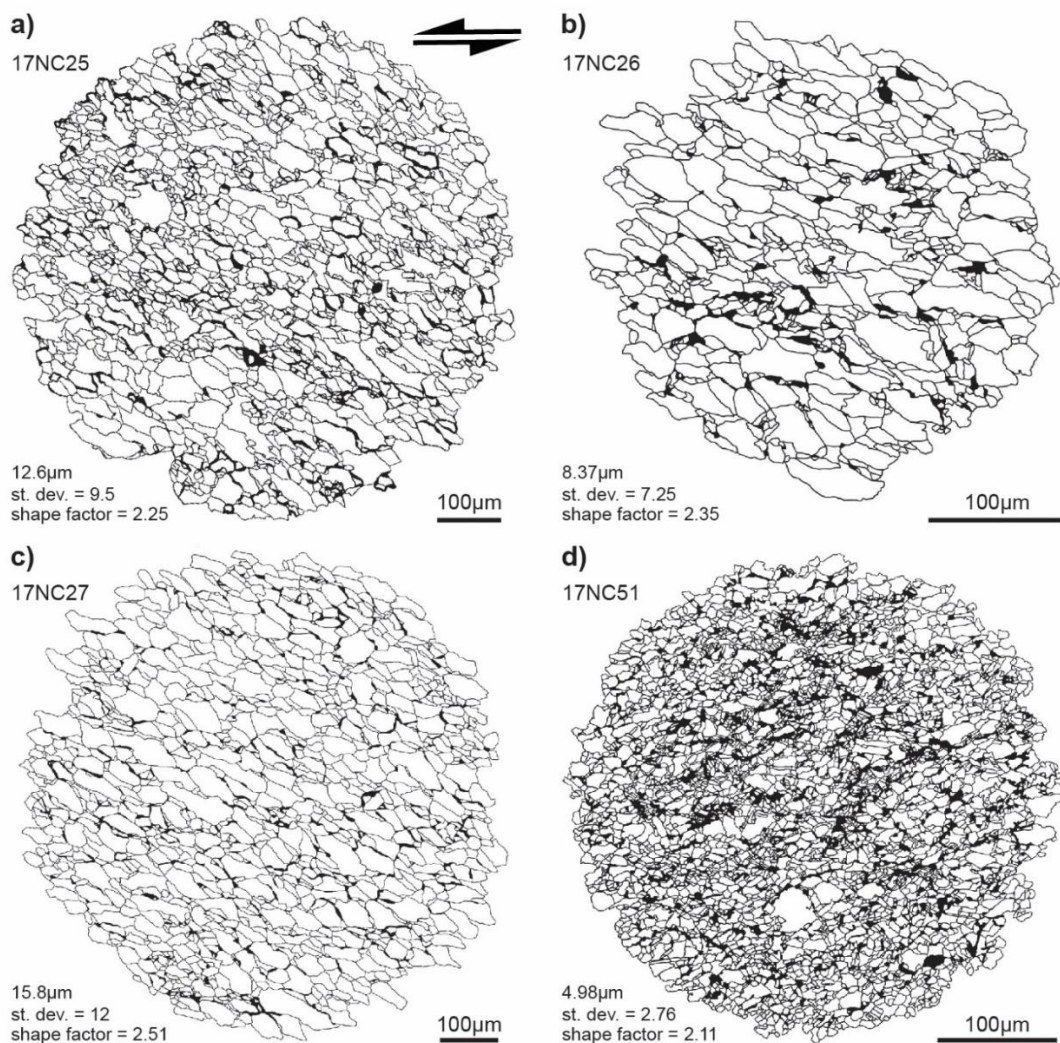


**Fig. 6.19.** Detailed sketch of grain boundaries from deformed (a, b, c) and non-deformed (d) samples. Grain elongation and SPO are observed in deformed samples, while slightly equant grain shape is observed in non-deformed. Shear sense and orientation is similar in all the samples.

Large grain sizes of the upper Cretaceous limestones from the ECM in monomineralic samples (~34 to ~36  $\mu\text{m}$ ), were identified in the most strained domains, e.g. from the deformed autochthon domain (Pic de Ger fold-thrust fan) and from the deformed ECN domain (overturned limb of the ECFN). The presence of fossil content enhances the mechanical heterogeneity of calcite matrix. On the other hand, high-strained samples with elevated contents of second phases, sometimes higher than 20%, inhibit the recrystallization in the calcite matrix. Here, the pinning effect dominates the deformation process by reducing the stresses in between the calcite and dolomite/quartz boundaries and promoting the calcite grain size reduction from the pinning effect and strain localization, as observed in samples 17NC27 and 17NC37 (Figs. 6.12, 6.13). Polymineralic mylonites are often organized in paralleled banding with second phases in wider matrix layers. Some of these samples show parallel banded structures between dolomite-rich layers and calcite-rich. In dolomite-rich layers, calcite grain size is smaller than compared in the areas where the calcite phase is dominant, with larger grain sizes. Large host grains and/or syntectonic veins also contribute to the size reduction by increasing of differential stresses due to the two-grain size domains, which induce grain-size reduction and the local activation of brittle-ductile processes. The content of the second phases not only affects the grain size, but also the fabric strength by weakening it by damping the deformation.

Regions with higher dolomite content embedded in the calcite matrix developed dolomite porphyroclasts, at all scales (e.g. Figs. 6.1, 6.12, 6.13). Those behave as rigid bodies which face opposition to deformation, deflecting it to the matrix phase which is affected by grain size reduction and strong SPO and CPO development. Eventually, large dolomite porphyroclasts create shadow zones in their tails preventing the calcite crystals from the strong deformation. This is observed at the microscale but probably can be extrapolated to the large-scale as identified in the field by the distribution of the mylonitic foliation around the large dolomite bodies.

### *6.6.3. Spatial distribution of the deformation*

As reported in previous chapters and before in this current, there exist two main domains of deformation at large-scale divided by the Gourzy transfer zone, the eastern and the western sectors (e.g. cf. chapter 4). Those domains are conditioned by different features largely previously discussed. At the microscale, the localization of deformation is mainly controlled by rheological constraints. Second phase content leads to the development of grain size-sensitive processes and enhances the pinning effect in the upper Cretaceous mylonites. From the spatial distribution of analysed samples, the main factor in conditioning the fabric strength may tentatively be attributed to the areas where of stronger rheological contrast, such as the unconformity between the Paleozoic basement and the Mesozoic cover (Fig. 6.20).

For the western sector, deformation is located very close to the Paleozoic-Mesozoic unconformity in the overturned limb, where deformation is strongly localized due to the granite forestop effect. To the welded syncline and in the hinge area deformation becomes moderate. On the contrary, the autochthon and normal limb are fairly protected from the affection of the strong deformation. It is worth mentioning that the normal limb does develop very low fabric strength, even the emplacement of the Montagnon d'Iseye nappe above it. We infer this low affection to the existence of the upper Triassic sheet in between both, which absorbs the main deformation during the expulsion of the evaporites by the south-directed movement of the MIN.



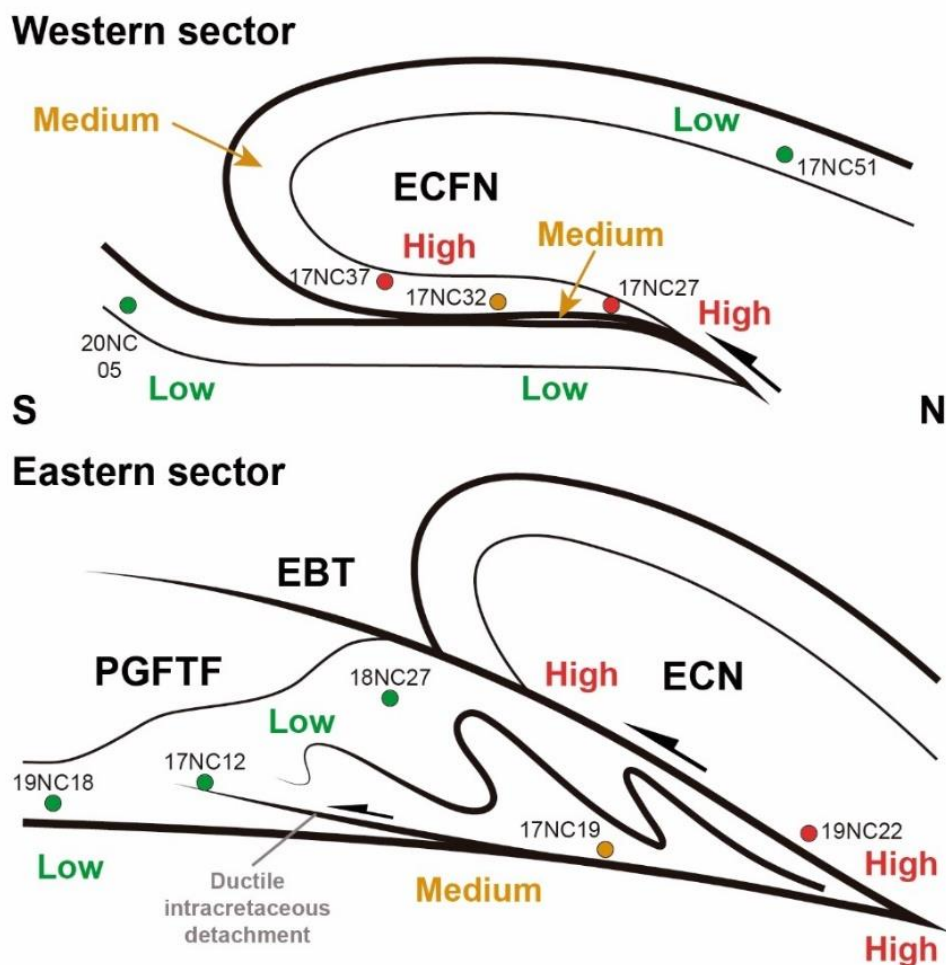


**Fig. 6.20.** Sketch of the relative fabric intensity observed for the two main sectors of the Eaux-Chaudes massif. ECFN: Eaux-Chaudes Fold Nappe; EBT: Eaux-Bonnes thrust; PGFTF: Pic de Ger fold-thrust fan; ECN: Eaux-Chaudes Nappe

For the eastern sector, deformation is localised on the hanging-wall, just above the Eaux-Bonnes thrust structure, and in the northern area of the fold-thrust fan in the footwall. At late stages, the brittle-ductile conditions facilitate the emplacement of large calcite veins, which become folded and a bit sheared with top-to-the-south sense. This does not occur in the western sector, where deformation is really intense and the mechanical contrast between the upper Cretaceous and Paleozoic is not so significant. Quartz veins affection is restricted to the main unconformity by the occurrence of the intracretaceous ductile detachments. To the south, deformation gets progressively damped due to its accommodation in ductile structures, such as folds and detachment levels.

## 6.7. Implications and conclusions

Microfabric analysis from the Cretaceous limestones of the ECM has provided information for the first time on microstructural data for the upper Cretaceous of the Pyrenees and the main ductile Alpine tectonic phase. Specifically, for the deformation mechanisms, grain size variations and approximation of the paleostresses that affected the Mesozoic of the ECM. The average grain size for the recrystallized calcite grains of the Cretaceous limestones is approximately 21.3  $\mu\text{m}$  in a range between 6.77 to 45.76  $\mu\text{m}$ . Those values may be specifically divided according to the four different domains of deformation proposed in this thesis with small variations in the average and range values. Those grain sizes resulted from the deformation that occurred under relatively low stresses in a range of approximately 10 to 70 MPa, with more confident interval of 20 to 60 MPa.

The distribution of the deformation along the samples is heterogeneous and quite dependent on the rheological properties of the rocks and on the position with respect to the large-scale structure (if we consider the large-scale observations exposed in chapter 4). From this study we propose a scenario for the deformation localization in both the western and eastern domains. Even the stronger microfabrics of the Cretaceous limestones are located near the Paleozoic rocks, the normal limb is prevented from deformation by the occurrence of the Keuper sheet in between. It exists a damping of the deformation to the south of the massif by its accommodation in the ductile structures.

Strong deformation is observed i.e. by well-developed S-C fabrics, asymmetric dolomitic porphyroclasts, mylonitic foliation and conspicuous dynamic recrystallization processes, which blurs the original sedimentary textures and fossil content. Stretching lineation and S-C composite fabrics are well-developed in pure carbonate mylonites. Those two features together with asymmetric porphyroclasts attest for a non-coaxial deformation and evidence of the south-directed tectonic transport previously reported by Ternet (1965), Majesté-Menjoulas (1979), Dumont et al. (2015) and Cochelin (2016), for the ECM.

Microfabrics are controlled by the rheological behaviour of the mineral phases. For the calcite-rich layers, we postulate an initial deformation along the massif dominated by pressure-solution seams

and develop the described features of weak fabrics. As deformation became intense in certain areas the dominant process turned into crystal-plastic deformation at moderate temperature reached, strengthening the fabrics. Dislocation creep mechanisms dominate in the strongest deformed samples being accommodated by slip on basal planes parallel to the *a*- and *m*-axes, with the development of a relatively fine-grained matrix, but coarser than those affected by second phases, and featuring grain shape and crystallographic preferred orientation. The crystallographic preferred orientation consists of *c*-axes oriented normal to the foliation, and *a*- and *m*-axes defining a girdle parallel to the foliation.

In polymineralic mylonites, dolomite and quartz phases (sometimes >20 vol%) enhance the anisotropy. Thin dolomite-rich layers are observed in some samples by weakening the fabric and inducing pinning processes. These layers show moderate plastic deformation, with occasional fold streaks and asymmetric porphyroclasts. Calcite matrix grains are considerably reduced by the pinning effect and the localization of deformation. All the microstructures observed at the ECM are consistent with the RSCM paleotemperature estimates and attest for a non-coaxial ductile deformation with top-to-the-south sense of shear, following the general kinematics indicated by large-scale field observations.

Quartz- and phyllosilicate-rich rocks (e.g. Buntsandstein and Cretaceous clastic limestones) show brittle-to-ductile behaviour, with weak intragranular deformation (undulose extinction) and slight evidence of quartz recrystallization by bulging in the microscale. It is worth mentioning the difference of behaviour of the chert elements in the uppermost Santonian limestones in the outcrop-scale. At some areas they behave as rigid blocks, featuring fracturing and bookshelf-like rotation structures, and at some other localities they became folded and stretched, mimicking dolomite porphyroclasts (e.g. Fig. 6.16).

## **Chapter 7: Cathodoluminescence of upper Cretaceous carbonates**

Cathodoluminescence (CL) petrography is an extensively used technique because it provides valuable insights from carbonate paragenetic processes according to the luminescent response of i.e. calcite and dolomite (e.g. Sommer, 1972a, b; Meyers, 1978; Frank, et al., 1982; Grover & Read, 1983; Barnaby & Rimstidt, 1989). CL is directly related to the presence (or absence) of trace elements in carbonates, activating or quenching the luminous response to an electron beam. For carbonate minerals the Mn is considered the most frequent luminescence activator (e.g. Schulman et al., 1947 and references therein; Gies, 1975; Marshall, 1988; Mason & Mariano, 1990 and references therein; Götte & Richter, 2009), but also Pb and REE provoke carbonate CL (Gies, 1975; Mason & Mariano, 1990; Machel et al., 1991; Habermann et al., 1996). On the contrary, Fe, Ni and Co represent the most important quenching element of luminescence (Sippel & Glover, 1965; Pierson, 1981; Fairchild, 1983; Mason, 1987; Mason & Mariano, 1990). The ratio between activators and quenchers in calcite is quite constricted for the Mn and Fe. In general, concentrations of Mn above 17 ppm may cause luminescence (Mason & Mariano, 1990) and this sole element is sufficient to activate this response in calcite (ten Have & Heijnen, 1985), even in a few ppm (Habermann et al., 1998). On the opposite, Fe conforms to the most common quencher element (e.g. Long & Agrell, 1965; Sippel & Glover, 1965) and concentrations >200ppm are required to be effective. Bright yellow, and orange to red colours result from the presence of Mn in calcite and dolomite, respectively. Higher contents of Fe turn the luminescence into very dark red, red-brown, or non-activated (Budd et al., 2000) (Fig. 7.1). In general, thinner overgrowths in grey, orange, and bright yellow colours postulate for a mixture of water source implying abrupt changes in chemical composition (Banner et al., 1988; Choquette & Hiatt, 2008). Burial fluids generally cause dull luminescence while relatively shallow or meteoric fluids result in brighter luminescence (e.g. Stoppa et al., 2021).



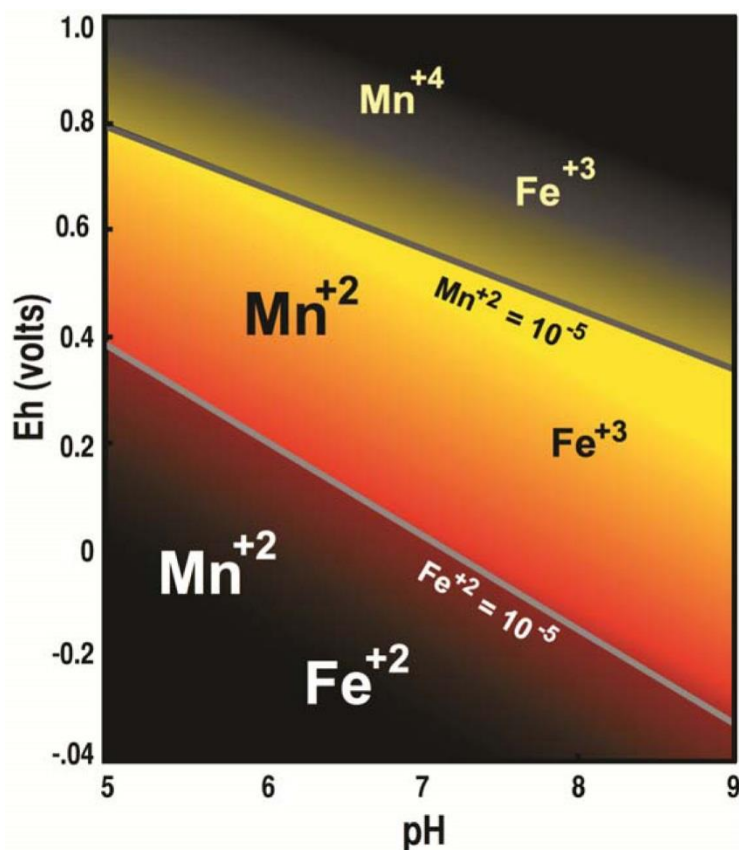


*Fig. 7.1. Eh/pH diagram for the aqueous species of Mn and Fe and expected CL colours for calcite. From Hiatt & Pufahl, 2014.*

It is known that differences in CL colours and intensities represent variations of carbonate Fe and Mn concentrations, motivated by changing redox (*Eh*) conditions during its emplacement (Hiatt & Pufahl, 2014). Complex crystal growth, replacements or retrograde processes can be disclosed.

The purpose of using this technique has been to explore significant signs of relationships between diagenetic and deformational processes in pure calcite, dolomitized and quartzitic carbonates of the Upper Cretaceous in the ECM, and try to unravel their link to the main deformational event. A total of 32 samples of deformed and non-deformed limestones were analysed by optical and cathodoluminescence petrography from different deformation domains (Fig. 7.2). EMPA results from 5 dolomitized samples (Table 5.2) show low contents of Mn and variable concentrations for the Fe.

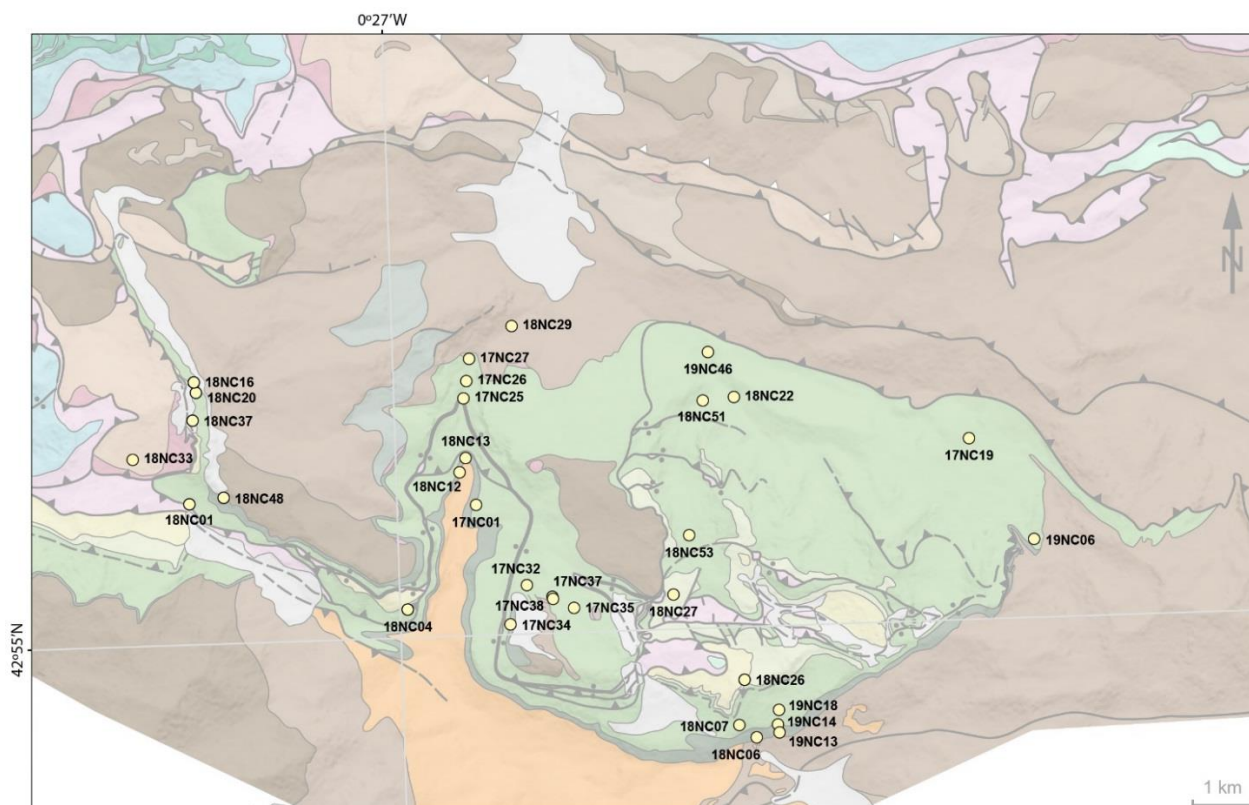


**Fig. 7.2.** Location of the analysed samples by cathodoluminescence.

## 7.1. Calcite

CL response from the calcite matrix crystals is very variable in intensity and colour. Generally, calcite grains are characterized by a homogeneous CL. Half of the samples show a signal of yellow colour with moderate intensity (e.g. Fig. 7.3b, d). Nonetheless, the colour intensity along the samples is shown from very faint or absent up to strong. Some samples show a non-luminescent response or light blue to dark-dull (Fig. 7.4) with sporadic bright yellow overgrowths in some large crystals, surrounding non-luminescent calcite core nuclei. Although yellow is the most frequent CL colour for calcite phase, orange, reddish and brownish nuances have been also identified in calcite matrix from five different samples (Fig. 7.5). Calcite veins with different compositions sometimes show strong predominantly yellow CL colour intensities. Porosity texture is witnessed by calcite matrix recrystallization and calcite void filling. From these observations a classification of 4 calcite are proposed: calcite 1 (yellow CL), calcite 2 (blue CL), calcite 3 (red-brownish CL) and calcite 4 (non-luminescent CL).



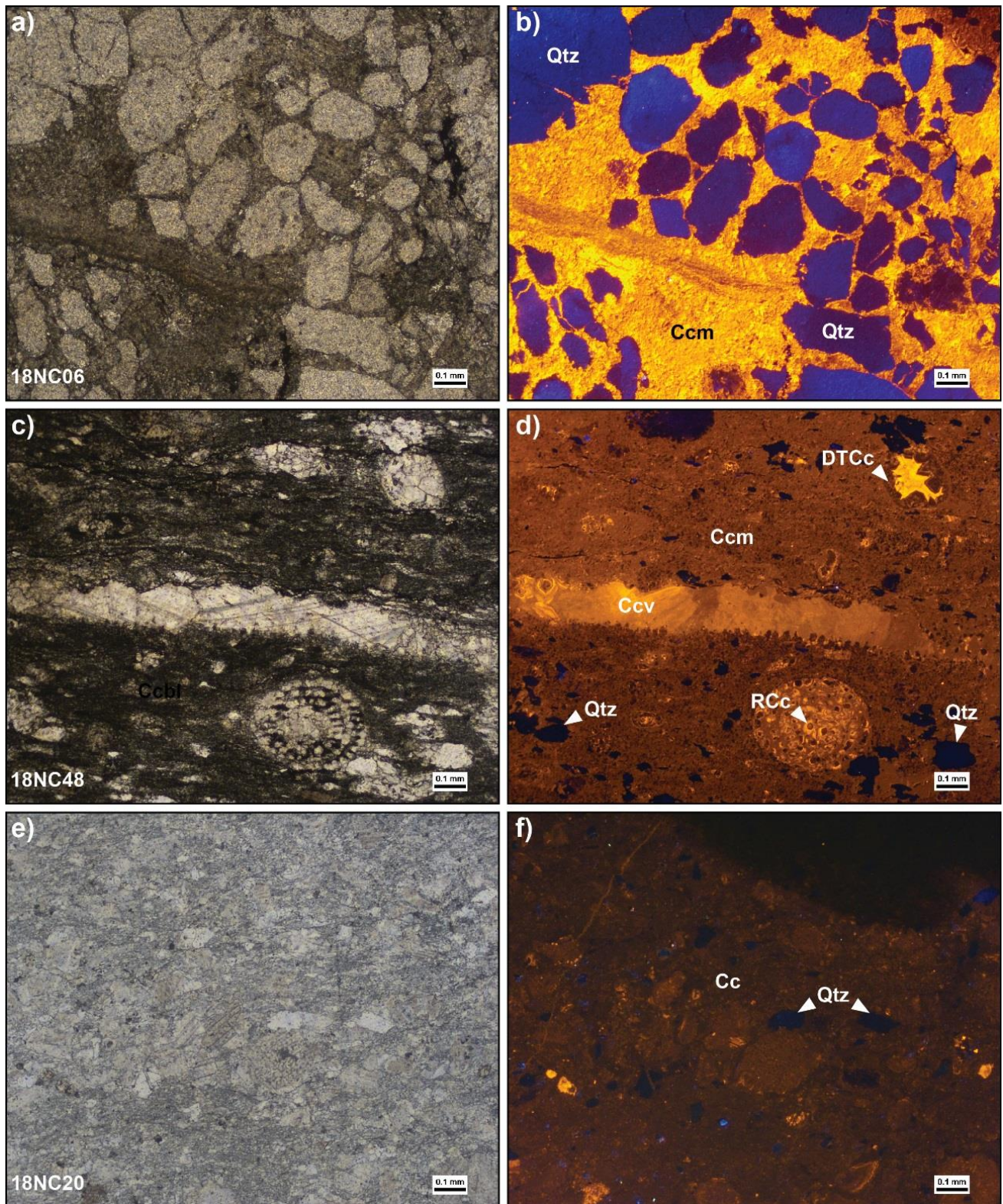


**Fig. 7.3.** Transmitted (left) and cathodoluminescence (right) light from Upper Cretaceous limestones of the ECM showing the response of the calcite phase. Three different yellow intensities are shown from very bright (b) to dark-dull (f). Quartz is represented by blue CL. Ccm: calcite matrix; Qtz: quartz; DTCc: dogtooth calcite; Ccv: calcite vein; Cc: calcite.

### 7.1.1. *Calcite 1 (yellow CL)*

Yellow cathodoluminescence is the most common response for the carbonates on the Eaux-Chaudes massif. Indeed, it is the most common response for calcite crystals containing Mn (Götte & Richter, 2009). A wide spectrum of different CL intensities is observed in both matrix and large crystals of calcite phase. For micritic or small grain-size matrix, very bright to dull-dark represent the two-endmembers of the yellow spectra (Fig. 7.3. b and f, respectively). Sample 18NC06 from the basal Cenomanian facies show a very bright yellow calcite matrix enclosing a varied range of quartz grains. Sample 18NC20 show a dull/dark yellow response with some brighter crystals performing either yellow or dull CL rims (Fig. 7.3f). Dogtooth cement has been identified replacing a large fossil fragment with bright to dull yellow luminescence, e.g. sample 18NC48 (Fig. 7.3d). Overgrowths and/or replacements have been developed in sample 17NC01 (Fig. 7.4d) with yellow luminescent in the micritic matrix in the first stage and by large non-luminescent to dull blue crystals as the late phase, sometimes performing bright yellow overgrowth rims.

### 7.1.2. *Calcite 2 (blue CL)*

Blue CL (bright to dark) has been identified in some pure calcite limestone (Fig. 7.4b) which present some isolated bright yellow spots randomly distributed along the matrix. Those yellow CL grains sometimes correspond to darker crystals in transmitted light maybe containing Mn impurities and, attributed to dolomite crystals. As explained in the previous section, other samples containing blue CL calcites are dolomitized limestones composed by large crystals, in blue, filling the porosity voids posterior to the yellow micritic phase (Fig. 7.4d). Blue CL emission is not common in calcites but not exceptional either. Some authors postulated for (1) a very low concentration or even the absence of Mn in the calcite phase (e.g. Richter & Zinkernagel, 1981; Amieux et al., 1989; Mason & Mariano, 1990), (2) intrinsic lattice distortions (Barbin, 1995; Toffolo et al., 2019), or (3) activation by Eu, Zn, Mn, or Ce cation (Barbin, 1995).



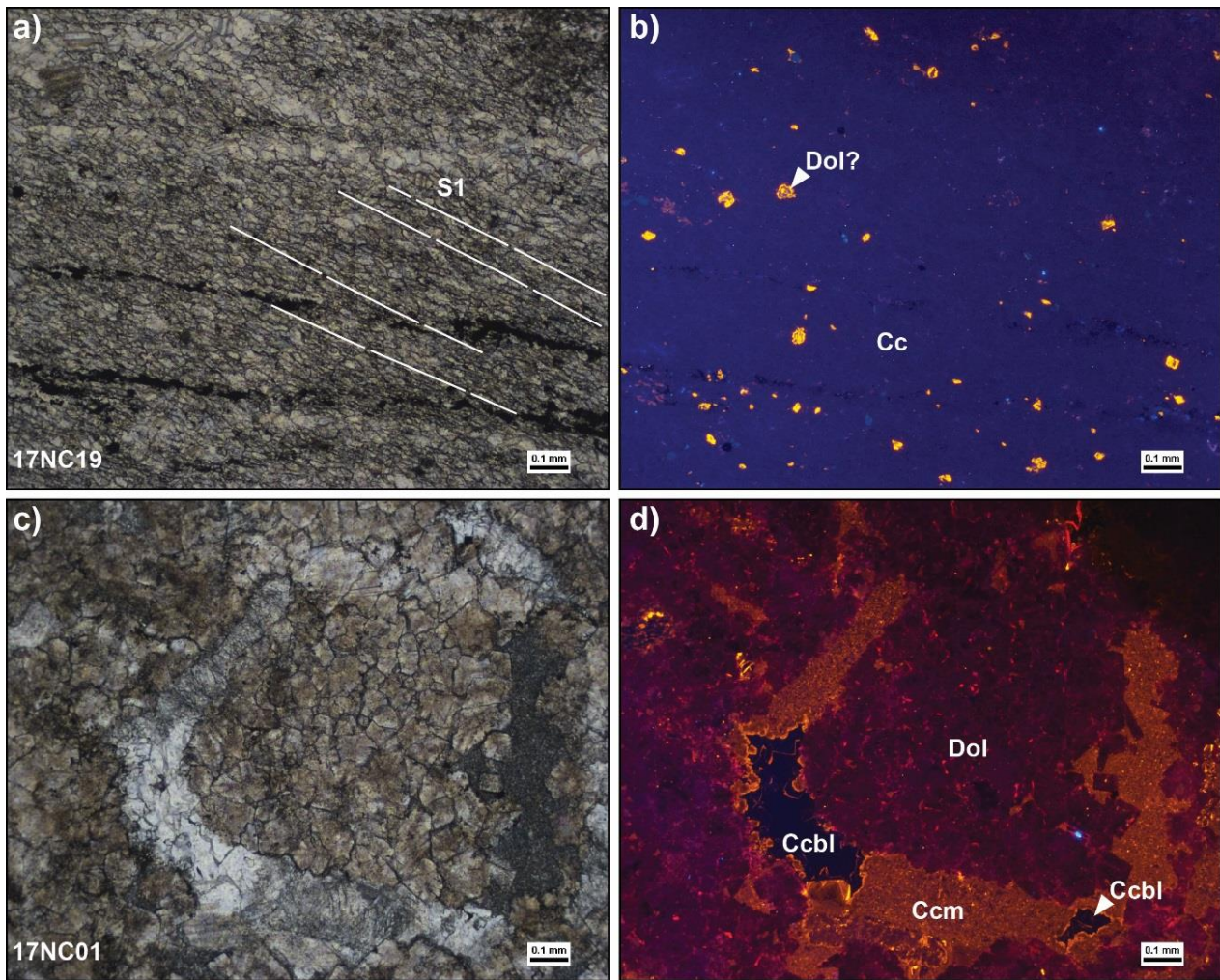


**Fig. 7.4.** Transmitted (left) and cathodoluminescence (right) light from Upper Cretaceous limestones of the ECM showing the response of the calcite phase. Two different blue intensities are shown from bright (b) to dark-dull (d). (d) Yellow small-size calcite phase in the matrix and blue large calcite crystals filling porosity voids with bright yellow rims. Ccm: calcite matrix; Dol: dolomite; Ccbl: calcite blue; Cc: calcite.

### 7.1.3. Calcite 3 (red-brownish CL)

Some samples show brownish, orange to reddish luminescence matrix (Figs. 7.5b; 7.6 (crystal edges)). It is not dependent on the crystal grain-size and neither on the presence of veins. Sometimes the brighter luminescence is developed on the border of crystals or grains.

### 7.1.4. Calcite 4 (non-luminescent)

Very few samples show a dull to non-luminescent response by the calcite matrix or even larger crystals (Figs. 7.5d). As an example, original non-luminescent to dark-dull nuclei of calcite crystals



are encircled by calcite with faint to medium intense reddish CL (sample 17NC27, Fig. 7.6). This texture is observed in highly deformed and recrystallized sample, and interpreted as an example of dynamic recrystallization by grain boundary migration assisted by fluids. Complex zonation or overgrowth rims are developed with yellow to orange-reddish colours by recrystallized calcite dependent on the chemistry meanwhile the recrystallization.

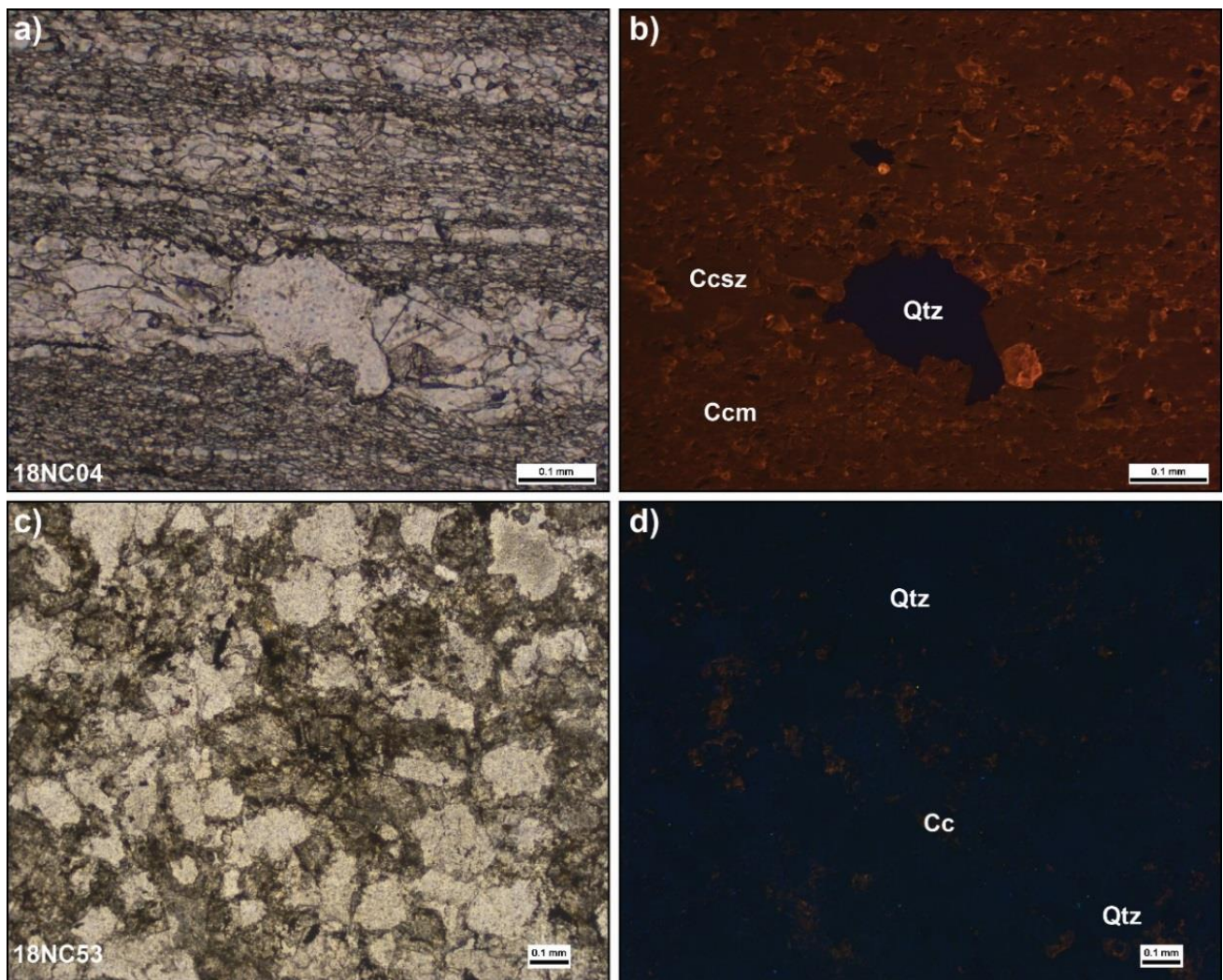


**Fig. 7.5.** Transmitted (left) and cathodoluminescence (right) light from upper Cretaceous limestones of the ECM showing the response of the calcite phase. (b) Brownish nuance of the calcite phase from the matrix and shadow zone with yellow bright borders. (d) Almost non-luminescent calcite phase with a very slight yellow response. Ccm: calcite matrix; Ccsz: calcite shadow zone; Qtz: quartz; Cc: calcite.



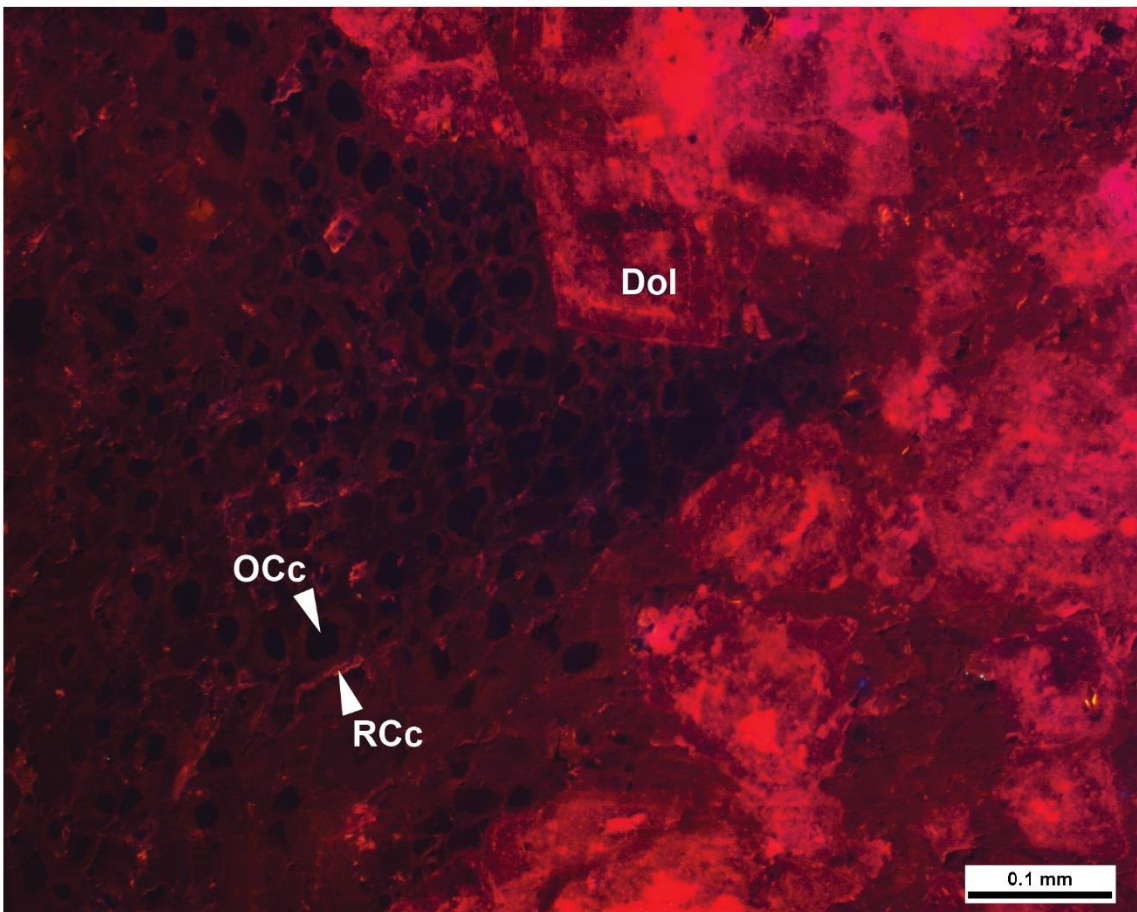
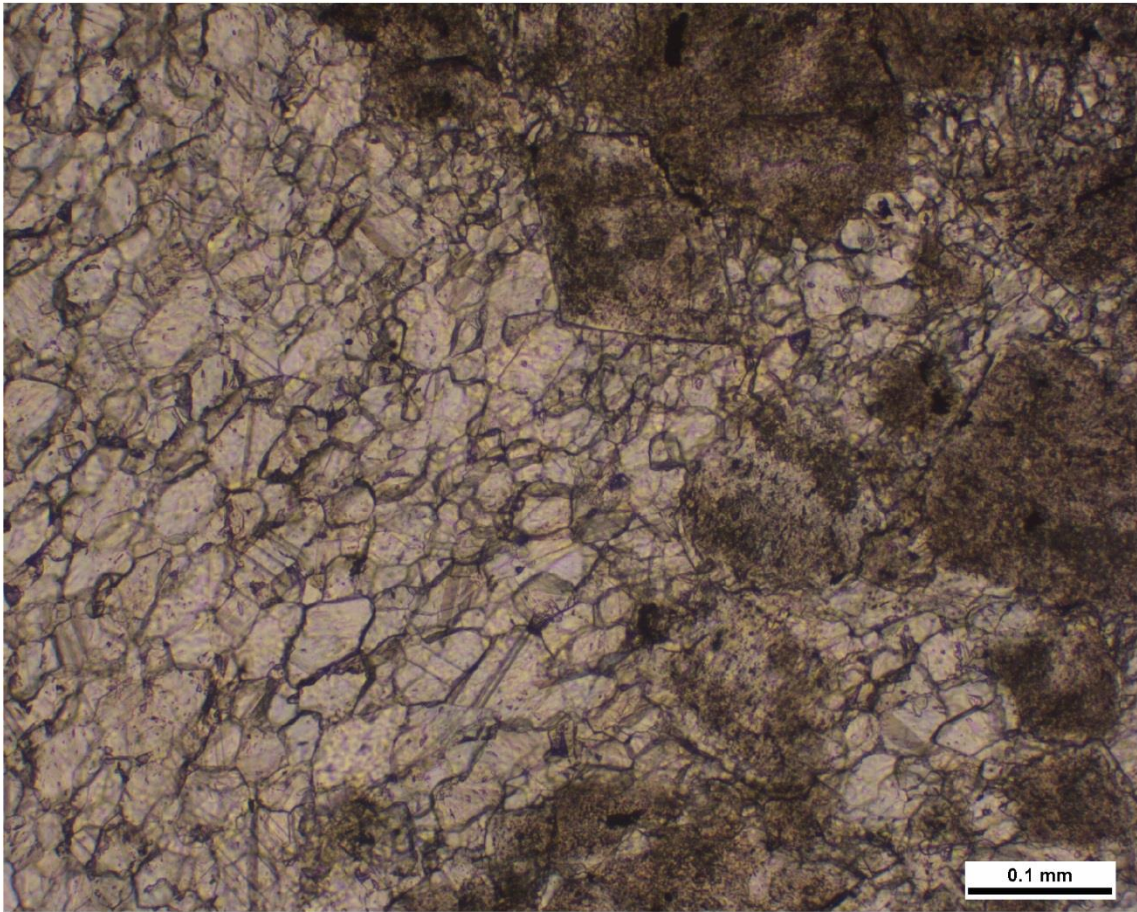


**Fig. 7.6.** Transmitted (top) and cathodoluminescence (bottom) light from sample 17NC27. Recrystallized reddish rim by grain boundary migration assisted by fluids, from original dull calcite crystals in a shadow zone of a dolomite porphyroclasts. Dol: dolomite; RCc: Recrystallized calcite; OCc: Original calcite.

## 7.2. Dolomite

Dolomite is characterized by polymodal distribution of crystal size and usually well-developed planar rhombic crystal shape following the combined dolomite textural classification (Fig. 7.7) proposed by Gregg & Sibley (1984) and Sibley & Gregg (1987). CL response is likewise very variable in intensity and colour, generally characterized by a heterogeneous colours with overgrowth rims and most of the samples showing dedolomitization textures (Fig. 7.8). Dolomitization is also heterogeneously developed, from partial to almost total on the analysed samples (Fig. 7.9), and displaying strata bound dolomite bodies in large-scale. The CL intensity is from very faint or absent up to strong, normally on the rims and external borders of the crystals, but sometimes also in the core. Multiphase growth is also observed in some dolomite specimens. Although red is the most frequent CL colour, orange, violet, magenta, yellow and brownish nuances cover the colour spectrum of dolomite phase. A great number of dolomite crystals show a complex pattern of colour along the crystal.

Accounting for the textures observed in the Cretaceous carbonates from the ECM, three different type of dolomite have been proposed: 1) Polymodal planar-s, 2) polymodal planar-p and 3) polymodal planar-e dolomites. Polymodal is referred to the heterogeneous size distribution due to multiple periods of nucleation, or variations in the growth rate according to the solute delivery (Sibley & Gregg, 1987). The term planar indicates the shape of interfaces in the crystalline faces which are usually straight and well-crystallized. The suffixes give a clue for the shape of the dolomite crystals and the amount of matrix in between (i.e. -s is referred to low porosity and/or low intercrystalline matrix; -p account for matrix-supported crystals; and -e is referred to crystal-supported with intercrystalline area filled by another mineral or porous).

Apart from the textural classification, three main groups of luminescence colours are identified and in four samples complex patterns of cathodoluminescence were observed.



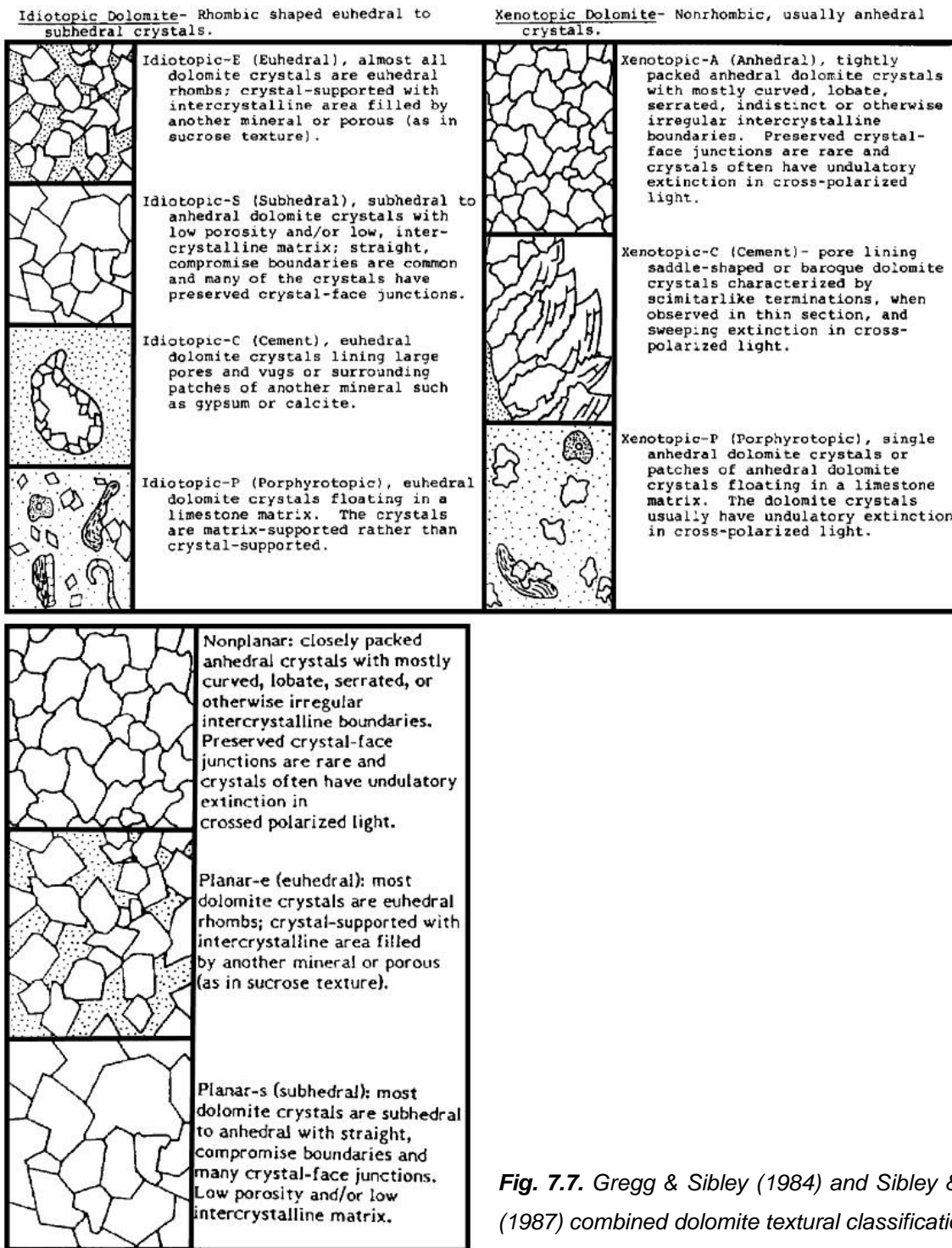
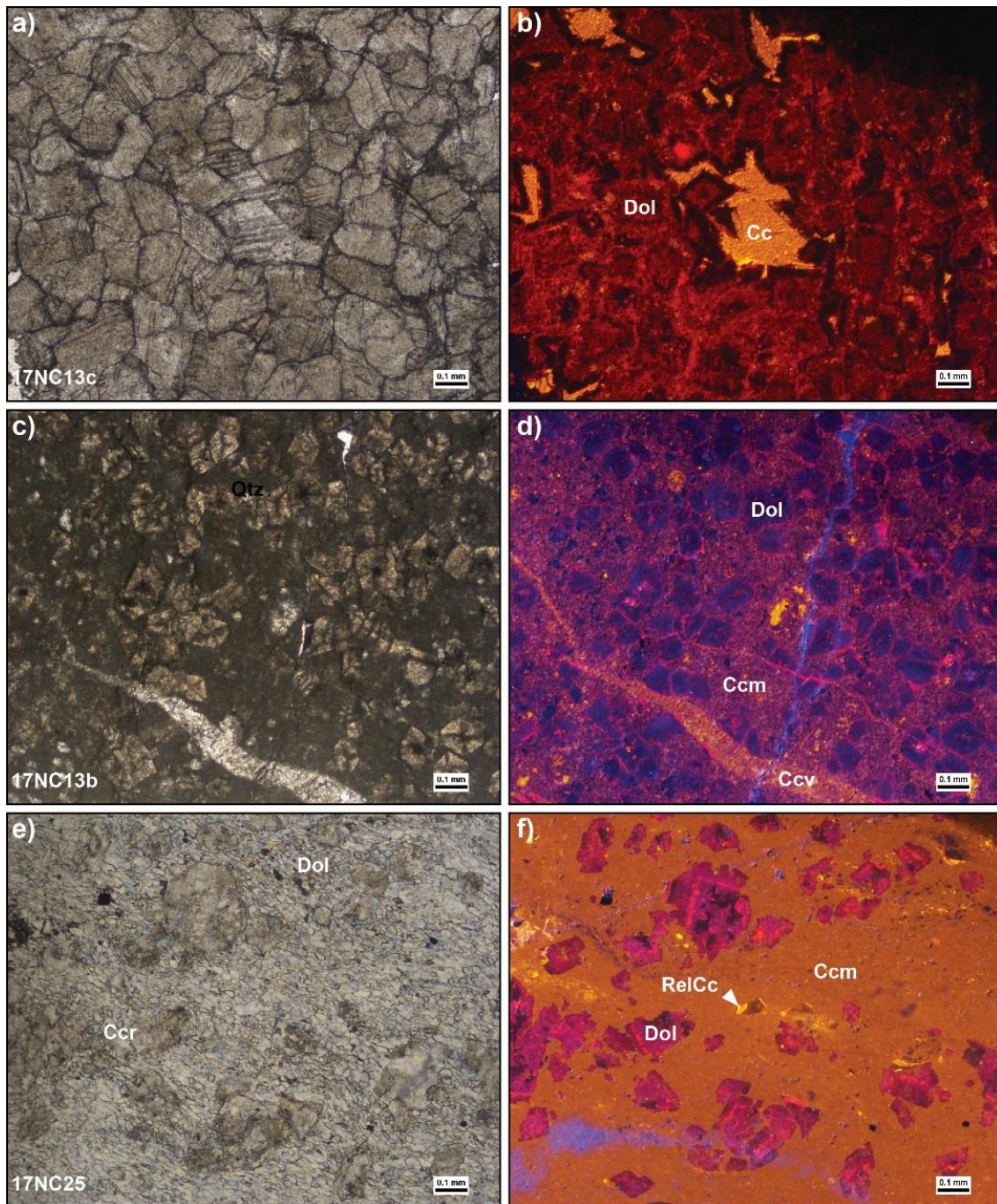
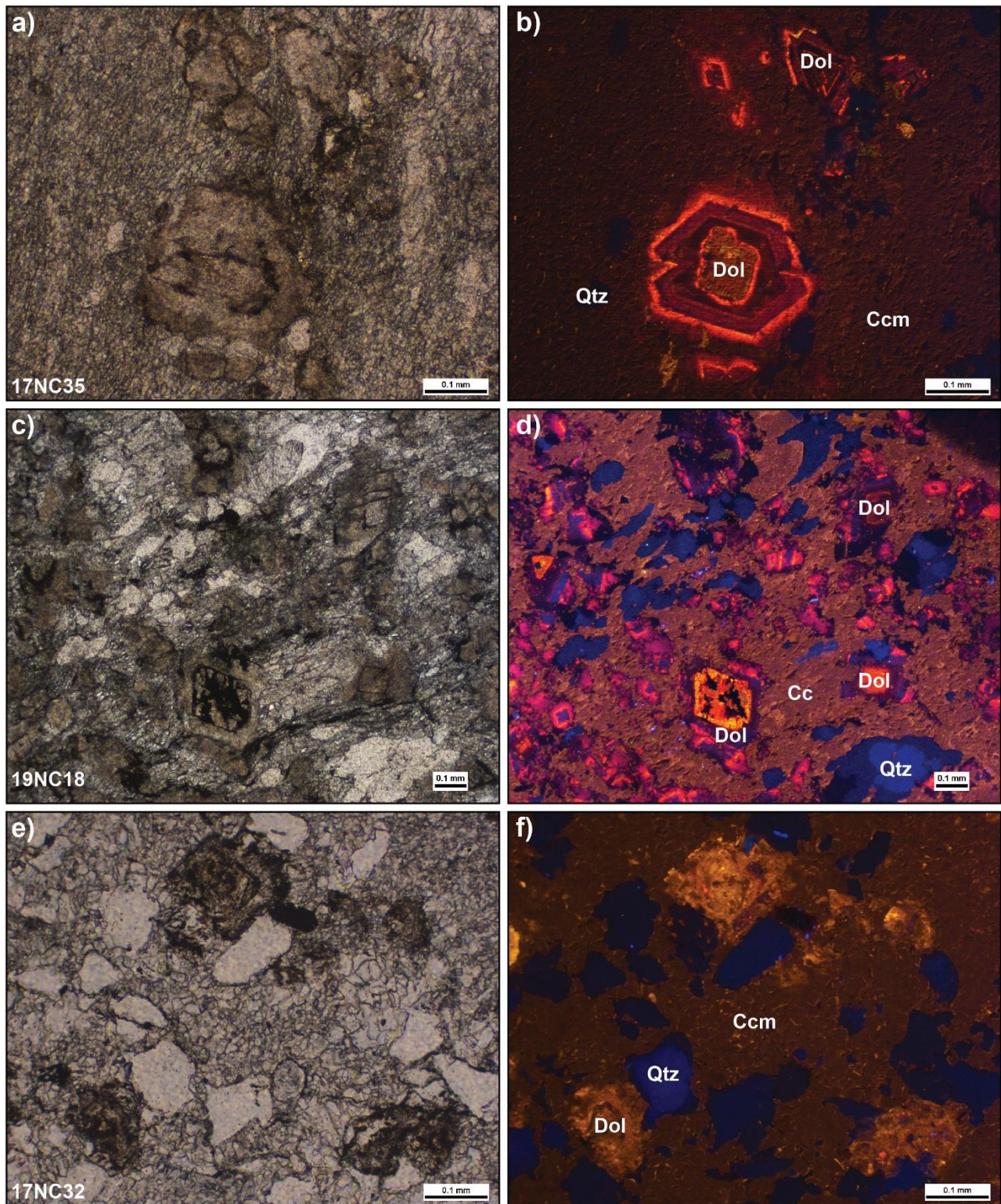


Fig. 7.7. Gregg & Sibley (1984) and Sibley & Gregg (1987) combined dolomite textural classification.



**Fig. 7.8.** Transmitted (left) and cathodoluminescence (right) light from Upper Cretaceous limestones of the ECM showing the response of the dolomite phase. Dolomitization is heterogeneous from almost total (b) to partial (d, f). (b) Polymodal planar-s dolomites with red to dark-dull luminescence and dark zonations. Large yellow calcite crystals fill the porosity generated by almost total dolomitization and provoking dedolomitization of the crystal border. (d) Polymodal planar-e dolomites with fairly homogeneous violet to dark-dull luminescence and certain brighter borders or dissolved nuclei, evidencing chemical changes in the last steps of dolomitization. (f) Polymodal planar-p dolomites with magenta luminescence and some dark nuclei. Dedolomitization is well-developed by the homogeneous recrystallized calcite matrix preserving some large relict calcite crystals with brighter yellow luminescence combined with darker zones. Dol: dolomite; Cc: calcite; Ccm: calcite matrix; Ccv: calcite vein; RelCc: relict calcite.





**Fig. 7.9.** Transmitted (left) and CL (right) light from upper Cretaceous limestones of the ECM showing the response of the dolomite phase. (b) Polymodal planar-p dolomites with multiphase growth shown by rims, performing idiomorphic crystal faces and enclosing an amorphous and altered nuclei. (d) Polymodal planar-e dolomites with heterogeneous CL from yellow-orange to magenta-violet with some dark nuclei. (f) Polymodal planar-p yellow dolomites with some orange nuances in the growth rims. Intense dedolomitization is performed in all the samples by the dull, brown and dark-yellow recrystallized calcite matrix in b, d and f, respectively.

### *7.2.1. Dolomite dull-violet CL*

Some samples are characterized by a dull or faint violet CL which is fairly homogeneous, and some specimens show an external rim of bright magenta nuance or in the core crystal (e.g. Fig. 7.8d). Usually, the crystalline face is well-developed and rarely affected by dedolomitization.

### *7.2.2. Dolomite dull to bright magenta CL*

Few samples distributed in both the autochthon and overturned limb show a CL response of dull to very bright magenta colour, especially in the external rims (Fig. 7.8d, f, Fig. 7.9d). Dedolomitization processes are even more intense than in the dull-violet dolomites dissolving up to half of the specimen by calcite recrystallization. Some nuclei are characterized by black or very dark luminescence.

### *7.2.3. Dolomite dull to bright red CL*

Three dolomitized samples show dull to bright red luminescence response (17NC37, 17NC25, 19NC13c) (Fig. 7.8b, f; 7.10). The CL intensities are variable. For example, the sample 17NC37 is characterised by quite homogeneous and rather dull combined with some brighter areas, while the sample 19NC13c shows an intense dolomitization, almost total, with thick overgrowth rims combining very bright to dark red colours. Recrystallization of calcite matrix infers dedolomitized faces and/or nuclei. Features of strong deformation are observed in the dolomite crystals (i.e. sample 17NC37) by dolomite porphyroclasts development and featuring small-scale folds (Fig. 7.10).



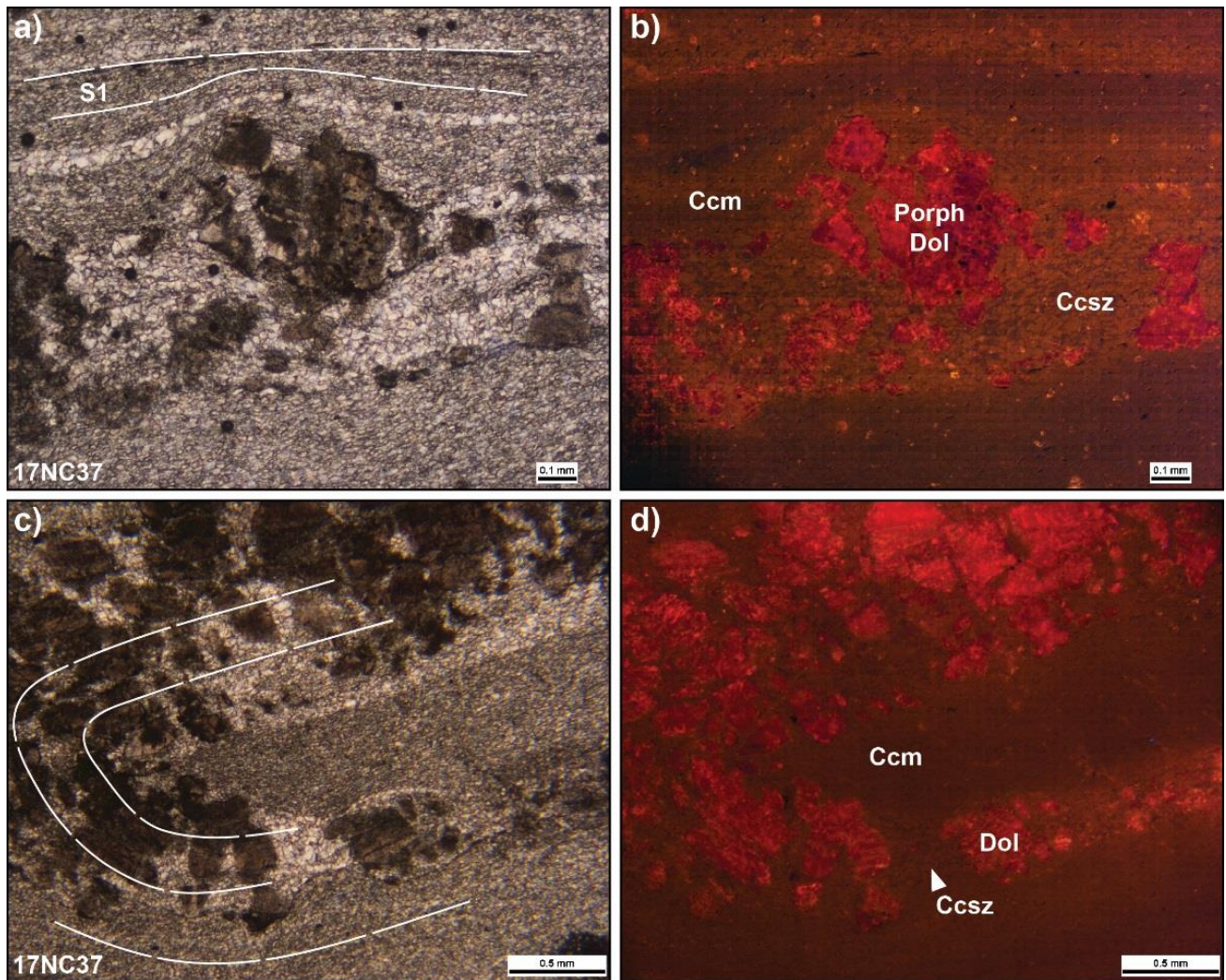


**Fig. 7.10.** Transmitted (left) and cathodoluminescence (right) light from Upper Cretaceous limestones of the ECM showing the response of the dolomite phase in a deformed sample. Intense red luminescence in polymodal planar-p dolomite performing porphyroclasts (a, b) and small-scale folds (c, d). Shadow zones are developed in between the dolomite crystals, occupied by calcite phase performing larger grain-size than the recrystallized matrix. Ccm: calcite matrix; Porph Dol: porphyroclasts of dolomite; Dol: dolomite; Ccsz: calcite shadow zone.

#### 7.2.4. Complex dolomitization processes

Some specific analysed samples are characterized by complex dolomitization textures. Multiple zonations are developed by cortical overgrowths on previous dedolomitized and altered core nuclei (Fig. 7.9b) and usually display a varied range of CL colours from dark yellow to bright magenta and dark violet or even dull luminescence by strong zonation (e.g. Fig. 7.9b, d). Orange or bright yellow nuances conform the core of dolomite crystals. Idiomorphic crystals characterize the late stage of

overgrowth development. Those samples evidence the coexistence of different dolomitization events, displaying heterogeneous CL (e.g. Fig. 7.9b, d). For example, in sample 17NC35, dull-violet dolomites were developed next to bright and zoned ones. Finally, different intensities of dedolomitization processes affect most of the dolomite crystals sometimes replacing up to the half of them by calcite matrix recrystallization (e.g. Fig. 7.8f; Fig. 7.9b, d).

### 7.3. Implications and conclusions

As previously envisaged, the main activators and quenchers of luminescence response in carbonates (Mn and Fe) are intimately related to the redox conditions of the parental fluid. Normally, burial fluids provide darker colours or dull intensities, while meteoric fluids turn into brighter response. Our cathodoluminescence results show a wide variety of colours and intensities in both dolomite and calcite phases stating for a diagenesis occurred under very variable environmental conditions. EMPA analysis from five samples of the overturned limb (Table 5.2) confirm the existence of enough Mn content in the crystal lattice structure to become a CL activator. Fe content is heterogeneous and usually higher in the dolomite phase, where darker zonations are developed (e.g. Fig. 7.9b).

Some calcite in a few samples show dull or dark blue colours (e.g. Fig. 7.4), probably as a consequence of low Mn content invoking for a specific and chemically stable origin into the depth, not affected later by meteoric sources. Some of them are almost completely represented by blue colours (e.g. 17NC19 in Fig. 7.4a) in the calcite matrix, evidencing recrystallization processes occurred in depth. Some others are represented by large blue calcite crystals, with bright yellow rims (e.g. Fig. 7.4d), filling the porosity voids probably developed during dolomitization processes. In that case, the last stages of recrystallization were assisted by meteoric fluids due to the colourfulness and the high intensity of CL in the crystal rims. Nonetheless, most of the samples are mainly represented by yellow colours, even the late calcite veins (e.g. Fig. 7.8d), indicating a higher mixture of fluid sources, whether meteoric or hydrothermal. Core and rim textures preserved in sample 17NC27 attest for grain-size increase during dynamic recrystallization. This increase of grain-size was not only driven by solid-

state diffusion but also assisted by fluid flow, as it is evidenced by the change of trace element content in calcite grains. From these observations, perhaps the term of blastomylonites is probably more coherent to describe this sample as deformation produced an increase of grain-size respect to the original (original grain size approx. 21.6  $\mu\text{m}$  from preserved nuclei). Related to deformation, the fluids involved in that processes have been commonly reported by CL and may induce the rock weakening accelerating solution-transfer processes by enhancing the ductility of rocks (e.g. Hobbs, 1984; Kronenberg & Tullis, 1984; Mainprice & Paterson, 1984; Tullis & Yund, 1989; Holyoke & Kronenberg, 2013; Wintsch & Yeh, 2013). The identification of calcite veins in the ECM is mainly related to the post-deformation event but not in the pre- or syn-event. Strong recrystallization difficult the preservation of these early structures.

Luminescent response of dolomite crystals shows an assorted variety of orange-red to purple colours along the samples. Dolomite growth is usually performed heterogeneous with well-developed zonations (Fig. 7.8a), and features of complex overgrowths with multiple nucleation events are also identified (Fig. 7.9). Complex dolomitization and matrix recrystallization processes are widespread along the massif, in both large- and small-scale, which attest for a very changing chemistry composition of the pore fluids (Choquette & Hiatt, 2008 and references therein). In some samples (e.g. Fig. 7.9b) those heterogeneous dolomites coexist with other family of homogeneous and slightly altered dolomites. The first type is usually affected by dedolomitization and/or multiphase growth accounting for a very dynamic environment, probably during the main deformation stage in ductile conditions. While the violet homogeneous dolomites, quite unaltered, suggest a post-deformation origin in relatively stable conditions and probably in the depth due to its low luminescence. Dolomitization processes are mainly attributed to the pre-ductile event, usually emplaced forming strata-bound geometries and usually affected by high fluid mixing activity, resulting in multiple overgrowth rims with different colours and intensities.

Three different types of partial dolomitization textures have been recognized in the upper Cretaceous limestones of the Eaux-Chaudes massif, with a polymodal crystal size distribution and planar crystal shape. Some of them have emplaced prior or during the ductile deformation event due to certain

folded features identified according to alpine deformation patterns (e.g. Fig. 7.10). Dolomite porphyroclasts are developed in the most deformed limestones and attest for a non-coaxial deformation due to its asymmetry. Heterogeneous CL response attest for a mixing of fluids (probably diagenetic and meteoric), while the homogeneous colours and unaltered appearance are interpreted to be emplaced during a period of stable diagenetic environment in the post-deformation.

To conclude, calcite crystals are affected by dynamic recrystallization processes, also identified by cathodoluminescence, occurred during the climax of the main ductile event replacing other calcite crystals (e.g. Fig. 7.5f) or even dolomite ones. Indeed, dedolomitization is developed (e.g. Fig. 7.9). The homogeneity of calcite colours attests for stable diagenetic conditions or a total chemical reset of the crystals by late and strong recrystallization. Grain boundary diffusion by assisted by fluids is also identified in some samples. On the other hand, dolomites show heterogeneous colours and intensities, attesting for a development mainly in the pre- and syn-deformation, but also in posterior stages, due to preserved calcite dissolution processes (dedolomitization), overgrowth zonations, folded dolomite crystals and multiple nucleation points. Dolomitization is developed in a more changeable diagenetic environment expressed by the strong heterogeneity in CL colours, and in with strata-bound geometries at large-scale, which may be consciously explored in future works.

All those characteristics play key role in the fabric evolution and may be observed by CL analysis. For the rocks of the ECM, however, is difficult to exactly attribute those processes to specific deformation steps due to the strong recrystallization and multiple fluids that affected diagenetic and metamorphic processes pre-, syn-, and post-ductile deformation.



## Chapter 8: General discussion

### 8.1. Alpine deformation of the west-central Pyrenean hinterland

#### 8.1.1. The upper Cretaceous carbonates of the Eaux-Chaudes massif

The classical structural interpretation of the Eaux-Chaudes massif proposed by Ternet (1965), and subscribed by successive works (e.g. Déramond et al., 1985; Alhamawi, 1992; Izquierdo-Llavall et al., 2012, 2020; Dumont et al., 2015; Cochelin, 2016), corresponds to a thrust duplex of upper Cretaceous rocks developed during the Alpine orogeny. The contractional deformation that occurred in the upper parts of the collided margins (Iberian and European) has been identified mainly as brittle along the Pyrenean belt (dominantly thrusts and fault-related folds related to faults developed in relatively shallow conditions), including that attributed to the ECM. Nevertheless, Ternet (1965) elaborated a series of sections across the massif, fairly consistent with the cropping geology, evidencing large-scale ductile features (i.e. Pic de Ger folds, Fig. 8.1) and also a small recumbent fold reported for the Cézy peak (cf. Fig. 1.5a).

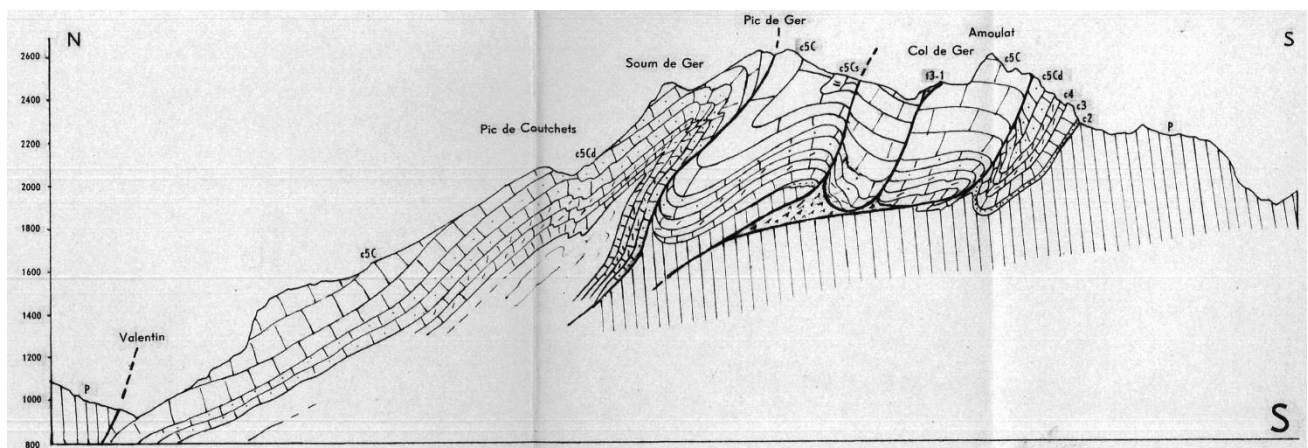


**Fig. 8.1.** Cross-section from Ternet (1965) of the Pic de Ger massif showing folding of the upper Cretaceous rocks and interpreted upper Triassic Keuper rocks as an autochthonous unit.

Ternet proposed the whole massif to conform a unique structural unit affected by similar deformation features (folds and thrusts). Upper Triassic Keuper evaporites and ophites were considered autochthonous, coming from the main unconformity between the Cretaceous and the Paleozoic basement and squeezed along fault zones (e.g. Fig. 8.1). The klippen of Paleozoic rocks on top of the upper Cretaceous (cf. Fig. 1.5) were proposed as roof thrusts coming from the north. Successive works maintained this structural framework for more than 50 years.

The revision performed in the present thesis led to the proposal of an alternative structural model and tectonic evolution of the massif, invoking ductile in unexpected moderate temperature and lower green-schist metamorphic conditions for the Alpine Pyrenees. For the first time a large ductile recumbent fold (the Eaux-Chaudes fold nappe, ECFN) has been proposed for the upper Cretaceous carbonates, and although it represents only the western portion of the ECM, strong ductile deformation is spread along the massif. Following Ternet's (1965) view, which we support, the upper Cretaceous rocks of the ECM may be subdivided into two domains according to the nature of the basement: 1) the granite domain (Eaux-Chaudes granite) or western sector and 2) the Paleozoic metasediments domain (i.e. Devonian limestones, schists) or eastern sector. Indeed, from the structural point of view, there is marked lateral variation, where different units may be defined (cf. Fig. 4.3). Thus, we can talk of the Eaux-Chaudes Nappe (ECN) conforming an important allochthonous unit which is in turn subdivided into two different sectors: 1) the ductile km-scale recumbent fold nappe (ECFN) and 2) the Eaux-Bonnes thrust unit not showing such a prominent structure. A complex transfer zone (Gourzy transfer zone) separates both domains and controls the structural development, guided by the rheological and structural inheritance of basement. In the upper Cretaceous of the ECN footwall, we can differentiate 3) the weakly deformed autochthon of the Ossau valley, Plateau d'Anouilhas and Montcouples peak area (basically, footwall of the ECFN), and 4) the strongly deformed autochthon corresponding to the Pic de Ger fold-thrust fan (footwall of the Eaux-Bonnes thrust). The Eaux-Chaudes massif is clue for the recognition of ductile deformation developed during the Alpine collision in the Axial Zone of the Pyrenees, as to the east there are no more evident markers to easily unravel it, such as post-Variscan rocks.

### 8.1.2. *The upper Triassic of the Eaux-Chaudes massif*

Contrary to what was classically proposed, there is no evidence of upper Triassic Keuper facies in the main unconformity between the Paleozoic basement and the upper Cretaceous cover of the ECM. The origin of the preserved ophiolites and Muschelkalk-Keuper rocks is attributed to an allochthonous sheet coming from the north, the known Bedous Unit (cf. Fig. 1.1), emplaced by the Lakora thrust system on the upper Cretaceous rocks before the initiation of the ECFN (cf. Figs. 4.16, 4.17). These weak Triassic rocks, probably containing salt originally (later squeezed and eroded-dissolved), facilitate the development of the large recumbent fold by providing an efficient upper detachment. Witness of this process are small slices of Triassic that remain trapped in between the Cretaceous rocks and can be considered as tertiary welds (*sensu* Jackson & Hudec, 2017), i.e. from the synclinal tightening in the western domain (Fig. 4.7), or from the inversion of extensional faults in the east (Fig. 4.15). The origin of the extensional faults is attributed to the early steps of the main deformation event, in the footwall of the advancing Lakora system. During compression, ophiolites and Muschelkalk rocks were down-dropped and trapped, successively, in between the Cretaceous limestones.

### 8.1.3. *The Paleozoic rocks of the Eaux-Chaudes massif*

The Paleozoic rocks have been considered to be allochthonous units emplaced on the upper Cretaceous rocks by discrete thrusts (Ternet, 1965). This is in part valid for the Paleozoic nappes of Montagnon d'Iseye, Montagne Verte and Cinq-Monts (MIN, MVN, 5MN, respectively), which we interpret to be thrust and detached in the upper Paleozoic (Silurian slates) so is the ECFN, lower in the pile. Otherwise, metasediments from the core of the ECFN are involved in the recumbent fold structure here proposed, with reverse polarity in the overturned limb. This is a clear sign of marked Alpine ductility affecting the pre-Mesozoic rocks, difficult to identify in the areas also affected by the Variscan orogeny, but without post-Paleozoic markers. The Paleozoic units mentioned above, emplaced over the ECN, and also developed recumbent folds during the Alpine orogeny evidenced by large overturned limbs, which are defined by lower Triassic Buntsandstein. Those recumbent folds

in the Paleozoic were commonly attributed to the Variscan orogeny (e.g. Aerden & Malavieille, 1999; Matte, 2002, and references therein; Bastida et al., 2014) accounting for a ductility only envisaged for this orogenic period.

#### *8.1.4. The fate of the upper Iberian margin*

Kinematic evolution schemes proposed for the upper Iberian rifted margin of the west-central Pyrenees (e.g. Teixell et al., 2016; Labaume & Teixell, 2020) take into account the well-preserved Mesozoic outcrops and account for simple transition between thin- and thick-skinned domains, the detached North Pyrenean Zone and the Paleozoic-bearing antiformal stack to the south, respectively. Otherwise, the dimensions and geometry of the latter are poorly constrained from the lack of good quality geophysical data, and limited surface exposure. The reconstructed geometry and style of the Iberian rifted margin in the post-rift stage (e.g. Teixell et al., 2016; Fig. 1.3) is similar to stretched margins of the Parentis basin reported by Bois et al. (1997) and Pinet et al. (1987).

The evolution schemes constructed in this thesis (cf. Figs. 4.16, 4.17) focus on the deformation of the uppermost Iberian margin, invoking basement-involved thin-skinned nappes (sensu Pfiffner, 2017) with ductile/plastic conditions mainly favoured by moderately high temperatures and weak levels (Keuper evaporites and Silurian slates). The Lakora thrust *s.l.* emplaces the detached Mesozoic sediments of the former hyperextended rift on top of the nappe stack of the ECM by true thin-skinned brittle deformation. In the study area, the Paleozoic shortcut reported in the Igountze massif (Teixell, 1993) is not developed, but there is an equivalent in the allochthonous Mendibelza conglomerates representative of the necking zone of the former upper margin. The basement antiformal stack (Gavarnie thrust and underlying ones), which is the last to be emplaced, developed by true thick-skinned tectonics, enhancing the structural relief, and favouring the exhumation of the study area, leading to the late north-directed backfolding in the ECM. The ECM, though, is interpreted to conform a ductile transition zone between the true thin-skinned and true thick-skinned deformation characterized by an intense simple shear regime of deformation favoured by the two detachment



levels, Silurian slates at the bottom and Triassic evaporites at the top, and by the forestop effect of the Eaux-Chaudes pluton (Fig. 8.2). This hypothesis perhaps would lead to the reconsideration of Alpine ductile deformation of the upper crust in future works, especially for the Iberian plate margin.

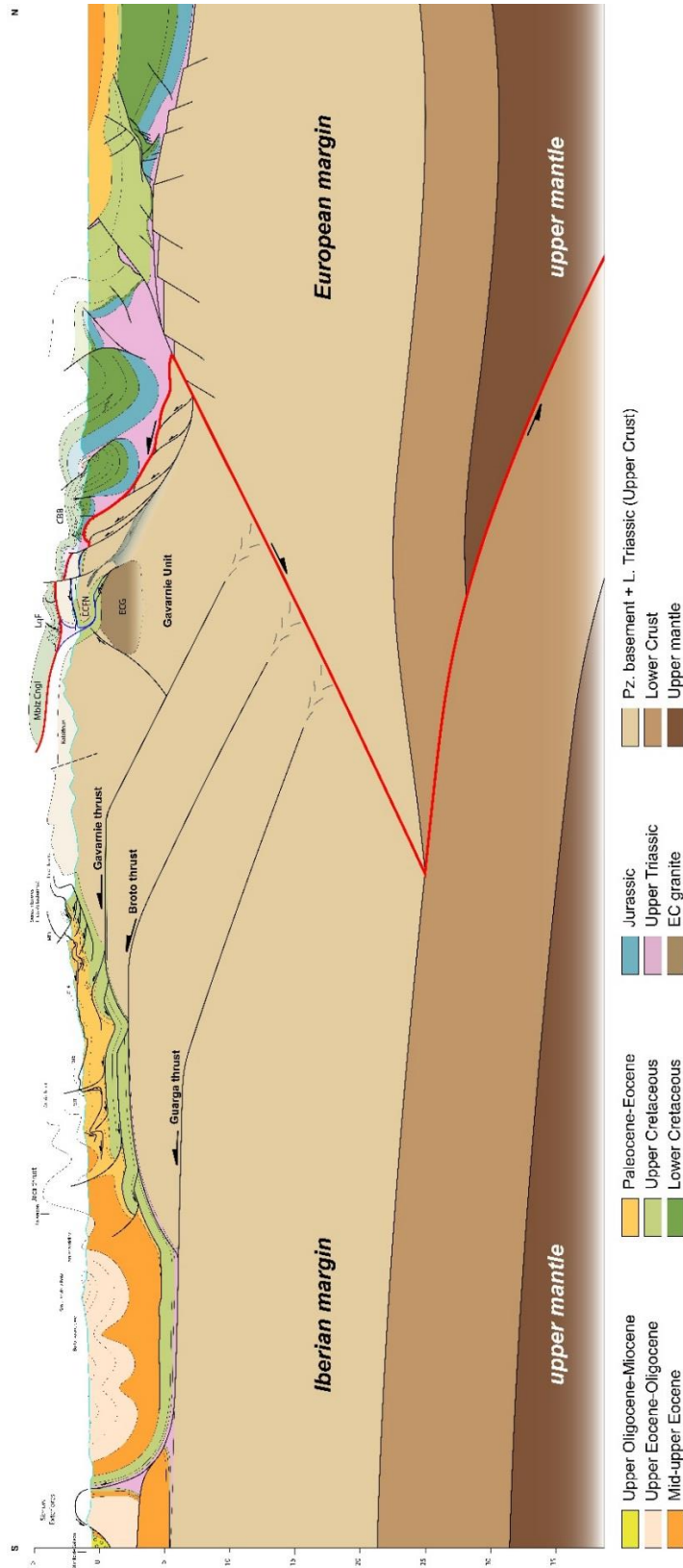


**Fig. 8.2.** Crustal cross-section compilation from Labaume et al. (1985), Biteau et al. (2006), Teixell (2016) and Labaume & Teixell (2020). Which shows the structural position of the ECM in the structural framework of the Pyrenean belt and the complexity of the root of the main crustal thrusts. Note the ductile thin-skinned thrusting in between the detached North Pyrenean Zone and the Paleozoic basement. Red line corresponds to the suture and the detachment of the former rift axis and Mesozoic cover by the Lakora thrust.

## 8.2. Paleotemperature of the Iberian plate

The high paleotemperatures recorded in Mesozoic rocks of the Pyrenees are all attributed to the mid-Cretaceous hyperextension with the mantle exhumation and hydrothermal fluid circulation (e.g. Clerc, 2012; Clerc et al., 2015, 2016; Chelalou et al., 2016; Menant et al., 2016; Villard, 2016; Corre, 2017; Ducoux, 2017; Espurt et al., 2019; Izquierdo-Llavall et al., 2020; Saspiturry et al., 2020; Ducoux et al., 2019, 2021). In the west-central Pyrenees high thermicity is specifically reported for the rift axis sediments of Jurassic to lower Cretaceous age of the Chaînons Béarnais Belt. The compilation performed in this work for the maximum paleotemperatures in the upper Cretaceous rocks of the Iberian plate (Fig. 5.2) are mainly attributed to the burial effect from the Alpine orogeny, and show a regional increase from west to east and from south to north, with a maximum located in the ECM by an average value of approximately 350°C. The heat map proposed for this area (Fig. 5.13) illustrates the maximum thermal peak in the Eaux-Chaudes carbonate massif by red colours, and the transition to lower paleotemperature values by yellow and green. The western closure of the Axial Zone accounts for moderate temperatures (<300°C) in the basal layers of the upper Cretaceous.

Maximum temperatures of 360°C, obtained for the Cretaceous carbonates in the ECM and recorded ductile features, suggest moderate deep burial deformation conditions of approximately 10-12 km if a standard orogenic geothermal gradient of 30°C/km is assumed. This is in line with the tectonic evolution proposal by Labaume et al. (2016) (e.g. Fig. 8.3), who inferred 8 to 10 km of burial for the Eaux-Chaudes massif, due to the general foreland flexure of the Iberian plate by late Eocene times. The heating effect occurring from the Paleozoic basement especially in the ECM, is proposed for the basal facies of Cretaceous limestones. The regional decrease of thermicity to the west and south of the Iberian margin could be attributed either to the regional flexure and/or to a differential exhumation due to the west plunge of the Axial Zone. This favoured the preservation of higher stratigraphic levels south and westwards, which were less buried and consequently affected by low heating. The exhumation of ECM also warns of the large amount of the potentially eroded stratigraphic record that enhanced the heating of the Cretaceous in the massif.

High geothermal gradients, as relict of the Mesozoic thinning phase, are proposed for other parts of the Iberian paleomargin (e.g. Bellahsen et al., 2019) from the elevated paleotemperatures provided. Nonetheless, the available observations in the ECM cannot unequivocally discriminate in between deep burial and/or high geothermal gradients as the constraints in causing the elevated thermicity. This represents an avenue for future research in exploring the origin of the elevated temperatures in the post-Paleozoic rocks.

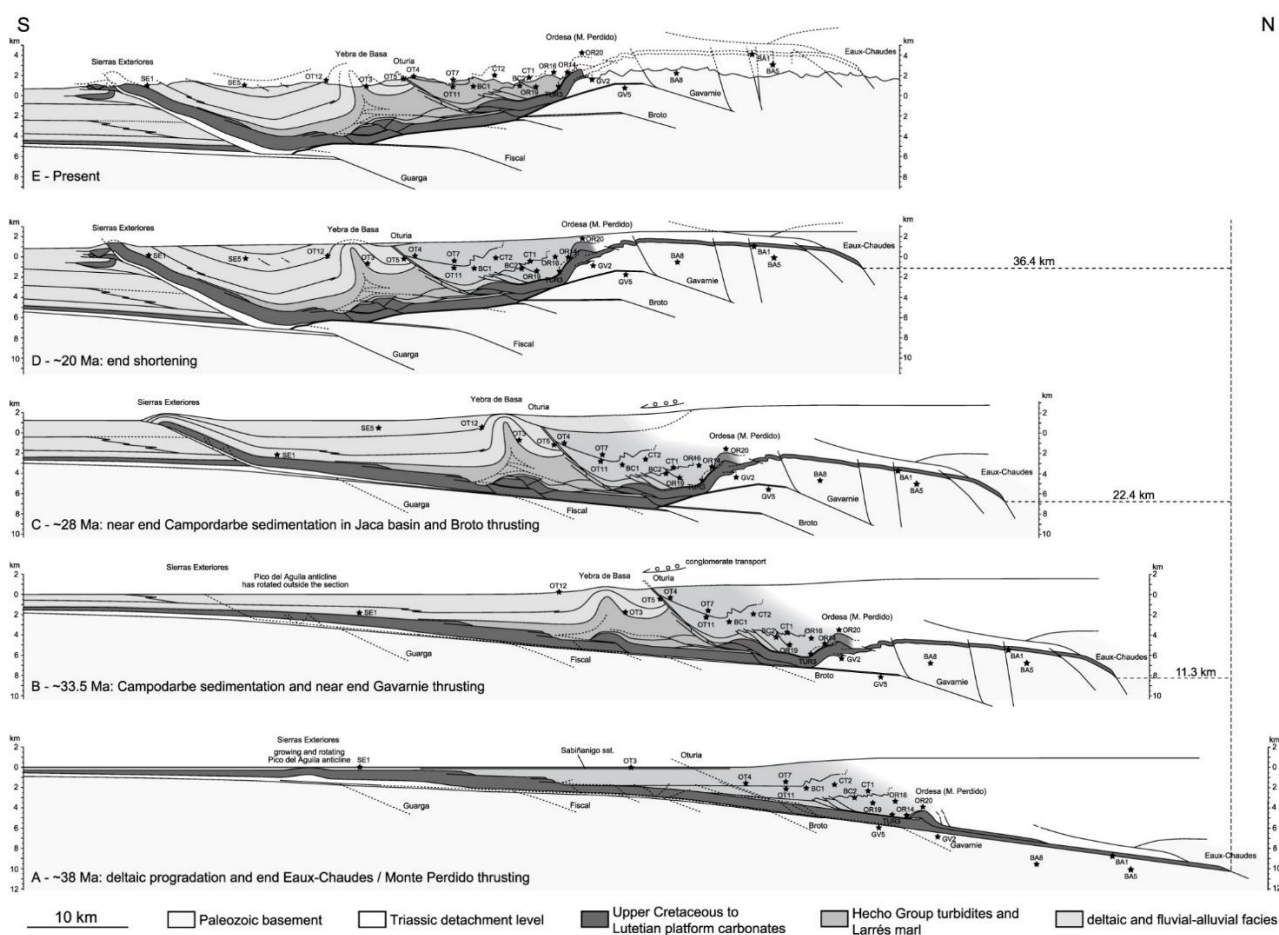


**Fig. 8.3.** Tectonic evolution of the eastern Jaca Basin and Axial Zone from Labaume et al. (2016) up to the interpreted ECM.

### 8.3. Microfabrics

Microstructural analysis of crystalline plasticity has been performed for the first time in the upper Cretaceous of the Pyrenees. Paleopiezometric estimations, domains of strain partitioning and

dominant mechanisms of deformation are led by mineral phase content and its distribution, and the physical conditions of deformation (temperature, strain rate). Half of the analysed samples can be considered monomineralic calcite aggregates while the other half contains a varied range of second phase content. Mean grain sizes measured in deformed samples account for a fine-grained recrystallized calcite matrix, in the range of 12 to 30  $\mu\text{m}$ . Piezometer indicates low differential stress between 20 to 60 MPa.

Deformation in the ECM occurred under greenschist facies metamorphic conditions (Caldera et al., 2021) and assuming dynamic equilibrium. For carbonate mylonites, temperatures as those recorded favour dislocation creep as the main deformation mechanism (e.g. Schmid & Handy, 1991; Kohlstedt et al., 1995). Results of microfabric strength and deformation mechanism maps (Figs. 6.8 and 6.15) are in line with the previous statement by the strong fabrics of calcite matrix (i.e. CPO) and from the relation between the mean grain size according to temperature in deformation mechanisms maps. From the latter it is deduced that dislocation creep acts as the main mechanism assisted by diffusion (Fig. 6.15c). Second phases strongly conditioned the strain localization in the calcite matrix by the Zener effect (Herwegh & Berger, 2004) inducing variations of effective stress and in grain size reduction by the pinning effect (e.g. Drury & Urai, 1990; Olgaard, 1990; Krabbendam et al., 2003; Herwegh & Berger, 2004; Ebert et al., 2008; Linckens et al., 2011). Other mechanism of deformation is twinning, mainly observed in large calcite host grains, which also have a high portion of internal misorientations, not identified in the smaller grains due to the higher effectiveness of recrystallization mechanisms. Grain growth occurred in the strongly strained monomineralic mylonites (in comparison with the original, fine-grained micritic limestones), and in the strain shadow zones located on the border of large second-phase porphyroclasts, such as dolomite or quartz, or fossils (e.g. Figs. 6.12, 6.13). Dynamic recrystallization by grain boundary migration assisted by fluids was also identified by cathodoluminescence inspection by brighter violet rims in dull or dark blue calcite grains located in the shadow zone of a dolomite porphyroclasts (Fig. 7.5), and also by dedolomitization processes led by calcite matrix recrystallization (e.g. Figs. 7.8f, 7.9d).



Second phases are affected by brittle-ductile deformation. Brittle features in dolomite crystals are recognized by extensional fractures orthogonal to the main foliation (e.g. Fig. 6.13), and in chert nodules by rigid bookshelf-type structures. Ductility is recorded by small-scale folds in both phases and by undulose extinction in quartz crystals.

Deformation domains in the ECM are clearly distinguished by the microfabrics results. The overturned limb of the ECFN and the Pic de Ger fold-thrust fan correspond to the highly strained areas of the massif, while the normal limb of the recumbent fold and its autochthon remain almost unaltered. Localisation of the deformation is mostly related to the contrasted rheology between the Paleozoic basement and the Mesozoic rocks (commonly near the unconformity), where strong microfabrics were developed, and the occurrence of detachment levels, such as Silurian and Triassic evaporites. The latter plays a key role in preventing the strain localization for the normal limb of the ECFN from the MIN emplacement. Microfabrics are there weakly developed, even after the emplacement of the overlying Montagnon d'Iseye nappe. On the other hand, deformation recorded in the footwall of the Eaux-Bonnes thrust is much more intense. Fluid circulation is evidenced by large and folded calcite veins.

In essence, temperature and microstructure observations account for non-expected deformation conditions for the upper Cretaceous rocks of the Alpine Pyrenees.

#### 8.4. Diagenetic evolution

Cathodoluminescence analysis accounts for a complex diagenetic evolution with multiple dolomitization events occurring in the pre- syn- and probably post-tectonic stages, and for intense calcite matrix recrystallization of ductily-deformed samples, which sometimes caused dedolomitization (Fig. 8.4). Pre-deformational stratabound dolomitization is identified from large folded and boudinaged dolomite bodies in between the large and moderately thick calcite layers (cf. Fig. 6.1). It is also observed at the microscale by the multilayering of these two mineral phases. Complex zonation or overgrowth rims in dolomites, is evidenced by amorphous cores and external

well-crystallized idiomorphic faces (e.g. Fig. 7.9b). Different dolomitization stages are perceived from the varied range of CL colours, but the attribution and recognition of each stage individually become challenging. The violet colours observed in the common external rims and also forming complete dolomite crystals of some samples, are considered to belong to the latest phase developed in the final deformation or post-deformation event. The low reset of the dolomite and multiple CL account for a pre-tectonic origin, maybe sedimentary, with abundant fluid mixing containing different trace elements recorded by the abrupt changes in colours and intensities.

Calcite is well-reset along the massif by dominant and homogeneous yellow colours along the crystal lattice. Fluid-assisted deformation enhance the brighter response of the calcite crystal borders, sometimes by the same CL of the core as a result of the occurrence of diffusion processes. Usually, late crystallization of this phase occurred by crystals showing blue colour or non-luminescent response. Syntectonic calcite veins are difficult to recognise due to the strong matrix recrystallization and homogenization of CL. The intensity of calcite recrystallization evokes for dedolomitization processes, sometimes really intense, and the total replacement of dolomite crystals by calcite phase preserving the original rhombohedral shape.

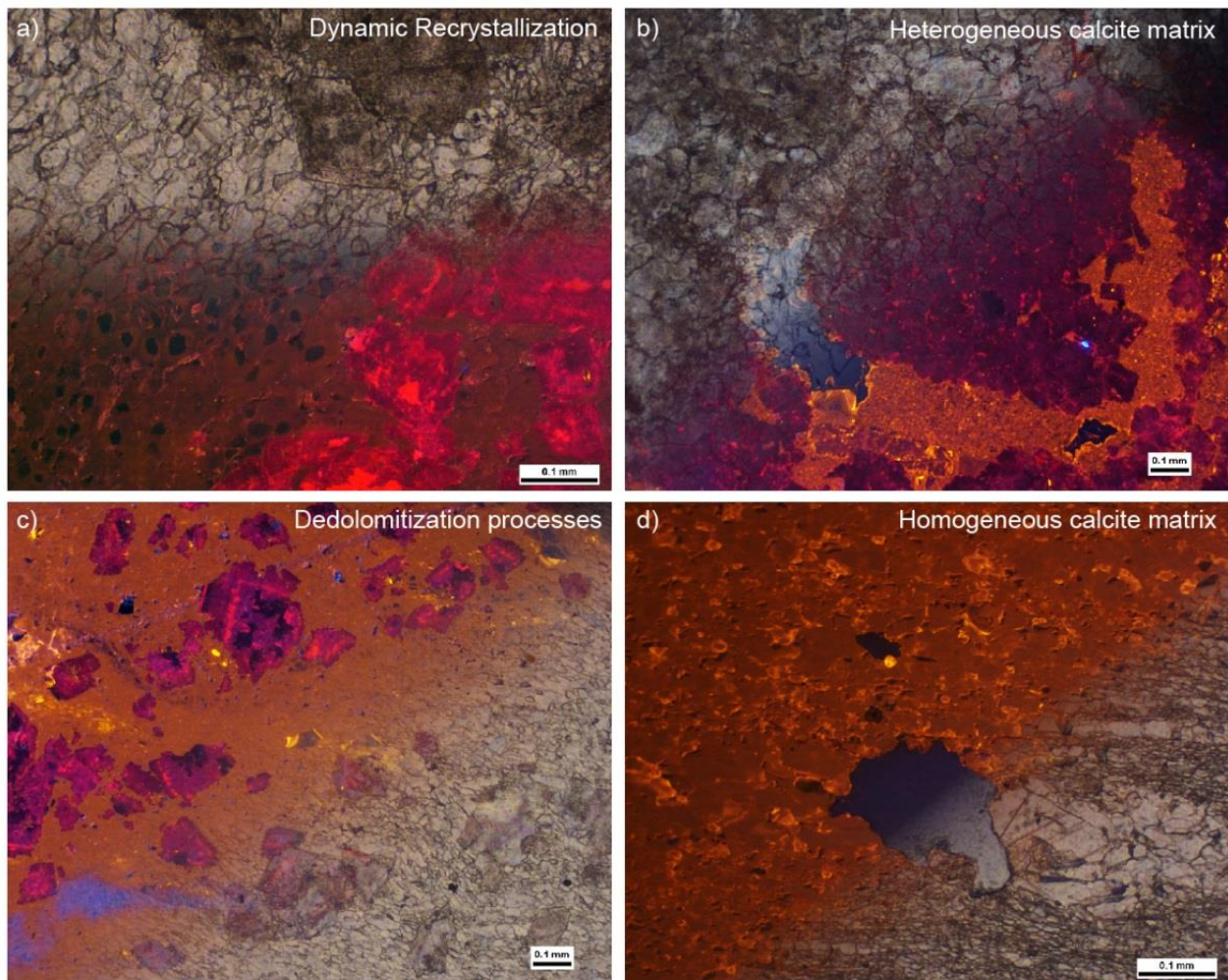


**Fig. 8.4.** Summary of the features observed by cathodoluminescence analysis in all the carbonate phases, from colour and intensity heterogeneities to dedolomitization processes and strong calcite matrix recrystallization.

## 8.5. Orogen-scale implications

The new proposal for the structure of the western Eaux-Chaudes massif, the ECFN, has similarities to other recumbent structures developed in larger orogens, such as the Helvetic Morcles-Doldenhorn nappes in the Alps. The latter are characterized by long overturned limbs and also involve low-grade Mesozoic metasedimentary rocks (e.g. Ramsay, 1981; Burkhard, 1988; Pfiffner, 1993; Casey & Dietrich, 1997; Herwegh & Pfiffner, 2005), although the Eaux-Chaudes nappe lacks the second-order folds conspicuous in the Helvetic nappes. Apart from the geometrical similarities, the temperature conditions and grain size of carbonate sediments are also comparable. Austin et al. (2008) obtained

average grain sizes between 7 and 22  $\mu\text{m}$  for samples deformed in a temperature range of 337-358°C in the Morcles nappe. Similar results were reported for the Doldenhorn and Glarus nappes by Herwegh & Pfiffner (2005) and Ebert et al. (2007, 2008). A late deformation stage is related, in both orogens, to more brittle deformation linked to the late exhumation processes.

Inheritance and structural reactivation may have determined the development and evolution of the ECM during the Pyrenean collision. Detachments on top of the Paleozoic basement led the development of kilometric fold nappes, favoured by the rheological and thermal constraints.

The analogies with the structural style reported in larger mountain belts pose the scope in the challenge of deformation recognition in the Pyrenean hinterland. Often the accessible outcrops of internal orogenic zones are dominated by rocks affected by multiple Wilson cycles including collision and rifting, hampering the attribution of the features and structures recognized to a specific event. The results of this work are a good example of the unperceived Alpine ductile deformation in the Pyrenean Axial Zone, which may be extensive eastwards.



## Chapter 9: Conclusions

In this chapter I summarize the main conclusions that resulted from the multidisciplinary structural and paleothermal study carried out in Eaux-Chaudes massif and vicinities to gain insights of the Alpine deformation and structural configuration of the hinterland of the Pyrenees.

### 9.1. Reinterpretation of the large-scale structure

- An inverted stratigraphic succession of Paleozoic and Mesozoic rocks has been identified for ~5 km in the Ossau valley by the occurrence of, also inverted, lower Triassic Buntsandstein preserved at the boundary. In addition, strong ductile deformation recognized in the overturned limestone panel led to the proposition of a style of deformation reported for the first time in the Alpine Pyrenees. It consists of a km-scale large recumbent fold nappe involving Paleozoic metasediments on its core, here named the Eaux-Chaudes fold nappe (ECFN).
- The ECFN changes laterally to the east to a simple thrust nappe, soled by the Eaux-Bonnes thrust (Bresson, 1903), where the Cretaceous of the hanging wall has been completely eroded. Both structures (fold nappe and thrust nappe) conform the large allochthonous unit of the massif named the Eaux-Chaudes nappe (ECN). The transition is controlled by a high-angle, west dipping transfer fault system, causing the recess of the nappe.
- The ductility observed in the overturned limb of the ECFN is also evident in the footwall of the Eaux-Bonnes thrust, which features an imbricate fold-thrust fan system, here named the Pic de Ger fan. Impressive and unexpected tight folds, associated with thrust faults, shape the landscape of this eastern area. Ductile deformation in the ECM is expressed by mylonitic foliation, stretching lineation, intrafolial folds, folded and boudinaged dolomite bodies, and composite S-C structures. Intracretaceous detachment levels have been identified in the Cenomanian-Turonian section of the fold-thrust fan, solving complex ductile detachment folds.

- Alpine folding also involves the Paleozoic metasediments, not only on the ECFN core. Three successive nappes overlie the Eaux-Chaudes massif, sometimes featuring recumbent folds in their frontal part, again identified by the occurrence of Buntsandstein deposits indicating overturned stratigraphy. Classically, recumbent fold structures in the Paleozoic basement are attributed to the Variscan orogeny, but the observations of this thesis demonstrate that tight folding of Paleozoic rocks can happen during the Alpine orogeny as well. The nappes reported in this work are detached in the Silurian slates, due to the involvement of this unit in the core of the ECFN as a large slice pinched by the Devonian limestones from the normal and the overturned limbs.
- The upper Triassic Keuper rocks of the Eaux-Chaudes massif are interpreted as the remains of an allochthonous sheet (Bedous Unit) emplaced in the early stages of the Alpine deformation. Triassic evaporites were clue in the development of recumbent folds and also in the emplacement of the nappes by providing an upper detachment reducing frictional forces. Triassic evaporites were expelled and pinched during subsequent folding of the underlying Cretaceous limestones, resulting in tertiary weld-like structures.
- The main cause for the transition from the fold nappe to the fold-thrust fan is the abrupt change in the rheology of the Paleozoic basement, from the Eaux-Chaudes granite pluton in the west to the Devonian limestones and schists in the east, and the Gourzy transfer zone. The pluton faced strong opposition to the deformation and localized it into the overturned limb of the recumbent fold. Devonian metasediments enabled the deformation distribution along the stratigraphic pile.

## 9.2. Paleothermal record of the Alpine orogeny

- Peak temperatures recorded in the upper Cretaceous carbonates of the ECM by Raman and microprobe analysis are around 320-360°C. These results are consistent with the observed ductile deformation and reveal unexpected conditions in the lower greenschist metamorphic

facies, reported for the first time for the Pyrenean orogeny. The source of this elevated thermicity is tentatively attributed to deep burial by nappes and syntectonic sediments aided by the orogenic flexure. A possible contribution was by heating from the Paleozoic basement after a persistent geothermal gradient from the hyperextension, by the effect of “radioactive” rocks (e.g. granite and zircon grains), or hydrothermal fluid circulation.

- A relatively high geothermal gradient (~30-45°C) can be deduced from the upper Cretaceous limestone samples at different elevation.

### 9.3. Micro-scale structure

- This work documents for the first time, by means of thin section and EBSD analysis, the microfabrics of upper Cretaceous rocks strongly strained by the Pyrenean orogeny. In the deformed carbonates of the ECM, grain-shape and crystallographic preferred orientation are observed, as well as dynamic recrystallization, suggesting a dominant deformation mechanism of dislocation creep. CPO and IPF results indicate maximum accommodation of crystal plastic deformation by basal-slip along the a-axis and m-axis.
- Paleopiezometric considerations account for a fine recrystallized calcite grain matrix (12-30  $\mu\text{m}$ ) resulting from relatively low stress (20-60 MPa).
- Second phase contents strongly conditioned the strain partitioning in the polymineralic mylonites by its spatial distribution. The pinning effect and the dominance of matrix calcite phase in between large dolomite bodies enhance the grain size reduction, while grain growth was favoured in the shadow zones.
- Ductility is also observed in the dolomite by folding and boudinage, but with a dominant brittle behaviour expressed by common intracrystalline extensional fractures developed in an orthogonal orientation with the main strain and low internal crystal plastic deformation. Quartz grains exhibit dominant brittle deformation, with occasional undulose extinction in thin section.

#### 9.4. Diagenetic evolution

- Strong differences in cathodoluminescence colours and intensities of the calcite phase argues for a diagenesis under very variable environmental conditions. Bright and yellow-orange colours indicate shallow conditions of formation and/or recrystallization, while darker and blue colours account for deformation in deeper environments.
- Strong recrystallization is evidenced by complex dedolomitization processes that occurred in numerous samples, and the homogenization of CL in calcite. Just in one sample from the shadow zone of a dolomite porphyroblast recrystallization is developed partially and calcite dark cores and bright violet rims are preserved.
- Multiphase dolomitization is identified from early altered nuclei and late idiomorphic crystallization. Cathodoluminescent colours are variable, by multiple rims and dolomitization stages.

#### 9.5. Orogen-scale conclusions

- This work poses the scope into the still unconstrained deformation that occurred during the main Alpine collision in the hinterland of the Pyrenean realm, which is attesting to be more intense and ductile than expected.
- Consequently, further work may explore the real implications for large-scale structures in Paleozoic rocks of the Axial Zone, attributed so far to the Variscan orogeny.
- The development of large recumbent structures, common in larger orogens, leads to a rethinking of the deformation processes and geodynamic evolution of the hyperextended margins during the posterior collision, especially for the Iberian margin.
- This work also highlights the importance of field research and recognition of the stratigraphic and structural evidence in the less accessible areas as the strong reliefs of the Eaux-Chaudes massif, due to the common lack of good marker outcrops in the interiors of the orogenic belts dominated by basement rocks.



## Chapter 10: References

- Abd Elmola, A., Charpentier, D., Buatier, M., Lanari, P. & Monié, P. (2017). Textural-chemical changes and deformation conditions registered by phyllosilicates in a fault zone (Pic de Port Vieux thrust, Pyrenees). *Applied Clay Science*, 144, 88-103. <https://doi.org/10.1016/j.clay.2017.05.008>
- Aerden, D. G. A. M. & Malavieille, J. (1999). Origin of a large-scale fold nappe in the Montagne Noire, Variscan belt, France. *Journal of Structural Geology*, 21 (10), 1321-1333. [https://doi.org/10.1016/S0191-8141\(99\)00098-X](https://doi.org/10.1016/S0191-8141(99)00098-X)
- Alhamawi, M. (1992). Sédimentologie, pétrographie sédimentaire et diagenèse des Calcaires du Crétacé supérieur de la Marge Ibérique: Bordeaux 1, 356 p.
- Amieux, P., Bernier, P., Dalongeville, R. & Medwecki, V. (1989). Cathodoluminescence of carbonate-cemented Holocene beachrock from the Togo coastline (West Africa): An approach to early diagenesis. *Sedim Geol*, 65, 261-272.
- Anovitz, L. M. & Essene, E. J. (1987). Phase equilibria in the system  $\text{CaCO}_3\text{-MgCO}_3\text{-FeCO}_3$ . *Journal of Petrology*, 28 (2), 389-415. <https://doi.org/10.1093/petrology/28.2.389>
- Austin, N. & Evans, B. (2007). Paleowattmeters: a scaling relation for dynamically recrystallized grain size. *Geology*, 35 (4), 343-346. <https://doi.org/10.1130/G23244A.1>
- Austin, N., Evans, B., Herwegh, M. & Ebert, A. (2008). Strain localization in the Morcles nappe (Helvetic Alps, Switzerland). *Swiss Journal of Geosciences*, 101, 341-360. <https://doi.org/10.1007/s00015-008-1264-2>
- Austin, N. & Evans, B. (2009). The kinetics of microstructural evolution during deformation of calcite. *Journal of Geophysical Research-Solid Earth*, 114 (B9). <https://doi.org/10.1029/2008JB006138>
- Banner, J. L., Hanson, G. N. & Meyers, W. J. (1988). Determination of initial Sr isotopic compositions of dolostones from the Burlington-Keokuk Formation (Mississippian); constraints from cathodoluminescence, glauconite paragenesis and analytical methods. *Journal of Sedimentary Research*, 58 (4), 673-687. <https://doi.org/10.2110/jsr.58.673>
- Bannère, P., Bois, J. P., Debon, F., Godechot, Y., Mirouse, R., Nicolaï, A., Reyx, J., Ternet, Y. & Villanova, M. (1980). Carte géologique au 1/50000 d'Argelès-Gazost [Geological map of Argelès-Gazost 1/50000]. BRGM, Orléans.
- Barber, D. J. & Wenk, H.-R. (2001). Slip and dislocation behaviour in dolomite. *European Journal of Mineralogy*, 13 (2), 221-243. <https://doi.org/10.1127/0935-1221/01/0013-0221>
- Barbin, V. (1995). Cathodoluminescence of carbonates: new applications in geology and archaeology. *Scanning Microscopy*, 9. <https://digitalcommons.usu.edu/microscopy/vol1995/iss9/9>
- Barker, C. E. & Goldstein, R. H. (1990). Fluid-inclusion technique for determining maximum temperature in calcite and its comparison to the vitrinite reflectance geothermometer. *Geology*, 18 (10), 1003-1006. [https://doi.org/10.1130/0091-7613\(1990\)018<1003:FITDM>2.3.CO;2](https://doi.org/10.1130/0091-7613(1990)018<1003:FITDM>2.3.CO;2)
- Barnaby, R. J. & Rimstidt, J. D. (1989). Redox conditions of calcite cementation interpreted from Mn and Fe contents of authigenic calcites. *Geological Society of America Bulletin*, 101 (6), 795-804. [https://doi.org/10.1130/0016-7606\(1989\)101<0795:RCOCCI>2.3.CO;2](https://doi.org/10.1130/0016-7606(1989)101<0795:RCOCCI>2.3.CO;2)
- Barnhoorn, A., Bystricky, M., Burlini, L. & Kunze, K. (2004). The role of recrystallisation on the deformation behaviour of calcite rocks: large strain torsion experiments on Carrara marble. *Journal of Structural Geology*, 26 (5), 885-903. <https://doi.org/10.1016/j.jsg.2003.11.024>
- Bastida, F., Aller, J., Fernández, F. J., Lisle, R. J., Bobillo-Ares, N. C. & Menéndez, O. (2014). Recumbent folds: Key structural elements in orogenic belts. *Earth-Science Reviews*, 135, 162-183. <https://doi.org/10.1016/j.earscirev.2014.05.002>
- Bellahsen, N., Bayet, L., Denele, Y., Waldner, M., Airaghi, L., Rosenberg, C., Dubacq, B., Mouthereau, F., Bernet, M., Pik, R., Lahfid, A. & Vacherat, A. (2019). Shortening of the axial zone, Pyrenees: Shortening sequence, upper crustal mylonites and crustal strength. *Tectonophysics*, 766, 433-452. <https://doi.org/10.1016/j.tecto.2019.06.002>

- Berastegui, X., Garcia, J. M. & Losantos, M. (1990). Structure and sedimentary evolution of the Organyà basin (Central South Pyrenean Unit, Spain) during the lower Cretaceous. *Bulletin de la Société Géologique de France*, VI (2), 251-264. <https://doi.org/10.2113/gssgfbull.VI.2.251>
- Bergman, T. L., Lavine, A. S., Incropera, F. P. & Dewitt, D. P. (1990). Introduction to Heat Transfer. 2nd ed. New York: John Wiley & Sons, Inc., (Appendix A)
- Bestmann, M. & Prior, D. J. (2003). Intragranular dynamic recrystallization in naturally deformed calcite marble: diffusion accommodated grain boundary sliding as a result of subgrain rotation recrystallization. *Journal of Structural Geology*, 25 (10), 1597-1613. [https://doi.org/10.1016/S0191-8141\(03\)00006-3](https://doi.org/10.1016/S0191-8141(03)00006-3)
- Beyssac, O., Goffé, B., Chopin, C. & Rouzaud, J.-N. (2002). Raman spectra of carbonaceous material in metasediments: A new geothermometer. *Journal of Metamorphic Geology*, 20 (9), 859-871. <https://doi.org/10.1046/j.1525-1314.2002.00408.x>
- Beyssac, O., Simoes, M., Avouac, J. P., Farley, K. A., Chen, Y.-G., Chan, Y.-C. & Goffé, B. (2007). Late Cenozoic metamorphic evolution and exhumation of Taiwan. *Tectonics*, 26. <https://doi.org/10.1029/2006TC002064>
- Biteau, J.-J., Le Marrec, A., Le Vot, M. & Masset, J. -M. (2006). The Aquitaine Basin. *Petroleum Geosciences*, 12 (3), 247-273. <http://dx.doi.org/10.1144/1354-079305-674>
- Blackwell, D. D. & Steele, J. L. (1989). Thermal conductivity of sedimentary rocks: Measurement and significance. In: Naeser, N. D., McCulloh, T. H. (eds). Thermal History of Sedimentary Basins. Springer, New York, NY. [https://doi.org/10.1007/978-1-4612-3492-0\\_2](https://doi.org/10.1007/978-1-4612-3492-0_2)
- Bois, C., Gariel, O., Lefort, J.-P., Rolet, J., Brunet, M.-F., Masse, P., Olivet, J.-L. (1997). Geologic contribution of the Bay of Biscay deep seismic survey: a summary of the main scientific results, a discussion of the open questions and suggestions for further investigations. *Mémoires de la Société géologique de France*, 171, 193-209.
- Bosch, G., Teixell, A., Jolive, M., Labaume, P., Stockli, D., Domènech, M. & Monié, P. (2016). Timing of Eocene-Miocene thrust activity in the Western Axial Zone and Chaînons Béarnais (west-central Pyrenees) revealed by multi-method thermochronology. *Comptes Rendus Geoscience* 348 (3-4), 246-256. <https://doi.org/10.1016/j.crte.2016.01.001>
- Bresson, A. (1903). Étude sur les formations anciennes des Hautes et Basses-Pyrénées (Haute-Chaîne). *Bulletin du Service de la Carte géologique de la France*, 93 (14), 278 p.
- Bresson, A. (1906). Réunion extraordinaire de la Société Géologique de France dans les Pyrénées occidentales en 1906. *Bulletin de la Société Géologique France*, 4<sup>o</sup> série, t. VI, 777-884.
- Bucher, K. & Grapes, R. (2011). Metamorphic Grade. In: Petrogenesis of Metamorphic Rocks. Springer, Berlin, Heidelberg. [https://doi.org/10.1007/978-3-540-74169-5\\_4](https://doi.org/10.1007/978-3-540-74169-5_4)
- Budd, D. A., Hammes, U. & Ward, W. B. (2000). Cathodoluminescence in calcite cements: New insights on Pb and Zn sensitizing, Mn activation, and Fe quenching at low trace-element concentrations. *Journal of Sedimentary Research*, 70 (1), 217-226. <https://doi.org/10.1306/2DC4090C-0E47-11D7-8643000102C1865D>
- Burkhard, M. (1988). L'Helvétique de la bordure occidentale du massif de l'Aar (évolution tectoniques et métamorphique). *Eclogae Geologicae Helvetiae*, 81 (1), 63-114.
- Burnham, A. K. & Sweeney, J. J. (1989). A chemical kinetic model of vitrinite maturation and reflectance. *Geochimica et Cosmochimica Acta*, 53 (10), 2649-2657. [https://doi.org/10.1016/0016-7037\(89\)90136-1](https://doi.org/10.1016/0016-7037(89)90136-1)
- Butler, R. W. H., Tavarnelli, E. & Grasso, M. (2006). Structural inheritance in mountain belts: An Alpine-Apennine perspective. *Journal of Structural Geology*, 28 (11), 1893-1908. <https://doi.org/10.1016/j.jsg.2006.09.006>
- Caldera, N., Teixell, A., Griera, A., Labaume, P. & Lahfid, A. (2021). Recumbent folding in the Upper Cretaceous Eaux-Chaudes massif: A Helvetic-type nappe in the Pyrenees?. *Terra Nova*, 33, 320-331. <https://doi.org/10.1111/ter.12517>
- Canérot, J. (2008). Les Pyrénées: histoire géologique et itinéraires de découverte. Biarritz: Atlantica/BRGM éd., 2 tomes, 646p.

- Cantarelli, V., Aldega, L., Corrado, S., Invernizzi, C. & Casas-Sainz, A. (2013). Thermal history of the Aragón-Béarn basin (Late Paleozoic, western Pyrenees, Spain); insights into basin tectonic evolution. *Italian Journal of Geosciences*, 132 (3), 443-462. <https://doi.org/10.3301/IJG.2012.41>
- Casey, M. & Dietrich, D. (1997). Overthrust shear in mountain building. In: Sengupta S. (eds) Evolution of Geological Structures in Micro- to Macro-scales, 119-142. *Springer*. [https://doi.org/10.1007/978-94-011-5870-1\\_8](https://doi.org/10.1007/978-94-011-5870-1_8)
- Casteras, M. (1956). Calcaire des Eaux-Chaudes (France, Basses, Pyrénées) – Garumnien – Poudingue de Mendibelza. In *Lexique stratigraphique internationale*, 1, 4a VI, Crétacé.
- Casteras, M. & Souquet, P. (1964). Sur la constitution et sur la structure de la couverture crétacée de la Zone primaire axiale pyrénéenne à l'Ouest du Pic d'Anie. *Comptes Rendus de l'Académie des Sciences, Paris*, 259 (17), 2881-2886.
- Chelalou, R., Nalpas, T., Bousquet, R., Prevost, M., Lahfid, A., Poujol, M., Ringenbach, J.-C. & Ballard, J.-F. (2016). New sedimentological, structural and paleo-thermicity data in the Boucheville Basin (eastern North Pyrenean Zone, France). *Comptes Rendus Geoscience*, 348 (3-4), 312-321. <https://doi.org/10.1016/j.crte.2015.11.008>
- Chevrot, S., Sylvander, M., Diaz, J., Martin, R., Mouthereau, F., Manatschal, G., Masini, E., Calassou, S., Grimaud, F., Pauchet, H. & Ruiz, M. (2018). The non-cylindrical crustal architecture of the Pyrenees. *Scientific Reports*, 8, 9591. <https://doi.org/10.1038/s41598-018-27889-x>
- Choquette, P. W. & Hiatt, E. E. (2008). Shallow-burial dolomite cement: a major component of many ancient sucrosic dolomites. *Sedimentology*, 55 (2), 423-460. <https://doi.org/10.1111/j.1365-3091.2007.00908.x>
- Clerc, C., Lagabrielle, Y., Neumaier, M., Reynaud, J.-Y. & de Saint Blanquat, M. (2012). Exhumation of subcontinental mantle rocks: evidence from ultramafic-bearing clastic deposits nearby the Lherz peridotite body, French Pyrenees. *Bulletin de la Société Géologique de France*, 183 (5), 443-459. <https://doi.org/10.2113/gssgfbull.183.5.443>
- Clerc, C. & Lagabrielle, Y. (2014). Thermal control on the modes of crustal thinning leading to mantle exhumation: Insights from the Cretaceous Pyrenean hot paleomargins. *Tectonics*, 33, 1340-1359. <https://doi.org/10.1002/2013TC003471>
- Clerc, C., Lahfid, A., Monié, P., Lagabrielle, Y., Chopin, C., Poujol, M., Boulvais, P., Ringenbach, J.-C., Masini, E. & de St Blanquat, M. (2015). High-temperature metamorphism during extreme thinning of the continental crust: a reappraisal of the North Pyrenean passive paleomargin. *Solid Earth*, 6 (2), 643-668. <https://doi.org/10.5194/se-6-643-2015>
- Clerc, C., Lagabrielle, Y., Labaume, P., Ringenbach, J.-C., Vauchez, A., Nalpas, T., Bousquet, R., Ballard, J.-F., Lahfid, A. & Fourcade, S. (2016). Basement – Cover decoupling and progressive exhumation of metamorphic sediments at hot rifted margin. Insights from the Northeastern Pyrenean analog. *Tectonophysics*, 686, 82-97. <https://doi.org/10.1016/j.tecto.2016.07.022>
- Cloix, A. (2017). Bréchification de la série prérift Nord-Pyrénéenne: Mécanismes tectoniques ou/et sédimentaires et place dans l'histoire tectono-métamorphique de la marge extensive crétacée et de son inversion Pyrénéenne (Chaînons Béarnais, Zone Nord-Pyrénéenne). *Mémoire de recherche Master 2 Géologie de l'Exploration et des Réservoirs*. Université de Montpellier.
- Cochelin, B. (2016). Champ de déformation du socle Paléozoïque des Pyrénées. Sciences de la Terre. Université Toulouse 3 Paul Sabatier (UT3 Paul Sabatier), Français. *Thèse de Doctorat*.
- Cochelin, B., Chardon, D., Denèle, Y., Gumiaux, C. & Le Bayon, B. (2017). Vertical strain partitioning in hot Variscan crust: Syn-convergence escape of the Pyrenees in the Iberian-Armorican syntax. *Bulletin de la Société Géologique de France*, 188 (6), 39. <https://doi.org/10.1051/bsgf/2017206>
- Cochelin, B., Lemirre, B., Denèle, Y. & de Saint Blanquat, M. (2021). Strain partitioning within bending orogens, new insights from the Variscan belt (Chilouret-Lesponne domes, Pyrenees). *Tectonics*, 40 (7), e2020TC006386. <https://doi.org/10.1029/2020TC006386>
- Conard, M. & Rioult, M. (1977). *Halimeda elliotti* nov. sp. Algue calcaire (chlorophyceae) du Turonien des Alpes-Maritimes (Sud-Est de la France). *Géologie Méditerranéenne*, 4 (2), 83-98.
- Corre, B., Lagabrielle, Y., Labaume, P., Fourcade, S., Clerc, C. & Ballèvre, M. (2016). Deformation associated with mantle exhumation in a distal, hot passive margin environment: New constraints from the Sarailié

- Massif (Chaînons Béarnais, North-Pyrenean Zone). *Comptes Rendus Geoscience*, 348 (3-4), 279-289. <https://doi.org/10.1016/j.crte.2015.11.007>
- Corre, B. (2017). La bordure nord de la plaque ibérique à l'Albo-Cénomaniens: architecture d'une marge passive de type ductile (Chaînons Béarnais, Pyrénées Occidentales). *Doctoral dissertation, Rennes 1*.
- Covey-Crump, S.J. & Rutter, E.H. (1989). Thermally-induced grain growth of calcite marbles on Naxos Island, Greece. *Contributions to Mineralogy and Petrology*, 101, 69–86. <https://doi.org/10.1007/BF00387202>
- Cuvillier, J., Henry, J., Ribis, R. & Villanova, M. (1964). Microfaunes cenomaniennes et santoniennes dans les 'calcaires des canons' (Vallee d'Aspe, Sainte-Engrace, Basses-Pyrenees). *Bulletin de la Société Géologique de France*, S7-VI (2), 273-277. <https://doi.org/10.2113/gssgfbull.S7-VI.2.273>
- de Bresser, J. H. P. (1991). Intracrystalline deformation of calcite. *Geologica Ultraiectina*, 79, 1-191.
- de Bresser, J. H. P. & Spiers, C. J. (1993). Slip systems in calcite single crystals deformed at 300-800°C. *Journal of Geophysical Research: Solid Earth*, 98 (B4), 6397-6409. <https://doi.org/10.1029/92JB02044>
- de Bresser, J. H. P. & Spiers, C. J. (1997). Strength characteristics of the r, f, and c slip systems in calcite. *Tectonophysics*, 272 (1), 1-23. [https://doi.org/10.1016/S0040-1951\(96\)00273-9](https://doi.org/10.1016/S0040-1951(96)00273-9)
- de Bresser, J. H. P., Peach, C. J., Reijjs, J. P. J. & Spiers, C. J. (1998). On dynamic recrystallization during solid state flow: Effects of stress and temperature. *Geophysical Research Letters*, 25 (18), 3457-3460. <https://doi.org/10.1029/98GL02690>
- de Bresser, J. H. P., ter Heege, J. H. & Spiers, C. (2001). Grain size reduction by dynamic recrystallization: can it result in major rheological weakening? *The International Journal of Earth Sciences (Geologische Rundschau)* 90, 28-45. <https://doi.org/10.1007/s005310000149>
- Debroas, E.-J. (1987). Modèle de bassin triangulaire à l'intersection de décrochements divergents pour le fossé albo-cénomaniens de la Ballongue (zone nord-pyrénéenne, France). *Bulletin de la Société Géologique de France*, III, 887-898.
- Debroas, E.-J. (1990). Le Flysch noir albo-cénomaniens témoin de la structuration albienne à sénonienne de la Zone nord-pyrénéenne en Bigorre (Hautes-Pyrénées, France). *Bulletin de la Société Géologique de France*, VI, 273-285.
- Déramond, J., Graham, R., Hossack, H., Baby, J. R., Crouzet, P. & Crouzet, G. (1985). Nouveau modèle de la chaîne des Pyrénées. *Comptes Rendus de l'Académie des Sciences, Paris*, 301, 1213-1216.
- Delvolvé, J. J. (1987). Un bassin synorogénique varisque: le Culm des Pyrénées centro-occidentales. *Thèse Doctoral Sciences, Toulouse*, 483 p.
- Dietrich, D. & Casey, M. (1989). A new tectonic model for the Helvetic nappes. *Geological Society, London, Special Publications*, 45, 47-63. <https://doi.org/10.1144/GSL.SP.1989.045.01.03>
- Drury, M. R. & Urai, J. L. (1990). Deformation-related recrystallization processes. *Tectonophysics*, 172 (3-4), 235-253. [https://doi.org/10.1016/0040-1951\(90\)90033-5](https://doi.org/10.1016/0040-1951(90)90033-5)
- Ducoux, M. (2017). Structure, thermicité et évolution géodynamique de la Zone Interne Métamorphique des Pyrénées. *Thèse de Doctorat. Université d'Orléans*.
- Ducoux, M., Jolivet, L., Callot, J.-P., Aubourg, C., Masini, E., Lahfid, A., Homonnay, E., Cagnard, F. Gumiaux, C. & Baudin, T. (2019). The Nappe des Marbres Unit of the Basque-Cantabrian Basin: the tectono-thermal evolution of a fossil hyperextended rift basin. *Tectonics*, 38 (11), 3881-3915. <https://doi.org/10.1029/2018TC005348>
- Ducoux, M., Jolivet, L., Cagnard, F. & Baudin, T. (2021a). Basement-cover decoupling the inversion of a hyperextended basin: Insights from the eastern Pyrenees. *Tectonics*, 40 (5), e2020TC006512. <https://doi.org/10.1029/2020TC006512>
- Ducoux, M., Jolivet, L., Masini, E., Augier, R., Lahfid, A., Bernet, M. & Calassou, S. (2021b). Distribution and intensity of High-Temperature Low-Pressure metamorphism across the Pyrenean-Cantabrian belt: constraints on the thermal record of the pre-orogenic hyperextension rifting. *Bulletin de la Société Géologique de France*, 192 (1), 43. <https://doi.org/10.1051/bsgf/2021029>
- Dumont, T., Replumaz, A., Rouméjon, S., Briais, A., Rigo, A. & Bouillin, J.-P. (2015). Microseismicity of the Béarn range: Reactivation of inversion and collision structures at the northern edge of the Iberian plate. *Tectonics*, 34 (5), 934-950. <https://doi.org/10.1002/2014TC003816>



- Ebert, A., Herwegh, M., Evans, B., Pfiffner, A., Austin, N. & Vennemann, T. (2007). Microfabrics in carbonate mylonites along a large-scale shear zone (Helvetic Alps). *Tectonophysics*, 444 (1-4), 1-26. <https://doi.org/10.1016/j.tecto.2007.07.004>
- Ebert, A., Herwegh, M., Berger, A. & Pfiffner, A. (2008). Grain coarsening maps for polymineralic carbonate mylonites: A calibration based on data from different Helvetic nappes (Switzerland). *Tectonophysics*, 457 (3-4), 128-142. <https://doi.org/10.1016/j.tecto.2008.05.007>
- Escher, A., Masson, H. & Steck, A. (1993). Nappe geometry in the Western Swiss Alps. *Journal of Structural Geology*, 15 (3-5), 501-509. [https://doi.org/10.1016/0191-8141\(93\)90144-Y](https://doi.org/10.1016/0191-8141(93)90144-Y)
- Espurt, N., Angrand, P., Teixell, A., Labaume, P., Ford, M., de Saint Blanquart, M. & Chevrot, S. (2019). Crustal-scale balanced cross-section and restoration of the Central Pyrenean belt (Nestes-Cinca transect): highlighting the structural control of Variscan belt and Permian-Mesozoic rift systems on mountains building. *Tectonophysics*, 764, 25-45. <https://doi.org/10.1016/j.tecto.2019.04.026>
- Etheridge, M. A. & Wilkie, J. C. (1979). Grainsize reduction, grain boundary sliding and flow strength of mylonites. *Tectonophysics*, 58 (1-2), 159-178. [https://doi.org/10.1016/0040-1951\(79\)90327-5](https://doi.org/10.1016/0040-1951(79)90327-5)
- Etheridge, M. A. & Wilkie, J. C. (1981). An assessment of dynamically recrystallized grainsize as a paleopiezometer in quartz-bearing mylonite zones. *Tectonophysics*, 78 (1-4), 475-508. [https://doi.org/10.1016/0040-1951\(81\)90025-1](https://doi.org/10.1016/0040-1951(81)90025-1)
- Fairchild, I.J. (1983). Chemical controls of cathodoluminescence of natural dolomites and calcites: new data and review. *Sedimentology*, 30 (4), 579-583. <https://doi.org/10.1111/j.1365-3091.1983.tb00695.x>
- Ferrill, D. A., Morris, A. P., Evans, M. A., Burkhard, M., Groshong Jr., R. H. & Onasch, C. M. (2004). Calcite twin morphology: a low-temperature deformation geothermometer. *Journal of Structural Geology*, 26 (8), 1521-1529. <https://doi.org/10.1016/j.jsg.2003.11.028>
- Fischer, M. P. & Woodward, N. B. (1992). The geometrical evolution of foreland thrust systems. In: McClay, K. R. (Ed). Thrust Tectonics. *Chapman and Hall, London*, pp. 181-189. [https://doi.org/10.1007/978-94-011-3066-0\\_16](https://doi.org/10.1007/978-94-011-3066-0_16)
- Frank, J. R., Carpenter, A. B. & Oglesby, T. W. (1982). Cathodoluminescence and composition of calcite cement in the Taum Sauk Limestone (upper Cambrian), Southeast Missouri. *Journal of Sedimentary Research*, 52 (2), 631-638. <https://doi.org/10.1306/212F7FB8-2B24-11D7-8648000102C1865D>
- Freund, D., Rybacki, E. & Dresen, G. (2001). Effect of impurities on grain growth in synthetic calcite aggregates. *Physics and Chemistry of Minerals*, 28, 737-745. <https://doi.org/10.1007/s002690100196>
- Frost, H. J. & Ashby, M. F. (1982). Deformation mechanism maps. *Pergamon Press, Toronto*, 1-166.
- Fitzgerald, P. G., Muñoz, J. A., Coney, P. J. & Baldwin, S.L. (1999). Asymmetric exhumation across the Pyrenean orogen: implications for the tectonic evolution of a collisional orogen. *Earth and Planetary Science Letters*, 173 (3), 157-170. [https://doi.org/10.1016/S0012-821X\(99\)00225-3](https://doi.org/10.1016/S0012-821X(99)00225-3)
- Floquet, M., Mathey, B., Rosse, P. & Vadot, J. P. (1988). Age cenomanien et turono-coniacien des calcaires de Sare (Pays Basque, France-Espagne); conséquences paleomorphologiques et tectogenetiques pour les Pyrenees occidentales. *Bulletin de la Société Géologique de France*, IV (6), 1021-1027. <https://doi.org/10.2113/gssgfbull.IV.6.1021>
- Ford, M., Hemmer, L., Vacherat, A., Gallagher, K. & Christophoul, F. (2016). Retro-wedge foreland basin evolution along the ECORS line, eastern Pyrenees, France. *Journal of the Geological Society of London*, 173 (3), 419-437. <https://doi.org/10.1144/jgs2015-129>
- Fournier, E. (1905). Etudes géologiques sur la partie occidentale de la chaîne des Pyrénées, entre la vallée d'Aspe et celle de la Nieve. *Bulletin de la Société Géologique de la France*, 5, 699-723.
- García-Sansegundo, J., Poblet, J., Alonso, J. L. & Clariana, P. (2011). Hinterland-foreland zonation of the Variscan orogen in the Central Pyrenees: Comparison with the northern part of the Iberian Variscan massif. *Geological Society, London, Special Publications*, 349 (1), 169-184. <https://doi.org/10.1144/sp349.9>
- García-Senz, J., Pedrera, A., Ayala, C., Ruiz-Constán, A., Robador, A. & Rodríguez-Fernández, L. R. (2019). Inversion of the north Iberian hyperextended margin: the role of exhumed mantle indentation during continental collision. In: Hammerstein, J. A. (Ed.), Fold and Thrust Belts: Structural Style, Evolution and Exploration. *Geological Society, London, Special Publications*. pp. 490. <https://doi.org/10.1144/SP490-2019-112>

- Giuntoli, F., Brovarone, A. V. & Menegon, L. (2020). Feedback between high-pressure genesis of abiotic methane and strain localization in subducted carbonate rocks. *Scientific Reports*, 10, 9848. <https://doi.org/10.1038/s41598-020-66640-3>
- Gleason, G. C., Tullis, J. & Heidelbach, F. (1993). The role of dynamic recrystallization in the development of lattice preferred orientations in experimentally deformed quartz aggregates. *Journal of Structural Geology*, 15 (9-10), 1145-1168. [https://doi.org/10.1016/0191-8141\(93\)90161-3](https://doi.org/10.1016/0191-8141(93)90161-3)
- Gregg, J. M. & Sibley, D. F. (1984). Epigenetic dolomitization and the origin of xenotopic dolomite texture. *Journal of Sedimentary Petrology*, 54 (3), 908-931. <https://doi.org/10.1306/212F8535-2B24-11D7-8648000102C1865D>
- Gies, H. (1975). Activation possibilities and geochemical correlations of photoluminescing carbonates, particularly calcites. *Mineral Deposita*, 10, 216-277. <https://doi.org/10.1007/BF00207138>
- Girault, J. B., Bellahsen, N., Boutoux, A., Rosenberg, C. L., Nanni, U., Verlaguet, A. & Beyssac, O. (2020). The 3-D thermal structure of the Helvetic Nappes of the European Alps: Implications for collisional processes. *Tectonics*, 39 (3). <https://doi.org/10.1029/2018TC005334>
- Golberg, J.M. (1987). Le métamorphisme mésozoïque dans la partie orientale des Pyrénées: relations avec l'évolution de la chaîne au Crétacé. *Doc Trav Centre Geol Geophys Montpellier* 14: 235 p
- Golberg, J. M. & Leyreloup, A. F. (1990). High temperature-low pressure Cretaceous metamorphism related to crustal thinning (Eastern North Pyrenean Zone, France). *Contributions to Mineralogy and Petrology*, 104, 194-207. <https://doi.org/10.1007/BF00306443>
- Goldsmith, J. R. (1983). Phase relations of rhombohedral carbonates. In: Reeder RJ (ed) Carbonates: Mineralogy and Chemistry. *Mineral Society of America Rev Mineral*, 11, 49-76.
- Götte, T. & Richter, D. K. (2009). Quantitative aspects of Mn-activated cathodoluminescence of natural and synthetic aragonite. *Sedimentology*, 56 (2). <https://doi.org/10.1111/j.1365-3091.2008.00980.x>
- Grool, A. R., Ford, M., Vergés, J., Huisman, R. S., Christophoul, F. & Dielforder, A. (2018). Insights into the crustal-scale dynamics of a doubly vergent orogen from a quantitative analysis of its forelands: a case study of the Eastern Pyrenees. *Tectonics*, 37 (2), 450-476. <https://doi.org/10.1002/2017TC004731>
- Grover, G. JR. & Read, J. F. (1983). Paleoaquifer and deep burial related cements defined by regional cathodoluminescent patterns, Middle Ordovician carbonates, Virginia. *AAPG Bulletin*, 67, 1275-1303.
- Guerrot, C. (2001). Datation du pluton des Eaux-Chaudes. In: Ternet, Y., Majesté-Menjoulas, C., Canérot, J., Baudin, T., Cocherie, A., Guerrot, C., Rossi, P. (eds) (2004). Notice explicative, Carte géol. France (1/50.000), feuille Laruns-Somport (1069). BRGM, Orléans, pp 185-187.
- Habermann, D., Neuser, R. D. & Richter, D. K. (1996). REE-activated cathodoluminescence of calcite and dolomite: high-resolution spectrometric analysis of CL emission (HRS-CL). *Sedimentary Geology*, 101 (1-2), 1-7. [https://doi.org/10.1016/0037-0738\(95\)00086-0](https://doi.org/10.1016/0037-0738(95)00086-0)
- Habermann, D., Neuser, R. D. & Richter, D. K. (1998). Low limit of Mn<sup>2+</sup>-activated cathodoluminescence of calcite: state of the art. *Sedimentary Geology*, 116 (1-2), 13-24. [https://doi.org/10.1016/S0037-0738\(97\)00118-8](https://doi.org/10.1016/S0037-0738(97)00118-8)
- Hacker, B. R., Yin, A., Christie, J. M. & Snoke, A. W. (1990). Differential stress, strain rate, and temperatures of mylonitization in the Ruby Mountains, Nevada: implications for the rate and duration of uplift. *Journal of Geophysical Research*, 95 (B6), 8569-8580. <https://doi.org/10.1029/JB095iB06p08569>
- Hacker, B. R., Yin, A., Christie, J. M. & Davis, G. A. (1992). Stress magnitude, strain rate, and rheology of extended middle continental crust inferred from quartz grain sizes in the Whipple Mountains, California. *Tectonics*, 11 (1), 36-46. <https://doi.org/10.1029/91TC01291>
- Herwegh, M. & Handy, M. R. (1996). The evolution of high-temperature mylonitic microfabrics: evidence from simple shearing of a quartz analogue (norcamphor). *Journal of Structural Geology*, 18 (5), 689-710. [https://doi.org/10.1016/S0191-8141\(96\)80033-2](https://doi.org/10.1016/S0191-8141(96)80033-2)
- Herwegh, M. & Berger, A. (2004). Deformation mechanisms in second-phase affected microstructures and their energy balance. *Journal of Structural Geology*, 26 (8), 1483-1498. <https://doi.org/10.1016/j.jsg.2003.10.006>

- Herwegh, M., de Bresser, J. H. P. & ter Heege, J. H. (2005). Combining natural microstructures with composite flow laws: an improved approach for the extrapolation of lab data to nature. *Journal of Structural Geology*, 27 (3), 503-521. <https://doi.org/10.1016/j.jsg.2004.10.010>
- Herwegh, M. & Pfiffner, O. A. (2005). Tectono-metamorphic evolution of a nappe stack: A case study of the Swiss Alps. *Tectonophysics*, 404 (1-2), 55-76. <https://doi.org/10.1016/j.tecto.2005.05.002>
- Herwegh, M., Linckens, J., Ebert, A., Berger, A. & Brodhag, S. H. (2011). The role of second phases for controlling microstructural evolution in polymineralic rocks: A review. *Journal of Structural Geology*, 33 (12), 1728-1750. <https://doi.org/10.1016/j.jsg.2011.08.011>
- Hiatt, E. E. & Pufahl, P. K. (2014). Cathodoluminescence petrography of carbonate rocks: a review of applications for understanding diagenesis, reservoir quality, and pore system evolution. In: Coulson, I.M. (ed.). Cathodoluminescence and its application to geoscience. *Mineralogical Association of Canada Short Course*, 45, 75-96.
- Hirth, G. & Tullis, J. (1992). Dislocation creep regimes in quartz aggregates. *Journal of Structural Geology*, 14 (2), 145-159. [https://doi.org/10.1016/0191-8141\(92\)90053-Y](https://doi.org/10.1016/0191-8141(92)90053-Y)
- Hobbs, B. E. (1984). Point defect chemistry of minerals under a hydrothermal environment. *Journal of Geophysical Research: Solid Earth*, 89 (B6), 4026-4038. <https://doi.org/10.1029/JB089iB06p04026>
- Holman, J.P. (1990). Heat Transfer. 7th ed., New York: McGraw-Hill, (Appendix A.3)
- Holyoke, C. W. & Kronenberg, A. K. (2013). Reversible water weakening of quartz. *Earth and Planetary Science Letters*, 374, 185-190. <https://doi.org/10.1016/j.epsl.2013.05.039>
- Ismail, W. B. & Mainprice, D. (1998). An olivine fabric database: an overview of upper mantle fabrics and seismic anisotropy. *Tectonophysics*, 296 (1-2), 145-157. [https://doi.org/10.1016/S0040-1951\(98\)00141-3](https://doi.org/10.1016/S0040-1951(98)00141-3)
- Izquierdo-Llavall, E., Román-Berdiel, T., Casas, A. M., Oliva-Urcia, B., Gil-Peña, I., Soto, R. & Jabaloy, A. (2012). Magnetic and structural study of the Eaux-Chaudes intrusion: understanding the Variscan deformation in the Western Axial Zone (Pyrenees). *International Journal of Earth Sciences (Geol. Rundsch)*, 101, 1817-1834. <https://doi.org/10.1007/s00531-012-0760-9>
- Izquierdo-Llavall, E., Menant, A., Aubourg, C., Callot, J. -P., Hoareau, G., Camps, P., Péré, E. & Lahfid, A. (2020). Preorogenic folds and syn-orogenic basement tilts in an inverted hyperextended margin: The northern Pyrenees case study. *Tectonics*, 39 (7), e2019TC005719. <https://doi.org/10.1029/2019TC005719>
- Jackson, M. P. A. & Hudec, M. R. (2017). Salt tectonics: Principles and practice. *Cambridge University Press*.
- Jammes, S., Manatschal, G., Lavier, L. & Masini, E. (2009). Tectonosedimentary evolution related to extreme crustal thinning ahead of a propagating ocean: Example of the western Pyrenees. *Tectonics*, 28 (4), 1-24. <https://doi.org/10.1029/2008TC002406>
- Jolivet, M., Labaume, P., Monié, P., Brunel, M., Arnaud, N. & Campani, M. (2007). Thermochronology constraints for the propagation sequence of the south Pyrenean basement thrust system (France-Spain). *Tectonics*, 26 (5), 1-17. <https://doi.org/10.1029/2006TC002080>
- Kohlstedt, D. L., Evans, B. & Mackwell, S. J. (1995). Strength of the lithosphere: Constraints imposed by laboratory experiments. *Journal of Geophysical Research: Solid Earth*, 100 (B9), 17587-17602. <https://doi.org/10.1029/95JB01460>
- Krabbendam, M., Urai, J. L. & van Vilet, L. J. (2003). Grain size stabilization by dispersed graphite in a high-grade quartz mylonite: an example from Naxos (Greece). *Journal of Structural Geology*, 25 (6), 855-866. [https://doi.org/10.1016/S0191-8141\(02\)00086-X](https://doi.org/10.1016/S0191-8141(02)00086-X)
- Kronenberg, A. K. & Tullis, J. (1984). Flow strengths of quartz aggregates: Grain size and pressure effects due to hydrolytic weakening. *Journal of Geophysical Research: Solid Earth*, 89 (B6), 4281-4297. <https://doi.org/10.1029/JB089iB06p04281>
- Labaume, P., Séguret, M. & Seyve, C. (1985). Evolution of a turbiditic foreland basin and analogy with an accretionary prism: Example of the Eocene South-Pyrenean Basin. *Tectonics*, 4 (7), 661-685. <https://doi.org/10.1029/TC004i007p00661>
- Labaume, P., Meresse, F., Jolivet, M., Teixell, A. & Lahfid, A. (2016). Tectonothermal history of an exhumed thrust-sheet-top basin: An example from the south Pyrenean thrust belt. *Tectonics*, 35 (5), 1280-1313. <https://doi.org/10.1002/2016TC004192>

- Labaume, P. & Teixell, A. (2018). 3D structure of subsurface thrusts in the eastern Jaca Basin, southern Pyrenees. *Geologica Acta*, 16 (4), 477-498. <https://doi.org/10.1344/GeologicaActa2018.16.4.9>
- Labaume, P. & Teixell, A. (2020). Evolution of salt structures of the Pyrenean rift (Chaînons Béarnais, France): From hyper-extension to tectonic inversion. *Tectonophysics*, 785, 228451. <https://doi.org/10.1016/j.tecto.2020.228451>
- Lacan, P. (2008). Activité Sismotectonique Plio-Quaternaire de l'Ouest des Pyrénées. *Ph.D. Thesis*, Université de Pau et des Pays de l'Adour, Pau. France.
- Lacan, P. & Ortuño, M. (2012). Active tectonics of the Pyrenees: A review, *Journal of Iberian Geology*, 38 (1), 9-30. [https://doi.org/10.5209/rev\\_JIGE.2012.v38.n1.39203](https://doi.org/10.5209/rev_JIGE.2012.v38.n1.39203)
- Lagabrielle, Y. & Bodinier, J. L. (2008). Submarine reworking of exhumed subcontinental mantle rocks: Field evidence from the Lherz peridotites, French Pyrenees. *Terra Nova*, 20 (1), 11-21. <https://doi.org/10.1111/j.1365-3121.2007.00781.x>
- Lagabrielle, Y., Labaume, P. & de Saint Blanquat, M. (2010). Mantle exhumation, crustal denudation, and gravity tectonics during Cretaceous rifting in the Pyrenean realm (SW Europe): Insights from the geological setting of the Iherzolite bodies. *Tectonics*, 29 (4), 1-26. <https://doi.org/10.1029/2009TC002588>
- Lagabrielle, Y., Asti, R., Fourcade, S., Corre, B., Poujol, M., Uzel, J., Labaume, P., Clerc, C., Lafay, R., Picazo, S. & Maury, R. (2019a). Mantle exhumation at magma-poor passive continental margins. Part I. 3D architecture and metasomatic evolution of a fossil exhumed mantle domain (Urdach Iherzolite, north-western Pyrenees, France). *Earth Sciences Bulletin*, 190 (8). <https://doi.org/10.1051/bsgf/2019007>
- Lagabrielle, Y., Asti, R., Fourcade, S., Corre, B., Labaume, P., Uzel, J., Clerc, C., Lafay, R., & Picazo, S. (2019b). Mantle exhumation at magma-poor passive continental margins. Part II: Tectonic and metasomatic evolution of large-displacement detachment faults preserved in a fossil distal margin domain (Sarailié Iherzolites, northwestern Pyrenees, France). *Earth Sciences Bulletin*, 190 (14). <https://doi.org/10.1051/bsgf/2019013>
- Lahfid, A., Beyssac, O., Deville, E., Negro, F., Chopin, C. & Goffé, B. (2010). Evolution of the Raman spectrum of carbonaceous material in low-grade metasediments of the Glarus Alps (Switzerland). *Terra Nova*, 22 (5), 354-360. <https://doi.org/10.1111/j.1365-3121.2010.00956.x>
- Linckens, J., Herwegh, M. & Müntener, O. (2011). Linking temperature estimates and microstructures in deformed polymineralic mantle rock. *Geochemistry, Geophysics, Geosystems*, 12 (8). <https://doi.org/10.1029/2011GC003536>
- Lloyd, G. E. & Freeman, B. (1994). Dynamic recrystallization of quartz under greenschist conditions. *Journal of Structural Geology*, 16 (6), 867-881. [https://doi.org/10.1016/0191-8141\(94\)90151-1](https://doi.org/10.1016/0191-8141(94)90151-1)
- Long, J. V. P. & Agrell, S. O. (1965). The cathodo-luminescence of minerals in thin section. *Mineralogical Magazine and Journal of the Mineralogical Society*, 34 (268), 318-326. <https://doi.org/10.1180/minmag.1965.034.268.27>
- Machel, H. G., Mason, R. A., Mariano, A. N. & Mucci, A. (1991). Causes and emission of luminescence in calcite and dolomite. In Barker, C. E. & Kopp, O. C., eds., *Luminescence microscopy and spectroscopy: qualitative and quantitative applications: SEPM Short Course, 25, Tulsa*. Oklahoma, 9-25.
- Mainprice, D. H. & Paterson, M. S. (1984). Experimental studies of the role of water in the plasticity of quartzites. *Journal of Geophysical Research: Solid Earth*, 89 (B6), 4257-4269. <https://doi.org/10.1029/JB089iB06p04257>
- Mainprice, D. & Silver, P. G. (1993). Interpretation of SKS-waves using samples from the subcontinental lithosphere. *Physics of the Earth and Planetary Interiors*, 78 (3-4), 257-280. [https://doi.org/10.1016/0031-9201\(93\)90160-B](https://doi.org/10.1016/0031-9201(93)90160-B)
- Majesté-Menjoulas, C. (1979). Evolution alpine d'un segment de chaîne varisque: Nappe de Gavarnie, chevauchement Cinq-Monts-Gentiane (Pyrénées centrales et occidentales). *Thèse Science*, Université Paul Sabatier, Toulouse, 343 pp.
- Majesté-Menjoulas, C., (1968). Le Peléozoïque au Nord du synclinorium des Eaux-Chaudes (Pyrénées Atlantiques). *Thèse Doctorel 3<sup>e</sup> cycle, Toulouse*.
- Manatschal, G., Chenin, P., Lescoutre, R., Miró, J., Cadenas, P., Saspiturry, N., Masini, E., Chevrot, S., Ford, M., Jolivet, L., Mouthereau, F., Thinon, I., Issautier, B. & Calassou, S. (2021). The role of inheritance in



- forming rifts and rifted margins and buildings collisional orogens: a Biscay-Pyrenean perspective. *Bulletin de la Société Géologique de France*, 192 (1), 55. <https://doi.org/10.1051/bsgf/2021042>
- Marshall, D. J. (1988). Cathodoluminescence of Geological Materials. *Unwin Hyman*, Boston, 146 p. <https://doi.org/10.1002/gj.3350260409>
- Masini, E., Manatschal, G., Tugend, J., Mohn, G. & Flament, J.-M. (2014). The tectono-sedimentary evolution of a hyper-extended rift basin: The example of the Arzacq-Mauléon rift system (Western Pyrenees, SW France). *International Journal of Earth Sciences*, 103, 1569-1596. <https://doi.org/10.1007/s00531-014-1023-8>
- Mason, R. A. (1987). Ion microprobe analysis of trace elements in calcite with an application to the cathodoluminescence zonation of limestone cements from the Lower Carboniferous of South Wales, U.K. *Chemical Geology*, 64 (3-4), 209-224. [https://doi.org/10.1016/0009-2541\(87\)90003-9](https://doi.org/10.1016/0009-2541(87)90003-9)
- Mason, R. A. & Mariano, A. N. (1990). Cathodoluminescence activation in manganese-bearing and rare earth-bearing synthetic calcites. *Chemical geology*, 88 (1-2), 191-206. [https://doi.org/10.1016/0009-2541\(90\)90113-L](https://doi.org/10.1016/0009-2541(90)90113-L)
- Matte, P. 2002. Les plis hercyniens kilométriques couchés vers l'ouest-sudouest dans la région du pic du Midi d'Ossau-col du Somport (zone axiale des Pyrénées occidentales). *Comptes Rendus Géoscience*, 334 (10), 773-779. [https://doi.org/10.1016/S1631-0713\(02\)01808-4](https://doi.org/10.1016/S1631-0713(02)01808-4)
- Matthies, S. & Wagner, F. (1996). On a 1/n law in texture related single orientation analysis. *Physica Status Solidi (b)*, 196 (2), k11-k15. <https://doi.org/10.1002/pssb.2221960225>
- Means, W. D. (1976). Stress and Strain. *Springer-Verlag*, New York. <https://doi.org/10.1007/978-1-4613-9371-9>
- Menant, A., Aubourg, C., Cuyala, J.-B., Hoareau, G., Callot, J.-P., Péré, E., Labaume, P. & Ducoux, M. (2016). Salt tectonics and thermal imprint along an inverted passive margin: the Montacou anticline, Chaînons Béarnais, North Pyrenean Zone. In: *Geophysical Research Abstracts*, 18, EGU2016-15281, E. G. U. Assembly, 17-22 April 2016, Vienna.
- Mercier, J.-C. C., Anderson, D. A. & Carter, N. L. (1977). Stress in the lithosphere: inferences from steady state flow of rocks. *Pure and Applied Geophysics*, 115, 199-226. <https://doi.org/10.1007/BF01637104>
- Metcalfe, J. R., Fitzgerald, P. G., Baldwin, S.L. & Muñoz, J. A. (2009). Thermochronology of a convergent orogen: Constraints on the timing of thrust faulting and subsequent exhumation of the Maladeta Pluton in the Central Pyrenean Axial Zone. *Earth and Planetary Science Letters*, 287 (3-4), 488-503. <https://doi.org/10.1016/j.epsl.2009.08.036>
- Meyers, W. J. (1978). Carbonate cements: their regional distribution and interpretation in Mississippian limestones of southwestern New Mexico. *Sedimentology*, 25 (3), 371-400. <https://doi.org/10.1111/j.1365-3091.1978.tb00318.x>
- Mirouse, R. (1962). Recherches géologiques dans la partie occidentale de la zone primaire axiale des Pyrénées. Thèse État, Toulouse. *Mémoires pour Servir la Carte Géologique de France*, (1966), 451 p. (Paris).
- Mouthereau, F., Filleaudeau, P.-Y., Vacherat, A., Pik, R., Lacombe, O., Fellin, M. G., Castelltort, S., Christophoul, F. & Masini, E. (2014). Placing limits to shortening evolution in the Pyrenees: Role of margin architecture and implications for the Iberia/Europe convergence. *Tectonics*, 33 (12), 2283-2314. <https://doi.org/10.1002/2014TC003663>
- Nemanich, R. J. & Solin, S. A. (1979). First- and Second-order Raman scattering from finite-size crystals of graphite. *Physical Review B*, 20, 392-401. <http://dx.doi.org/10.1103/physrevb.20.392>
- Nibourel, L., Berger, A., Egli, D., Luensdorf, N. K. & Herwegh, M. (2018). Large vertical displacements of a crystalline massif recorded by Raman thermometry. *Geology*, 46, 879-882. <https://doi.org/10.1130/G45121.1>
- Nishikawa, O. & Takeshita, T. (1999). Dynamic analysis and two types of kink bands in quartz veins deformed under subgreenschist conditions. *Tectonophysics*, 301 (1-2), 21-34. [https://doi.org/10.1016/S0040-1951\(98\)00219-4](https://doi.org/10.1016/S0040-1951(98)00219-4)
- Nunn, J. A. & Lin, G. (2002). Insulating effect of coals and organic rich shales: implications for topography-driven fluid flow, heat transport, and genesis of ore deposits in the Arkoma basin and Ozark plateau. *Basin Research*, 14 (2), 129-145. <https://doi.org/10.1046/j.1365-2117.2002.00172.x>

- Olgaard, D. L. (1990). The rôle of second phase in localizing deformation. *Geological Society, London, Special Publications*, 54, 175-181. <https://doi.org/10.1144/GSL.SP.1990.054.01.17>
- Ortí, F., Pérez-López, A. & Salvany, J. M. (2017). Triassic evaporites of Iberia: Sedimentological and palaeogeographical implications for the western Neotethys evolution during the Middle Triassic-Earliest Jurassic. *Palaeogeography, Palaeoclimatology, Palaeoecology*, 471, 157-180. <https://doi.org/10.1016/j.palaeo.2017.01.025>
- Passchier, C. W. (2001). Flanking structures. *Journal of Structural Geology*, 23, (6-7), 951-962. [https://doi.org/10.1016/S0191-8141\(00\)00166-8](https://doi.org/10.1016/S0191-8141(00)00166-8)
- Paterson, M. S. (1995). A theory for granular flow accommodated by material transfer via an intergranular fluid. *Tectonophysics*, 245 (3-4), 135-151. [https://doi.org/10.1016/0040-1951\(94\)00231-W](https://doi.org/10.1016/0040-1951(94)00231-W)
- Pfiffner, O. A. (1993). The structure of the Helvetic nappes and its relation to the mechanical stratigraphy. *Journal of Structural Geology*, 15 (3-5), 511-521. [https://doi.org/10.1016/0191-8141\(93\)90145-Z](https://doi.org/10.1016/0191-8141(93)90145-Z)
- Pfiffner, O. A., Lehner, P., Heitzmann, P., Mueller, St. & Steck, A. (1997). Deep Structure of the Swiss Alps: Results from NFP 20. *Birkhäuser Verlag, Basel, Switzerland*, 460pp. ISBN 3-7643 5254 X, Hardback, DM 228.
- Pfiffner, O. A. (2017). Thick-skinned and thin-skinned tectonics: A global perspective. *Geosciences*, 7 (3), 71. <https://doi.org/10.3390/geosciences7030071>
- Pierson, B. J. (1981). The control of cathodoluminescence in dolomite by iron and manganese. *Sedimentology*, 28 (5), 601-610. <https://doi.org/10.1111/j.1365-3091.1981.tb01924.x>
- Pinet, B., Montadert, L. & the ECORS Scientific Party. (1987). Deep seismic reflection and refraction profiling along the Aquitaine shelf (Bay of Biscay). *Geophysical Journal Royal Astronomical Society*, 89 (1), 305-312. <https://doi.org/10.1111/j.1365-246X.1987.tb04423.x>
- Platt, J. P. & Behr, W. M. (2011). Grainsize evolution in ductile shear zones: Implications for strain localization and the strength of the lithosphere. *Journal of Structural Geology*, 33 (4), 537-550. <https://doi.org/10.1016/j.jsg.2011.01.018>
- Pollack, H. N. & Cercone, K. R. (1994). Anomalous thermal maturities caused by carbonaceous sediments. *Basin Research*, 6 (1), 47-51. <https://doi.org/10.1111/j.1365-2117.1994.tb00074.x>
- Powell, R., Condliffe, D. M. & Condliffe, E. (1984). Calcite-dolomite geothermometry in the system CaCO<sub>3</sub>-MgCO<sub>3</sub>-FeCO<sub>3</sub>: an experimental study. *Journal of Metamorphic Geology*, 2 (1), 33-41. <https://doi.org/10.1111/j.1525-1314.1984.tb00283.x>
- Price, L. C. (1983). Geologic time as a parameter in organic metamorphism and vitrinite reflectance as an absolute paleogeothermometer. *Journal of Petroleum Geology*, Vol. 6, 1, 5-37. <https://doi.org/10.1111/j.1747-5457.1983.tb00260.x>
- Prior, D. J., Boyle, A. P., Brenker, F., Cheadle, M. C., Day, A., Lopez, G., Peruzzo, L., Potts, G. J., Reddy, S., Spiess, R., Timms, N. E., Trimby, P., Wheeler, J. & Zetterström, L. (1999). The application of electron backscatter diffraction and orientation contrast imaging in the SEM to textural problems in rocks. *American Mineralogist*, 84, 1741-1759. <https://doi.org/10.2138/am-1999-11-1204>
- Prior, D. J., Martant, E. & Wheeler, J. (2009). EBSD in the earth sciences: applications, common practice and challenges. *Electron Backscatter Diffraction in Materials Science* (eds. By A. J. Schwartz, M. Kumar, B. L. Adams & D. P. Field), pp. 345-360. *Springer US*, New York, NY, USA.
- Purser, B. H., Tucker, M. E. & Zenger, D. H. (1994): Problems, progress and future research concerning dolomites and dolomitization. *In* Purser, B. H., Tucker, M. E. & Zenger, D. H., eds., *Dolomites – a volume in honour of Dolomieu: International Association of Sedimentologists, Special Publications*, 21, 3-20. <https://doi.org/10.1002/9781444304077.ch1>
- Puigdefàbregas, C. (1975). La sedimentación molásica en la cuenca de Jaca. Pirineos. 104: 1-188.
- Puigdefàbregas, C. & Souquet, P. (1986). Tecto-sedimentary cycles and depositional sequences of the Mesozoic and Tertiary from the Pyrenees. *Tectonophysics*, 129 (1-4), 173-203. [https://doi.org/10.1016/0040-1951\(86\)90251-9](https://doi.org/10.1016/0040-1951(86)90251-9)
- Ramsay, J. G. (1967). *Folding and Fracturing of Rocks*. *Mc-Graw-Hill*, New York, NY.

- Ramsay, J. G. (1981). Tectonics of the Helvetic nappes. *Geological Society, London, Special Publications*, 9, 293-309. <https://doi.org/10.1144/GSL.SP.1981.009.01.26>
- Razin, P. (1989). Evolution tecto-sédimentaire alpine des Pyrénées Basques à l'Ouest de la transformante de Pamplona (province du Labourd). *Thèse Doctorat Université de Bordeaux III*, Bordeaux, 464 p.
- Regenauer-Lieb, K. & Yuen, D. A. (2003). Modeling shear zones in geological and planetary sciences: solid- and fluid-thermal-mechanical approaches. *Earth-Science Reviews*, 63 (3-4), 295-349. [https://doi.org/10.1016/S0012-8252\(03\)00038-2](https://doi.org/10.1016/S0012-8252(03)00038-2)
- Ricard, Y. & Bercovici, D. (2009). A continuum theory of grain size evolution and damage. *Journal of Geophysical Research: Solid Earth*, 114 (B1). <https://doi.org/10.1029/2007JB005491>
- Richter, D. K. & Zinkernagel, U. (1981). Zur Anwendung der Kathodolumineszenz in der Karbonat-petrographie. (Application of cathodoluminescence in carbonate petrography). *Geol Rundschau*, 70, 1276-1302.
- Roigé, M., Gómez-Gras, D., Remacha, E., Daza, R., Boya, S. (2016). Tectonic control on sediment sources in the Jaca basin (Middle and Upper Eocene of the South-Central Pyrenees). *Comptes Rendus Geosciences*, 348 (3-4), 236-245. <https://doi.org/10.1016/j.crte.2015.10.005>
- Rougier, G., Ford, M., Christophoul, F. & Bader, A.-G. (2016). Stratigraphic and tectonic studies in the central Aquitaine Basin, northern Pyrenees: Constraints on the subsidence and deformation history of a retro-foreland basin. *Comptes Rendus Geoscience*, 348 (3-4), 224-235. <https://doi.org/10.1016/j.crte.2015.12.005>
- Rutter, E. H. (1995). Experimental study of the influence of stress, temperature, and strain on the dynamic recrystallization of Carrara marble. *Journal of Geophysical Research*, 100 (B12), 24651-24663. <https://doi.org/10.1029/95JB02500>
- Saspiturry, N., Lahfid, A., Baudin, T., Guillon-Frottier, L., Razin, P., Issautier, B., Le Bayon, B., Serrano, O., Lagabrielle, Y. & Corre, B. (2020). Paleogeothermal gradients across an inverted hyperextended rift system: example of the Mauléon fossil rift (western Pyrenees). *Tectonics*, 39 (10), e2020TC006206. <https://doi.org/10.1029/2020TC006206>
- Saspiturry, N., Allanic, C., Serrano, O., Courrioux, G., Baudin, T., Le Bayon, B., Lahfid, A., Razin, P., Villasenor, A., Cevrot, S. & Issautier, B. (2022). Upper lithospheric transfer zones driving the non-cylindricity of the West-Pyrenean orogenic prism (Mauléon hyperextended basin). *Journal of Structural Geology*, 156, 104535. <https://doi.org/10.1016/j.jsg.2022.104535>
- Schmid, S. M., Paterson, M. S. & Boland, J. N. (1980). High temperature flow and dynamic recrystallization in Carrara marble. *Tectonophysics*, 65 (3-4), 245-280. [https://doi.org/10.1016/0040-1951\(80\)90077-3](https://doi.org/10.1016/0040-1951(80)90077-3)
- Schmid, S. M., Zingg, A. & Handy, M. (1987). The kinematics of movements along the Insubric Line and the emplacement of the Ivrea Zone. *Tectonophysics*, 135 (1-3), 47-66. [https://doi.org/10.1016/0040-1951\(87\)90151-X](https://doi.org/10.1016/0040-1951(87)90151-X)
- Schmid, S. M. & Handy, M. R. (1991). Towards a genetic classification of fault rocks: geological usage and tectonophysical implications. In: Müller, D. W., McKenzie, J. A., Weissert, H. (eds.). *Controversies in Modern Geology*. Academic Press, London. 95-110.
- Schulman, J. H., Evans, L. W., Ginther, R. J. & Murata, K. J. (1947). The sensitized luminescence of manganese-activated calcite. *Journal of Applied Physics*, 18, 732-739. <https://doi.org/10.1063/1.1697831>
- Séguret, M. 1972. Étude tectonique des nappes et séries décollées de la partie centrale du versant sud des Pyrénées. Caractère synsédimentaire, rôle de la compression et de la gravité. *Série Géologie Structurale, vol 2*, Publications de l'Université des Sciences et Techniques du Languedoc, Montpellier, France.
- Sibley, D. F. & Gregg, J. M. (1987): Classification of dolomite rock textures. *Journal of Sedimentary Petrology*, 57 (6), 967-975. <https://doi.org/10.1306/212F8CBA-2B24-11D7-8648000102C1865D>
- Sippel, R. F. & Glover, E. D. (1965). Structures in carbonate rocks made visible by luminescence petrography. *Science*, 150 (3701), 1283-1287. <https://doi.org/10.1126/science.150.3701.1283>
- Skemer, P., Katayama, I., Jiang, Z. & Karato, S.-I. (2005). The misorientation index: Development of a new method for calculating the strength of lattice-preferred orientation. *Tectonophysics*, 411 (1-4), 157-167. <https://doi.org/10.1016/j.tecto.2005.08.023>

- Sommer, S. E. (1972a). Cathodoluminescence of carbonates, 1. Characterization of cathodoluminescence from carbonate solid solutions. *Chemical Geology*, 9 (1-4), 275-284. [https://doi.org/10.1016/0009-2541\(72\)90064-2](https://doi.org/10.1016/0009-2541(72)90064-2)
- Sommer, S. E. (1972b). Cathodoluminescence of carbonates, 2. Geological applications. *Chemical Geology*, 9 (1-4), 275-284. [https://doi.org/10.1016/0009-2541\(72\)90065-4](https://doi.org/10.1016/0009-2541(72)90065-4)
- Soto, J. I., Flinch, J. F. & Tari, G. (2017). Permo-Triassic Salt Provinces of Europe, North Africa and the Atlantic margins: Tectonics and hydrocarbon potential. *Oxford: Elsevier, Print*.
- Souquet, P. (1967). Le Crétacé supérieur sud-pyrénéen en Catalogne, Aragon et Navarre. *Thèse Doctorat Sciences*, Université de Toulouse.
- Stevaux, J. & Winnock, E. (1974). Les bassins du Trias et du Lias inférieur d'Aquitaine et leurs épisodes évaporitiques. *Bulletin de la Société Géologique de France*, S7, 16 (6), 679-695. <https://doi.org/10.2113/gssgfbull.S7-XVI.6.679>
- Stevaux, J. & Zolnai, G. (1975). Les Olistostromes du Sud de l'Aquitaine dans la dynamique du Bassin. *IXe Congrès International de Sédimentologie*, Nice.
- Stipp, M., Stünitz, H., Heilbronner, R. & Schmid, S. M. (2002a). Dynamic recrystallization of quartz: correlation between natural and experimental conditions. *Geological Society of London, Special Publications*, 200 (1), 171-190. <https://doi.org/10.1144/GSL.SP.2001.200.01.11>
- Stipp, M., Stünitz, H., Heilbronner, R. & Schmid, S. M. (2002b). The eastern Tonale fault zone: a "natural laboratory" for crystal plastic deformation of quartz over a temperature range from 250 to 700°C. *Journal of Structural Geology*, 24 (12), 1861-1884. [https://doi.org/10.1016/S0191-8141\(02\)00035-4](https://doi.org/10.1016/S0191-8141(02)00035-4)
- Stipp, M. & Tullis, J. (2003). The recrystallized grain size piezometer for quartz. *Geophysical Research Letters*, 30 (21). <https://doi.org/10.1029/2003GL018444>
- Stoppa, F., Cirilli, S., Sorci, A., Broom-Fendley, S., Principe, C., Grazia Perna, M. & Rosatelli, G. (2021). Igneous and sedimentary 'limestones': the puzzling challenge of a converging classification. *Geological Society, London, Special Publications (2021)*, SP520-2021-120. <https://doi.org/10.1144/SP520-2021-120>
- Svahnberg, H. & Piazzolo, S. (2010). The initiation of strain localization in plagioclase-rich rocks: Insights from detailed microstructural analyses. *Journal of Structural Geology*, 32 (10), 1404-1416. <https://doi.org/10.1016/j.jsg.2010.06.011>
- Teixell, A. (1992). Estructura alpina en la transversal de la terminación occidental de la zona axial pirenaica. *Tesis Doctoral, Universitat de Barcelona*. 252 p.
- Teixell, A. (1993). Coupe géologique du massif d'Igoutze: implications sur l'évolution structurale de la bordure sud de la Zone nord-pyrénéenne occidentale. *Comptes Rendus de l'Académie des Sciences, Paris*, 316, 1789-1796.
- Teixell, A. (1996). The Ansó transect of the southern Pyrenees: Basement and cover thrust geometries. *Journal of the Geological Society of London*, 153 (2), 301-310. <https://doi.org/10.1144/gsjgs.153.2.0301>
- Teixell, A. (1998). Crustal structure and orogenic material budget in the west central Pyrenees. *Tectonics*, 17 (3). <https://doi.org/10.1029/98TC00561>
- Teixell, A., Labaume, P. & Lagabrielle, Y. (2016). The crustal evolution of the west-central Pyrenees revisited: Inferences from a new kinematic scenario. *Comptes Rendus – Geoscience*, 348 (3-4), 257-267. <https://doi.org/10.1016/j.crte.2015.10.010>
- Teixell, A., Labaume, P., Ayarza, P., Espurt, N., de Saint Blanquart, M. & Lagabrielle, Y. (2018). Crustal structure and evolution of the Pyrenean-Cantabrian belt: A review and new interpretations from recent concepts and data. *Tectonophysics*, 724-725, 149-170. <https://doi.org/10.1016/j.tecto.2018.01.009>
- ten Have, T. & Heijnen, W. (1985). Cathodoluminescence activation and zonation in carbonate rocks: an experimental approach. *Geologie en Mijnbouw*, 64, 297-310.
- ter Heege, J. H., de Bresser, J. H. P. & Spiers, C. J. (2002). The influence of dynamic recrystallization on the grain size distribution and rheological behavior of Carrara marble deformed in axial compression. In: de Meer, S., Drury, M. R., de Bresser, J. H. P., Pennock, G. M. (eds.). *Deformation Mechanisms, Rheology and Tectonics: Current Status and Future Perspectives*. Geological Society of London, *Special Publications*, 200 (1), 331-353. <https://doi.org/10.1144/GSL.SP.2001.200.01.19>



- Ternet, Y. (1965). Étude du synclinal complexe des Eaux-Chaudes (Basses-Pyrénées), *Thèse Doctorat 3<sup>o</sup> Cycle: Faculté des sciences de l'Université de Toulouse*, 332 p.
- Ternet, Y., Majeste-Menjoulas, C., Canérot, J., Baudin, T., Cocherie, A., Guerrot, C. & Rossi, P. (2004). *Carte géologique de la France: Laruns-Somport*. Bureau de Recherches Géologiques et Minières, scale 1:50.000, feuille n°1069.
- Ternois, S., Odlum, M., Ford, M., Pik, R., Stockli, D., Tibari, B., Vacherat, A. & Bernard, V. (2019). Thermochronological evidence of early orogenesis, eastern Pyrenees, France. *Tectonics*, 38 (4), 1308-1336. <https://doi.org/10.1029/2018TC005254>
- Toffolo, M. B., Ricci, G., Caneve, L. & Kaplan-Ashiri, I. (2019). Luminescence reveals variations in local structural order of calcium carbonate polymorphs formed by different mechanisms. *Scientific Reports*, 9, 16170. <https://doi.org/10.1038/s41598-019-52587-7>
- Tugend, J., Manatschal, G., Kuszniir, N. J., Masini, E., Mohn, G. & Thinon, L. (2014). Formation and deformation of hyperextended rift Systems: insights from rift domain mapping in the Bay of Biscay-Pyrenees. *Tectonics*, 33 (7), 1239-1276. <https://doi.org/10.1002/2014TC003529>
- Tuinstra, F. & Koenig, J. L. (1970). Characterization of graphite fiber surfaces with Raman spectroscopy. *Journal of Composite Materials*, 4 (4). <https://doi.org/10.1177/002199837000400405>
- Tullis, J. & Yund, R. A. (1989). Hydrolytic weakening of quartz aggregates: The effects of water and pressure on recovery. *Geophysical Research Letters*, 16 (11), 1343-1346. <https://doi.org/10.1029/GL016i011p01343>
- Twiss, R. J. (1977). Theory and applicability of a recrystallized grain size paleopiezometer. *Pure and Applied Geophysics*, 115, 227-244. <https://doi.org/10.1007/BF01637105>
- Twiss, R., J. (1986). Variable sensitivity piezometric equations for dislocation density and subgrain diameter and their relevance to olivine and quartz. In: Hobbs, B. E. & Heard, H. C. (eds) *Mineral and Rock Deformation: Laboratory Studies. Geophysical Monograph*, 36, 247-261. <https://doi.org/10.1029/GM036p0247>
- Valcke, S. L. A., Pennock, G. M., Drury, M. R. & De Bresser, J. H. P. (2006). Electron backscattered diffraction as a tool to quantify subgrains in deformed calcite. *Journal of Microscopy*, 224 (3), 264-276. <https://doi.org/10.1111/j.1365-2818.2006.01698.x>
- Valcke, S. L. A., De Bresser, J. H. P., Pennock, G. M. & Drury, M. R. (2014). Influence of deformation conditions on the development of heterogeneous recrystallization microstructures in experimentally deformed Carrara marble. *Geological Society of London, Special Publications*, 409 (1), 175-200. <http://dx.doi.org/10.1144/SP409.4>
- van der Wal, D., Chopra, P., Drury, M. & Fitz Gerald, J. (1993). Relationship between dynamically recrystallized grain size and deformation conditions in experimentally deformed olivine rocks. *Geophysical Research Letters*, 20 (14), 1479-1482. <https://doi.org/10.1029/93GL01382>
- Vernon, R. H. (1981). Optical microstructure of partly recrystallized calcite in some naturally deformed marbles. *Tectonophysics*, 78 (1-4), 601-612. [https://doi.org/10.1016/0040-1951\(81\)90031-7](https://doi.org/10.1016/0040-1951(81)90031-7)
- Vernon, R. H. (2004). A practical guide to rock microstructure. *University Press Cambridge, Cambridge*, 394 pp. <http://dx.doi.org/10.1017/CBO9780511807206>
- Villard, J. (2016). Déformation et thermicité de la couverture mésozoïque dans une structure salifère des Chaînons Béarnais (Zone Nord Pyrénéenne). Master Géosciences, *Mémoire de Master Université de Montpellier*, pp. 58. [https://rgf.brgm.fr/sites/default/files/upload/documents/production-scientifique/Masters/rgf\\_amipyr2015\\_ma7\\_memoire\\_villard.pdf](https://rgf.brgm.fr/sites/default/files/upload/documents/production-scientifique/Masters/rgf_amipyr2015_ma7_memoire_villard.pdf)
- Walker, A. N., Rutter, E. H. & Brodie, K. H. (1990). Experimental study of grain-size sensitive flow of synthetic, hot-pressed calcite rocks. In: Knipe, R. J. & Rutter, E. H. (eds) *Deformation Mechanisms, Rheology and Tectonics, Geological Society, London, Special Publications*, 54 (1), 259-284. <https://doi.org/10.1144/GSL.SP.1990.054.01.24>
- Weber, J. C., Ferrill, D. A. & Roden-Tice, M. K. (2001). Calcite and quartz microstructural geothermometry of low-grade metasedimentary rocks, Northern Range, Trinidad. *Journal of Structural Geology*, 23 (1), 93-112. [https://doi.org/10.1016/S0191-8141\(00\)00066-3](https://doi.org/10.1016/S0191-8141(00)00066-3)
- Wenk, H.-R. (2002). Texture and anisotropy. *Reviews in Mineralogy and Geochemistry*, 51 (1), 291-329. <https://doi.org/10.2138/gsrmg.51.1.291>

- Wheeler, J., Prior, D. J., Jiang, Z., Spiess, R. & Trimby, P. W. (2001). The petrological significance of misorientations between grains. *Contributions to Mineralogy and Petrology*, 141 (1), 109-124. <https://doi.org/10.1007/s004100000225>
- Wintsch, R. P. & Yeh, M.-W. (2013). Oscillating brittle and viscous behavior through the earthquake cycle in the Red River Shear Zone: Monitoring flips between reaction and textural softening and hardening. *Tectonophysics*, 587, 46-62. <https://doi.org/10.1016/j.tecto.2012.09.019>
- Wopenka, B. & Pasteris, J. D. (1993). Structural characterization of kerogens to granulite-facies graphite: Applicability of Raman microprobe spectroscopy. *American Mineralogist*, 78 (5-6), 533-557.

## Agraïments / Acknowledgments

Ja fa 5 anys de l'inici d'aquest meravellós projecte professional, acadèmic i, sobretot, personal, en un indret idíl·lic dels Pirineus, i ara toca finalitzar-lo. Encara me'n faig creus de tot el que ha suposat viure aquesta experiència, i de la sort que he tingut de tothom qui m'ha acompanyat i ha contribuït de múltiples maneres a fer d'aquesta una de les més enriquidores. De ben segur que faig curt amb les paraules següents, tot i així, el més sincer i profund agraïment a tothom.

A qui sempre estaré agraït per aquest projecte és als directors de tesi, Toni Teixell i Albert Griera, per la confiança dipositada en mi i l'oportunitat de treballar i aprendre amb i de vosaltres. Vull destacar el suport i acompanyament constant i incondicional que m'heu ofert en les discussions científiques, campanyes de camp, congressos i estades. Que sempre trobeu un moment per revisar el que us envio i de comentar-ho. La llibertat d'orientar i organitzar la feina. Destaco la vostra traça en guiar la formació científica de qui tutoritzeu, m'heu fet adonar que la ciència és un treball col·lectiu i de petits objectius per assolir-ne de més grans. Toni, vull agrair-te que em proposessis aquesta zona d'estudi i que m'hagis introduït a la geologia del Pirineu a través del teu coneixement i experiència. Per brindar-me el plaer de compartir amb tu la docència al camp als Pirineus i, a l'hora, tenir temps per fer-me fixar en tots els petits detalls. Albert, et vull agrair la confiança plena i incondicional i el fet d'haver-me introduït en la disciplina de la microestructura i fer-me desenvolupar la destresa d'integració de la geologia a totes les escales. Per orientar el treball de laboratori i les nombroses revisions de les làmines primes i resultats analítics. Ha estat un plaer compartir docència al camp i ha suposat un aprenentatge molt enriquidor.

Vull agrair a tots els membres del departament de geologia el suport, acompanyament i consells. Especialment a la María Luisa i al Paco Martínez per compartir congressos i discussions interessants. Al David Gómez sempre amb ànims i ajudant amb tot. A l'Eduard Saura, la confiança de treballar conjuntament en diversos projectes. Al Pini sempre amb bones paraules i bons dinars compartits. A la Mercè Corbella i el Dídac Navarro la confiança pel projecte SEM-CAT. Al Marc Furió i al Joan Reche per l'ajuda amb la burocràcia del doctorat.

A tot l'equip de secretaria, especialment a Teresa Puga, Sara Flotats, Eva del Pino, Sílvia Ballbé, Isabel Mercader i Lara González, que sempre ens heu facilitat enormement tota la feina burocràtica i amb un gran somriure a la cara. Gràcies per la vostra estima i professionalitat.

A l'equip de laborants de làmines primes Luis Gordón, Marc Puigcerver i Pepi Murillo, que sempre ens ajudeu amb professionalitat a tenir a punt les mostres tallades, en làmina prima o triturades.

Un sincère remerciement à Pierre pour son aide désintéressée tout au long du processus de thèse, la publication d'articles et surtout pendant le séjour à Montpellier. Pour m'avoir emmené sur le terrain et avoir toujours trouvé un moment pour discuter et partager des points de vue.

Je suis très reconnaissant à Abdeltif Lahfid de m'avoir introduit dans le monde de Raman et pour sa patience et sa volonté de m'enseigner la technique et de discuter des résultats. Et pour votre disponibilité à venir à Barcelone pour nous conseiller sur notre équipement et résultats.

Merci à toutes les personnes du projet Orogen pour l'opportunité de discuter et de contribuer à l'avancement des connaissances scientifiques sur les Pyrénées.

Je souhaite remercier Stéphane Dominguez de m'avoir permis de travailler avec lui dans le laboratoire de modélisation analogique et d'avoir pris le temps de m'enseigner et de discuter de la préparation et des résultats des expériences.

Un grand merci à Michel Séranne, Roger Soliva et aux collègues de Géosciences Montpellier pour les discussions intéressantes sur la structure et la déformation du massif des Eaux-Chaudes.

Muchas gracias a Marco López Sánchez por su desinteresada ayuda con el tratamiento de los datos de EBSD y su compromiso con el proyecto, ya sea desde Montpellier, Barcelona u Oviedo. Sin tu ayuda no hubiera podido finalizar la tesis en este momento.

A en Juan Diego per la didàctica introducció a la catodoluminescència. A l'Enrique Gómez i la Gemma Llorens per ajudar-nos amb els congressos i discussions científiques. A tots els doctorands per acollir-nos als dinars dels dies d'adquisició.

Als companys doctorands, i els ja doctors, per fer més suportable els daltabaixos emocionals. Especialment al Gerard Casado, qui m'ha acompanyat des del grau, i la Laura Burrel, una gran amiga que admiro molt. Al Marc Guardia per totes les celebracions i "patiment" tant al camp com al despatx.



A Juan Camilo Ruiz, un gran amigo con un extenso repertorio de grandes experiències. Al Xavier Coll per ajudar-me amb el Raman (supervisat pel Narcís Mestres) i al camp. Al Guillem Piris per la teva generositat i acollir-nos a la Vall. A l'Anna Anglisano, la teva empenedoria. Al Sabí Peris la teva energia i empena incansables. A María Carrión por tu alegría, empeño en sacar las cosas adelante y las charlas filosóficas. A Carla Garrido por tu perseverancia y fortaleza. A Esteban Mellado por tu visión crítica del mundo. A la Gisela Leoz pel llarg bagatge. Al Jandro pels dinars entretinguts. A tothom de qui he après tan de la geologia i com de la vida, Marta Roigé (i l'Oreig), Salva Boya, Isaac Corral, per la vostra empena i suport al llarg de la tesi, al Miquel Poyatos per la teva simpatia i la Marina Martínez per les discussions interessants i les "butis" d'aquests últims mesos. Vull incloure als amics de grau amb qui hem compartit i seguim compartint tants bons moments i records.

Je tiens à remercier Caroline et Joseph pour l'excellent accueil et les facilités d'hébergement et alimentation qu'ils m'ont toujours offerts pendant le travail de terrain à Eaux-Chaudes.

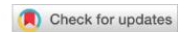
Als professors de batxillerat, Josep Lluís Badal, Montse Boqueras i Marc Ferrer, que m'han servit d'exemple i em van guiar i obrir camí cap a la ciència.

A Sergio Llana-Fúnez y Juan Luis Alonso por su confianza, pasión por la geología y guía científica en el trabajo de fin de máster, tanto en campo como en la facultad y laboratorio. Y por empujarme a compartir y participar de debates científicos.

Un agraïment enorme a tots els amics i amigues dels col·lectius que heu facilitat la desconexió mental del doctorat i l'esbarjo físic, en concret amb els jocs de taula (Tasta Jocs), amb la reconexió amb el bàsquet (Caravanas 1000), i amb el ball (Gitanes).

A tu, Bea, que m'has recolzat, acompanyat i tingut una paciència envejable, ja fa anys, i especialment durant tot aquest procés, sobretot, els últims mesos de feina intensiva. Gràcies per la teva estima i comprensió i per distreure'm quan ho he necessitat. T'estimo!

Finalment, a tota la meva família, que sempre m'ha recolzat, cuidat i donat suport i amb qui he crescut personal i emocionalment. Espero seguir celebrant la vida amb tots vosaltres. Especialment als meus pares i germana, per iniciar-me als Pirineus, pels vostres consells, la vostra estima incondicional, paciència infinita i constància per ajudar-me a créixer i formar-me com a persona. Us estimo molt!



Received: 13 January 2020 | Revised: 28 October 2020 | Accepted: 9 December 2020

DOI: 10.1111/ter.12517

## RESEARCH ARTICLE

Terra Nova WILEY

# Recumbent folding in the Upper Cretaceous Eaux-Chaudes massif: A Helvetic-type nappe in the Pyrenees?

Norbert Caldera<sup>1</sup> | Antonio Teixell<sup>1</sup> | Albert Grieria<sup>1</sup> | Pierre Labaume<sup>2</sup> | Abdeltif Lahfid<sup>3,4</sup> <sup>1</sup>Departament de Geologia, Universitat Autònoma de Barcelona, Barcelona, Spain<sup>2</sup>Géosciences Montpellier, Université de Montpellier, CNRS, Université des Antilles, Montpellier, France<sup>3</sup>BRGM, Orléans, France<sup>4</sup>UMR 7327 ISTO, Université d'Orléans, CNRS, BRGM, Orléans**Correspondence**Norbert Caldera, Departament de Geologia, Universitat Autònoma de Barcelona, 08193 Bellaterra, Barcelona, Spain.  
Email: norbert.caldera@uab.cat**Funding information**

Spanish MINECO/MCIU, Grant/Award Number: CGL2014-54180 and PGC2018-093903-B-C21

**Abstract**

We describe a singular structure in Upper Cretaceous rocks of the Eaux-Chaudes massif of the western Pyrenees, consisting of a kilometre-scale fold nappe with a sheared overturned limb. High ductile strain attests a deformation style rarely reported for the alpine Pyrenees, and peak temperature in Upper Cretaceous carbonates is estimated by Raman spectroscopy of carbonaceous material palaeothermometry in the lower greenschist facies (>300°C). The normal fold limb retains the original sedimentary textures, while the overturned limb shows calcite crystal-plastic deformation and dynamic recrystallization, with crystallographic preferred orientation. The observed ductility and metamorphic temperature bear similarities with the lower Helvetic nappes of the Alps, suggesting deep burial and/or possibly high geothermal gradient in this part of the Pyrenees.

## 1 | INTRODUCTION

In orogens formed by tectonic inversion, the reactivation of extensional structures and the formation of thrust-related basement uplifts commonly accommodate the compressional deformation (e.g. Herwegh et al., 2020; Lacombe & Bellahsen, 2016; Pfiffner, 2017). The interiors of basement uplifts are often poorly understood due to structural complexity and limited outcrops of post-basement rocks. This study focusses on the Axial Zone of the Pyrenees, an Alpine orogen resulting from the inversion of a Mesozoic hyperextended rift (Jammes et al., 2009; Lagabrielle et al., 2010; Masini et al., 2014; Teixell et al., 2016, 2018). The Pyrenees conform to an asymmetric doubly verging wedge (Choukroune et al., 1989; Muñoz, 1992; Teixell, 1998) which formed from late Cretaceous to early Miocene times (Alpine orogeny; Figure 1). The Axial Zone comprises a system of thrust sheets made of Iberian Palaeozoic basement (previously deformed by the Variscan orogeny) which connects to a south-verging thin-skinned thrust system of Mesozoic and Tertiary rocks (South Pyrenean Zone). North of the Axial Zone, the North Pyrenean Zone

(NPZ) comprises the inverted Mesozoic basin axis which overrides both the Aquitaine foreland by the North Pyrenean Frontal Thrust and the Axial Zone by the North Pyrenean Fault and the Lakora thrust (Mouthereau et al., 2014; Muñoz, 1992; Teixell, 1998; Teixell et al., 2016).

The Eaux-Chaudes massif (ECM) comprises an inlier of Upper Cretaceous rocks surrounded by Palaeozoic rocks in the north-western Axial Zone (Figure 2). The massif has been classically interpreted as a duplex structure with a roof thrust carrying Palaeozoic basement (Déramond et al., 1985; Dumont et al., 2015; Ternet, 1965). The Upper Cretaceous sedimentary cover constitutes a key-marker to constrain the structural history and palaeotemperature conditions during the Alpine orogeny.

We present a novel view of the Eaux-Chaudes structure (Figure 3), documented by structural mapping, microstructure and palaeotemperature data, which highlights a kilometre-scale recumbent fold nappe. Our observations evidence the importance of alpine ductile folding not recognized hitherto in the hinterland of the Pyrenees.

## 2 | TECTONIC SETTING

Palaeotectonic reconstructions place the Upper Cretaceous platform carbonates of the ECM in the upper margin of the Iberian plate during the Mesozoic post-rift stage (e.g. Teixell et al., 2016 and references therein). These carbonates later became sandwiched between Palaeozoic rocks during the Pyrenean convergence.

The Upper Cretaceous sequence lies unconformably on Silurian to Carboniferous metasedimentary rocks, mainly shales, limestones and sandstones, and on the late Palaeozoic Eaux-Chaudes granite. Occasionally lower Triassic Buntsandstein conglomerate pods are preserved in between the Palaeozoic and the Upper Cretaceous (Ternet, 1965). The Cretaceous sequence consists of a lower unit of mudstones and grainstones ("Calcaires des Cañons," Cenomanian to Santonian) followed by sandstone-shale Flysch of Campanian–Maastrichtian age (Ternet, 1965), a sequence which represents the early stages of subsidence related to the Pyrenean orogeny (Teixell, 1993). Cenomanian–Turonian formations are discontinuous due to local erosion events, as observed elsewhere in the western Axial Zone (Souquet, 1967; Teixell et al., 1994). The ECM is overlain by the Lakora thrust complex (Figure 2), here represented by Palaeozoic (Montagnon d'Iseye thrust unit) and Upper Triassic rocks (mostly Keuper and ophiolites, Bedous unit), which is in turn overlain by the detached Jurassic–Lower Cretaceous rocks of the southern Chaînons Béarnais (Labaume & Teixell, 2020; Ternet et al., 2004). The whole system was uplifted in the hangingwall of the Gavarnie thrust that raised the Axial Zone, imparting local back-thrusting deformation in the ECM (D2 in Dumont et al., 2015). Thrusting of the Lakora–Eaux-Chaudes units is attributed to the latest Cretaceous to mid-Eocene, while subsequent Gavarnie thrusting in the western Axial Zone is attributed to the late Eocene–early Oligocene (Labaume et al., 2016; Teixell, 1996).

## 3 | METHODOLOGY

Field structural analysis and mapping were combined with cross-section construction to interpret the large-scale structure. Samples were analysed by thin section and scanning electron microscopy (SEM) coupled with electron backscattered diffraction (EBSD) and energy dispersive spectrometry. EBSD data were collected at the University of Montpellier on a CamScan Crystal Probe X500FE.

Raman spectroscopy of carbonaceous material (RSCM) was performed at the BRGM (Orléans) to calculate peak temperatures ( $T_{max}$ ) using a diode-pumped solid-state laser source excitation of 514.5 nm. The laser power reaching the sample surface, through the 100× objective of a Leica DM2500 microscope, did not exceed 1 mW. We followed the procedures described by Beyssac et al. (2002, 2003, 2007) and Lahfid et al. (2010).

## Significance statement

The Pyrenean orogenic deformation is most often characterized by thrust-fold systems formed under brittle conditions. The Eaux-Chaudes massif is an inlier of Upper Cretaceous sediments within the hinterland Axial Zone of the Pyrenees which allows to characterize the post-Variscan structure in this basement massif. Here we report for the first time a recumbent fold structure, developed under ductile conditions in the Upper Cretaceous carbonates, with upper Palaeozoic metasediments in the core. The fold nappe displays a kilometre-scale, large overturned limb affected by high non-coaxial deformation (mylonitic fabric and strong crystallographic preferred orientation of calcite). Recorded palaeotemperatures  $>300^{\circ}\text{C}$  in the Upper Cretaceous rocks are consistent with the microstructure observed. This is a novel deformation style previously unreported for the alpine Pyrenees, comparable with other analogues as for example the lower Helvetic nappes of the Alps. The results reported in the manuscript are of broad general interest, especially for the community focused on mountain building processes, and provide a unique example to decipher the thermomechanical evolution in complex hinterland areas, as the Axial Zone of the Pyrenees. Our interpretations are supported with new cartography and structural cross-section, palaeotemperature using Raman spectroscopy of carbonaceous material technique and microstructure analysis using SEM-EBSD.

## 4 | RESULTS

We propose a new structural profile of the ECM showing an unexpected large-scale ductile structure defined by the Upper Cretaceous rocks (Figures 3 and 4), consisting of a south-verging ~5-km-long recumbent fold nappe cored by folded Silurian–Devonian metasediments with a near-horizontal axial plane and a large overturned limb. The Palaeozoic core shows minor folds with subhorizontal axial planes and heterogeneously distributed foliation. The overturned limb is in thrust contact over an autochthonous panel of weakly deformed Upper Cretaceous carbonates (Figures 2–4). Occasional Keuper and ophiolite slices are found along the contact (Ternet, 1965). The Eaux-Chaudes recumbent structure shows an immersion to the west, consistent with the regional plunge of the western Axial Zone, and hence it disappears laterally below overlying thrust sheets. East of the Ossau valley it is largely eroded, so the valley area provides a unique opportunity to observe the proposed structural relationships.

Sample analyses were performed in the Upper Cretaceous of the autochthon, the overturned limb and the normal limb of the fold nappe (Figures 3 and 4).



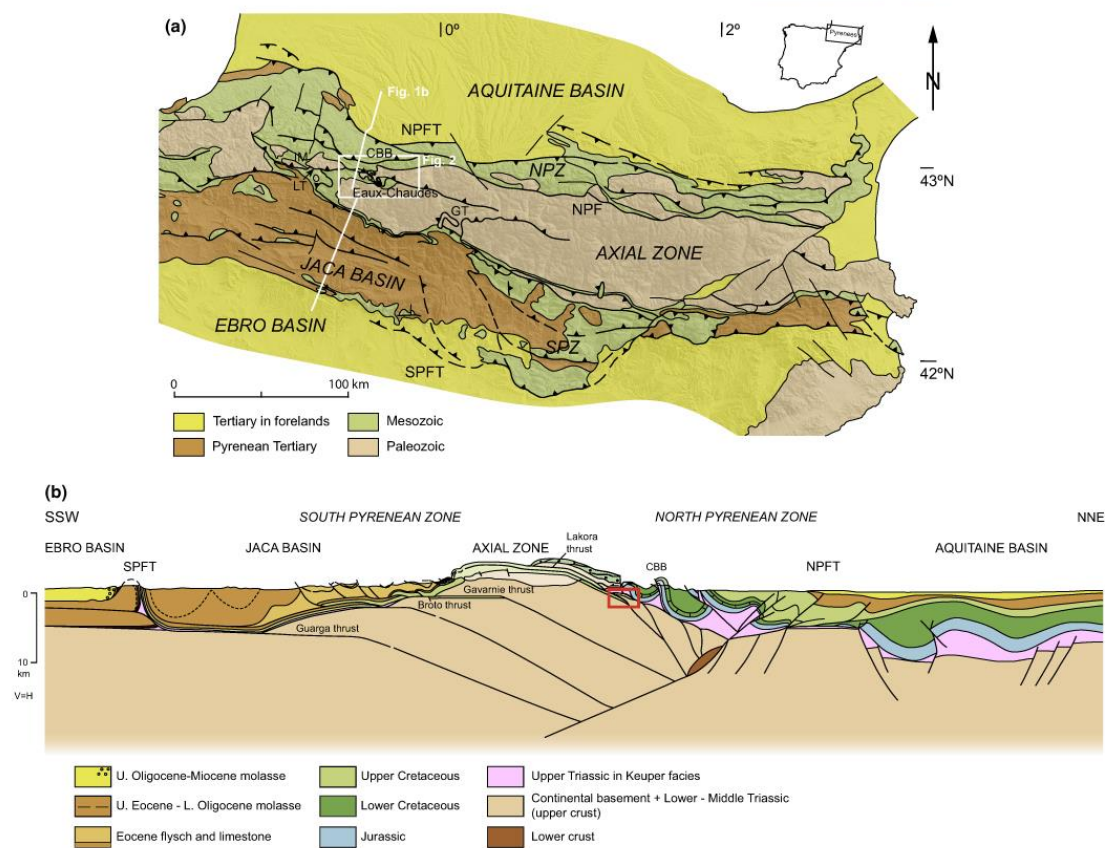


**FIGURE 1** (a) Geological sketch map of the Pyrenees showing the location of the Eaux-Chaudes massif. White frame indicates the mapped area (Figure 2) and white line indicates cross-section in (b). (b) Crustal cross-section of the Pyrenees west of the study zone (simplified from Teixell et al., 2016) showing the tectonic setting of the: Eaux-Chaudes structure (red frame); CBB, Chaînons Béarnais Belt; GT, Gavarnie thrust; IM, Igountze Mendibelza; LT, Lakora thrust; NPF, North-Pyrenean fault; NPFT, North-Pyrenean Frontal thrust; NPZ, North-Pyrenean Zone; SPFT, South-Pyrenean Frontal Thrust; SPZ, South-Pyrenean Zone

#### 4.1 | Structural analysis

In the Upper Cretaceous of the autochthonous and normal-limb domains, sedimentary textures are preserved, despite small-scale brittle faults, and a spaced pressure-solution cleavage. Generally, fossils are unstrained apart from solution seams, and ductile deformation at the grain scale is not observed. EBSD analysis of calcite aggregates show random distribution of crystallographic  $a$ -,  $m$ - and  $c$ -axes (Figure 5). The average grain size is  $\sim 32 \mu\text{m}$ , ranging between 16 and  $100 \mu\text{m}$ . Occasionally, deformation twins of type III-IV (Ferrill et al., 2004) are observed in coarser calcite grains.

The overturned limb is characterized by strong ductile deformation that obliterates fossil content. It shows a mylonitic foliation subparallel to bedding at the mesoscale, and stretching lineation, both inclined to the north (Figure 5). Microfabrics are controlled by the rheological

behaviour of the mineral phases. In calcite-rich layers, crystal-plastic deformation is dominant with development of a fine-grained matrix ( $9\text{--}28 \mu\text{m}$ , decreasing grain size with increasing deformation intensity) featuring grain shape preferred orientation and S-C composite fabrics (Figure 5). We observed evidence of grain boundary migration, such as lobate and interfingering grain boundaries and subgrains. Well-developed crystallographic preferred orientation is recorded, with  $c$ -axes oriented normal to the foliation, and  $a$ - and  $m$ -axes defining a girdle parallel to the foliation (Figure 5). Aligned oxide minerals ( $<1 \text{ vol}\%$ ) parallel to the main foliation enhance the anisotropic fabric. Thin dolomite-rich layers are observed in some samples. These layers show moderate plastic deformation, with occasional fold streaks and asymmetric porphyroclasts (Figure 6). Quartz- and phyllosilicate-rich layers (e.g. Buntsandstein and Cretaceous clastic limestones) show brittle-to-ductile behaviour, with weak intragranular deformation (undulose extinction) and slight evidence of quartz recrystallization by



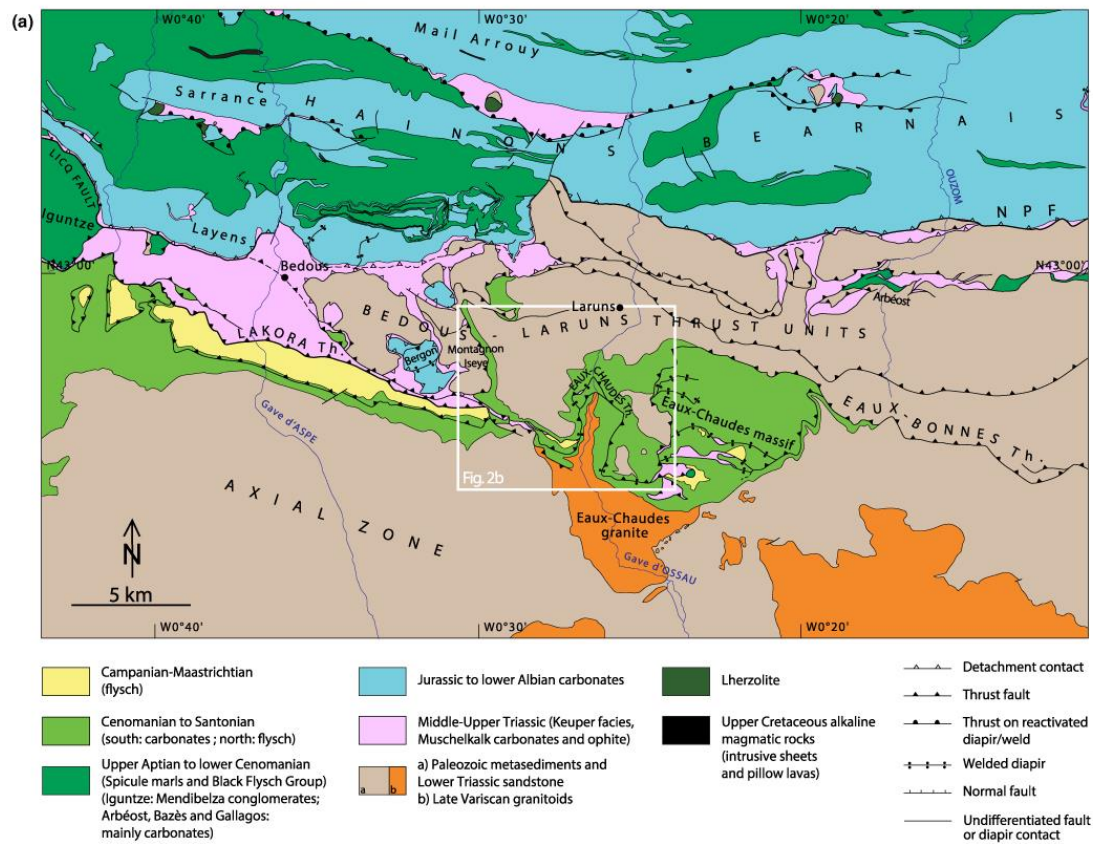


**FIGURE 2** 2(a) Geological map of the Chaînons Béarnais belt (North-Pyrenean Zone) and Eaux-Chaudes massif, location in Figure 1a; NPF, North-Pyrenean fault. Modified from Labaume and Teixell (2020). (b) Detailed geological map of the study area in the Ossau Valley, western Eaux-Chaudes massif (location in Figure 2b). Data compiled from published maps (Ternet, 1965; Ternet et al., 2004), completed with additional own field studies. White line indicates cross-section in Figure 3

bulging. S-C fabrics and asymmetric porphyroclasts attest a non-coaxial deformation and evidence the south-directed tectonic transport previously reported by Cochelin (2016), Dumont et al. (2015), Majesté-Menjoulas (1979) and Ternet (1965). Microstructure and EBSD of monomineralic calcite aggregates suggest plastic deformation by dislocation creep accommodated by slip on basal planes parallel to the *a*- and *m*-axes.

#### 4.2 | RSCM palaeothermometry

Raman spectroscopy of carbonaceous material is based on the analysis of the degree of structural organization of carbonaceous material (CM) as a proxy for the  $T_{max}$ . CM structure is not sensitive to retrograde transformations, remaining on the maximum temperature reached during metamorphism (Beysac et al., 2002).

Raman spectra are composed in the first region (Nemanich & Solin, 1979; Tuinstra & Koenig, 1970) by the graphite band (G) and defect bands ( $D_{1-4}$ ).

The spectra from the autochthonous and overturned limb were fitted by the Beysac et al. (2002) method, since it is well adapted to the temperature range 320–650°C. Samples from the normal limb best fittings were obtained by the method of Lahfid et al. (2010), which works better in the temperature range 150–320°C. In either case,  $T_{max}$  values obtained for all samples range between 315 and 350°C (Figure 7; Table 1). Representative Raman spectra (Figure 7) from the undeformed autochthonous unit and overturned limb show differences between the intensities of D1 and G bands with D1 band more intense. This indicates a temperature higher than 330°C. In the normal limb, both D1 and G bands show a very similar intensity, implying a lower temperature of approximately 315°C.

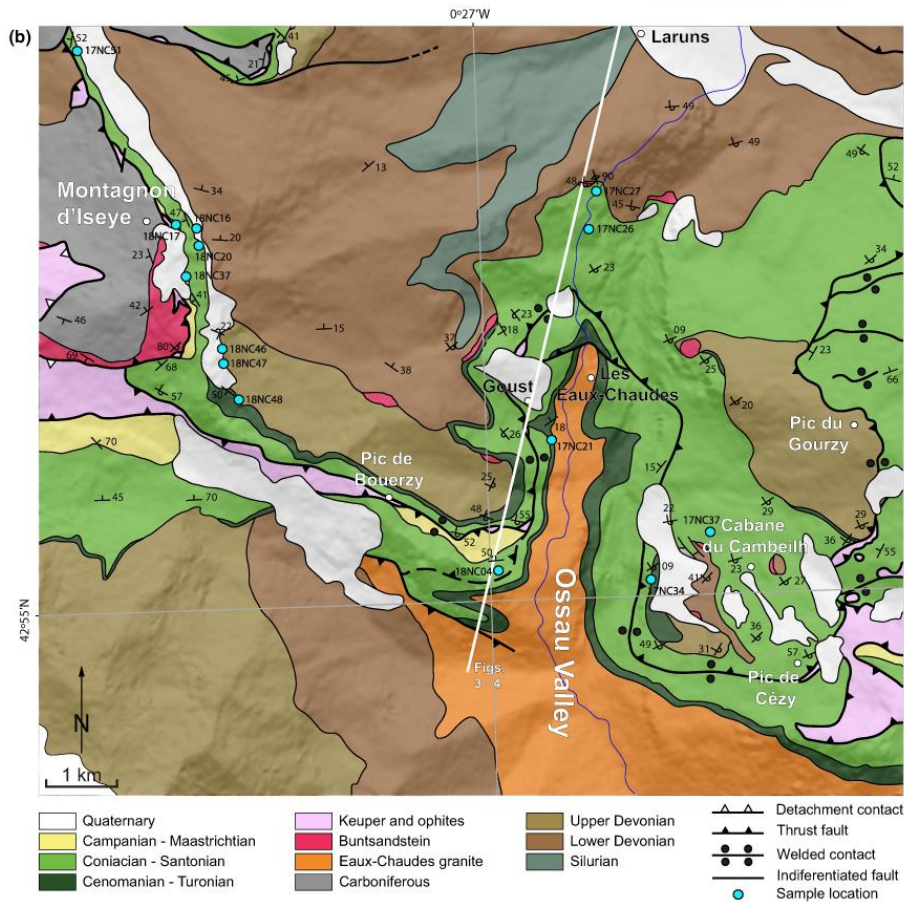


FIGURE 2. (Continued)

## 5 | DISCUSSION

The ECM represents the inverted Iberian rifted margin where Upper Cretaceous rocks have been ductilely folded. Large-scale recumbent folding is accompanied by high-strain shearing in the overturned limb, with extensive crystal-plastic deformation and recrystallization, not reported hitherto for the compressional deformation of the post-Palaeozoic rocks of the Pyrenees.

The Pyrenean Axial Zone is interpreted as a stack of basement units buried and deformed during the Cenozoic at temperatures in general <300°C (e.g. Abd Elmola et al., 2017; Bellahsen et al., 2019; Fitzgerald et al., 1999; Jolivet et al., 2007; Metcalf et al., 2009). This work shows for the first-time evidence for ductile basement-involved thin-skinned deformation (i.e. Pfiffner, 2017) in the Pyrenees, affecting the Upper Palaeozoic metasediments and the overlying Mesozoic sedimentary rocks. RSCM geothermometric results for the Jurassic–Lower Cretaceous rocks of the

NPZ in the vicinity are in a range of 300–400°C (Clerc et al., 2015; Corre, 2017). However, this metamorphic peak is associated with the mid-Cretaceous episode of crustal hyperextension in the Pyrenean rift (Clerc & Lagabrielle, 2014; Golberg & Leyreloup, 1990; Saspiturry et al., 2020), and not with the Alpine orogeny as in the Upper Cretaceous at Eau-Chaudes. The microstructural features observed at ECM are consistent with the RSCM estimates. Type IV deformation twins are indicative of temperatures >250°C (Ferrill et al., 2004), complete recrystallization of calcite is commonly reported at temperatures >300°C (Weber et al., 2001), and incipient bulging recrystallization in quartz is documented for the range 300–400°C (Stipp et al., 2002).

Our proposed cross-sectional geometry differs notably from previously published structural interpretations (Cochelin, 2016; Déramond et al., 1985; Dumont et al., 2015; Ternet, 1965). The recumbent fold poses the question of the mechanical behaviour of the Palaeozoic metasediments located in the deformed core of the



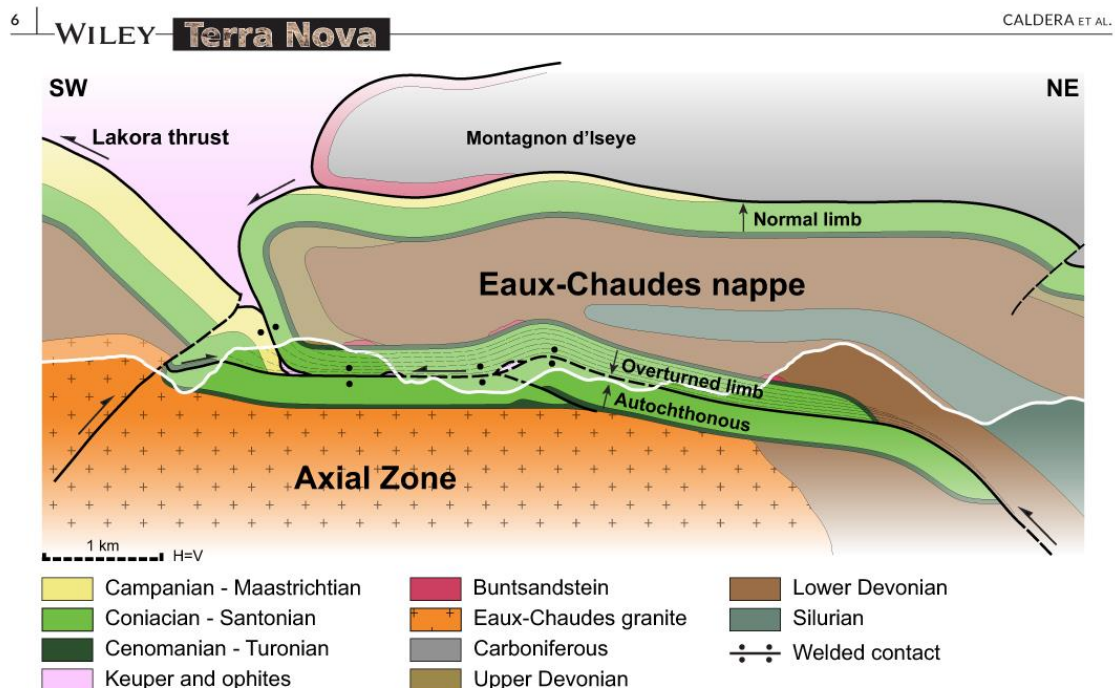


FIGURE 3 Cross-section of the recumbent Eaux-Chaudes fold nappe in the western side of the Ossau valley (see Figure 2b for location)

structure. The bulk of these rocks is rich in phyllosilicates, that is, slates with limestone and sandstone intercalations of Devonian age, and graphitic Silurian slates. The main foliation observed in these rocks is consistent with the large structure, although could partly derive from an earlier Variscan fabric (Cochelin, 2016; Dumont et al., 2015) that was reworked during Alpine deformation. Mapping suggests that the Eaux-Chaudes fold nappe was detached in the weak Silurian rocks. The contact that is usually mapped as the Eaux-Chaudes thrust in the Ossau valley (e.g. Ternet et al., 2004) is here reinterpreted as an overturned stratigraphic boundary between Palaeozoic and Upper Cretaceous carbonates, supported by (1) the occurrence of overturned Buntsandstein pods along the contact, (2) a large-scale folded Palaeozoic stratigraphy cored by Silurian slates and (3) the recognition by Ternet (1965) of an overturned panel involving Palaeozoic and Cretaceous rocks at Bouerzy and Cézy peaks (Figure 2) in the hinge of the structure. Along the Ossau valley, the highly deformed Upper Cretaceous carbonates of the overturned limb are in sharp contact with the low deformed and sub-horizontal autochthonous Upper Cretaceous carbonates (Figures 3 and 4). The Keuper and ophite bodies along the contact may represent relicts of the Triassic sole of the overlying Lakora thrust sheet, squeezed out from the faulted (welded) synform during recumbent folding (Figure 8).

This Pyrenean structure has similarities to the lower Helvetic Morcles-Doldenhorn nappes of the Alps, which are recumbent folds with long overturned limbs involving low-grade Mesozoic metasedimentary rocks (e.g. Burkhard, 1988; Casey

& Dietrich, 1997; Herwegh & Pfiffner, 2005; Pfiffner, 1993; Ramsay, 1981). Palaeotemperature data (315–350°C), grain size (9–28 µm) and microstructure (dislocation creep-induced textures, dynamic recrystallization and associated grain size reduction) are also comparable. For example, Austin et al. (2008) reported average grain size between 7 and 22 µm for samples deformed in a temperature range 337–358°C in the Morcles Nappe. Similar grain sizes and palaeotemperatures were also reported for the Doldenhorn and Glarus nappes by Ebert et al. (2007, 2008) and Herwegh and Pfiffner (2005).

A challenge resides in explaining the high temperatures recorded by the Upper Cretaceous rocks in the ECM. In the Helvetic case, high temperature can be explained by tectonic burial by the overlying Penninic and Austroalpine nappes, with a structural pile >15 km (Dietrich & Casey, 1989; Herwegh & Pfiffner, 2005; Nibourel et al., 2018; Pfiffner et al., 1997). Such deep burial is more difficult to envisage for the Pyrenees where the thrust stack is considered much thinner (e.g. Bellahsen et al., 2019; Teixell, 1998). The measured ~30°C difference between the normal and overturned limbs at Eaux-Chaudes, for samples ~1 km apart vertically, could indicate a normal geothermal gradient in the fold domain, although this difference lies within the RSCM error margins and, therefore, cannot be conclusive. A 30°C/km gradient for the Iberian margin is near to the 34°C/km gradient estimated for the European conjugate margin by Saspiturry et al. (2020). However, a 30°C/km gradient would imply ~11 km of burial over the fold nappe, which is hard

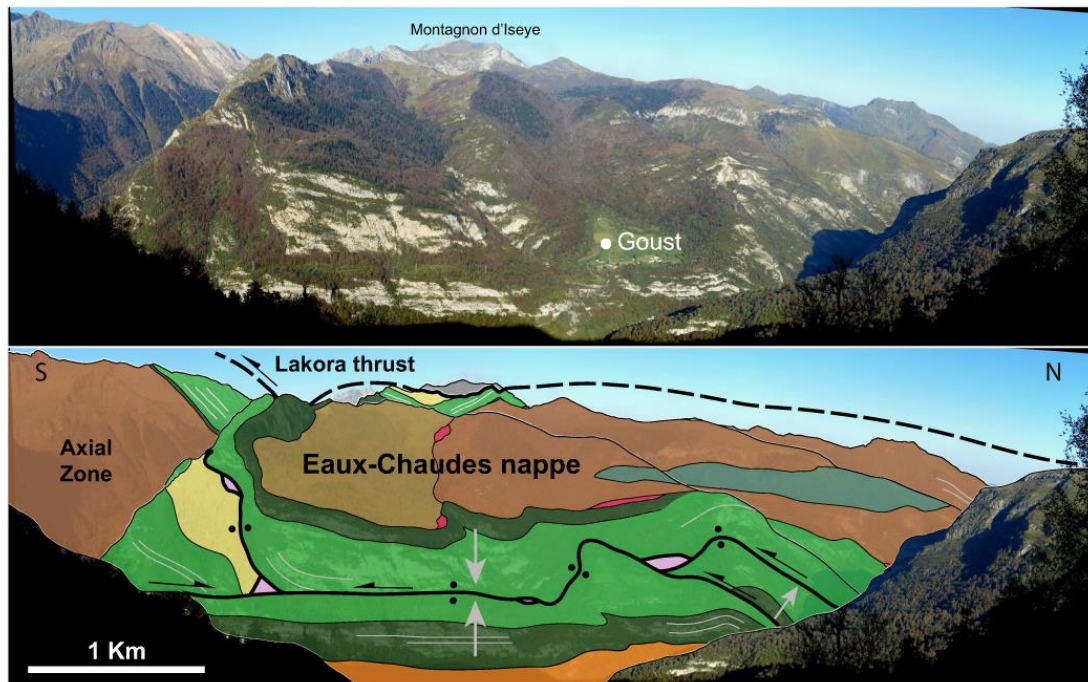


FIGURE 4 Outcrop photo and interpreted profile of the Eaux-Chaudes nappe structure at the western side of the Ossau valley (see Figure 2b for location). Grey arrows indicate bedding polarity. Colour codes correspond to those given in Figure 3

to reconcile with the tectonic pile that can be reconstructed above (Labaume & Teixell, 2020). Labaume et al. (2016), based on thermochronology-assisted restoration, estimated ~8 km of total burial over the Eaux-Chaudes thrust units (including synorogenic Flysch), representing a 40°C/km gradient using our palaeotemperatures. The available observations cannot unequivocally discriminate between deep burial and high geothermal gradient, the latter a relict of the Mesozoic thinning phase as proposed by Bellahsen et al. (2019) for other parts of the Iberian palaeomargin in the Axial Zone.

## 6 | CONCLUSIONS

We propose a novel structural interpretation for the Upper Cretaceous of the ECM with a style reported for the first time in post-Palaeozoic rocks of the Pyrenees. It consists of a large recumbent fold nappe, cored by Palaeozoic phyllosilicate-rich metasediments and comprising a kilometre-long overturned and sheared limb, showing similarities with the fold nappes of the lower Helvetic Alps.

According to RSCM palaeothermometry, the Upper Cretaceous carbonates of the Eaux-Chaudes nappe reached the lower greenschist facies with peak temperature of ~350°C. Mylonitic foliation and stretching lineation are well developed in the overturned fold

limb. Crystallographic and shape-preferred orientations in calcite are consistent with plastic deformation and extensive dynamic recrystallization indicating top-to-the-south shear sense. These observations evidence a high temperature of the Axial Zone during Alpine deformation and rend challenging its interpretation between a deep burial and/or a high geothermal gradient relict from the Mesozoic thinning phase.

## ACKNOWLEDGEMENTS

This work was supported by the Spanish MINECO/MCIU projects CGL2014-54180 and PGC2018-093903-B-C21. We thank the OROGEN project for enabling the acquisition of RSCM data, co-funded by Total S.A., BRGM and Institut national de sciences de l'Univers (INSU). Fabrice Barou is thanked for EBSD acquisition assistance and data treatment at Géosciences Montpellier. We thank T. Dumont, D. Westerman, B. Cochelin and anonymous reviewers for comments that helped to improve the original manuscript.

## CONFLICT OF INTEREST

None.

## DATA AVAILABILITY STATEMENT

The data that support the findings of this study are available from the corresponding author upon a reasonable request.



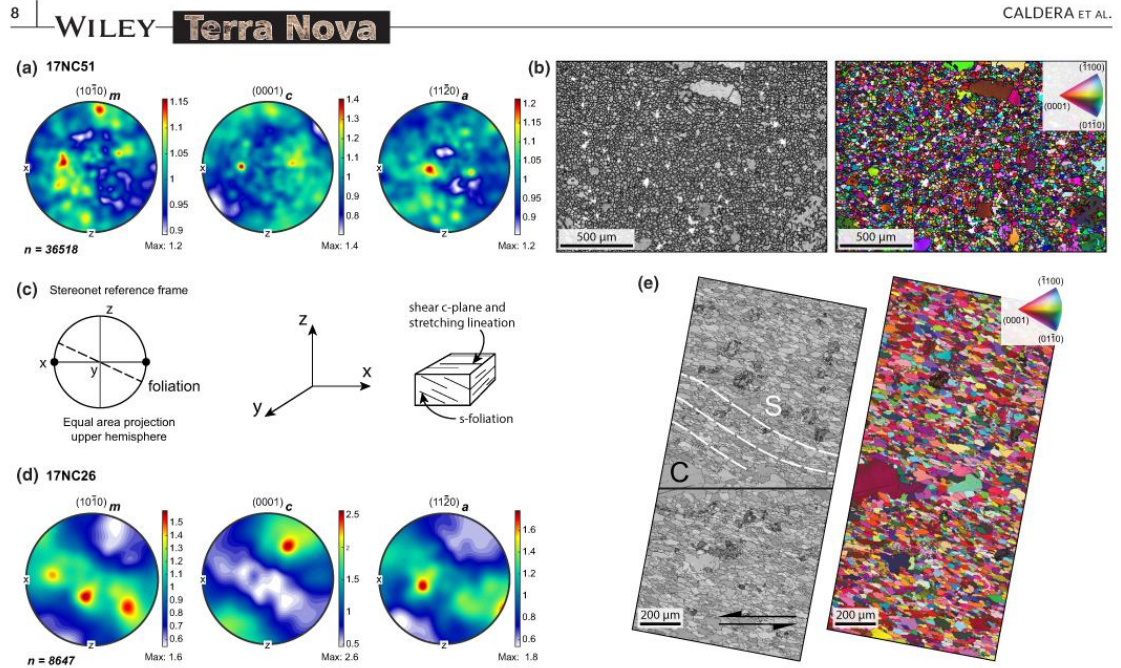


**FIGURE 5** (a) Equal area upper hemisphere pole figures of calcite *a*-, *m*- and *c*-axes measured by EBSD for the undeformed Upper Cretaceous limestone from the normal limb of the Eau-Chaudes fold nappe (sample 17NC51, cut perpendicular to bedding), showing random crystallographic orientation. (b) Band contrast image and Inverse Pole Figure (IPF) map for sample 17NC51. (c) Stereonet reference frame with xyz spatial axes for deformed samples of the overturned limb. Pole figures and images correspond to the xz plane. (d) Equal area upper hemisphere pole figures of calcite *a*-, *m*- and *c*-axes fabrics deformed of sample 17NC26, showing a moderate crystallographic preferred orientation. (e) Band contrast image and IPF map of sample 17NC26 showing S-C composite structure (see Figure 2b and Table 1 for sample location)

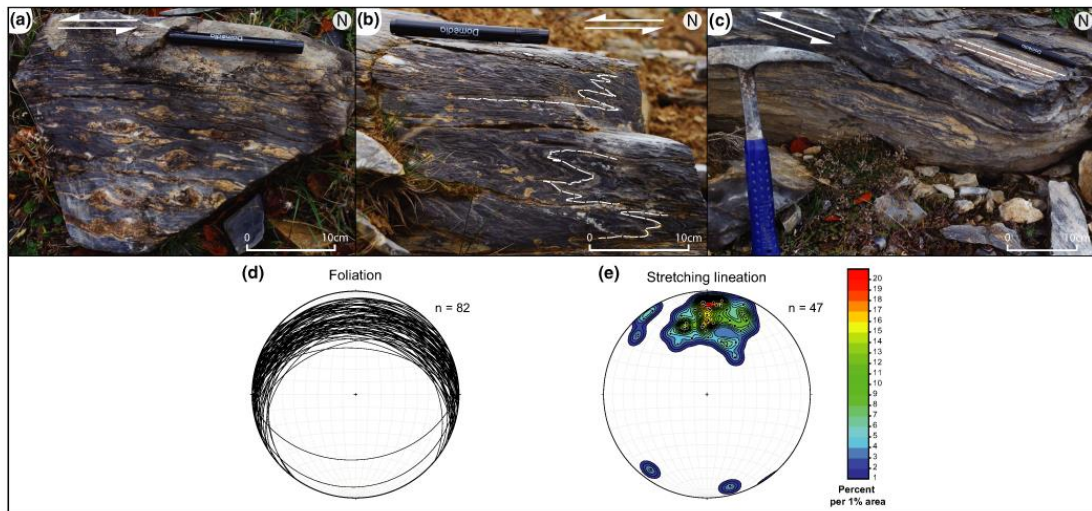


**FIGURE 6** Deformed samples from the overturned limb at the locality of Cambailh (see Figure 2 for location). Arrows indicate the shear direction. (a) Asymmetric dolomite porphyroclasts in a dark recrystallized calcite matrix. (b) Intramylonitic folds (dashed white lines) in sheared limestone. (c) Stretching lineation (dashed white lines) on the mylonitic foliation planes. All of these structures indicate top to the south sense of tectonic transport. (d, e): Stereographic projection of (d) main foliation and (e) stretching lineation measured in the Upper Cretaceous rocks. (lower hemisphere, equal area)

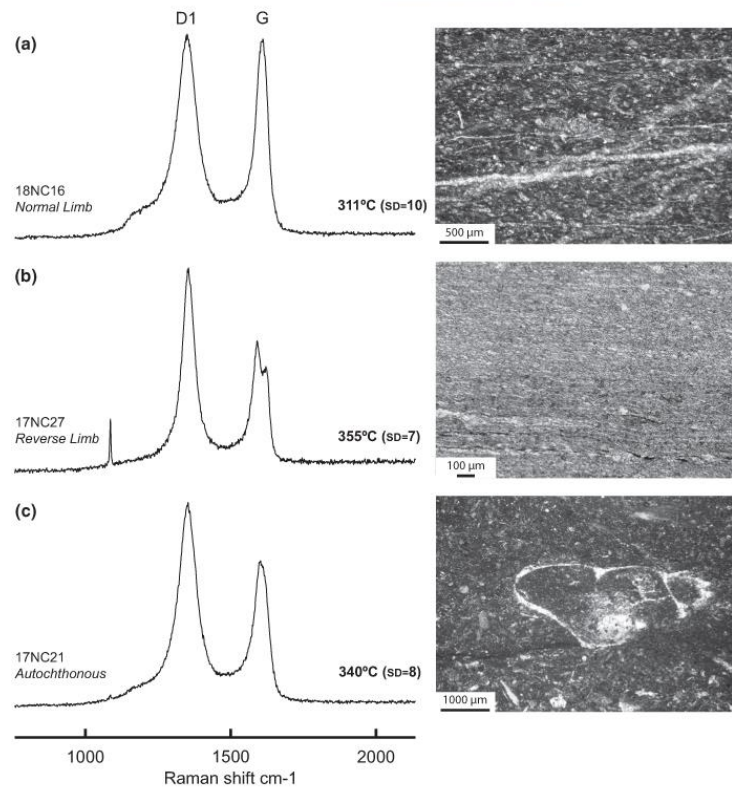


**FIGURE 7** Representative Raman spectra of carbonaceous material and photomicrographs of three samples from the Upper Cretaceous rocks, in a vertical profile across the Eaux-Chaudes fold nappe. (a) Undeformed sample from the normal limb of the recumbent fold. (b) Deformed sample from the overturned limb of the recumbent fold. (c) Undeformed sample from the autochthon (see Figure 2b and table 1 for sample location)

**TABLE 1** Summary of samples used in Raman and electron backscattered diffraction (EBSD) study. Zone indicates the structural position of samples (Au, autochthonous; OL, overturned Limb; NL, normal limb). RA1 and RA2 values were retrieved from peak fitting of Raman spectra (mean and standard deviation). RA1,  $(D1 + D4)/(D1 + D2 + D3 + D4 + G)$ ; RA2,  $(D1 + D4)/(D2 + D3 + G)$ ; Maximum temperatures were estimated after the methods by Beyssac et al. (2002) and Lahfid et al. (2010). Asterisks indicate EBSD analysed samples

Sample	Latitude N	Longitude W	Zone	R2 parameter		RA1 parameter		Number of spectra	T (°C)	
				Mean	SD	Mean	SD		Mean	SD
17NC21	42°56'44.69"	0°26'39.45"	Au	0.67	0.03	—	—	17	340	8
17NC26*	42°58'3.27"	0°26'20.03"	OL	0.65	0.02	—	—	16	348	8
17NC27*	42°58'14.39"	0°26'17.28"	OL	0.64	0.02	—	—	22	355	7
17NC34*	42°55'52.68"	0°25'52.96"	OL	0.66	0.02	—	—	21	344	6
17NC37*	42°56'7.22"	0°25'22.92"	OL	0.68	0.02	—	—	18	337	8
18NC04	42°56'2.59"	0°27'7.40"	OL	0.68	0.03	—	—	15	334	7
18NC46	42°57'19.84"	0°29'21.50"	NL	0.70	0.01	—	—	15	328	5
18NC47	42°57'17.08"	0°29'21.61"	NL	0.72	0.01	—	—	12	321	4
18NC16	42°58'5.81"	0°29'36.55"	NL	—	—	0.62	0.01	14	311	10
18NC17	42°58'6.62"	0°29'37.71"	NL	—	—	0.63	0.01	10	316	15
18NC20	42°58'0.87"	0°29'34.21"	NL	—	—	0.63	0.01	14	317	11
18NC37	42°57'46.53"	0°29'37.65"	NL	—	—	0.63	0.01	10	313	15
18NC48	42°57'5.41"	0°29'17.86"	NL	—	—	0.63	0.01	12	315	13
17NC51*	42°59'13.80"	0°30'27.30"	NL	—	—	—	—	—	—	—



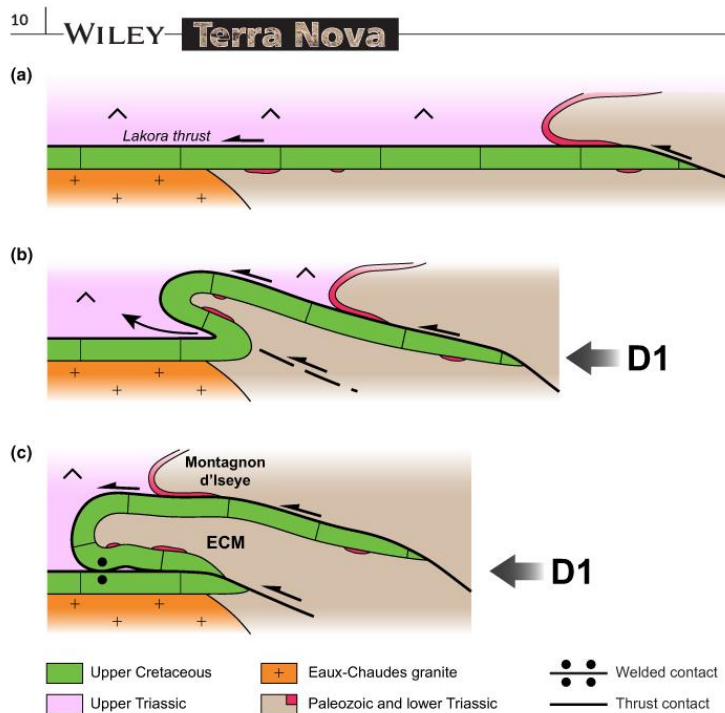


**FIGURE 8** Cartoon (not to scale) illustrating the development and evolution of the Eaux-Chaudes recumbent fold during the D1 stage of the Pyrenean compressional deformation. Thickness of Upper Triassic and subsequent units are poorly constrained. Relicts of Upper Triassic rocks (Keuper and ophites) between the overturned limb and autochthon remain from its extrusion while the fold nappe progressively evolved

#### ORCID

Norbert Caldera [ID https://orcid.org/0000-0002-2383-4097](https://orcid.org/0000-0002-2383-4097)  
 Antonio Teixell [ID https://orcid.org/0000-0002-7423-6361](https://orcid.org/0000-0002-7423-6361)  
 Albert Griera [ID https://orcid.org/0000-0003-4598-8385](https://orcid.org/0000-0003-4598-8385)  
 Pierre Labaume [ID https://orcid.org/0000-0002-1151-3317](https://orcid.org/0000-0002-1151-3317)  
 Abdeltif Lahfid [ID https://orcid.org/0000-0002-1203-3438](https://orcid.org/0000-0002-1203-3438)

#### REFERENCES

- Abd Elmola, A., Charpentier, D., Buatier, M., Lanari, P., & Monié, P. (2017). Textural-chemical changes and deformation conditions registered by phyllosilicates in a fault zone (Pic de Port Vieux thrust, Pyrenees). *Applied Clay Science*, 144, 88–103. <https://doi.org/10.1016/j.clay.2017.05.008>
- Austin, N., Evans, B., Herwegh, M., & Ebert, A. (2008). Strain localization in the Morcles nappe (Helvetic Alps, Switzerland). *Swiss Journal of Geosciences*, 101, 341–360. <https://doi.org/10.1007/s00015-008-1264-2>
- Bellahsen, N., Bayet, L., Denele, Y., Waldner, M., Airaghi, L., Rosenberg, C., Dubacq, B., Mouthereau, F., Bernet, M., Pik, R., Lahfid, A., & Vacherat, A. (2019). Shortening of the axial zone, Pyrenees: Shortening sequence, upper crustal mylonites and crustal strength. *Tectonophysics*, 766, 433–452. <https://doi.org/10.1016/j.tecto.2019.06.002>
- Beyssac, O., Goffé, B., Chopin, C., & Rouzaud, J.-N. (2002). Raman spectra of carbonaceous material in metasediments: A new geothermometer. *Journal of Metamorphic Geology*, 20, 859–871. <https://doi.org/10.1046/j.1525-1314.2002.00408.x>
- Beyssac, O., Goffé, B., Petitet, J.-P., Froigneux, E., Moreau, M., & Rouzaud, J.-N. (2003). On the characterization of disordered and heterogeneous carbonaceous materials by Raman spectroscopy. *Spectrochimica Acta Part A: Molecular and Biomolecular Spectroscopy*, 59, 2267–2276. [https://doi.org/10.1016/S1386-1425\(03\)00070-2](https://doi.org/10.1016/S1386-1425(03)00070-2)
- Beyssac, O., Simoes, M., Avouac, J. P., Farley, K. A., Chen, Y.-G., Chan, Y.-C., & Goffé, B. (2007). Late Cenozoic metamorphic evolution and exhumation of Taiwan. *Tectonics*, 26. <https://doi.org/10.1029/2006TC002064>
- Burkhard, M. (1988). L'Helvetique de la bordure occidentale du massif de l'Aar (evolution tectonique et metamorphique). *Eclogae Geologicae Helveticae*, 81, 63–114.
- Casey, M., & Dietrich, D. (1997). Overthrust shear in mountain building. In S. Sengupta (Eds.), *Evolution of geological structures in micro- to macro-scales* (pp. 119–142). Springer. [https://doi.org/10.1007/978-94-011-5870-1\\_8](https://doi.org/10.1007/978-94-011-5870-1_8)
- Choukroune, P., & ECORS Team. (1989). The ECORS deep seismic profile reflection data and the overall structure of an orogenic belt. *Tectonics*, 8, 23–29.
- Clerc, C., & Lagabrielle, Y. (2014). Thermal control on the modes of crustal thinning leading to mantle exhumation: Insights from the Cretaceous Pyrenean hot paleomargins. *Tectonics*, 33, 1340–1359. <https://doi.org/10.1002/2013TC003471>
- Clerc, C., Lahfid, A., Monié, P., Lagabrielle, Y., Chopin, C., Poujol, M., Boulvais, P., Ringenbach, J. C., Masini, E., & de St Blanquat, M. (2015). High-temperature metamorphism during extreme thinning of the continental crust: A reappraisal of the North Pyrenean passive paleomargin. *Solid Earth*, 6, 643–668. <https://doi.org/10.5194/se-6-643-2015>
- Cochelin, B. (2016). Champ de deformation du socle paléozoïque des Pyrénées. *Sciences de la Terre. Université Toulouse 3 Paul Sabatier (UT3 Paul Sabatier)*. Français.
- Corre, B. (2017). *La bordure nord de la plaque Ibérique à l'Albo-Cénomanién. Architecture d'une marge passive de type ductile (Chaînes Béarnais, Pyrénées Occidentales)*. Sciences de la Terre. PhD thesis, Université Rennes 1, France.
- Déramond, J., Graham, R., Hossack, H., Baby, J. R., Crouzet, P., & Crouzet, G. (1985). Nouveau modèle de la chaîne des Pyrénées. *Comptes Rendus de L'Académie des Sciences, Paris*, 301, 1213–1216.
- Dietrich, D., & Casey, M. (1989). A new tectonic model for the Helvetic nappes. *Geological Society, London, Special Publications*, 45, 47–63. <https://doi.org/10.1144/GSL.SP.1989.045.01.03>

- Dumont, T., Replumaz, A., Rouméjon, S., Briais, A., Rigo, A., & Bouillin, J.-P. (2015). Microseismicity of the Béarn range: Reactivation of inversion and collision structures at the northern edge of the Iberian plate. *Tectonics*, 34, 934–950. <https://doi.org/10.1002/2014TC003816>
- Ebert, A., Herwegh, M., Berger, A., & Pfiffner, O. A. (2008). Grain coarsening maps for polyminerale carbonate mylonites: A calibration based on data from different Helvetic nappes (Switzerland). *Tectonophysics*, 457, 128–142. <https://doi.org/10.1016/j.tecto.2008.05.007>
- Ebert, A., Herwegh, M., Evans, B., Pfiffner, A., Austin, N., & Vennemann, T. (2007). Microfabrics in carbonate mylonites along a large-scale shear zone (Helvetic Alps). *Tectonophysics*, 444, 1–26. <https://doi.org/10.1016/j.tecto.2007.07.004>
- Ferrill, D. A., Morris, A. P., Evans, M. A., Burkhard, M., Groshong Jr., R. H., & Onasch, C. M. (2004). Calcite twin morphology: A low-temperature deformation geothermometer. *Journal of Structural Geology*, 26(8), 1521–1529. <https://doi.org/10.1016/j.jsg.2003.11.028>
- Fitzgerald, P. G., Muñoz, J. A., Coney, P. J., & Baldwin, S. L. (1999). Asymmetric exhumation across the Pyrenean orogen: Implications for the tectonic evolution of a collisional orogen. *Earth and Planetary Science Letters*, 173(3), 157–170. [https://doi.org/10.1016/S0012-821X\(99\)00225-3](https://doi.org/10.1016/S0012-821X(99)00225-3)
- Golberg, J. M., & Leyreloup, A. F. (1990). High temperature-low pressure Cretaceous metamorphism related to crustal thinning (Eastern North Pyrenean Zone, France). *Contributions to Mineralogy and Petrology*, 104, 194–207. <https://doi.org/10.1007/BF00306443>
- Herwegh, M., Berger, A., Glotzbach, C., Wangenheim, S., Mock, S., Wehrens, P., Baumberger, R., Egli, D., & Kissling, E. (2020). Late stages of continent-continent collision: Timing, kinematic, evolution and exhumation of the Northern rim (Aar Massif) of the Alps. *Earth-Science Reviews*, 200, 102959. <https://doi.org/10.1016/j.earscirev.2019.102959>
- Herwegh, M., & Pfiffner, O. A. (2005). Tectono-metamorphic evolution of a nappe stack: A case study of the Swiss Alps. *Tectonophysics*, 404, 55–76. <https://doi.org/10.1016/j.tecto.2005.05.002>
- Jammes, S., Manatschal, G., Lavier, L., & Masini, E. (2009). Tectonosedimentary evolution related to extreme crustal thinning ahead of a propagating ocean: Example of the western Pyrenees. *Tectonics*, 28, 1–24. <https://doi.org/10.1029/2008TC002406>
- Jolivet, M., Labaume, P., Monié, P., Brunel, M., Arnaud, N., & Campani, M. (2007). Thermochronology constraints for the propagation sequence of the south Pyrenean basement thrust system (France–Spain). *Tectonics*, 26(5), 1–17. <https://doi.org/10.1029/2006TC002080>
- Labaume, P., Meresse, F., Jolivet, M., Teixell, A., & Lahfid, A. (2016). Tectonothermal history of an exhumed thrust-sheet-top basin: An example from the south Pyrenean thrust belt. *Tectonics*, 35, 1280–1313. <https://doi.org/10.1002/2016TC004192>
- Labaume, P., & Teixell, A. (2020). Evolution of salt structures of the Pyrenean rift (Chainons Béarnais, France): From hyper-extension to tectonic inversion. *Tectonophysics*, 785, 228451. <https://doi.org/10.1016/j.tecto.2020.228451>
- Lacombe, O., & Bellahsen, N. (2016). Thick-skinned tectonics and basement-involved fold-thrust belts: Insights from selected Cenozoic orogens. *Geological Magazine*, 153, 763–810. <https://doi.org/10.1017/S0016756816000078>
- Lagabrielle, Y., Labaume, P., & de Saint Blanquat, M. (2010). Mantle exhumation, crustal denudation, and gravity tectonics during Cretaceous rifting in the Pyrenean realm (SW Europe): Insights from the geological setting of the Iherzolite bodies. *Tectonics*, 29, 1–26. <https://doi.org/10.1029/2009TC002588>
- Lahfid, A., Beyssac, O., Deville, E., Negro, F., Chopin, C., & Goffé, B. (2010). Evolution of the Raman spectrum of carbonaceous material in low-grade metasediments of the Glarus Alps (Switzerland). *Terra Nova*, 22, 354–360. <https://doi.org/10.1111/j.1365-3121.2010.00956.x>
- Majesté-Menjoulas, C. (1979). *Evolution alpine d'un segment de la chaîne varisque*. Nappe de Gavarnie, chevauchements Cinq-Monts-Gentiane (Pyénées centrales et occidentales). Thesis Université de Toulouse, 343 pp.
- Masini, E., Manatschal, G., Tugend, J., Mohn, G., & Flament, J.-M. (2014). The tectono-sedimentary evolution of a hyper-extended rift basin: The example of the Arzacq-Mauléon rift system (Western Pyrenees, SW France). *International Journal of Earth Sciences*, 103, 1569–1596. <https://doi.org/10.1007/s00531-014-1023-8>
- Metcalfe, J. R., Fitzgerald, P. G., Baldwin, S. L., & Muñoz, J. A. (2009). Thermochronology of a convergent orogen: Constraints on the timing of thrust faulting and subsequent exhumation of the Maladeta Pluton in the Central Pyrenean Axial Zone. *Earth and Planetary Science Letters*, 287(3–4), 488–503. <https://doi.org/10.1016/j.epsl.2009.08.036>
- Mouthereau, F., Filleaudeau, P.-Y., Vacherat, A., Pik, R., Lacombe, O., Fellin, M. G., Castelltort, S., Christophoul, F., & Masini, E. (2014). Placing limits to shortening evolution in the Pyrenees: Role of margin architecture and implications for the Iberia/Europe convergence. *Tectonics*, 33, 2283–2314. <https://doi.org/10.1002/2014TC003663>
- Muñoz, J. A. (1992). Evolution of a continental collision belt: ECORS-Pyrenees crustal balanced cross-section. In *Thrust tectonics* (pp. 235–246). [https://doi.org/10.1007/978-94-011-3066-0\\_21](https://doi.org/10.1007/978-94-011-3066-0_21)
- Nemanich, R. J., & Solin, S. A. (1979). First- and second-order Raman scattering from finite-size crystals of graphite. *Physical Review B*, 20, 392–401. <https://doi.org/10.1103/PhysRevB.20.392>
- Nibourel, L., Berger, A., Egli, D., Luensdorf, N. K., & Herwegh, M. (2018). Large vertical displacements of a crystalline massif recorded by Raman thermometry. *Geology*, 46, 879–882. <https://doi.org/10.1130/G45121.1>
- Pfiffner, O. A. (1993). The structure of the Helvetic nappes and its relation to the mechanical stratigraphy. *Journal of Structural Geology*, 15, 511–521. [https://doi.org/10.1016/0191-8141\(93\)90145-Z](https://doi.org/10.1016/0191-8141(93)90145-Z)
- Pfiffner, O. A. (2017). Thick-skinned and thin-skinned tectonics: A global perspective. *Geosciences*, 7(3), 71. <https://doi.org/10.3390/geosciences7030071>
- Pfiffner, O. A., Lehner, P., Heitzmann, P., Mueller, S. T., & Steck, A. (1997). *Deep structure of the Swiss Alps: Results from NFP 20*. Birkhäuser Verlag.
- Ramsay, J. G. (1981). Tectonics of the Helvetic nappes. *Geological Society, London, Special Publications*, 9, 293–309. <https://doi.org/10.1144/GSL.SP.1981.009.01.26>
- Saspiturry, N., Lahfid, A., Baudin, T., Guillou-Frotier, L., Razin, P., Issautier, B., Le Bayon, B., Serrano, O., Lagabrielle, Y., & Corre, B. (2020). Paleogeothermal gradients across an inverted hyperextended rift system: Example of the Mauléon Fossil Rift (Western Pyrenees). *Tectonics*, 39. <https://doi.org/10.1029/2020TC006206>
- Souquet, P. (1967). *Le Crétacé supérieur sudpyrénéen en Catalogne*. Aragon et Navarre. Thèse d'Etat: Université de Toulouse, 529 pp.
- Stipp, M., Stünitz, H., Heilbronner, R., & Schmid, S. M. (2002). Dynamic recrystallization of quartz: Correlation between natural and experimental conditions. *Geological Society of London, Special Publications*, 200(1), 171–190. <https://doi.org/10.1144/GSL.SP.2001.200.01.11>
- Teixell, A. (1993). Coupe géologique du massif d'Igoutze: Implications sur l'évolution structurale de la bordure sud de la Zone nord-pyrénéenne occidentale. *Comptes Rendus de l'Académie des Sciences, Paris*, 316, 1789–1796.
- Teixell, A. (1996). The Ansó transect of the southern Pyrenees: Basement and cover thrust geometries. *Journal of the Geological Society of London*, 153, 301–310. <https://doi.org/10.1144/gsjgs.153.2.0301>
- Teixell, A. (1998). Crustal structure and orogenic material budget in the west central Pyrenees. *Tectonics*, 17(3), 395–406. <https://doi.org/10.1029/98TC00561>
- Teixell, A., García Sansegundo, J., & Zamorano, M. (1994). Memoria de la Hoja no 144 (Anso). *Mapa Geológico de España E. 1:50.000 (MAGNA)*, Segunda Serie, Primera edición. IGME, 62 pp.
- Teixell, A., Labaume, P., Ayarza, P., Espurt, N., de Saint Blanquat, M., & Lagabrielle, Y. (2018). Crustal structure and evolution of the Pyrenean-Cantabrian belt: A review and new interpretations from recent concepts and data. *Tectonophysics*, 724–725, 149–170. <https://doi.org/10.1016/j.tecto.2018.01.009>



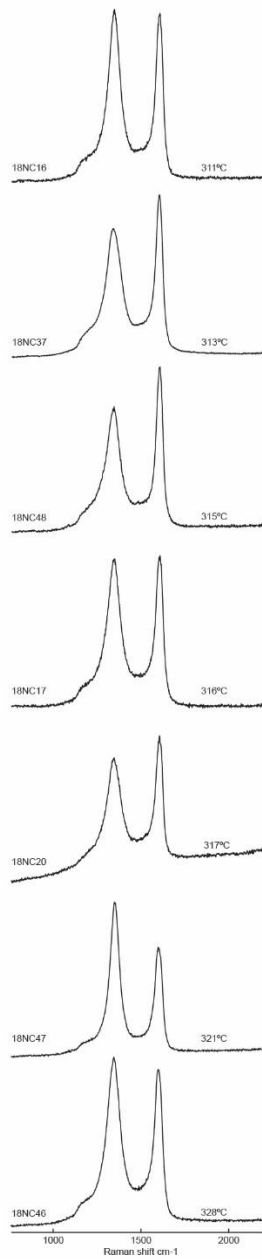
- Teixell, A., Labaume, P., & Lagabrielle, Y. (2016). The crustal evolution of the west-central Pyrenees revisited: Inferences from a new kinematic scenario. *Comptes Rendus - Geoscience*, 348, 257–267. <https://doi.org/10.1016/j.crte.2015.10.010>
- Ternet, Y. (1965). Étude du synclinal complexe des Eaux-Chaudes (Basses-Pyrénées), *Thèse Doctorat 3<sup>e</sup> Cycle: Faculté des sciences de l'Université de Toulouse*, 332 pp.
- Ternet, Y., Majeste-Menjoulas, C., Canerot, J., Baudin, T., Cocherie, A., Guerrot, C., & Rossi, P. (2004). *Carte géologique de la France: Laruns-Somport*. Bureau de Recherches Géologiques et Minières, scale 1:50,000, feuille no 1069.
- Tuinstra, F., & Koenig, J. L. (1970). Raman spectrum of graphite. *The Journal of Chemical Physics*, 53, 1126–1130. <https://doi.org/10.1063/1.1674108>
- Weber, J. C., Ferrill, D. A., & Roden-Tice, M. K. (2001). Calcite and quartz microstructural geothermometry of low-grade metasedimentary rocks, Northern Range, Trinidad. *Journal of Structural Geology*, 23(1), 93–112. [https://doi.org/10.1016/S0191-8141\(00\)00066-3](https://doi.org/10.1016/S0191-8141(00)00066-3)

**How to cite this article:** Caldera N, Teixell A, Grier A, Labaume P, Lahfid A. Recumbent folding in the Upper Cretaceous Eaux-Chaudes massif: A Helvetic-type nappe in the Pyrenees?. *Terra Nova*. 2021;00:1–12. <https://doi.org/10.1111/ter.12517>

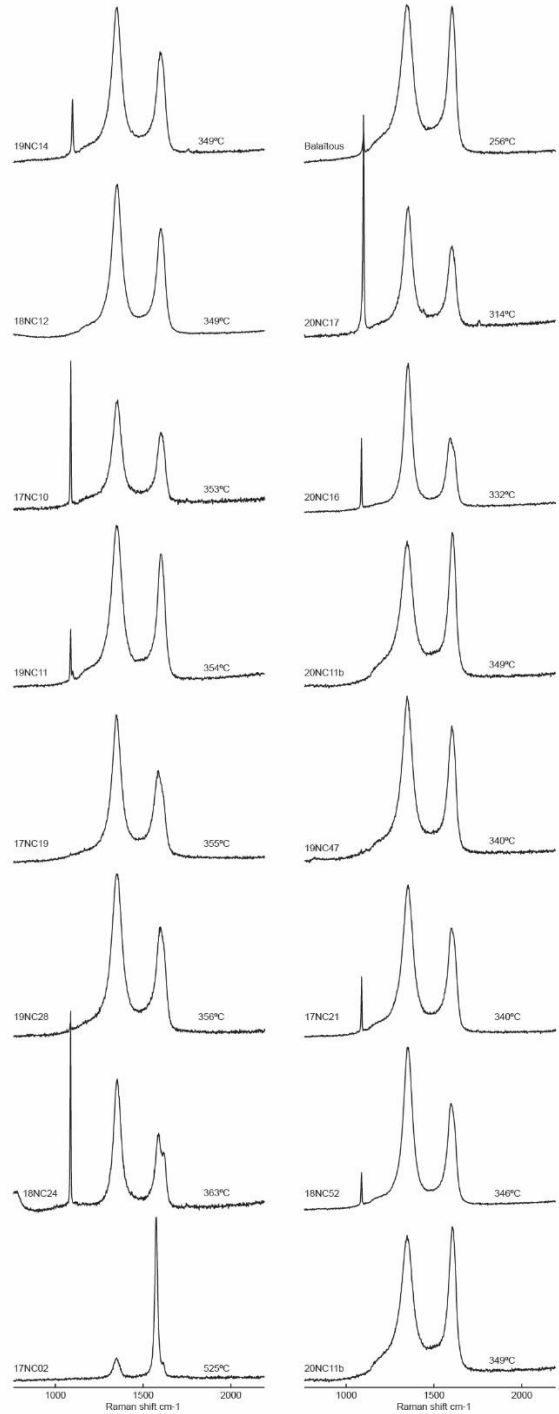
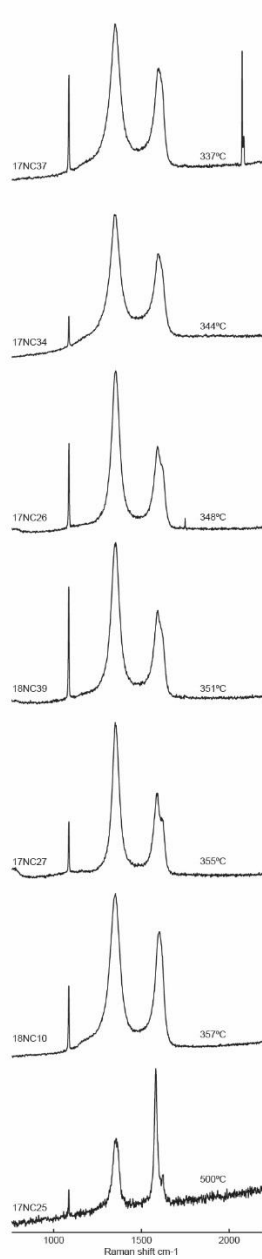
## Appendix II

### Autochthon Upper Cretaceous

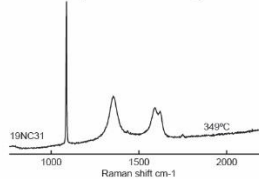
#### Normal Limb



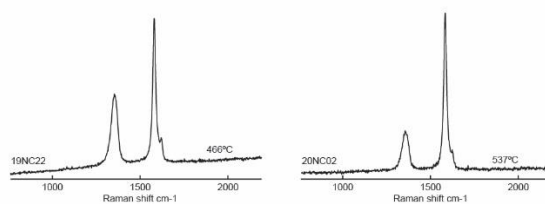
#### Overtured Limb



#### Upper Triassic (Muschelkalk)



#### Paleozoic basement







Petroleum Experts